Achieving Enantiopurity Through Directed Evolution and Crystallization under on-Equilibrium Conditions

Clément Pinètre

Normandie Université

UNIVERSITÉ DE ROUEN NORMANDIE

THÈSE

Pour obtenir le diplôme de doctorat

Spécialité **PHYSIQUE**

Préparée au sein de l'**Université de Rouen Normandie**

Achieving Enantiopurity Through Directed Evolution and Crystallization under Non-Equilibrium Conditions

Présentée et soutenue par

PINÈTRE CLÉMENT

Thèse soutenue le 16/12/2024

devant le jury composé de :

MME DUPRAY VALÉRIE	Maître de Conférences - Université de Rouen Normandie (URN)	Directeur de thèse
MME GOUTAUDIER CHRISTELLE	Professeur des Universités - Université Claude Bernard - Lyon 1	Président du jury
M. BRANDEL CLEMENT	Maître de conférences - Université de Rouen Normandie (URN)	Co-encadrant
MME BAUDEQUIN CHRISTINE	Maître de Conférences - Université de Rouen Normandie (URN)	Membre du jury
M. LEYSSENS TOM	Professeur des Universités - LOUVAINS	Rapporteur du jury
M. NOORDUIN WIM L	Professeur des Universités - Université d'Amsterdam	Rapporteur du jury

Thèse dirigée par **DUPRAY VALÉRIE** (SCIENCES ET METHODES SEPARATIVES)

ED 591 PSIME

SMS Sciences et Méthodes Séparatives

To S. and S.

"Despite knowing the journey… and where it leads… I embrace it, and I welcome every moment of it."

Villeneuve, D. (2016). *Arrival*. Paramount Pictures

Chapter II: Solid-State Deracemization & Non-Equilibrium Conditions

Chapter III: Enantiopurity by Directed Evolutionary Design: The case of praziquantel

Chapter IV: Towards a generalized directed evolution: the case of proxyphylline

Acknowledgments

First of all, I would like to thank both our new and former head of the lab, Prof. Pascal Cardinael and Prof. Gérard Coquerel, who gave me the opportunity to achieve my thesis in the SMS laboratory. Gérard, thank you for all the opportunity you brought to me since the past 6 years, your communicative passion for solid-state chemistry and chiral resolution, your availability, for having believed in me since my first step in the lab and the ongoing research we are still doing together. Thanks are also due to Prof. Joop H. ter Horst who initiated the research project RIN Recherche 2020 Chair of Excellence ICF “Industrial Crystallization Fundamentals”

My deepest thanks to my supervision team, Dr. Valérie Dupray and Dr. Clément Brandel, for your unwavering support and confidence throughout these three years. You gave me a complete freedom to explore, always believing in my potential and pushed me to be the best Ph.D. student I could be. Valérie, thank you for handling, among many other things, the administrative matters and allowing to focus on my work with peace of mind over these three years, despite the various setbacks we faced along the way. Your support made a world of difference. Clément, I am especially grateful for the countless hours you spent reviewing drafts and helping me improve my writing skills. This thesis would not be what it is today without your help, guidance and valuable knowledge you shared with me.

During these three years, I was lucky enough to supervise nine interns on the different research projects I had. They have all contributed, each in their own way, to the success of these projects, allowing me in turn to extend the same opportunities that were once given to me. In this regard, I would like to thank Azahari, Lars, Hafsa, Ines, Maxime, Max, Mohammed, Ludovic and Loïc.

I want to take this opportunity to sincerely thank Dr. Christine Baudequin for the helping hand you offered to a poor student in need of an internship six years ago. That first experience in a research lab was transformative for me, and I would not have embarked on this Ph.D. journey without it. While it may have seemed like a small gesture to you, it had a profound impact on my life. You are the kind of teacher who truly shapes your students’ futures. Please continue to be the inspiring teacher and researcher that you are.

I would also want to extend my gratitude to Prof. Christelle Goutaudier, Dr. Christine Baudequin Prof. Tom Leyssens and Prof. Wim L. Noorduin for agreeing to be part of the jury for the present thesis, thank you for your availably and kindness. I look forward to your comments and the engaging discussion that will arise during the defence.

My sincere thanks also go to Dr. Yohann Cartigny, for your generous help and support, even though you were under no obligation to provide it. Your passion for teaching is truly contagious and have been inspiring, and like Christine, you are the kind of teacher who leaves a lasting impact on your student.

During this thesis, I was lucky enough to work with several worldwide scientist without whom the different aspect of this work would not be as it looks like now. In this regard, I would like to thank Prof. Joop H. ter Horst, Prof. Richard M. Kellog, Dr. Michel Leeman, Dr. Paul T. Tinnemans, Sjoerd W. van Dongen and Prof Wim. L. Noorduin.

I want to thank all the permanent members of the SMS laboratory, Morgane (stay ready to receive crystals of a known, or perhaps unknown, molecule), Nicolas, Loïc, Ivo and Gabin. I also want to thank the different student who have passed through the lab: Marine, Aurelien, Laureline, Mélody, Charline, Jin, Chuey, Félix, Chrystal, Chang, Nino, Zoe, Elisa, Luis. A special thanks to Hugo, more than just a friend, you truly became part of my “famille d’ici”.

Thanks to my family, mum, dad and grandma, my sisters Justine and Barbara, my brother Julien and my entire family-in-laws. Your unwavering support has meant a world to me.

Finally, and most importantly, my heartfelt thanks to my wife, Sarah and my son Sacha. You have been my source of strength and positivity throughout this journey. You gave me reasons to achieve this thesis and allowed me to be in the good mind set. You represent the most important part of my life, and I could not ask for anything better.

GENERAL INTRODUCTION

¨All boundaries are conventions waiting to be transcended. One may transcend any conventions, if only one can first conceive of doing so¨

Tykwer, T., Wachowski, L., & Wachowski, L. *(2012). Cloud Atlas. Warner Bros.*

The past decades have witnessed an increasing interest in the design of chiral materials. Indeed, the use of enantiomerically pure chiral substances offers unique and innovative properties to several products, including optical and electrochemical sensors, molecular selectors, catalysts and bioactive substances. This allows the development of highly selective chiral stationary phases, active pharmaceutical ingredients, asymmetric catalysts etc. Accessing pure enantiomer is therefore of paramount importance.

Among the various chiral resolution methods developed so far (*e.g.* asymmetric or chiral pool synthesis, preparative chromatography, biocatalysis etc.), the crystallization-based approaches, for instance solid-state deracemization or preferential crystallization, stand out as the most promising. Even though efficient and economically sustainable, it is commonly admitted that most of these methods require the enantiomers to spontaneously sort into separate enantiopure crystals (*i.e.* racemic conglomerates). Unfortunately, this behaviour is rare and unpredictable: the overwhelming majority of enantiomeric mixtures crystallize together into thermodynamically favoured racemic compounds (90-95%), which hinders such separation. However, although the poor conglomerate prevalence stands as a severe constraint for crystallization-based chiral resolution methods, this thermodynamic limitation overlooks the inherent out-of-equilibrium nature of crystallization. This aspect will be addressed in the present Ph.D. thesis through the study of three different families of chemically related compound based on bio-relevant chiral cores.

Chapter I provides the fundamental concepts required for a comprehensive understanding of this work and a literature review of key topics relevant to this study.

Then, the manuscript is divided in three chapters followed by a general discussion and conclusion:

Chapter II will cover new chiral resolution strategies adapted to systems unsuitable for solid-state deracemization by (i) using an out-of-equilibrium asymmetric dissolution rate between non-racemizable enantiomers forming a conglomerate and (ii) making use of a highly discriminative chiral recognition phenomenon occurring during the formation of conglomerate host-guest mixed crystal structures between chemically related chiral triazole ketone. It presents the first result of an alternative chiral resolution of systems that exhibit a

stable racemic compound but also a closely related conglomerate-forming system, renewing interest in the study of libraries of chemically related compounds.

Chapter III is devoted to the study of chemically related compounds based on the bio-relevant chemical core praziquantel through a fruitful collaboration with Richard M. Kellogg and Michel Leeman (Symeres company), as well as Sjoerd W. van Dongen and Willem L. Noorduin (AMOLF). The results reported in this chapter represent the most important portion of the results produced by this thesis, both in terms of scientific impact and time spent. Several chiral derivatives of Praziquantel are synthesized and thermodynamically characterized, with their solid-state landscape investigated. The vast majority of these system formed racemic compounds. However, the present work shows that a large proportion of these "unfavourable" chiral systems are suitable for crystallization-based chiral resolution methods, by taking advantage of the kinetics of crystallization. In particular, this work allowed the design of what is likely the most important and innovative concept of this PhD work: among this family of racemic compounds, we identify a thermodynamic quantity that is correlated to the molecular features of the different derivatives of praziquantel. We show that this thermodynamic quantity is a powerful tool to identify systems that can actually be resolved by preferential crystallization, notwithstanding the quasi-systematic presence of stable racemic compound. Thus, in view to elect a system that could undergo facile preferential crystallization, we propose a directed evolution strategy that permits, starting from a given racemic compound deemed unresolvable, to straightforwardly identify the most promising chemical derivation. The generality of these finding is discussed in detail.

Chapter IV provides an application of this directed evolution strategy based on the synthesis of a family of 1,3-dimethylxantine-based chiral derivatives. This family is made of molecules built from a rigid xanthine core, with few H-bonding capabilities, and a flexible moiety from which the H-bond character is chemically modulated. Two racemic compounds of this family, proxyphylline and diprophylline, have already been investigated prior to this PhD thesis: both compounds could actually be resolved by preferential crystallization by maintaining long induction times for the spontaneous crystallization of the racemic compounds. However, the solid-state landscape between proxyphylline enantiomers was missing, and it was necessary to re-investigate their associated stable and metastable equilibria. Then, since nucleation inhibitions have been attributed to the conformational

features of these molecules, the present work aimed at modulating both their flexibility and the H-bonding capacity. This allowed to study the impact of such chemical derivation on racemic compound stabilities and polymorphism. In particular, we show that enhancing the H-bonding capacity of these molecules permits the engineering of a stable conglomerate-forming system. That is in good agreement with the theory developed in Chapter III.

The study of chemically related derivatives and the chiral resolution by crystallization under non-equilibrium conditions are thus at the centre of the present work. The general concept of this Ph.D. manuscript is to show that the conventionally accepted boundaries of crystallization-based chiral resolution methods can actually be bypassed by the clever use of both thermodynamic and kinetics.

CHAPTER I

CRYSTALLOGENESIS AND THERMODYNAMIC OF CHIRAL COMPOUNDS

This first chapter is devoted to a broad overview of crystallogenesis (*i.e.,* crystallization and crystallography), chirality and thermodynamics of chiral compounds. While all aspects of these vast scientific fields will not be exhaustively covered, the essential information required for a good understanding of this work will be provided.

I.1 - Chirality

The story of chirality arises from an interplay between chemists, physicists, and biologists. The inception of this exploration can be traced back to the observations of the French mineralogist René-Just Haüy, who, in noting symmetrical hemihedral facets on quartz crystals, set the stage for the intricate study of chirality.[1] In 1815, further strides were made by the French physicist Jean Baptiste Biot by announcing the discovery of optically active compounds, for instance symmetrical quartz crystals rotating the plane of the polarized light in opposite direction.[2] However, it was not until 1820 that this discovery took on new significance when Sir John Herschel, an English polymath, demonstrated the correlation between the rotation of polarized light and the symmetry of hemihedral facets, establishing the first relationship between crystal morphology and the physical property of optically active compounds.[3]

Thereby, the French chemist Louis Pasteur worked on Tartaric acid in 1848, referred to as 'racemic acid' by French scientist Gay-Lussac due to its lack of deviation of the polarized light whereas conventional Tartaric acid extract from wine did.[4] Pasteur noticed that the tetrahydrated double salt Sodium-Ammonium of Tartaric Acid could crystallize into two populations of mirror-images crystals. Emulating Herschel's approach with quartz crystals, he manually separated the two populations of crystals and discerned their opposite deviations of the polarized light. In achieving the first chiral resolution through crystallization, Pasteur not only made a significant breakthrough but also postulated that these symmetric crystals were composed of mirror-image molecules, laying the foundational understanding of chirality.[5–8]

In 1874, Jacobus Henricus Van't Hoff and Joseph Achille Le Bel independently proposed that tetrahedral carbon atoms could be source of molecular chirality.[9–11] Their insights posited that a carbon atom bonded to four different substituents could give rise to non-superimposable mirror image molecules. This conceptual leap marked a crucial advancement in the understanding of molecular chirality.

I.1.1 - Definition

The first definition of chirality was introduced by the English physicist Lord Kelvin. An object, or group of objects, is defined as chiral if its image in a plane mirror cannot be brought to coincide with itself.[12] The terms “chiral” is derived from “cheir”, the Greek word for hand, indeed one of the most familiar chiral objects (Figure I - 1).

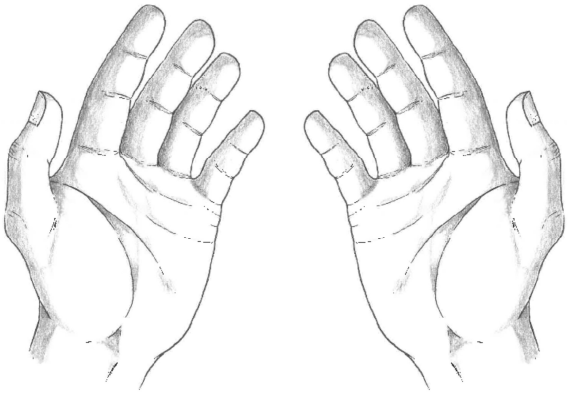

Figure I - 1. Right and left hand are image of each other in mirror but cannot be superimposed.[13]

I.1.2 - Chirality in chemistry

Molecular chirality can arise from three distinct elements. The first element is a stereogenic atom which is the most prevalent form of chirality in organic compounds (carbon, sulfur, phosphorus, transition metal).[14–16] A typical example is that of a tetrahedral carbon linked to four different substituents. The second element is axial chirality which is commonly observed in atropoisomeric substituted biaryl compounds wherein the aryl-aryl bond rotation is constrained. The third element is a planar chirality which is well illustrated by substituted Ferrocene derivative where the two non-coplanar rings are fixed in a specific configuration (Figure I - 2).

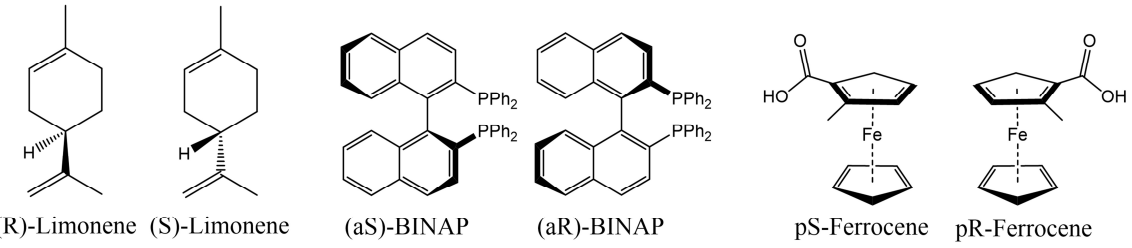

Figure I - 2. Chirality induced by a stereogenic centre on Limonene (Left). Chirality induced by an axis of chirality (steric strain) on 2,2’-bis(diphenylphosphino)-1,1’-binaphthyl (BINAP, middle). Planar chirality in substituted Ferrocene derivative (right).

I.1.2.1 - Nomenclature

A chiral molecule with one stereogenic centre has two possible 3D configurations. The two stereoisomers are mirror image of each other and are termed enantiomers. Various nomenclatures are employed to describe the chirality of enantiomers. According to the Cahn-Ingol-Prelog rules (CIP),[17,18] an asymmetric carbon is assigned *R* for rectus (right) or *S* for sinister (left) based on the priority of its substituents (Figure I - 3).

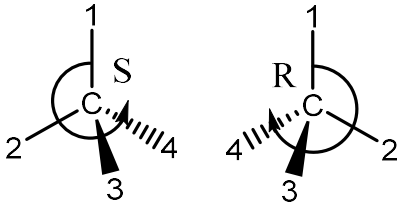

Figure I - 3. Determination of the configuration of an asymmetric carbon using the Cahn-Ingol-Prelog rules: clockwise R, anti-clockwise S.

The CIP rules extend beyond stereogenic centres to include axial and planar chirality. In these instances, enantiomers are designated as *aR* and *aS* for axial chirality, and *pR* and *pS* for planar chirality. The labels *aR* and *aS* denote configurations with distinct spatial arrangements around the chiral axis, while *pR* and *pS* distinguish configurations in the context of planar chirality. This comprehensive application of the CIP rules allows for precise characterization of enantiomeric relationships in molecules exhibiting axial or planar chirality.

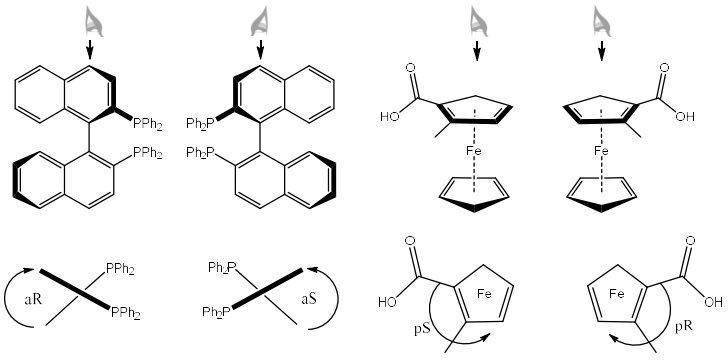

Figure I - 4. Configuration of BINAP (left) : order of priorities of the groups attached to the axial section viewed along this axis. Configuration of substituted Ferrocene derivatives (right) : Newman projection looking from the substituted ring.

The (*D*)- and (*L*)- labelling is commonly employed for sugars and amino acids depending on the position of the substituent with the highest priority in the Fisher projection. (Figure I - 5). This system, originally proposed by Emil Fischer,[19] assigns the (*D*)-configuration when the highest

priority substituent is on the right side in the Fischer projection and (*L*)-configuration when it is on the left side. The (*D*)- and (*L*)- labels provide a convenient and standardized way to denote the stereochemistry of chiral centres in these biomolecules.

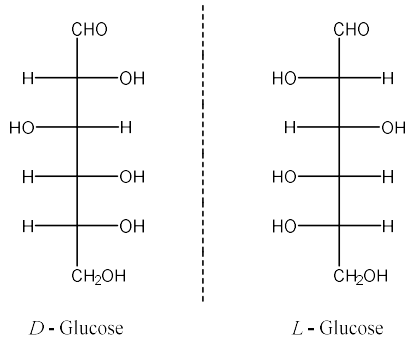

Figure I - 5. Fisher projection of *D*- and *L*-Glucose.

All these nomenclatures are possible if the 3D configuration of the molecule is known. Otherwise, their opposite interaction with the polarized light serves as a valuable tool for differentiation. Enantiomers that rotate the plane of polarized light to the right are termed (+) or *d*- (dextrogyre), while those rotating it to the left are designated (-) or *l*- (levogyre). This optical activity provides a practical means to distinguish between enantiomers in the absence of explicit knowledge about their three-dimensional arrangements.

I.1.2.2 - Chiral Active Pharmaceutical Ingredient (API)

Enantiomers have identical scalar properties (*e.g.,* solubility, melting temperature, associated enthalpies, density etc.) but share opposite vectorial properties, as illustrated by their opposite interaction with the polarized light. Thus, their interaction with a chiral medium depends on their handedness.

As the human body can be considered as a chiral entity due to the homochirality of life, two enantiomers of a chiral API can therefore have different toxicologic effects, pharmacokinetics etc. Indeed, drugs are assimilated through biological receptors, depending on their tri-dimensional shape: a specific receptor could therefore interact with one enantiomer while the other enantiomer could not (Figure I - 6).

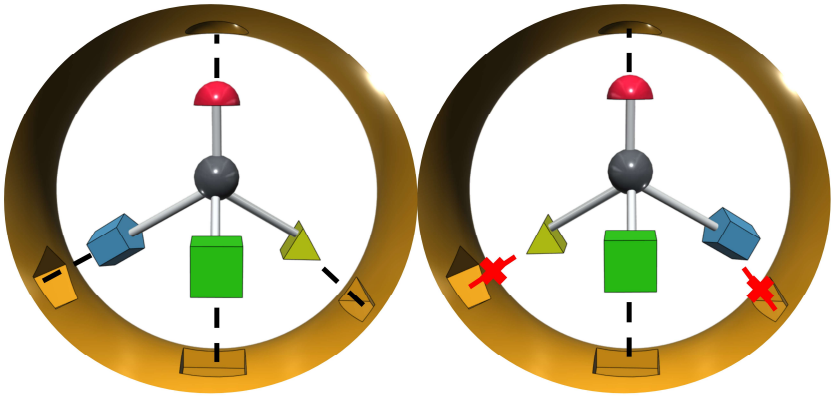

Figure I - 6. Schematic representation of an interaction between a chiral API and a biological receptor.

This symmetrical behaviour can be useful in some cases as illustrated by the API Thyroxine: one enantiomer is used to treat thyroid hormone deficiencies while the other enantiomer is a cholesterol-lowering drug.[20] Nevertheless, in many cases, the counter enantiomer is often considered as an impurity (*i.e.* distomer), either because of its inactive behaviour (*e.g.,* Praziquantel, Ibuprofen) or because of its harmful effects.[21,22] These concerns are of paramount importance considering that half of the commercialized drugs consists of chiral substances, in some cases marketed as racemic mixtures (*i.e.* an equimolar mixtures of both enantiomers).[23] One striking example is Thalidomide, causing birth defects to nearly 10,000 new-born children.[24]

Since 1992, the development and approval of new stereoisomeric drugs were submitted to drastic rules by a rather strict policy from the *United States Food and Drug Administration* (FDA), as the undesirable enantiomer is considered as an impurity of the active enantiomer (*i.e.* eutomer).[25] Figure I - 7 displays the evolution of the New Molecular Entities (NMEs) approved by the FDA between 1991 and 2020.[26–28] It clearly shows that the proportion of newly-marketed racemates fell sharply from 2002 onwards to the benefit of achiral and enantiopure drugs to represent only a tiny proportion nowadays.

This policy stands out as a key factor influencing the prevailing trend of FDA-approved NMEs of recent decades. Therefore, accurate data are needed to ensure the safety and effectiveness of resulting racemate drugs.[29] However, obtaining such adequate data proves challenging in many cases, necessitating the pursuit of *de novo* enantiopure drug developments.[30] While achiral drugs undergo thorough scrutiny before approval as well, they are exempt of the aforementioned requirement as they exist solely as a single entity.

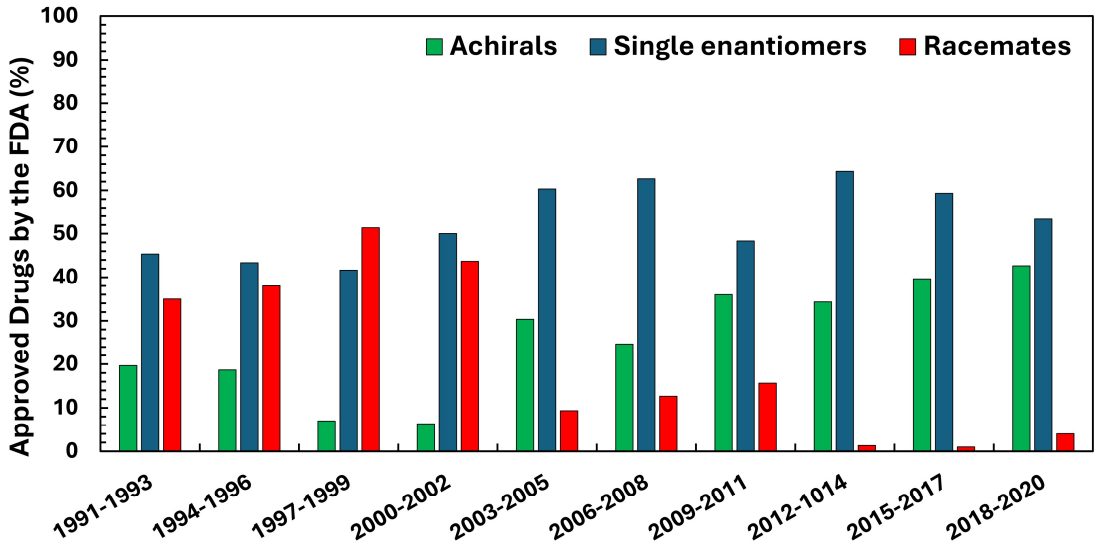

Figure I - 7. Distribution of FDA-approved drugs according to their chirality in the period 1991-2020. Diastereomeric mixtures are considered as racemates.

Additionally, another factor contributing to this phenomenon is the emergence of chiral switch processes. Halfway between therapeutical benefit and marketing strategy, such process refers to chiral drugs that have already been claimed, approved and marketed as racemates or mixtures of diastereomers, but have since been redeveloped as single enantiomers.[31–33] Besides having potentially significant improvement of therapeutic effect (*e.g.,* Cetirizine, Omeprazole),[34,35] chiral switch is also an opportunity for the pharmaceutical industry to provide relatively low-cost line extension of already marketed racemic drugs. The prevailing strategy is to introduce the single enantiomer version of a blockbuster racemate drug before the expiration of the racemic patent, preventing potential market competition from generic manufacturers. This approach is efficient as newly patented single enantiomer drugs frequently achieve rapid market dominance although the therapeutical benefits remains a subject of debate in some cases.[36–41]

I.2 - Crystallogenesis

Various administration routes are available for APIs, tailored to the specific attributes of the drug (*e.g.* tablets, capsules, pills, ointments, syrups, injections etc.). However, solid-state APIs are strongly favoured by manufacturers. They offer a relatively simplified isolation process, a high purity, provides remarkable physico-chemical stability and ease of handling.[42–45]

Nevertheless, before integrating solid-state APIs into industrial processes, it was imperative to enhance the fundamental comprehension of the solid-state and its properties.

I.2.1 - Crystallography

The solid-state represents one of the fundamental states of matter, alongside liquid, gas and plasma, distinguished by particles densely packed together resulting in structural rigidity. When the constituting particles (atoms or molecules) arrange themselves in a regular and repeating pattern throughout three dimensions, exhibiting a Long-Range Order (LRO, Figure I - 8a), the solid is termed crystalline. Conversely, when the particles lack of regular arrangement, displaying Short-Range Order (SRO, Figure I - 8b), the solid is considered as amorphous.[46,47] It should be noted that intermediate cases exist, such as liquid crystal or quasi-crystal, but will not be encountered in this work.[48,49]

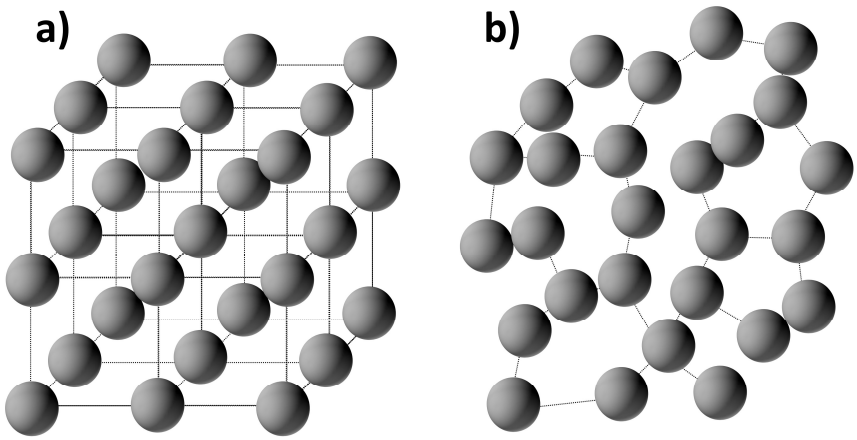

Figure I - 8. 3D schematic representation of (a) a Long-Rage Order (LRO) and (b) a Short-Range Order (SRO) in solids.

I.2.1.1 - Crystal systems, symmetries and point groups

Initially suggested by an abstract conceptualization of the solid-state matter,[50–52] the periodicity induced by a LRO has been demonstrated experimentally by diffraction of X-rays by crystals.[53] The entire crystal structure can be therefore fully described by a unit cell (*i.e.* the smallest volume with the highest symmetry), resulting from the association of a three-dimensional lattice (*x, y ,z ; α, β, γ)* and a chemical motif (Figure I - 9a).

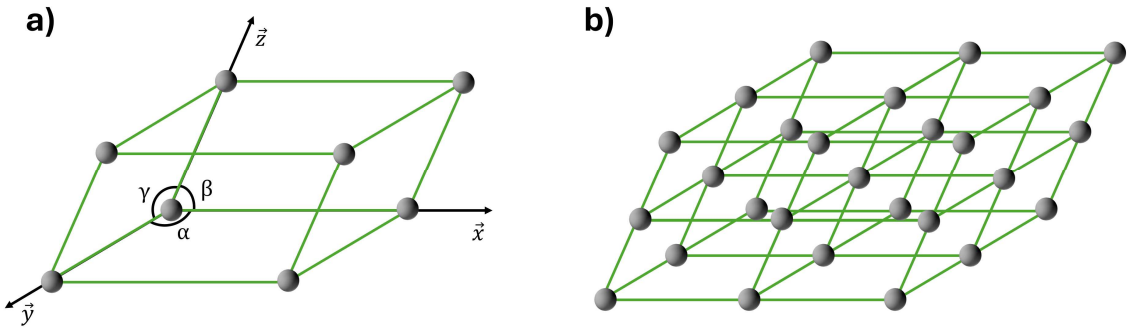

Figure I - 9. Schematic view of (a) a three-dimension lattice and (b) the crystalline packing induced by the periodicity. It should be noted that the values of *x, y, z and α, β, γ* are arbitrary chosen.

Seven crystal systems are derived from the different combinations of lattice parameters (Table I - 1). Moreover, the nodes of a unit cell (grey spheres in Figure I - 9) are periodically repeated to form the resulting crystal packing (Figure I - 9b), following the lattice translation $\vec{r} = \vec{a}u + \vec{b}v + \vec{c}w$ (where *u*, *v* and *w* are natural integers). Bravais referred to this lattice translation as the Primitive mode (P) alongside more complex ones, namely base-centred (A, B, C), body-centred (I) and face-centred (F) where ½ is a possible value for *u*, *v* and *w*. However, it is important to acknowledge that not every mode of translation is compatible with each crystal system, resulting in the 14 Bravais lattices (Table I - 1).[54,55]

The mathematical conceptualization of the group theory describes the inner symmetry of a chemical motif (Z). Indeed, a chemical motif is composed of an asymmetric unit (Z'), which is the smallest unit of repetition that can be used to generate the complete unit cell by applying 2D and 3D symmetry elements. Nevertheless, a limited number of 2D symmetry elements are compatible with the different crystal lattices, ranging from proper rotation n where $n \in [2; 6]\backslash\{5\}$ to improper rotation $\bar{n}$ where $\bar{n} \in [\bar{2}; \bar{6}]\backslash\{\bar{5}\}$, resulting in 32 point groups (PG) classified according to the dominant symmetry of the crystal lattice (Table I - 1).

Table I - 1. List of the 7 crystal systems and their respective point groups.

Crystal System	Mode compatibility	Cell parameters	Point group		
			NC	NA	CA
triclinic	P	a ≠ b ≠ c; α ≠ β ≠ γ	1		$\bar{1}$
monoclinic	P, C	a ≠ b ≠ c; α = γ = 90°; β ≠ 90°	2	m	2/m
orthorhombic	P, C, I, F	a ≠ b ≠ c; α = β = γ = 90°	222	mm2	mmm
trigonal	P	a = b = c; α = β = γ ≠ 90°	3 32	3m	$\bar{3}$ $\bar{3}$m
quadratic	P, I	a = b ≠ c; α = β = γ = 90°	4 422	$\bar{4}$ $\bar{4}$2m 4mm	4/m 4/mm m
hexagonal	P	a = b ≠ c; α = β =90°; γ = 120°	6 622	$\bar{6}$ $\bar{6}$m2 6mm	6/m 6/mm m
cubic	P, I, F	a = b = c; α = β = γ = 90°	23 432		m3 $\bar{4}$3m m3m

Although 2D symmetries are sufficient to generate the 32 PG, the addition of 3D symmetry elements remains necessary to fully construct a crystal structure. These symmetries are screw axes n_m (where $n \in [2;6]\backslash\{5\}, m \in [1;n-1]$) and glide planes (*a*, *b*, *c*, *n*, *d*) and give rise to the 230 space groups (SG).[56]

More importantly, three categories are derived from the 32 PG according to their compatibility with chirality: Non-Centrosymmetric Chiral (NC), Non-Centrosymmetric Achiral (NA) and Centrosymmetric Achiral (CA) (Table I - 1).[57] Indeed, the inherent symmetry of chiral molecules is affected by PG having improper rotation and/or mirror symmetries. In such space groups belonging to NA and CA PG, these symmetries prevent the preservation of the initial handedness as the opposite chirality is intrinsically reproduce within the same crystal. Consequently, determining the space group of a crystal structure plays a crucial role for assessing the chirality of molecules within that crystal as it may directly influence the physical

properties of the material, with significant implications for scientific fields as drug design for instance.

I.2.1.2 - Crystallography of small organic chiral molecules

Small organic chiral molecules have a high propensity to crystallize into crystal systems with low symmetry (*e.g.* triclinic, monoclinic, orthorhombic) as a result of their anisotropic electronic density and their low symmetry.[58]

The intermolecular interactions that ensure crystal cohesion are numerous. They range from the weakest chemical forces, for instance van der Waals forces (*i.e.* interactions between either permanent or induced molecular dipoles), π stacking (*i.e.* interactions between polarized aromatic cycles) or halogen bond (*i.e.* interactions between halogens atoms) to stronger chemical forces such as hydrogen bonds (*i.e.* interactions between strongly polarized hydrogens with heteroatoms) or coulombic interaction (*i.e.* interactions between ions of opposite charges).[59–71] These interactions lead to a periodic bond network called periodic bond chain (PBC).

I.2.1.3 - Introduction to polymorphism

Owing to the wide variety of atomic compositions and the typically high molecular flexibility of small organic chiral molecules, several PBCs and therefore several crystal structures are possible for a given compound: this phenomenon is referred to as Polymorphism.[72] This can be induced by different molecular conformations (*i.e.* conformational polymorphism) or different 3D packing while maintaining the same molecular conformation (*i.e.* packing polymorphism) (Figure I - 10).[73–77] This aspect will be further described in the manuscript (*cf.* I.3.1).

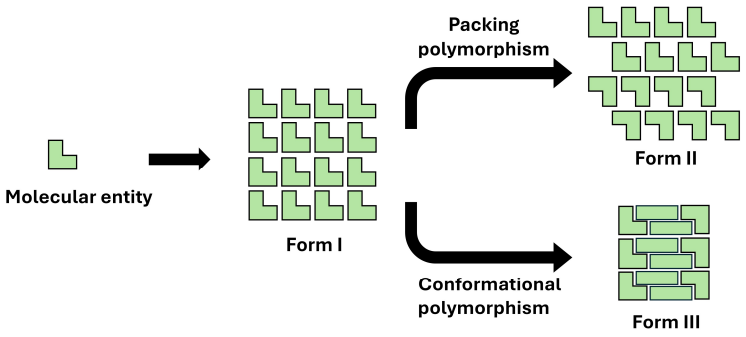

Figure I - 10. Schematic representation of packing and conformational polymorphisms.

I.2.2 - Crystallization

Crystallization is the process by which an ordered crystal emerges from an initially disordered state. This phase transition can therefore occur through many crystallization routes, ranging from vapor phases (*i.e.* condensation), molten phases (*i.e.* melt crystallization), amorphous solids (*i.e.* devitrification) or solution phases (*i.e.* solution crystallization). As it is the case with any physical phenomenon, development of theoretical frameworks is essential for a better understanding of such phenomena.

I.2.2.1 - Crystallization theories

A fundamental conceptualization of the crystallization process was provided by the classical nucleation theory (CNT).[78,79] This thermodynamic approach states that the crystallization proceeds through the stochastic formation and growth of ordered critical molecular aggregates, called nuclei. Assumed as spherical, these nuclei are a result of the balance between a destabilizing surface-based contribution ($\Delta G_s = 4\pi r^2\gamma$) and a stabilizing volume-based contribution ($\Delta G_v = \frac{4}{3}\pi r^3 \Delta g_v$). Indeed, the resulting surface formed by the molecular agglomeration results in an unfavourable interfacial tension (γ) with the surrounding disordered state (*e.g.* solution, vapor etc.) while generating a beneficial interfacial energy per unit of volume (Δg_v) between molecules of the same nature (Eq. I - 1).

$$\Delta G_n^{homo} = \Delta G_v + \Delta G_s = \frac{4}{3}\pi r^3 \Delta g_v + 4\pi r^2 \gamma \qquad \text{Eq. I - 1}$$

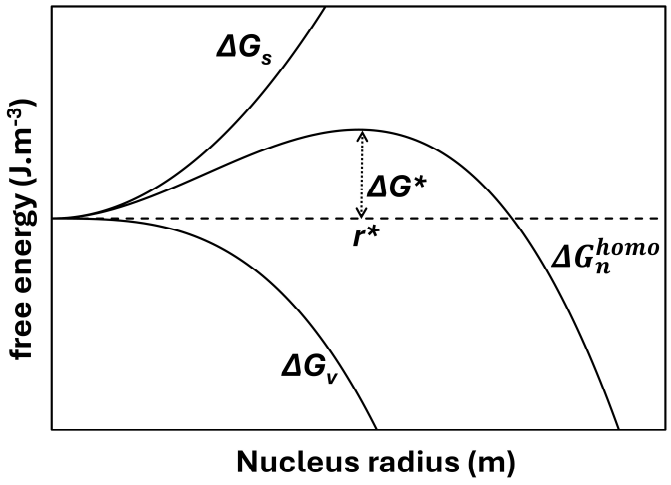

Figure I - 11. Evolution of the nucleus free energy ΔG_n resulting from the surface-based and volume-based terms predicted by the CNT in case of homogenous nucleation as function of the nucleus radius using arbitrary γ and Δg_v constants (Eq. 1).

Since the term Δg_v is always negative when crystallization occurs, the function $\Delta G_n = f(r)$ (Figure I - 11) combines a positive r^2 and a negative r^3 terms (with $r \in \mathbb{R}^+$). The qualitative functional analysis of ΔG_n reveals an initial dominance of the quadratic term until a critical nucleus radius is reached, where the cubic term takes over, causing ΔG_n to decreases (r^* in Figure I - 11).

These properties of ΔG_n are meaningful: While an aggregate with $r < r^*$ should redissolve, growth of a nucleus is expected for $r > r^*$. It also rationalizes the stochastic behaviour of crystallization by introducing an energy barrier (ΔG^*) that must be overcome, at least locally, to initiate the crystallization process. The critical radius r^* marks the extremum of the ΔG_n function, which is easily accessible by resolving the first derivative $\left[\frac{d\,\Delta G}{d\,r}\right]_{r \to r^*}$ (Eq. I - 2). Moreover, Eq. I - 2 can be used in conjunction with Eq. I - 1 to derive the associate energy barrier ΔG^* (Eq. I - 3).

$$r^* = \frac{-2\gamma}{\Delta g_v} \qquad \text{Eq. I - 2}$$

$$\Delta G_n^* = \frac{16\pi\gamma^3}{3(\Delta g_v)^2} \qquad \text{Eq. I - 3}$$

The abovementioned equations postulate that the spherical nuclei are surrounded by the crystallization bulk. However, agglomerates are more likely to be formed on templates (*e.g.* stirrer, glassware, insoluble particles etc.), thus reducing the destabilizing ΔG_s term by adding interfacial contributions Agglomerate-Template and Template-Bulk in Eq. I - 1. These contributions can be derived from the contact angle (θ) of each interface, leading to a stabilizing function $f(\theta)$. ΔG_n^{Hetero} is therefore the product of ΔG_n^{homo} and $f(\theta)$, indicating that ΔG_n^{Hetero} is always lower than ΔG_n^{hom} (Eq. I - 4).

$$\Delta G_n^{Hetero} = \Delta G_n^{homo}\, f(\theta) \qquad \text{with } f(\theta) = \frac{2 - 3\cos\theta + \cos^3\theta}{4} \qquad \text{Eq. I - 4}$$

However, several limitations are observed while confronting the CNT predictions with experiments.[80] By definition, a theory is based on the current knowledge and is bound to evolves. Hence, successful modifications of the CNT (*e.g.* EMLD-DNT model, DFT, DIT etc.)[81–83] and alternative non-classical mechanism (2-step nucleation mechanism)[84–86] were considered, but will not be developed in this manuscript.

I.2.2.2 - Driving forces and solubility

Crystallization is performed out of equilibrium since an activation energy is necessary to initiate this process, which consequently corresponds to a return to equilibrium.[87] This self-assembly process requires therefore a driving force (*e.g.* supercooled melt, supersaturated liquid, supersaturated vapour etc.), which is well quantified by the change in chemical potentials of the system ($\Delta\mu$).[88,89]

In the case of solution crystallization, one must consider the maximum quantity x_A^1 of a solute A that can be dissolved in a solvent (*i.e.* solubility) at fixed intensive parameters. The change in chemical potentials is thus given by Eq. I - 5 where x_A^2 corresponds to the actual concentration of a solute A, and approximated to Eq. I - 6 while assuming the activity coefficients ratio to 1 (*i.e.* thermodynamic ideality).

$$\Delta\mu_A = \mu_A^1 - \mu_A^2 \qquad \text{with } \mu_i^y = \mu_i^0 + k_b T \ln(x_i^y \gamma_i^y) \qquad \text{Eq. I - 5}$$

$$\Delta\mu_A = k_b T \ln\left(\frac{x_A^2}{x_A^1}\right) \qquad \text{with } \frac{\gamma_A^{OP}}{\gamma_A^{DP}} \text{ approximated to unity} \qquad \text{Eq. I - 6}$$

Crystallization cannot occur if the solubility x_A^1 is greater than or equal to the actual concentration x_A^2. In such cases, the system is said undersaturated ($x_A^1 > x_A^2$) and saturated ($x_A^1 = x_A^2$), respectively, indicating the absence of any driving force for crystallization ($\Delta\mu_A \geq 0$) whereas such driving force exists once the system is supersaturated (*i.e.* $x_A^1 < x_A^2$). However, spontaneous nucleation can only occur if $\Delta\mu_A$ is important enough to overcome ΔG_n^*. This behavior gives rise to a concentration range for which the spontaneous crystallization is hindered despite crystals being thermodynamically favoured. This range is known as the metastable zone width (MSZW, Figure I - 12).

The intrinsic properties of this metastable zone are beneficial for crystallization processes as spontaneous nucleation (*i.e.* primary nucleation) is inhibited within the MSZW. This inhibition allows for precise control over crystal growth through intentional seeding using well-characterized crystals (*i.e.* secondary nucleation), enabling the production of crystals with desired structure and properties.

The computation of a temperature-dependent solubility (*i.e.* solubility curve) is accessible through the Van't Hoff equation, assuming an ideal thermodynamic behaviour (Eq. I - 7).

Moreover, both enthalpic and entropic contribution can be assessed by the experimental determination of few solubility points and plotting $\ln(x_A^1) = f\left(\frac{1}{T}\right)$.

$$\ln(x_A^1) = -\frac{\Delta_{dis}H}{R}\frac{1}{T} + \frac{\Delta_{dis}S}{R} \qquad \text{Eq. I - 7}$$

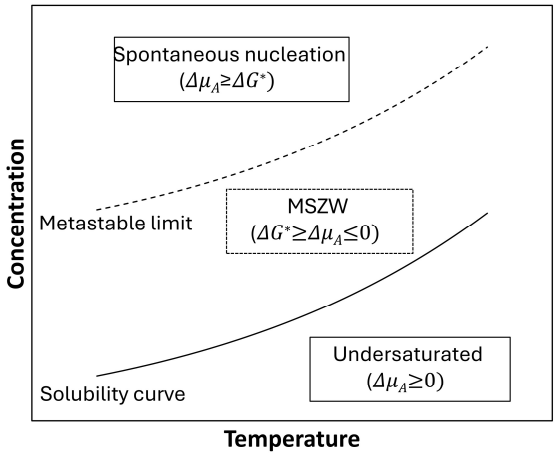

Figure I - 12. Illustration of a solubility curve and the different stability domains associated.

As inferred by Figure I - 12, a supersaturated solution can be either obtained via solvent evaporation (*i.e.* increase of the concentration) or via temperature change (*i.e.* decrease of the solubility). In most cases, solubility decreases as the temperature is lowering (*i.e.* direct solubility), but the reverse remains possible (*i.e.* inverse solubility). Although several methods are available to quantify the supersaturation (*e.g.* solubility product, absolute or relative supersaturation etc.), the supersaturation ratio $\beta = \frac{x_A^2}{x_A^1}$ will be exclusively used in this manuscript.

I.3 - Thermodynamics

The chemical potential μ_i of a compound *i* is considered as the change in Gibbs free energy (*G*) related to infinitesimal molar changes ∂n_i, which is the definition of a partial molar free energy (Eq. I - 8). Therefore, the total Gibbs free energy *G* or its variation dG of a system containing *i* constituents at constant temperature and pressure is the contribution of the products of the chemical potential of each constituent with respect to their number of moles n_i or their molar change dn_i (Eq. I - 9). The Gibbs free energy is defined as the maximum reversible work (*i.e.* maximum available energy) in a closed system at a constant temperature

and pressure. Since the molar enthalpy *H* is equivalent to all internal energies and pressure-volume work, the Gibbs free energy and its changes are given by Eq. I - 10.[90]

$$\mu_i = \left(\frac{\partial G}{\partial n_i}\right)_{T,P,n_{j\neq i}} \quad \text{Eq. I - 8}$$

$$G_{T,P} = \sum_i \mu_i n_i \; ; \; dG_{T,P} = \sum_i \mu_i dn_i \quad \text{Eq. I - 9}$$

$$G = U + pV - TS = H - TS \; ; \; \mathrm{d}G = dH - TdS \quad \text{Eq. I - 10}$$

The aforementioned equations impose that the most stable state is achieved once the lowest *G* value of the system is reached. Consequently, a negative *dG* denotes a spontaneous transformation. However, this state may be difficult to attain as the stability landscape of a system is analogue to a hilly surface energy with local minima (*i.e.* local stability) separated from each other by local maxima (*i.e. e*nergy barrier). A classic example of this phenomenon is the well-known case of metastable polymorph: diamond.[91]

I.3.1 - Polymorphism

As introduced in part I.2.1.3, polymorphism is the ability of a chemical substance to crystallize into more than one crystal structure.[92] Echoing chirality, the difference in the PBC between polymorphs induces different physico-chemical properties, including different melting points and solubilities.[93,94] In an industrial context, polymorphism is of paramount importance because two polymorphs of the same active pharmaceutical ingredient (API) can have different dissolution rates and the efficacy of a drug can be impacted by the presence of undesired polymorphs.[95,96] The stability relationships between the crystal forms must be thoroughly established since solid form conversion at a later stage of process development can have serious consequences.[97] This concern is all the more important if one considers that almost half of the marketed API exhibits polymorphism.[98–100]

At fixed pressure, two polymorphs are enantiotropically related if there exists a transition temperature T_{tr} at which both phases are equally stable (Figure I - 13b). Above T_{tr}, one of the two forms becomes metastable and should convert into the stable form. The reverse occurs below T_{tr}. For a system with *n* polymorphs, even more complex situations can arise. Furthermore, if no thermodynamic transition temperature exists between two polymorphs, they are monotropically related (Figure I - 13a).[101]

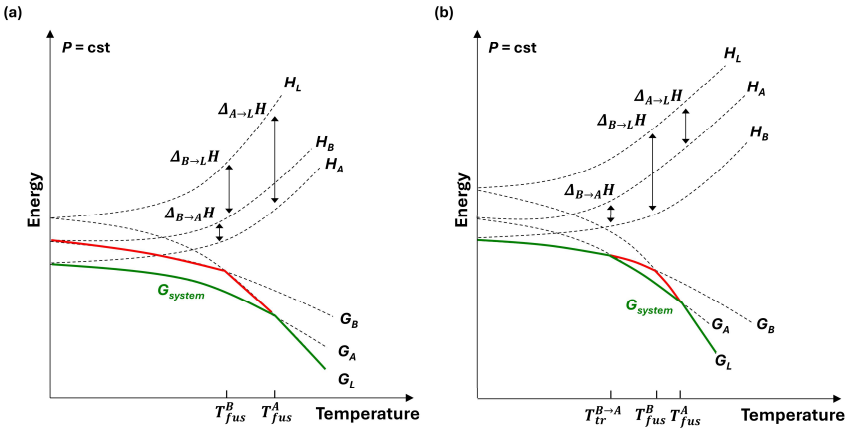

Figure I - 13. Theoretical Gibbs free energy (*G*) and enthalpy (*H*) curves of a hypothetical dimorphic compound representing (a) a monotropy and (b) an enantiotropy. Black arrows stand for the melting enthalpies associated to the considered phase transitions. Green lines represent the most stable state of the system whereas red curves stand for metastable equilibria.

Assessing the stability relationship between polymorphs may be a complex task. For this purpose, Burger & Ramberger introduce a rule of thumb, known as the heat of fusion rule, stating that "*If the higher melting form has the lower beat of fusion the two forms are usually enantiotropic, otherwise they are monotropic*".[102] This is easily understood by looking at the enthalpy curves in Figure I - 13: if the higher melting form is the only stable form whatever the temperature (*i.e.* monotropy), its melting enthalpy ($\Delta_{A\to L}H$ in Figure I - 13) must be higher than any other metastable forms ($\Delta_{B\to L}H$ in Figure I - 13) and reversely.

The crystallization of a metastable phase is not a rare event: most organic molecules, often as a result of their high degree of conformational flexibility,[103] can be crystallized as metastable forms, in particular if the crystallization process is performed far from equilibrium. This phenomenon is known as the Ostwald's rule of stages.[104,105] Moreover, the metastable nature of a crystal form can remain unknown until its sudden, usually unpredicted, conversion into a more stable form: this can have dramatic consequences such as in the well-known disappearing polymorphism cases of the APIs Ritonavir and Rotigotine.[97,106] To prevent such cases of disappearing polymorphs,[107,108] it is therefore important to investigate the stability relationships between polymorphs of new APIs, which are best rationalized by the experimental construction of phase diagrams, involving polymorph screening and solid state characterization.[109] If the compound undergoing crystallization is chiral, as it is often the case with APIs,[110] the solid-state landscape becomes more complicated since one must consider both enantiomers to be separate chemical entities.

I.3.2 - Phase diagrams of chiral molecules

A phase diagram is a graphical representation of the minimization of the Gibbs free energy of a heterogeneous system. It represents the relative stability of phase domains as function of the composition and intensive parameter(s), usually temperature and/or pressure. Only the condensed solid and liquid phases will be discussed below.[87,90,111–113]

I.3.2.1 - Variance

A limited number of variables must be fixed to completely define a system, which represents the degrees of freedom or variance (Eq. I - 11). This equation, known as the Gibbs phase rule, gives clear insight into the different possible equilibrium and the maximum number of phases in equilibrium for a given system in specific conditions.

$$v = c + k - \varphi$$ Eq. I - 11

v: Variance
c: number of independent component(s)
k: number of intensive variable(s)
φ: number of phase(s) in equilibrium

I.3.2.2 - Unary phase diagram

The phase diagram of an enantiopure substance, known as a unary phase diagram (*c* = 1), is often represented in a 2D *T, P* diagram (Figure I - 14). The slopes of the phase boundaries, which represent domains between two coexisting phases, can be modelled using the Clausius-Clapeyron equation (Eq. I - 12).

$$\left(\frac{dP}{dT}\right) = \frac{\Delta_{1\to2}H}{T\Delta_{1\to2}V_m}$$ Eq. I - 12

$\left(\frac{dP}{dT}\right)$: Slope of the coexistence curve
$\Delta_{1\to2}H$: Enthalpy changes
T: Temperature
$\Delta_{1\to2}V_m$: Specific volume changes

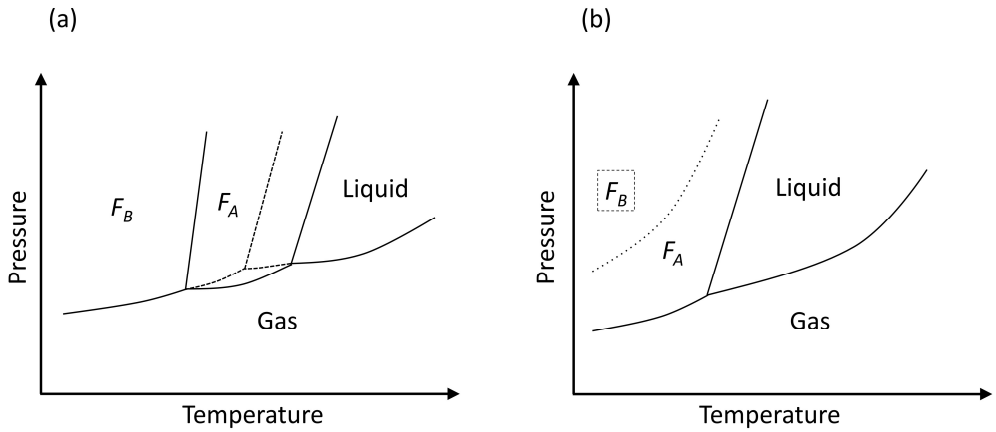

Figure I - 14. Theoretical unary phase diagrams of a hypothetical dimorphic compound representing (a) an enantiotropy and (b) a monotropy. Dashed lines stand for metastable equilibria.

I.3.2.3 - Binary phase diagram

A chiral molecule is composed, at its racemic composition, of 50% of each enantiomer (c = 2). Their behaviour vs. temperature is commonly represented by an isobaric 2D *T, c* diagram (Figure I - 15).

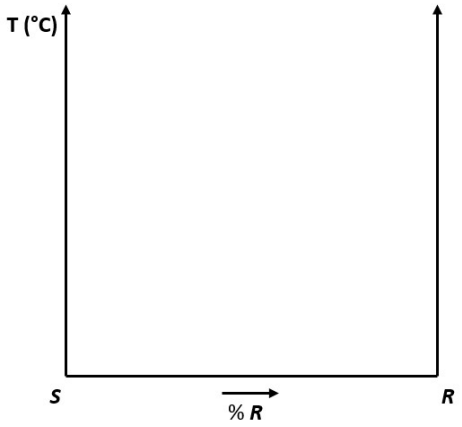

Figure I - 15. Isobaric binary construction.

Although binary phase diagrams are often represented through their isobaric construction, it should be noted that such systems are completely defined by a 3D *T, P, c* construction, therefore including pressure as a supplementary variable. There are three different phase equilibria concerning phase diagrams of chiral systems and different variations can be encountered from these three main cases.

I.3.2.3.1 - Racemic compound

Enantiomers can crystallize together as a single entity and form a defined compound called racemic compound; it is the most common case of all known chiral systems (90-95%),[114] characterized by an ordered crystal of an equal ratio of both enantiomers at the racemic composition. Theoretical phase diagram of such systems is plotted in Figure I - 16, representing the melting point of the pure enantiomer on the edges and the melting point of the stable racemic crystal at the middle racemic composition at constant pressure (usually P = 1 atm). Phase diagrams of chiral systems are completely symmetrical with respect to the racemic composition. Therefore, the melting of a racemic crystal must be congruent (*i.e.* the composition of the molten liquid is the same as that of the solid before melting). It should be noted that the melting temperature of this racemic phase can be lower (as it is the case in Figure I - 16) or higher than the pure enantiomers.

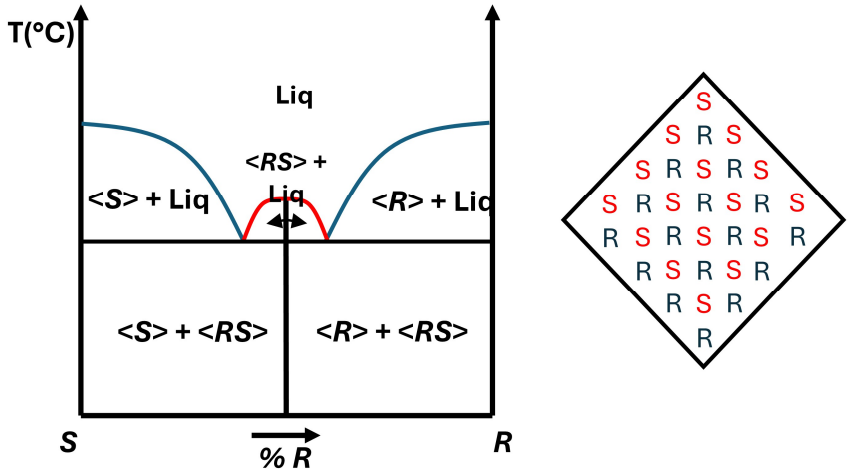

Figure I - 16. Theoretical isobaric binary phase diagram of a chiral system crystallizing as a racemic compound (left) and representation of racemic compounds crystal (right). Blue and red lines correspond to the liquidus of the pure enantiomer and the racemic compound respectively.

The liquidus lines associated to the pure enantiomers (blue lines in Figure I - 16 and the racemic compound (red lines in Figure I - 16) can be computed using the Schröeder-van Laar (Eq. I - 13) and Prigogine-Defay (Eq. I - 14) simplified equation, assuming an ideal thermodynamic behaviour and neglecting the contribution of the heat capacity changes.[115,116] The intersection of the two equations is used to determine the theoretical eutectic point composition and temperature, assessing therefore the relative stability of the racemic compound.

$$\ln x = \frac{\Delta_{fus}^{R} H}{R}\left(\frac{1}{T_{fus}^{R}} - \frac{1}{T_x}\right) \qquad \text{Eq. I - 13}$$

$$\ln(4x(1-x)) = \frac{2\Delta_{fus}^{RS} H}{R}\left(\frac{1}{T_{fus}^{RS}} - \frac{1}{T_x}\right) \qquad \text{Eq. I - 14}$$

I.3.2.3.2 - Conglomerate

Enantiomers can crystallize separately and form a conglomerate, which represents only 5-10% of known chiral systems. Phase diagram of such systems is depicted in Figure I - 17, characterized by a eutectic invariant in which the addition of the counter enantiomer decreases the melting temperature down to the eutectic temperature. Regardless of the composition and temperature, complete chiral discrimination occurs in the solid state (*i.e.* crystals of pure enantiomer). By contrast with racemic compound, the use of Eq. I - 13 is sufficient for estimating the eutectic temperature.

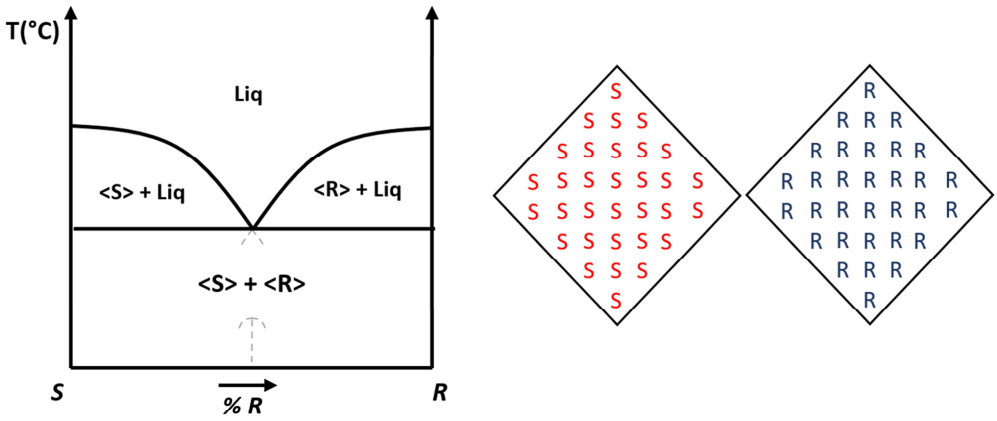

Figure I - 17. Theoretical isobaric binary phase diagram of a chiral system crystallizing as a conglomerate (left) and representation of conglomerate crystals (right).

I.3.2.3.3 - Total solid solution

The rarest case of heterogeneous equilibria between enantiomers is the total solid solution (<1% of the cases). It is total miscibility between enantiomers which compete for the same lattice positions in the solid phase.[117,118] Consequently, composition of crystals is related to the starting composition of the system. Phase diagram of such system presenting a minimum solid solution is plotted in Figure I - 18 (ideal and maximum solid solutions also exist).

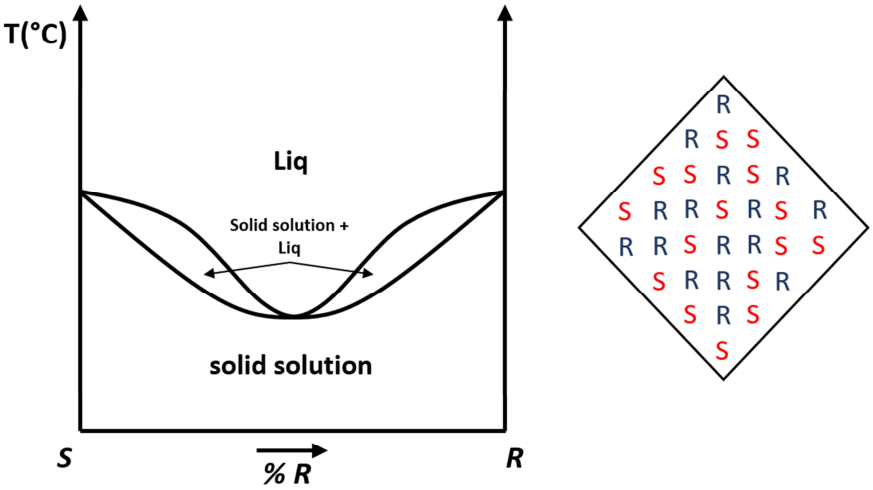

Figure I - 18. Theoretical isobaric binary phase diagram of a chiral system crystallizing as a solid solution (left) and representation of solid solution crystals (right).

I.3.2.3.4 - Extra cases

The phase transition involved in three main different phase equilibria discussed above are not the only possible ones. Indeed, several aspects of crystallization may influence these equilibria, including:

- Polymorphism (*cf* parts I.2.1.3 and I.3.1)
- Reversible transition between racemic compound and conglomerate
- Partial solid solutions
- Metastable phases

Figure I - 19 presents an example for each variation. This figure also provides cases of metastable phases represented as grey dashed lines. These metastable phases (polymorphic form, racemic compound, conglomerate etc.) are the reflect of local minima in Gibbs free energy, whose accessibility is often encountered according to the Ostwald's rule of stages.[105] Therefore, it is essential to account for kinetic effects in crystallization processes, rather than focusing solely thermodynamic phase equilibria.

It is important to mention that (i) polymorphism and partial solid solution can also occurs for a racemic crystal (ii) eutectoid is also possible (*i.e.* stable conglomerate at low temperature and stable racemic compound at high temperature) (iii) mix of polymorphism, metastable phases, partial solid solutions and peritectoid/eutectoid can be observed.

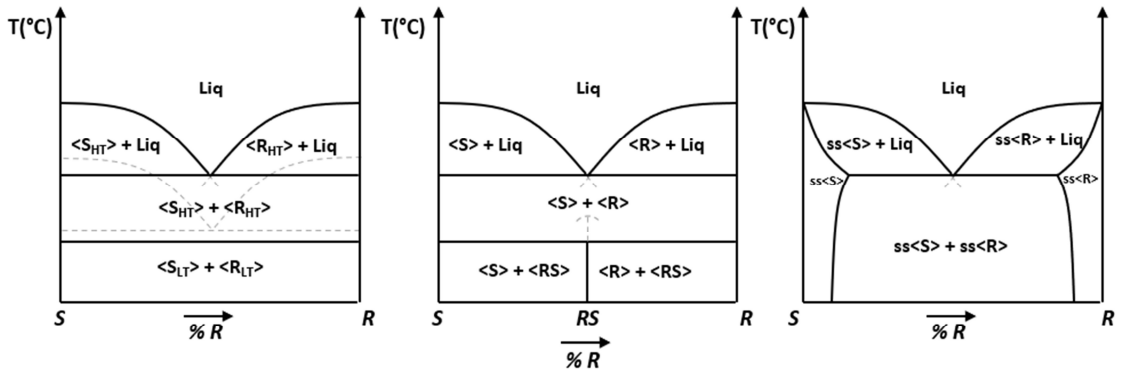

Figure I - 19. Chiral system crystallizing as a conglomerate and presenting two polymorphs of the pure enantiomers (left), Chiral system crystallizing as a racemic compound at low temperature and conglomerate at high temperature (middle) and Chiral system crystallizing as a conglomerate and presenting partial solid solutions between enantiomers (right). Dashed lines are for metastable equilibria.

I.3.2.4 - Ternary phase diagrams

Crystallization of organic compounds is typically performed in a solvent. Such systems are composed of three independent components (c = 3), which are described by ternary phase diagrams. Their behaviour versus temperature is represented by an isobaric 3D *T,* c construction. Usually, the complete ternary phase diagram is not investigated as only few sections at the working temperatures are sufficient, leading to an isobaric/isothermal 2D construction (Figure I - 20).

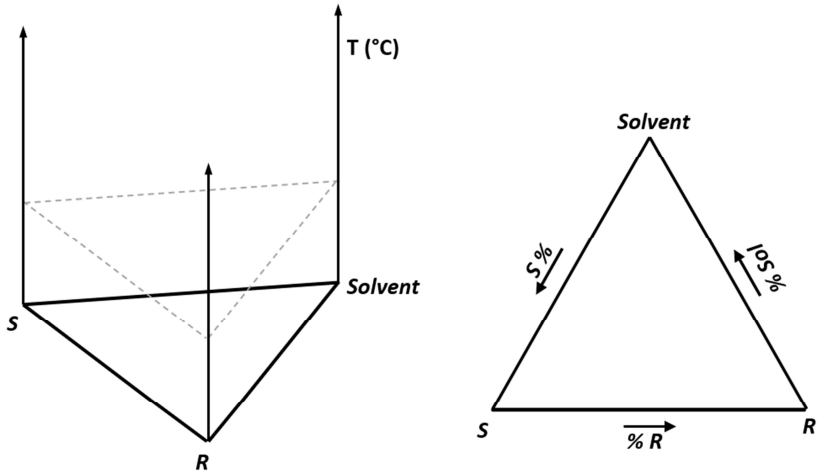

Figure I - 20. Schematic representations of an isobaric ternary construction of a chiral system and a solvent (left) and isobaric/isothermal section of a chiral system and a solvent (right)

Isothermal sections of the three main phase equilibria between enantiomers are depicted in Figure I - 21. The isothermal ternary section of a conglomerate is composed of four domains: (i) two biphasic domains composed of one pure enantiomer in equilibrium with a non-racemic saturated solution (*sat.sol*) (ii) a triphasic domain composed of the two enantiomers and a doubly saturated racemic solution (*d.s.s.*) (iii) a monophasic domain composed of an undersaturated solution (*u.s.s.*).

In addition to the phase domains of a conglomerate, the isothermal ternary section of a racemic compound presents three more domains (six domains in total): (i) one biphasic domain composed of the racemic compound in equilibrium with the saturated solution (ii) two triphasic domains composed of one pure enantiomer, the racemic compound, and doubly saturated solutions.

The isothermal ternary section of a total solid solution is composed of two domains: (i) a biphasic domain composed of the non-stoichiometric solid phase and the doubly saturated solution and (ii) a monophasic domain composed of the undersaturated solution.

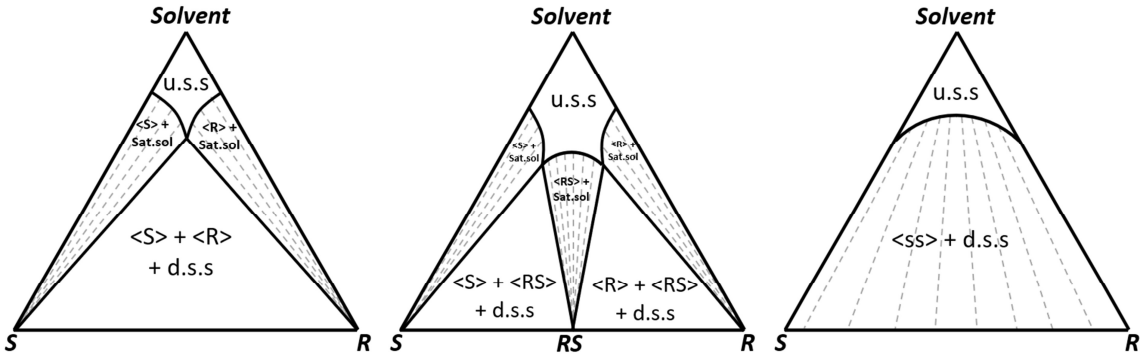

Figure I - 21. Isothermal section of a solvent and a chiral system crystallizing as a conglomerate (left), racemic compound (middle) and total solid solution (right). Compositions of the biphasic domains are determined by the tie-lines (dashed lines)

As for binary phase diagrams, many variations are possible for the ternary phase diagrams (*e.g.* formation of cocrystal(s), solvate(s) etc.). This behaviour will be discussed later in this manuscript.

I.3.2.5 - Quaternary phase diagrams

Phase diagrams involving four independent components will also be discussed in this manuscript, particularly in the context of mixing two chemically related chiral systems or optimizing a Pasteurian resolution process.

These systems, often encountered for the derivatization of chiral systems crystallizing as racemic compounds, are thermodynamically described by an isobaric and isothermal tetrahedron with each component represented on the apexes. Figure I - 22 shows a system of a chiral molecule (<*R*> ; <*S*>), an additional crystalline material (*C*) and a solvent. Each face corresponds to an isolated isothermal ternary phase diagram (<*R*> + <*S*> + solvent; <*R*> + <*C*> + solvent; <*S*> + <*C*> + solvent and <*R*> + <*S*> + <*C*>) (Figure I - 22). It represents the simplest case as there is no define compound, polymorphism, solid-solid phase transition or partial solid solution.

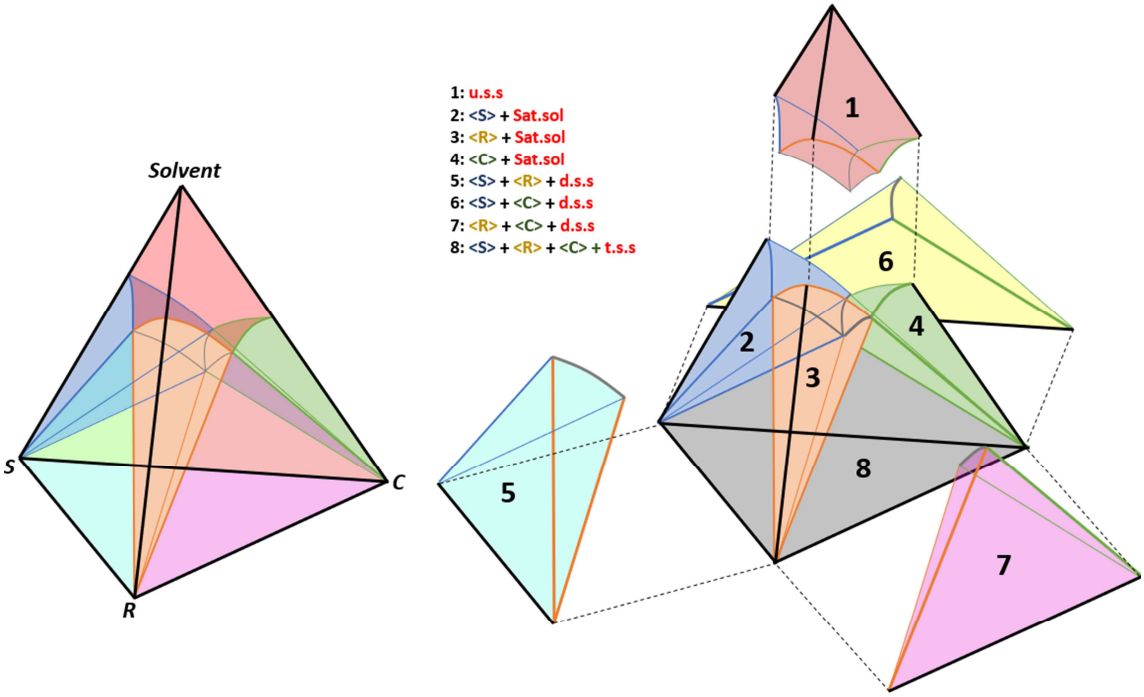

Figure I - 22. Phase domains of a quaternary system <R> + <S> + <C> + Solvent.

The representation of a polythermal quaternary phase diagram would involve a fourth dimension. The addition of a new variable (*e.g.* temperature) implies fixing another variable constant (compositions) : this is called an isoplethal section. Isoplethal section of a quaternary

phase diagram involving a constant composition ratio are called ternary isopleth (Figure I - 23, green) and isopleth section of a quaternary phase diagram involving two compositions and/or compositions ratio constant are called binary isopleth (Figure I - 23, orange).

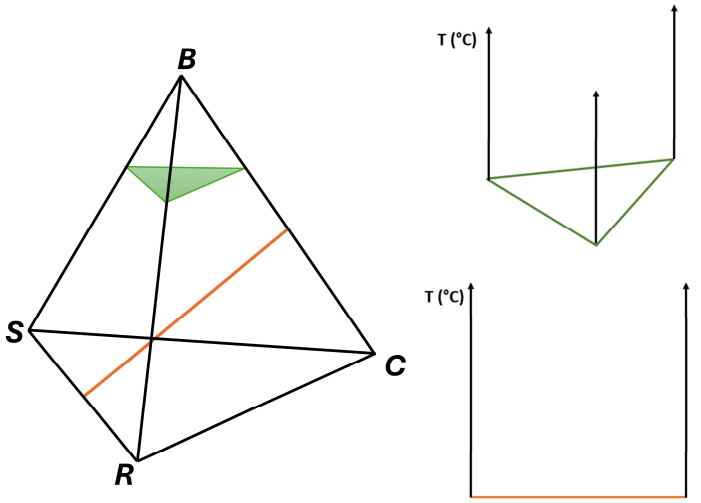

Figure I - 23. Schematic representations of an isobaric/isothermal quaternary construction of a chiral system, a solvent and an additional component <C> (left), ternary isoplethal section of this system maintaining the solvent composition constant (green) and a binary isoplethal section of this system maintaining a fixed (*R*)/(*S*) and (*C*)/(*B*) ratio (orange).

I.3.3 - Conglomerate formation

Ever since the first sorting of enantiomers by Louis Pasteur (*cf.* I.1.2), crystallization has become a powerful method for isolating molecules of a desired handedness. Although in the past century many variations of this method have been developed,[119–124] the widespread use of many chiral purification methods by crystallization are still hindered by a fundamental requirement: enantiomers must spontaneously separate into distinct enantiopure crystals (*i.e.* racemic conglomerates). Unfortunately, the overwhelming majority of enantiomeric mixtures crystallize together into thermodynamically favoured racemic compounds (90-95%) which hinders such separation techniques. Since predicting crystallization behaviour is still a major challenge,[125–128] no systematic approach has been developed so far to overcome this thermodynamic limitation. However, several derivatization methods have been developed to maximize the chance of forming conglomerate-forming system and bypass this fundamental hurdle.[129–131]

I.3.3.1 - Metastable conglomerate

Only 5-10% of the known chiral systems crystallize as conglomerate assuming that heterogenous equilibria are exclusively driven by thermodynamic. As discussed in part I.3.1 and I.3.2.3.4, this approach entirely overlooks the inherent out-of-equilibrium nature of crystallization and disregards all kinetic considerations. As demonstrated in Figure I - 24, any system crystallizing as racemic compound has the opportunity to form a metastable conglomerate, whose accessibility remains unknown.

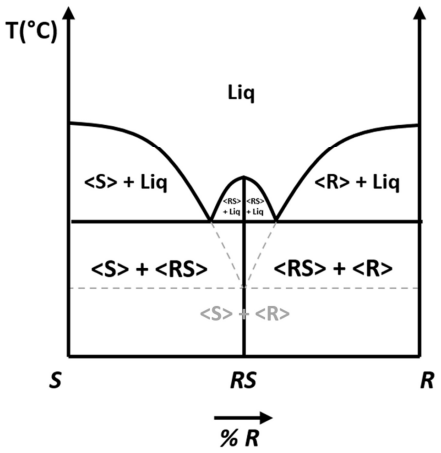

Figure I - 24. Metastable conglomerate (grey) of a chiral system crystallizing as a racemic compound (black)

A rough estimation of the energetic difference between the local minima (metastable conglomerate) and global minima stable (racemic compound) may be assessed by determining the difference in melting temperature between these two racemic phases :

- Theoretically: by extending the computed liquidus line of the pure enantiomer up to the racemic composition using the Schröeder-van Laar simplified equation.[132]
- Experimentally: by manually mixing both enantiomers together in racemic proportion.[133]

However, this energetic difference is indicative of a relative thermal stability. In case of solvent crystallization, several additional parameters must be considered (*e.g.* solvents, interfacial tension, solid-liquid interaction etc.). In the later, the experimental determination of the doubly saturated point(s) composition may serve as a valuable tool for assessing the relative stability of a racemic compound (*d.s.p.c* hereafter). As inferred by Figure I - 21, the closer to

the racemic composition the *d.s.p.c* is, the lower the relative stability of the racemic compound.

Supporting this statement, there have already been reports of racemic compounds converting into enantiopure crystals under far-from equilibrium conditions such as grinding of crystals or steep temperature gradients.[126,134–137] Although promising, it remains unclear if such cases are incidental reports on systems with specific trades, or if there are general guidelines that can be exploited to extend these principles for systematic isolation of enantiomers by crystallization.[138]

I.3.3.2 - Multicomponent crystals

Multicomponent molecular solids are materials that are composed of more than one type of molecular entities, typically in specific stoichiometry ratios. These multicomponent solids have garnered significant interest since the past decades due to their potential for tailored properties of the materials.[139,140] More specifically, this versatility allows for the precise design of chiral molecules with specific characteristics,[141,142] for instance engineer a chiral material crystallizing as the coveted conglomerate-forming system.

Several subclasses of multicomponent molecular solid exist and are classified based on the intermolecular interactions existing between crystal buildings blocks.[143,144] Although these materials may be structured as amorphous solids (*cf.* part I.2.1), only crystalline multicomponent solids will be discussed.

I.3.3.2.1 - Cocrystals

Self-sorting of enantiomers into separate enantiopure crystal can be achieved through the formation of cocrystals, that is a crystalline material composed of two or more molecules in the same crystal lattice.[145,146] These molecules are typically neutral and interact through non-covalent intermolecular interactions (*e.g.* H-bonding, π-π interaction, van der Waals forces etc.).[147]

By forming cocrystals with a suitable molecule (*i.e.* Coformer) from a chiral system crystallizing as a racemic compound, new solid phases are obtained. These new solid phases are independent of the initial system and therefore, conglomerate-forming system could

cocrystallize with 5-10% of occurrence (Figure I - 25). Echoing part I.3.3.1, one must also consider the metastable equilibria in case of racemic compound cocrystal formation.

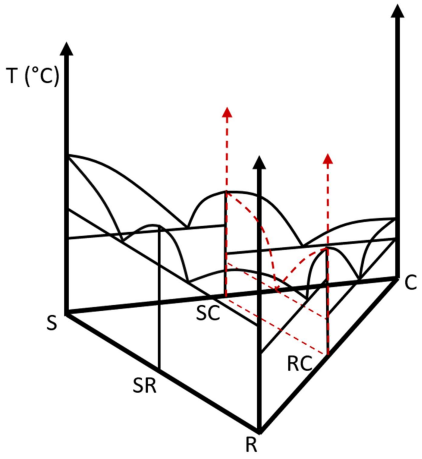

Figure I - 25. Ternary phase diagram of a coformer and a chiral system crystallizing as a racemic compound in which the isopleth section of a cocrystallized conglomerate-forming system is highlighted in red dashed lines.

I.3.3.2.2 - Solvates

A solvate is a crystalline material composed of two or more molecules with at least one being a solvent molecule (*i.e.* liquid at ambient condition).[148,149] As for cocrystals, the solvated materials are independent of the initial system and therefore, a solvated conglomerate-forming system could crystallize (Figure I - 26). It should be noted that solvated solid may be unstable as a result of solid-gas equilibria: these solvated crystal forms are called efflorescent and can only be characterized using an *in-situ* characterization.

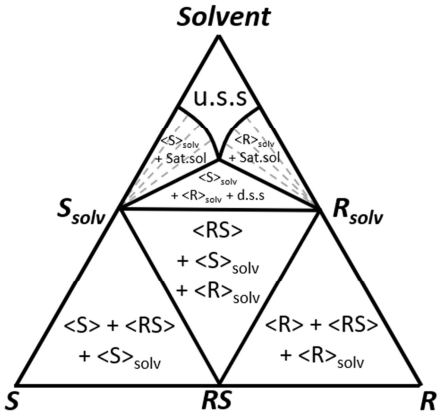

Figure I - 26. Isothermal ternary phase diagram of a solvent and a chiral system crystallizing as a racemic compound exhibiting a solvated conglomerate-forming system.

I.3.3.2.3 - Clathrate, Ionic, metallic and mixed type multicomponent solids

In addition the abovementioned cocrystals and solvates, molecular entities of multicomponent solids may also interact with each other in the crystal lattice through either electrostatic forces (Ionic cocrystal, also referred as salt),[150–152] metallic bonding (metal complexes)[153,154] or even a mixed of all of these interactions (mixed-type cocrystal).[153,155–158] Furthermore, in case of a crystalline material composed of two or more molecules with at least one being a gas molecule (*i.e.* gaseous at ambient condition): the solid form is called clathrate.[159–161] However, aside the different nomenclature and type of intermolecular interactions existing for these multicomponent solids, their implication in a conglomerate screening remains the same: the engineered crystal form has 5-10% chance to form a conglomerate-forming system.

It should be mentioned that multicomponent solids may also deviate from the stoichiometric ratio to form non-stoichiometric solids: these are called mixed crystals.[162–165]

I.3.4 - Detection of conglomerate-forming systems

The rare occurrence of conglomerates constitutes a sever limitation for many crystallization-based techniques. Hence, several methods have been developed for the efficient identification of such coveted systems. However, we must remember that "*Spotting a conglomerate is just halfway to achieving a preparative resolution […]*". [166] Epitaxial growth, lamellar twinning, partial solid solution or slow crystallization kinetics are potential issues that may still hinder such resolution process of conglomerate-forming systems.[167–173]

I.3.4.1 - Determination of phase diagram

The inherent symmetry of a conglomerate-forming system induces a perfect symmetry of the heterogenous equilibria. This statement imposes that (i) the eutectic point composition must imperatively be racemic (ii) a scalemic suspension must be in equilibrium with a saturated racemic mother liquor. This data can be easily accessible experimentally through the determination, at least partial, of phase diagram:

- Determination of the *d.s.p.c* through the analysis of the composition of a scalemic suspension and its mother liquor.[174]

- Partial determination of the clear points at different enantiomeric composition but constant ratio solid-solvent (*i.e.* isoplethal section)[175]
- Comparison between the racemic melting point with the eutectic temperature[113]

These methods are based on thermodynamic principles, allowing for the identification of stable-conglomerate forming system exclusively. Moreover, it should be noted that racemic compound may have a *d.s.p.c* or a eutectic point composition close to the racemic composition.

I.3.4.2 - Non-linear optics

Discrimination between conglomerate and racemic compound can be explored by using Second Harmonic Generation (SHG hereafter), which is a useful tool for a conglomerate pre-screening process considering its non-destructive behaviour, the small quantity of crystalline particles needed and its high sensitivity. More specifically, it is a non-linear optic phenomenon in which two colinear electromagnetic waves of same frequency (*i.e.* same wavelength) are interacting while they propagate thought non-centrosymmetric materials. This interaction is characterized by the formation of a new wave with a frequency twice the incident one (*i.e.* wavelength divided by two).[176,177] SHG can be detected using setup such as the one schematized in Figure I - 27.

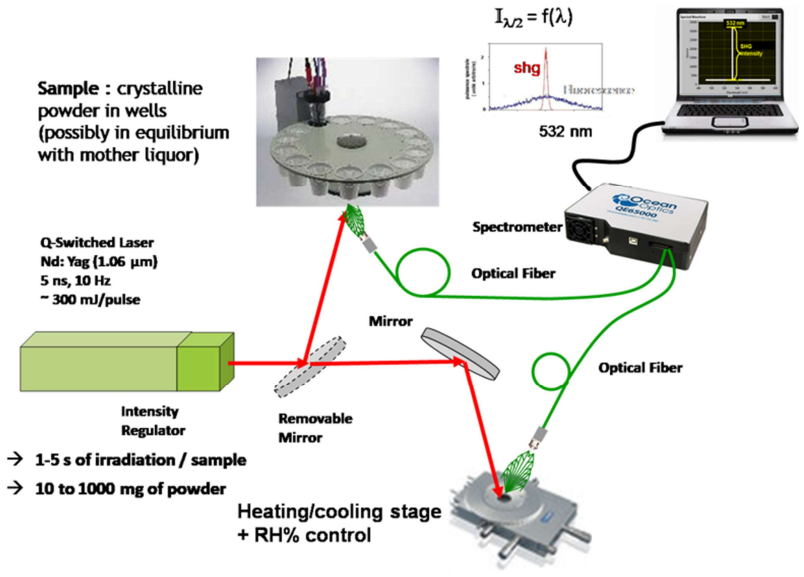

Figure I - 27. Second Harmonic Generation setup.

Conglomerate-forming systems must crystallize in a non-centrosymmetric chiral structure (*cf* I.2.1.1), but an accurate screening of conglomerate through SHG measurement remains biased considering the frequency of non-centrosymmetric material exhibiting achiral structure (*i.e.* kryptoracemates, solid solutions or racemic compounds crystallizing in a non-centrosymmetric achiral space group (NA)), exceptions from the Kleinman Symmetry rules (*i.e.* 422 and 622) and Neumann principle (*i.e.* 432).[178,179] Actually, the probability that a SHG positive racemic mixture is actually a conglomerate forming system is about 64%.[178,180,181]

I.3.4.3 - Spectroscopic data

A conglomerate has the particular property of being a physical mixture of enantiopure crystals that exhibit mirror image crystal packings. By contrast, the crystal packing of a racemic compound differs entirely from that of its pure enantiomers. Based on this distinction, the spectroscopic data (*e.g.* FTIR, Raman, Solid-State NMR, Solid-state CD etc.) or structural analyses (*e.g.* X-Ray Diffraction, Small-angle X-ray scattering, Wide-angle X-ray scattering) of a chiral system crystallizing as a conglomerate would be identical in both its racemic and enantiopure forms. Conversely, this data would differ significantly for a racemic compound (Figure I - 28).

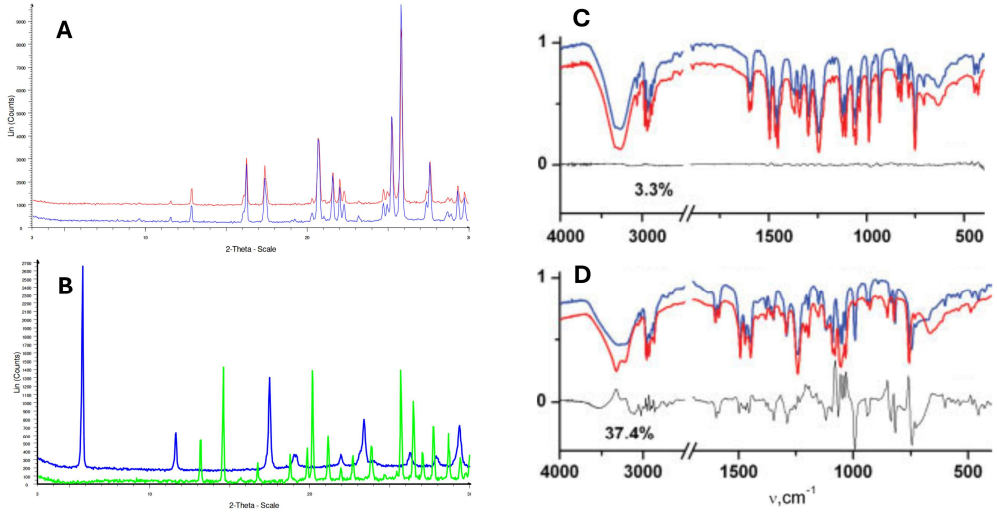

Figure I - 28. Examples of X-ray diffractograms and FTIR spectra comparison between enantiopure and racemic samples of (A) a conglomerate forming systems (Baclofen/maleic acid cocrystal) and (B) a racemic-compound forming system (baclofen enantiomer), as well as (C) a conglomerate forming systems (3-(2-Ethylphenoxy)-propane-1,2-diol) and (b) a racemic-compound forming system (3-(2-Isopropylphenoxy)-propane-1,2-diol). These data are respectively sourced from Gendron[182,183] and Bredikhin *et al.*[184]

I.3.4.4 - Structural resolution

In the case that enantiopure crystals are not accessible, the solid-state classification could be obtained through the structural resolution by Single-Crystal X-Ray Diffraction (SCXRD). It is the most accurate method to determine whether the chiral system crystallizes as a conglomerate or a racemic compound. However, it is necessary to grow single crystals from the racemic mixture, which are often obtained in static condition. It should be noted that metastable phases are accessible under such static conditions (*i.e.* Ostwald's rule of stages), for instance metastable polymorphs.

I.3.5 - Crystallization-based chiral resolution or deracemization methods

Many methods are used to obtain pure enantiomers, ranging from synthesis (asymmetric synthesis, chiral pool, enzymatic catalysis) to purification step (chiral chromatography, biocatalytic process etc.).[185–187] Since these methods are extensively documented in the literature, this manuscript will focus exclusively on crystallization-based chiral resolution techniques.[165,188,189]

I.3.5.1 - Diastereomeric salt formation

The diastereomeric salt resolution,[190] also known as Pasteurian or classical resolution, consists in breaking the symmetry existing between enantiomers by forming diastereomeric salts. To this end, an enantiomerically pure chiral agent is added to a racemic mixture of enantiomers, leading to the formation of diastereomeric salts. The difference between the solubility of the two salts, induced by the formation of diastereomers, makes the crystallization of pure enantiomers possible from an equimolar medium (Figure I - 29). In case of non-congruent solubilities, one must consider the quaternary phase diagram of this four-component system to find suitable conditions for selective and optimized crystallization of enantiopure diastereomeric salt.

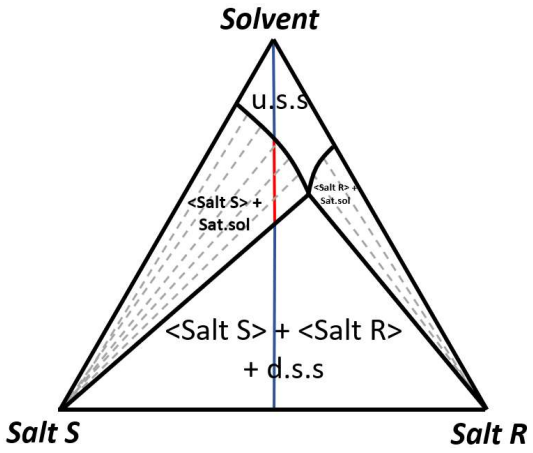

Figure I - 29. Ternary section of a diastereomeric salt system and a solvent. Crystallization pathway from the racemic mixture is represented by the blue/red line. Upper blue line : salts are solubilized, red line : selective crystallization of the <Salt S>, lower blue line : crystallization of both salts.

Moreover, an improved Pasteurian resolution method has recently been introduced, in which a family of chiral resolving agent are used simultaneously instead of a single enantiomerically pure resolving agent: this method is referred to as the Dutch resolution.[191–194]

I.3.5.2 - Preferential crystallization

Preferential crystallization, originally known as crystallization by entrainment, was initially observed in 1866 by Gernez.[195] Although it holds as an attractive method for chiral resolution, significant practical advancements in this technique have only emerged since Secor's comprehensive review in 1962.[196]

Preferential crystallization can be described as a stereoselective crystallization from a supersaturated racemic or slightly enantioenriched medium, either solution or melt, of a system crystallizing as a conglomerate.[197,198] The stereoselective crystallization is induced by intentional seeding with enantiopure crystals prior to any primary nucleation, favouring therefore secondary nucleation and crystal growth of the seeded enantiomer and leading to a metastable equilibrium in which the counter enantiomer remains supersaturated. This method relies on (i) the high chiral discrimination capabilities provided by the solid-state and (ii) the favourable crystallization kinetics of enantiopure crystals whilst thermodynamic dictates that both enantiomers should crystallize. This is therefore an out-of-equilibrium chiral resolution method based on nucleation kinetics: nucleation from a supersaturated solution is not instantaneous considering that the system must cross the energy barrier of formation of

a critical size nucleus (*cf.* I.2.2.1 and I.2.2.2). However, the system must be filtered before the crystallization of the counter enantiomer.

Figure I - 30 depicts the cyclic Seeded Isothermal Preferential Crystallization process (SIPC hereafter). The operating sequence is the following: a racemic clear solution at T_1 is cooled down to T_2 at which the solution in supersaturated in both enantiomers, then seeding with <*R*> crystals is performed (point *a*), inducing the preferential crystallization by secondary nucleation of <*R*> along [*ab*] until filtration. All along [*ab*], primary nucleation of <*S*> enantiomer does not occur, but its supersaturation is increasing. After filtration of pure <*R*>, the solution is heated at T_1 and compensated with the racemic mixture ([*ba'*] in Figure I - 30). Then, a symmetrical operation using <*S*> crystals seed is performed, inducing the preferential crystallization of <*S*> along [*a'b'*] and so on.

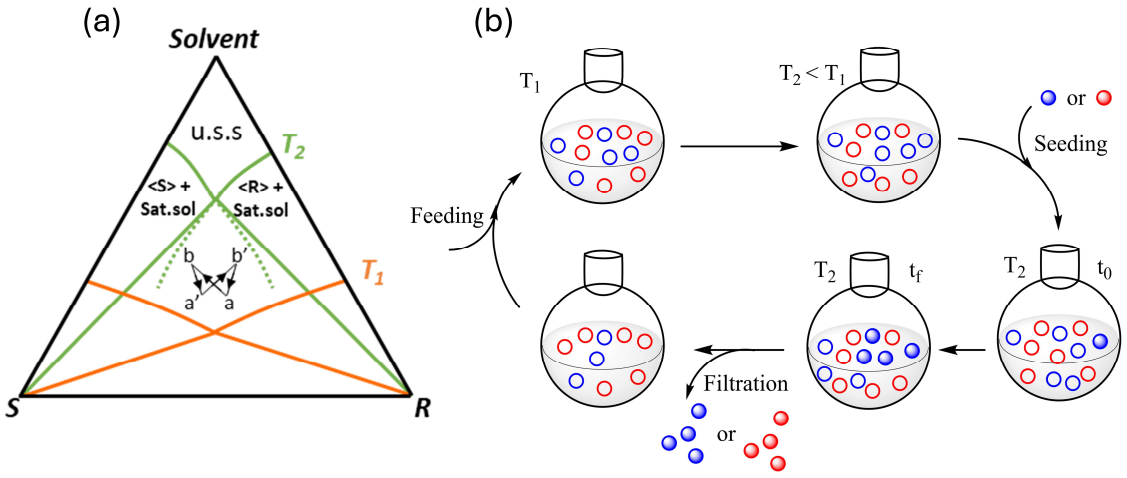

Figure I - 30. Cyclic SIPC process : (a) isothermal ternary phase diagram and (b) experimental schematic view.

Several methods of preferential crystallization exist and are listed below :

- Seeded Polythermic Programmed Preferential Crystallization (S3PC): this variation implies that seeding occurs at a temperature in which a supersaturation is reached. This supersaturation is then continuously increased by reducing the temperature afterward. This method requires therefore accurate knowledge on the heterogenous equilibia of the system but maximizes the recovery of the targeted enantiomer.
- Auto-Seeded Polythermic Programmed Preferential Crystallization (AS3PC): this variation differs from S3PC by the mode of seeding: the seeds are generated *in-situ* from the biphasic domain (*i.e.* only one enantiomer is supersaturated) using a slightly

enantioenriched clear solution. The resulting mother liquor, enriched with the counter enantiomer, is recycled to perform the preferential crystallization of the counter enantiomer.

- Auto-Seeded Preferential Crystallization Induced by Solvent Evaporation (ASPreCISE): this variation imposes a supersaturation through solvent evaporation at constant temperature, but overall mechanisms remain similar as the AS3PC.[199]
- Second Order Asymmetric Transformation (SOAT): a particular resolution method combining preferential crystallization and *in-situ* racemization leading to a theoretical yield of 100% in one step.[122,200,201]

An accurate monitoring of the crystallization parameters and kinetics is therefore essential: for instance seed properties (initial mass, particle size distribution, structural and chemical purity etc.), stirring (rate and geometry), temperature profiles (Holding temperature / time and cooling rates), working solvent etc. However, although optimal conditions are established, the efficiency of such chiral resolution process may be constrained by specific factors such as a partial chiral discrimination, an epitaxial growth or a crystallization of metastable racemic compounds.[168,170,202–204]

Moreover, it has long been assumed that only conglomerate-forming system, representing 5-10% of the known chiral systems, are suitable for this resolution methods, overlooking the inherent out-of-equilibrium nature of preferential crystallization. Since then, few examples of preferential crystallization on metastable conglomerate have been published.[135,137] Although promising, it remains unclear if such cases are incidental reports on systems with specific traits, or if there are general guidelines that can be exploited to extend these principles for systematic isolation of enantiomers by crystallization in case of racemic compound-forming systems.

I.3.5.3 - Solid-state deracemization

Solid-state deracemization, also known as spontaneous symmetry breaking, is a chiral amplification method occurring close to thermodynamic equilibrium. In this process, a racemic suspension of a conglomerate-forming system in equilibrium with its racemized saturated solution results in a chiral amplification until a single population of enantiopure crystals remains.[205] The mechanism behind deracemization is still discussed,[206–215] although

mathematical model introduced by Iggland and Mazzotti pointed out that no deracemization occur without *in situ* racemization, growth, dissolution, and agglomeration, wherein dissolution kinetics must be faster than growth kinetics.[211,212,216] However, this method necessitates an energy input (temperature cycling, ultrasound, attrition etc.) as the overall solid-state deracemization kinetics are rather low.

A schematic representation of the deracemization process is depicted in Figure I - 31:

- The process starts with a racemic suspension of a dual population of enantiopure crystals in equilibrium with their racemized saturated solution. The ternary system is degenerated as the liquid phase can only contain an equimolar amount of enantiomer.
- Meanwhile, changes in solid-phase attributes (*e.g.* crystal size distribution, growth rate dispersion etc.) occur, inducing a stochastic enantiomeric imbalance in the solid-state. This imbalance is also known as “take-off”.
- Then, this slight enantiomeric excess is auto-amplified through an auto-catalytic process involving agglomeration of crystal with the same handedness and Ostwald ripening, leading *in fine* to an enantiopure suspension. Although this process may theoretically result in the recovery of 100% of the initial material involved, part of it remains racemized in solution resulting to an experimental global recovery that could hardly exceed 90%.[212,217]

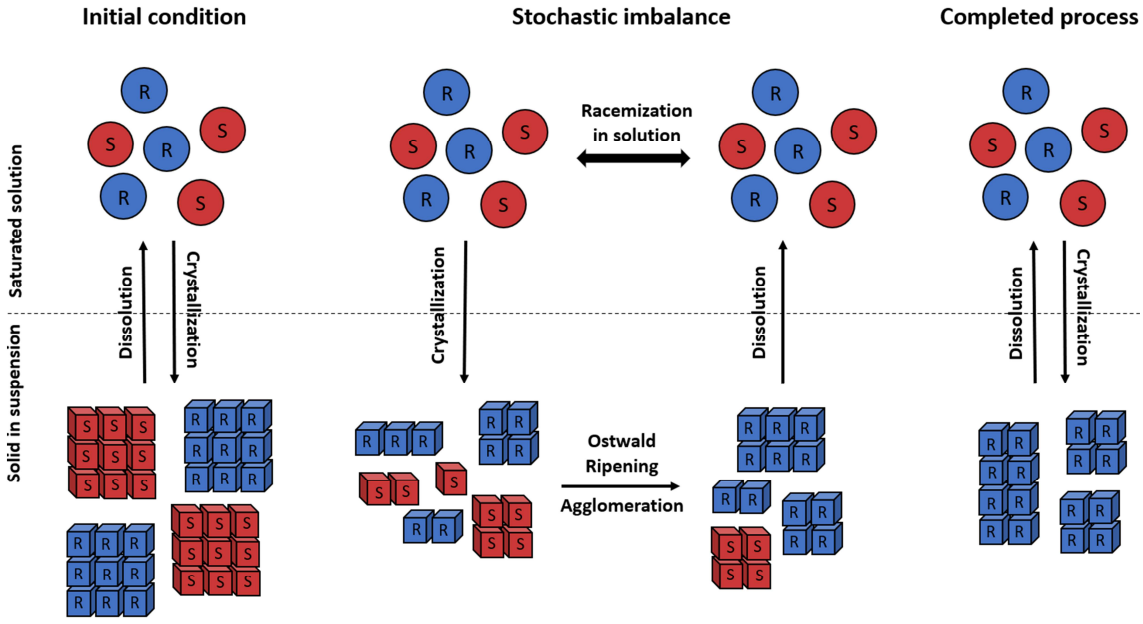

Figure I - 31. Schematic representation of the deracemization process.

The system could evolve stochastically toward a single population of either the left-handed or right-handed enantiomer without specific control. However, the final evolution of this spontaneous process can be directed by intentionally introducing a small enantiomeric imbalance of the targeted enantiomer. Furthermore, the greater the imbalance the faster the evolution toward a homochiral population is, demonstrating that the kinetic of this spontaneous evolution is of the first order and emphasizing its auto-catalytic nature. More importantly, solid-state deracemization processes offer the advantage compared to traditional chiral resolution methods to convert the counter enantiomer into the desired one. This spontaneous symmetry breaking is therefore not only economically sustainable but also maximizes efficiency, achieving a theoretical yield of 100 %.[206,207,212,218]

An intense research activity has been taking place in the domain of solid-state deracemization since the seminal paper of Viedma in 2005,[119,120] for which the abrasive effect of glass beads led to a fast and spontaneous symmetry breaking by inducing crystal attrition, favouring the clustering of enantiopure particles and thus enhancing the Ostwald's ripening phenomenon. Ever since, temperature cycling, ultrasound, microwave, solvent evaporation, high-energy milling or even pressure stress have proven effective in achieving spontaneous evolution towards a single chirality.[121,217,219–225]

References

(1) Partington, J. R. *A History of Chemistry*; Macmillan Education UK: London, 1964. https://doi.org/10.1007/978-1-349-00554-3.

(2) Biot, J. Phénomènes de Polarisation Successive, Observés Dans Des Fluides Homogènes. *Bull. Soc. Philomath* **1815**, *190*.

(3) Lowry, T. M. Pasteur as Chemist. *Proceedings of the Royal Society of Medicine* **1923**, *16* (Gen_Rep), 16–20. https://doi.org/10.1177/003591572301600603.

(4) Gay Lussac, L. J. *Cours de Chimie Par M. Gay-Lussac, Comprenant l'histoire Des Sels, Ia Chimie Vegetale et Animale*, Pichon et Didier.; Paris, 1828; Vol. 24th Lecture.

(5) Pasteur, L. Memoires Sur La Relation Qui Peut Exister Entre La Forme Crystalline et al Composition Chimique, et Sur La Cause Dela Polarization Rotatoire. *C R Acad Sci* **1848**, *26*, 535–538.

(6) Debré, P. *Louis Pasteur*, JHU Press.; 2000.

(7) Geison, G. *The Private Science of Louis Pasteur*, Princeton legacy library.; 2016.

(8) Pasteur, L. Sur les relations qui peuvent exister entre la forme cristalline, la composition chimiques et le sens de la polarisation rotatoire. *Annales de chimie et de physique* **1848**, *24*, 442–459.

(9) Le Bel, J. A. Sur les relations qui existent entre les formules atomiques des corps organiques et le pouvoir rotatoire de leurs dissolution. *Bulletin de la Société chimique de Paris* **1874**, *22*, 337–347.

(10) Emptoz, G. Achille le bel (1847-1930), un chimiste innovant tenu à l'écart par ses pairs. *cahierscfv* **2015**, No. II-6/7, 121–135. https://doi.org/10.4000/cahierscfv.2943.

(11) Van't Hoff, J. H. Sur Les Formules de Structure Dans l'espace. *Bulletin de la Société chimique de Paris* **1875**, *23*, 295–301.

(12) Kelvin, Lord. *Baltimore Lectures on Molecular Dynamics and the Wave Theory of Light*; Cambridge University Press, 1904.

(13) Garnier, M. *Illustration of Chirality*; 2023.

(14) Büschleb, M.; Dorich, S.; Hanessian, S.; Tao, D.; Schenthal, K. B.; Overman, L. E. Synthetic Strategies toward Natural Products Containing Contiguous Stereogenic Quaternary Carbon Atoms. *Angewandte Chemie International Edition* **2016**, *55* (13), 4156–4186. https://doi.org/10.1002/anie.201507549.

(15) Lemouzy, S.; Giordano, L.; Hérault, D.; Buono, G. Introducing Chirality at Phosphorus Atoms: An Update on the Recent Synthetic Strategies for the Preparation of Optically Pure P-Stereogenic Molecules. *European Journal of Organic Chemistry* **2020**, *2020* (23), 3351–3366. https://doi.org/10.1002/ejoc.202000406.

(16) Otocka, S.; Kwiatkowska, M.; Madalińska, L.; Kiełbasiński, P. Chiral Organosulfur Ligands/Catalysts with a Stereogenic Sulfur Atom: Applications in Asymmetric Synthesis. *Chem. Rev.* **2017**, *117* (5), 4147–4181. https://doi.org/10.1021/acs.chemrev.6b00517.

(17) Cahn, R. S.; Ingold, C.; Prelog, V. Specification of Molecular Chirality. *Angew. Chem. Int. Ed. Engl.* **1966**, *5* (4), 385–415. https://doi.org/10.1002/anie.196603851.

(18) Cahn, R. S.; Ingold, C. K.; Prelog, V. The Specification of Asymmetric Configuration in Organic Chemistry. *Experientia* **1956**, *12* (3), 81–94. https://doi.org/10.1007/BF02157171.

(19) Kunz, H. Emil Fischer—Unequalled Classicist, Master of Organic Chemistry Research, and Inspired Trailblazer of Biological Chemistry. *Angew. Chem. Int. Ed.* **2002**, *41* (23), 4439–4451. https://doi.org/10.1002/1521-3773(20021202)41:23<4439::AID-ANIE4439>3.0.CO;2-6.

(20) Gorman, C. A.; Jiang, N.-S.; Ellefson, R. D.; Elveback, L. R. Comparative Effectiveness of Dextrothyroxine and Levothyroxine in Correcting Hypothyroidism and Lowering Blood Lipid Levels in Hypothyroid Patients. *The Journal of Clinical Endocrinology & Metabolism* **1979**, *49* (1), 1–7. https://doi.org/10.1210/jcem-49-1-1.

(21) Kovač, J.; Vargas, M.; Keiser, J. In Vitro and in Vivo Activity of R- and S- Praziquantel Enantiomers and the Main Human Metabolite Trans-4-Hydroxy-Praziquantel against Schistosoma Haematobium. *Parasites Vectors* **2017**, *10* (1), 365. https://doi.org/10.1186/s13071-017-2293-3.

(22) Evans, A. M. Comparative Pharmacology of S(+)-Ibuprofen and (RS)-Ibuprofen. *Clin Rheumatol* **2001**, *20* (S1), 9–14. https://doi.org/10.1007/BF03342662.

(23) Singh, M.; Sethi, S.; Bhushan, R. Liquid Chromatographic Methods for Separation, Determination, and Bioassay of Enantiomers of Etodolac: A Review. *Journal of Separation Science* **2020**, *43* (1), 18–30. https://doi.org/10.1002/jssc.201900649.

(24) Ito, T.; Ando, H.; Handa, H. Teratogenic Effects of Thalidomide: Molecular Mechanisms. *Cell. Mol. Life Sci.* **2011**, *68* (9), 1569–1579. https://doi.org/10.1007/s00018-010-0619-9.

(25) De Camp, W. H. Chiral Drugs: The FDA Perspective on Manufacturing and Control. *Journal of Pharmaceutical and Biomedical Analysis* **1993**, *11* (11–12), 1167–1172. https://doi.org/10.1016/0731-7085(93)80100-F.
(26) Caner, H.; Groner, E.; Levy, L.; Agranat, I. Trends in the Development of Chiral Drugs. *Drug Discovery Today* **2004**, *9* (3), 105–110. https://doi.org/10.1016/S1359-6446(03)02904-0.
(27) Orlandini, S.; Hancu, G.; Szabó, Z.-I.; Modroiu, A.; Papp, L.-A.; Gotti, R.; Furlanetto, S. New Trends in the Quality Control of Enantiomeric Drugs: Quality by Design-Compliant Development of Chiral Capillary Electrophoresis Methods. *Molecules* **2022**, *27* (20), 7058. https://doi.org/10.3390/molecules27207058.
(28) Agranat, I.; Wainschtein, S. R.; Zusman, E. Z. The Predicated Demise of Racemic New Molecular Entities Is an Exaggeration. *Nat Rev Drug Discov* **2012**, *11* (12), 972–973. https://doi.org/10.1038/nrd3657-c1.
(29) Kumkumian, C. S. Chirality and Drug Development. *Science* **1992**, No. 257, 145.
(30) Calcaterra, A.; D'Acquarica, I. The Market of Chiral Drugs: Chiral Switches versus de Novo Enantiomerically Pure Compounds. *Journal of Pharmaceutical and Biomedical Analysis* **2018**, *147*, 323–340. https://doi.org/10.1016/j.jpba.2017.07.008.
(31) Agranat, I.; Caner, H.; Caldwell, J. Putting Chirality to Work: The Strategy of Chiral Switches. *Nat Rev Drug Discov* **2002**, *1* (10), 753–768. https://doi.org/10.1038/nrd915.
(32) H. Brooks, W.; C. Guida, W.; G. Daniel, K. The Significance of Chirality in Drug Design and Development. *CTMC* **2011**, *11* (7), 760–770. https://doi.org/10.2174/156802611795165098.
(33) Hancu, G.; Modroiu, A. Chiral Switch: Between Therapeutical Benefit and Marketing Strategy. *Pharmaceuticals* **2022**, *15* (2), 240. https://doi.org/10.3390/ph15020240.
(34) Asghar, W.; Pittman, E.; Jamali, F. Comparative Efficacy of Esomeprazole and Omeprazole: Racemate to Single Enantiomer Switch. *DARU J Pharm Sci* **2015**, *23* (1), 50. https://doi.org/10.1186/s40199-015-0133-6.
(35) Strolin Benedetti, M.; Plisnier, M.; Kaise, J.; Maier, L.; Baltes, E.; Arendt, C.; McCracken, N. Absorption, Distribution, Metabolism and Excretion of [14C]Levocetirizine, the R Enantiomer of Cetirizine, in Healthy Volunteers. *Eur J Clin Pharmacol* **2001**, *57* (8), 571–582. https://doi.org/10.1007/s002280100364.
(36) Ali, I.; Gupta, V. K.; Aboul-Enein, H. Y.; Singh, P.; Sharma, B. Role of Racemization in Optically Active Drugs Development. *Chirality* **2007**, *19* (6), 453–463. https://doi.org/10.1002/chir.20397.
(37) Hao, H.; Wang, G.; Sun, J. Enantioselective Pharmacokinetics of Ibuprofen and Involved Mechanisms. *Drug Metabolism Reviews* **2005**, *37* (1), 215–234. https://doi.org/10.1081/DMR-200047999.
(38) Wsol, V.; Skalova, L.; Szotakova, B. Chiral Inversion of Drugs: Coincidence or Principle? *CDM* **2004**, *5* (6), 517–533. https://doi.org/10.2174/1389200043335360.
(39) Smith, S. W. Chiral Toxicology: It's the Same Thing…Only Different. *Toxicological Sciences* **2009**, *110* (1), 4–30. https://doi.org/10.1093/toxsci/kfp097.
(40) Agranat, I.; Wainschtein, S. R. The Strategy of Enantiomer Patents of Drugs. *Drug Discovery Today* **2010**, *15* (5–6), 163–170. https://doi.org/10.1016/j.drudis.2010.01.007.
(41) Tucker, G. T. Chiral Switches. *The Lancet* **2000**, *335* (9209), 1085–1087. https://doi.org/10.1016/S0140-6736(00)02047-X.
(42) Almarsson, Ö.; Zaworotko, M. J. Crystal Engineering of the Composition of Pharmaceutical Phases. Do Pharmaceutical Co-Crystals Represent a New Path to Improved Medicines? *Chem. Commun.* **2004**, No. 17, 1889. https://doi.org/10.1039/b402150a.
(43) Cheney, M. L.; Shan, N.; Healey, E. R.; Hanna, M.; Wojtas, L.; Zaworotko, M. J.; Sava, V.; Song, S.; Sanchez-Ramos, J. R. Effects of Crystal Form on Solubility and Pharmacokinetics: A Crystal Engineering Case Study of Lamotrigine. *Crystal Growth & Design* **2010**, *10* (1), 394–405. https://doi.org/10.1021/cg901010v.
(44) Adepu, S.; Ramakrishna, S. Controlled Drug Delivery Systems: Current Status and Future Directions. *Molecules* **2021**, *26* (19), 5905. https://doi.org/10.3390/molecules26195905.
(45) Verma, P.; Thakur, A. S.; Deshmukh, K.; Jha, D. A. K.; Verma, S. ROUTES OF DRUG ADMINISTRATION.
(46) Levy, R. M. *Principles of Solid State Physics*; Elsevier, 2012.
(47) Harrison, W. A. *Solid State Theory*; Courier Corporation, 1980.
(48) Binnemans, K. Ionic Liquid Crystals. *Chem. Rev.* **2005**, *105* (11), 4148–4204. https://doi.org/10.1021/cr0400919.
(49) Levine, D.; Steinhardt, P. J. Quasicrystals. I. Definition and Structure. *Phys. Rev. B* **1986**, *34* (2), 596–616. https://doi.org/10.1103/PhysRevB.34.596.
(50) Rousseau, J. J.; Gibaud, A. *Cristallographie Géométrique et Radiocristallographie*; SCIENCES SUP; DUNOD: PARIS, 2000.

(51) Romé de L'Isle, J.-B. L. de (1736-1790) A. du texte. *Des caractères extérieurs des minéraux, ou Réponse à cette question : Existe-t'il dans les substances du règne minéral des caractères qu'on puisse regarder comme spécifiques ; & au cas qu'il en existe, quels sont ces caractères ? : avec un apperçu des différens systèmes lithologiques... ; suivi de deux Tableaux synoptiques des substances pierreuses et métalliques, pour servir de suite à la "Cristallographie" / Par M. de Romé de L'Isle,...*; 1784.

(52) Haüy, R.-J. (1743-1822) A. du texte. *Essai d'une théorie sur la structure des crystaux, appliquée à plusieurs genres de substances crystallisées / par M. l'abbé Haüy,...*; 1784.

(53) Dunitz, J. D. X-Ray Analysis and the Structure of Organic Molecules. In *X-Ray Analysis and the Structure of Organic Molecules*; John Wiley & Sons, Ltd, 1995. https://doi.org/10.1002/9783906390390.fmatter.

(54) Bravais, A. (1811-1863) A. du texte. *Etudes cristallographiques ; Mémoire sur les systèmes formés par des points distribués régulièrement sur un plan ou dans l'espace / par M. Auguste Bravais,...*; 1866.

(55) *International Tables for Crystallography. A: Space-Group Symmetry*, 5., rev. ed., repr. with corr.; Springer: Dordrecht, 2005.

(56) Meerssche, M. V.; Feneau-Dupont, J.; Van Meerssche, M. *INTRODUCTION A LA CRISTALLOGRAPHIE ET A LA CHIMIE STRUCTURALE : 2ème Édition*, 2e ed.; Oyez: Leuven, 1976.

(57) Flack, H. D. Chiral and Achiral Crystal Structures. *Helvetica Chimica Acta* **2003**, *86* (4), 905–921. https://doi.org/10.1002/hlca.200390109.

(58) Pertsin, A. J.; Kitaigorodsky, A. I. *The Atom-Atom Potential Method*, Springer Berlin, Heidelberg.; Applications to Organic Molecular Solids; Berlin; Vol. 1.

(59) Parsegian, V. A. *Van Der Waals Forces: A Handbook for Biologists, Chemists, Engineers, and Physicists*; Cambridge University Press, 2005.

(60) Dunitz, J. D. Weak Interactions in Molecular Crystals. In *Implications of Molecular and Materials Structure for New Technologies*; Howard, J. A. K., Allen, F. H., Shields, G. P., Eds.; Springer Netherlands: Dordrecht, 1999; pp 175–184. https://doi.org/10.1007/978-94-011-4653-1_12.

(61) A. Hunter, C.; R. Lawson, K.; Perkins, J.; J. Urch, C. Aromatic Interactions. *Journal of the Chemical Society, Perkin Transactions 2* **2001**, *0* (5), 651–669. https://doi.org/10.1039/B008495F.

(62) Aromatic-Aromatic Interaction: A Mechanism of Protein Structure Stabilization | Science. https://doi.org/10.1126/science.3892686.

(63) Steiner, T. The Hydrogen Bond in the Solid State. *Angewandte Chemie International Edition* **2002**, *41* (1), 48–76. https://doi.org/10.1002/1521-3773(20020104)41:1<48::AID-ANIE48>3.0.CO;2-U.

(64) Steiner, T.; Desiraju, G. R. Distinction between the Weak Hydrogen Bond and the van Der Waals Interaction. *Chemical Communications* **1998**, *0* (8), 891–892. https://doi.org/10.1039/A708099I.

(65) Brammer, L.; Bruton, E. A.; Sherwood, P. Understanding the Behavior of Halogens as Hydrogen Bond Acceptors. *Crystal Growth & Design* **2001**, *1* (4), 277–290. https://doi.org/10.1021/cg015522k.

(66) Csöregh, I.; Brehmer, T.; Bombicz, P.; Weber, E. Halogen···halogen versus OH···O Supramolecular Interactions in the Crystal Structures of a Series of Halogen and Methyl Substituted Cis-9,10-Diphenyl-9,10-Dihydroanthracene-9,10-Diols. *Crystal Engineering* **2001**, *4* (4), 343–357. https://doi.org/10.1016/S1463-0184(01)00026-0.

(67) Desiraju, P. The Nature of Halogen...Halogen Interactions: Are Short Halogen Contacts Due to Specific Attractive Forces or Due to Close Packing of Non Spherical Atoms.

(68) Politzer, P.; Lane, P.; Concha, M. C.; Ma, Y.; Murray, J. S. An Overview of Halogen Bonding. *J Mol Model* **2007**, *13* (2), 305–311. https://doi.org/10.1007/s00894-006-0154-7.

(69) Prasanna, M. D.; Guru Row, T. N. C–Halogen···π Interactions and Their Influence on Molecular Conformation and Crystal Packing: A Database Study. *Crystal Engineering* **2000**, *3* (2), 135–154. https://doi.org/10.1016/S1463-0184(00)00035-6.

(70) Hunter, C. A.; Sanders, J. K. M. The Nature of .Pi.-.Pi. Interactions. *J. Am. Chem. Soc.* **1990**, *112* (14), 5525–5534. https://doi.org/10.1021/ja00170a016.

(71) Kruszynski, R.; Sierański, T. Can Stacking Interactions Exist Beyond the Commonly Accepted Limits? *Crystal Growth & Design* **2016**, *16* (2), 587–595. https://doi.org/10.1021/acs.cgd.5b00852.

(72) Bernstein, J. *Polymorphism in Molecular Crystals*, Oxford University Press.; New York, 2002.

(73) Haisa, M.; Kashino, S.; Maeda, H. The Orthorhombic Form of P-Hydroxyacetanilide. *Acta Cryst B* **1974**, *30* (10), 2510–2512. https://doi.org/10.1107/S0567740874007473.

(74) Haisa, M.; Kashino, S.; Kawai, R.; Maeda, H. The Monoclinic Form of P-Hydroxyacetanilide. *Acta Cryst B* **1976**, *32* (4), 1283–1285. https://doi.org/10.1107/S0567740876012223.

(75) Cruz-Cabeza, A. J.; Bernstein, J. Conformational Polymorphism. *Chem. Rev.* **2014**, *114* (4), 2170–2191. https://doi.org/10.1021/cr400249d.

(76) Bernstein, J.; Hagler, A. T. Conformational Polymorphism. The Influence of Crystal Structure on Molecular Conformation. *J. Am. Chem. Soc.* **1978**, *100* (3), 673–681. https://doi.org/10.1021/ja00471a001.
(77) Vippagunta, S. R.; Brittain, H. G.; Grant, D. J. W. Crystalline Solids. *Advanced Drug Delivery Reviews* **2001**, *48* (1), 3–26. https://doi.org/10.1016/S0169-409X(01)00097-7.
(78) Kashchiev, D. *Nucleation Basic Theory with Applications*; Butterworth-Heinemann: Oxford, 2000.
(79) Kalikmanov, V. I. Classical Nucleation Theory. In *Nucleation Theory*; Kalikmanov, V. I., Ed.; Springer Netherlands: Dordrecht, 2013; pp 17–41. https://doi.org/10.1007/978-90-481-3643-8_3.
(80) Karthika, S.; Radhakrishnan, T. K.; Kalaichelvi, P. A Review of Classical and Nonclassical Nucleation Theories. *Crystal Growth & Design* **2016**, *16* (11), 6663–6681. https://doi.org/10.1021/acs.cgd.6b00794.
(81) Nyquist, R. M.; Talanquer, V.; Oxtoby, D. W. Density Functional Theory of Nucleation: A Semiempirical Approach. *The Journal of Chemical Physics* **1995**, *103* (3), 1175–1179. https://doi.org/10.1063/1.469827.
(82) Zeng, X. C.; Oxtoby, D. W. Binary Homogeneous Nucleation Theory for the Gas–Liquid Transition: A Nonclassical Approach. *The Journal of Chemical Physics* **1991**, *95* (8), 5940–5947. https://doi.org/10.1063/1.461615.
(83) Reguera, D.; Bowles, R. K.; Djikaev, Y.; Reiss, H. Phase Transitions in Systems Small Enough to Be Clusters. *The Journal of Chemical Physics* **2003**, *118* (1), 340–353. https://doi.org/10.1063/1.1524192.
(84) Gebauer, D.; Cölfen, H. Prenucleation Clusters and Non-Classical Nucleation. *Nano Today* **2011**, *6* (6), 564–584. https://doi.org/10.1016/j.nantod.2011.10.005.
(85) Jiang, H.; Debenedetti, P. G.; Panagiotopoulos, A. Z. Nucleation in Aqueous NaCl Solutions Shifts from 1-Step to 2-Step Mechanism on Crossing the Spinodal. *The Journal of Chemical Physics* **2019**, *150* (12), 124502. https://doi.org/10.1063/1.5084248.
(86) Perala, S. R. K.; Kumar, S. On the Two-Step Mechanism for Synthesis of Transition-Metal Nanoparticles. *Langmuir* **2014**, *30* (42), 12703–12711. https://doi.org/10.1021/la503199m.
(87) Coquerel, G. Crystallization of Molecular Systems from Solution: Phase Diagrams, Supersaturation and Other Basic Concepts. *Chem. Soc. Rev.* **2014**, *43* (7), 2286–2300. https://doi.org/10.1039/C3CS60359H.
(88) Sadeghi, M.; Rasmuson, Å. C. On the Estimation of Crystallization Driving Forces. *CrystEngComm* **2019**, *21* (34), 5164–5173. https://doi.org/10.1039/C9CE00747D.
(89) Gibbs, J. W. (Josiah W.; Tyndall, J.; Connecticut Academy of Arts and Sciences; Burndy Library, donor D. *On the Equilibrium of Heterogeneous Substances*; [New Haven : Published by the Academy], 1874.
(90) Alper, A. M. *Phase Diagrams, Materials Science and Technology. Vol. I: Theory, Principles, and Techniques of Phase Diagrams.*, Academic Press.; New York-London, 1970; Vol. I.
(91) Zeng, Y.; Szymanski, N. J.; He, T.; Jun, K.; Gallington, L. C.; Huo, H.; Bartel, C. J.; Ouyang, B.; Ceder, G. Selective Formation of Metastable Polymorphs in Solid-State Synthesis. *Science Advances* **2024**, *10* (3), eadj5431. https://doi.org/10.1126/sciadv.adj5431.
(92) Bernstein, J. *Polymorphism in Molecular Crystals*; International Union of Crystallography monographs on crystallography; Oxford University Press: OxfordClarendon Press ; New York, 2002.
(93) *Polymorphism in Pharmaceutical Solids*, 2nd ed.; Brittain, H. G., Ed.; CRC Press: Boca Raton, 2018. https://doi.org/10.3109/9781420073225.
(94) Sheth, A. R.; Grant, D. J. W. Relationship between the Structure and Properties of Pharmaceutical Crystals. *KONA Powder and Particle Journal* **2005**, *23*, 36–48. https://doi.org/10.14356/kona.2005008.
(95) *Polymorphism in Pharmaceutical Solids*, 2nd ed.; Brittain, H. G., Ed.; Drugs and the pharmaceutical sciences; Informa Healthcare, 2009; Vol. 192.
(96) Sheth, A. R.; Grant, D. J. W. Relationship between the Structure and Properties of Pharmaceutical Crystals. *KONA* **2005**, *23* (0), 36–48. https://doi.org/10.14356/kona.2005008.
(97) Chemburkar, S. R.; Bauer, J.; Deming, K.; Spiwek, H.; Patel, K.; Morris, J.; Henry, R.; Spanton, S.; Dziki, W.; Porter, W.; Quick, J.; Bauer, P.; Donaubauer, J.; Narayanan, B. A.; Soldani, M.; Riley, D.; McFarland, K. Dealing with the Impact of Ritonavir Polymorphs on the Late Stages of Bulk Drug Process Development. *Org. Process Res. Dev.* **2000**, *4* (5), 413–417. https://doi.org/10.1021/op000023y.
(98) Hilfker, R.; Raumer, M. vob. *Polymorphism in the Pharmaceutical Industry*; Wiley-VCH Verlag GmbH & Co. KGaA: Weinheim, 2006.
(99) *Polymorphism in the Pharmaceutical Industry*; Hilfiker, R., Ed.; Wiley-VCH Verlag GmbH & Co. KGaA: Weinheim, 2006.
(100) Brittain, H. G. The Impact of Polymorphism on Drug Development A Regulator's Viewpoint. *American Pharmaceutical Review* **2000**, *3*.
(101) Mullin, J. W. *Crystallization*, 4th ed.; Butterworth-Heinemann: Oxford ; Boston, 2001.

(102) Burger, A.; Ramberger, R. On the Polymorphism of Pharmaceuticals and Other Molecular Crystals. I. *Mikrochim Acta* **1979**, *72* (3–4), 259–271. https://doi.org/10.1007/BF01197379.

(103) Hursthouse, M. B.; Huth, L. S.; Threlfall, T. L. Why Do Organic Compounds Crystallise Well or Badly or Ever so Slowly? Why Is Crystallisation Nevertheless Such a Good Purification Technique? *Org. Process Res. Dev.* **2009**, *13* (6), 1231–1240. https://doi.org/10.1021/op900169b.

(104) Schmelzer, J. W. P.; Abyzov, A. S. How Do Crystals Nucleate and Grow: Ostwald's Rule of Stages and Beyond. In *Thermal Physics and Thermal Analysis: From Macro to Micro, Highlighting Thermodynamics, Kinetics and Nanomaterials*; Šesták, J., Hubík, P., Mareš, J. J., Eds.; Hot Topics in Thermal Analysis and Calorimetry; Springer International Publishing: Cham, 2017; pp 195–211. https://doi.org/10.1007/978-3-319-45899-1_9.

(105) Threlfall, T. Structural and Thermodynamic Explanations of Ostwald's Rule. *Org. Process Res. Dev.* **2003**, *7* (6), 1017–1027. https://doi.org/10.1021/op030026l.

(106) Chaudhuri, K. R. Crystallisation within Transdermal Rotigotine Patch: Is There Cause for Concern? *Expert Opinion on Drug Delivery* **2008**, *5* (11), 1169–1171. https://doi.org/10.1517/17425240802500870.

(107) Dunitz, J. D.; Bernstein, J. Disappearing Polymorphs. *Acc. Chem. Res.* **1995**, *28* (4), 193–200. https://doi.org/10.1021/ar00052a005.

(108) Bučar, D.; Lancaster, R. W.; Bernstein, J. Disappearing Polymorphs Revisited. *Angew Chem Int Ed* **2015**, *54* (24), 6972–6993. https://doi.org/10.1002/anie.201410356.

(109) Coquerel, G. Phase Diagrams for Process Design. In *Engineering Crystallography: From Molecule to Crystal to Functional Form*; Roberts, K. J., Docherty, R., Tamura, R., Eds.; NATO Science for Peace and Security Series A: Chemistry and Biology; Springer Netherlands: Dordrecht, 2017; pp 215–233. https://doi.org/10.1007/978-94-024-1117-1_12.

(110) *Chirality in Drug Research*, 1st ed.; Francotte, E., Lindner, W., Eds.; Wiley-VCH Verlag GmbH & Co. KGaA, 2006.

(111) Ricci, J. E. The Phase Rule and Heterogeneous Equilibrium. In *The Phase Rule and Heterogeneous Equilibrium*; Dover: New York, 1951.

(112) Coquerel, G. Review on the Heterogeneous Equilibria between Condensed Phases in Binary Systems of Enantiomers. *Enantiomer A Journal of Stereochemistry* **2000**, *5*, 481–498.

(113) Legendre, B.; Querniard, F. Glossary for Binary Phase Diagram Reactions. *J. Phase Equilib. Diffus.* **2014**, *35* (1), 11–14. https://doi.org/10.1007/s11669-013-0266-6.

(114) Jacques, J.; Collet, A.; Wilen, S. H. *Enantiomers, Racemates, and Resolutions*; Krieger Publishing Company: Malabar, 1994.

(115) Prigogine, I.; Defay, R. Chemical Thermodynamics. **1958**.

(116) Hoff, J. H. van't (1852-1911) A. du texte. *Études de dynamique chimique / par J. H. Van 't Hoff*; 1884.

(117) Brandel, C.; Petit, S.; Cartigny, Y.; Coquerel, G. Structural Aspects of Solid Solutions of Enantiomers. *CPD* **2016**, *22* (32), 4929–4941. https://doi.org/10.2174/1381612822666160720164230.

(118) Rekis, T.; Agris, B. On the Structural Aspects of Solid Solutions of Enantiomers: An Intriguing Case Study of Enantiomer Recognition in the Solid State. *CrystEngComm*. 2018, pp 6909–6918.

(119) Viedma, C. Chiral Symmetry Breaking During Crystallization: Complete Chiral Purity Induced by Nonlinear Autocatalysis and Recycling. *Phys. Rev. Lett.* **2005**, *94* (6), 065504. https://doi.org/10.1103/PhysRevLett.94.065504.

(120) Viedma, C. Chiral Symmetry Breaking and Complete Chiral Purity by Thermodynamic-Kinetic Feedback Near Equilibrium: Implications for the Origin of Biochirality. *Astrobiology* **2007**, *7* (2), 312–319. https://doi.org/10.1089/ast.2006.0099.

(121) Suwannasang, K.; Flood, A. E.; Coquerel, G. A Novel Design Approach To Scale Up the Temperature Cycle Enhanced Deracemization Process: Coupled Mixed-Suspension Vessels. *Crystal Growth & Design* **2016**, *16* (11), 6461–6467. https://doi.org/10.1021/acs.cgd.6b01139.

(122) Oketani, R.; Marin, F.; Tinnemans, P.; Hoquante, M.; Laurent, A.; Brandel, C.; Cardinael, P.; Meekes, H.; Vlieg, E.; Geerts, Y.; Coquerel, G. Deracemization in a Complex Quaternary System with a Second-Order Asymmetric Transformation by Using Phase Diagram Studies. *Chem. Eur. J.* **2019**, *25* (61), 13890–13898. https://doi.org/10.1002/chem.201903338.

(123) Hein, J. E.; Huynh Cao, B.; Viedma, C.; Kellogg, R. M.; Blackmond, D. G. Pasteur's Tweezers Revisited: On the Mechanism of Attrition-Enhanced Deracemization and Resolution of Chiral Conglomerate Solids. *J. Am. Chem. Soc.* **2012**, *134* (30), 12629–12636. https://doi.org/10.1021/ja303566g.

(124) Sui, J.; Wang, N.; Wang, J.; Huang, X.; Wang, T.; Zhou, L.; Hao, H. Strategies for Chiral Separation: From Racemate to Enantiomer. *Chem. Sci.* **2023**, *14* (43), 11955–12003. https://doi.org/10.1039/D3SC01630G.

(125) Borchardt-Setter, K. A.; Yu, L. Assessing the Potential for Chiral Separation by Crystallization Using Crystal Energies. *Crystal Growth & Design* **2023**, *23* (5), 3615–3622. https://doi.org/10.1021/acs.cgd.3c00077.

(126) Hoquante, M.; Sanselme, M.; Rietveld, I. B.; Coquerel, G. Disappearing Conglomerates, Assessment of the Threat. *Crystal Growth & Design* **2019**, *19* (12), 7396–7401. https://doi.org/10.1021/acs.cgd.9b01316.

(127) Xiouras, C.; Cameli, F.; Quilló, G. L.; Kavousanakis, M. E.; Vlachos, D. G.; Stefanidis, G. D. Applications of Artificial Intelligence and Machine Learning Algorithms to Crystallization. *Chem. Rev.* **2022**, *122* (15), 13006–13042. https://doi.org/10.1021/acs.chemrev.2c00141.

(128) Zheng, Y.; Wang, X.; Wu, Z. Machine Learning Modeling and Predictive Control of the Batch Crystallization Process. *Ind. Eng. Chem. Res.* **2022**, *61* (16), 5578–5592. https://doi.org/10.1021/acs.iecr.2c00026.

(129) Viedma, C.; Ortiz, J. E. A New Twist in Eutectic Composition: Deracemization of a Racemic Compound Amino Acid by Viedma Ripening and Temperature Fluctuation. *Israel Journal of Chemistry* **2021**, *61* (11–12), 758–763. https://doi.org/10.1002/ijch.202100075.

(130) Buol, X.; Caro Garrido, C.; Robeyns, K.; Tumanov, N.; Collard, L.; Wouters, J.; Leyssens, T. Chiral Resolution of Mandelic Acid through Preferential Cocrystallization with Nefiracetam. *Crystal Growth & Design* **2020**, *20* (12), 7979–7988. https://doi.org/10.1021/acs.cgd.0c01236.

(131) Valenti, G.; Tinnemans, P.; Baglai, I.; Noorduin, W. L.; Kaptein, B.; Leeman, M.; ter Horst, J. H.; Kellogg, R. M. Combining Incompatible Processes for Deracemization of a Praziquantel Derivative under Flow Conditions. *Angew. Chem.* **2021**, *133* (10), 5339–5342. https://doi.org/10.1002/ange.202013502.

(132) Pinètre, C.; Ritou, L.; Gerard, C. J. J.; Cercel, H.; Leeman, M.; Kellogg, R. M.; Tinnemans, P.; Sanselme, M.; Brandel, C.; Dupray, V.; ter Horst, J. H. Rare Case of Polymorphism in the Binary System of Enantiomers of a Praziquantel Derivative. *Org. Process Res. Dev.* **2024**. https://doi.org/10.1021/acs.oprd.4c00035.

(133) Pinetre, C.; Harfouche, L.; Brandel, C.; Bendeif, E.-E.; Sanselme, M.; Cartigny, Y.; Couvrat, N.; Dupray, V. Investigation of the Binary System of Proxyphylline Enantiomers: Structural Resolution and Phase Diagram Determination. *Mol. Pharmaceutics* **2024**, *21* (2), 845–853. https://doi.org/10.1021/acs.molpharmaceut.3c00922.

(134) Engwerda, A. H. J.; Meekes, H.; Kaptein, B.; Rutjes, F. P. J. T.; Vlieg, E. Speeding up Viedma Ripening. *Chem. Commun.* **2016**, *52* (81), 12048–12051. https://doi.org/10.1039/C6CC06766B.

(135) Brandel, C.; Amharar, Y.; Rollinger, J. M.; Griesser, U. J.; Cartigny, Y.; Petit, S.; Coquerel, G. Impact of Molecular Flexibility on Double Polymorphism, Solid Solutions and Chiral Discrimination during Crystallization of Diprophylline Enantiomers. *Mol. Pharmaceutics* **2013**, *10* (10), 3850–3861. https://doi.org/10.1021/mp400308u.

(136) Brandel, C.; Cartigny, Y.; Coquerel, G.; ter Horst, J. H.; Petit, S. Prenucleation Self-Assembly and Chiral Discrimination Mechanisms during Solution Crystallisation of Racemic Diprophylline. *Chemistry—A European Journal* **2016**, *22* (45), 16103–16112. https://doi.org/10.1002/chem.201602707.

(137) Harfouche, L. C.; Brandel, C.; Cartigny, Y.; ter Horst, J. H.; Coquerel, G.; Petit, S. Enabling Direct Preferential Crystallization in a Stable Racemic Compound System. *Mol. Pharmaceutics* **2019**, *16* (11), 4670–4676. https://doi.org/10.1021/acs.molpharmaceut.9b00805.

(138) Gavezzotti, A.; Rizzato, S. Are Racemic Crystals Favored over Homochiral Crystals by Higher Stability or by Kinetics? Insights from Comparative Studies of Crystalline Stereoisomers. *J. Org. Chem.* **2014**, *79* (11), 4809–4816. https://doi.org/10.1021/jo500528k.

(139) Gryl, M.; Kozieł, M.; Stadnicka, K. M. A Proposal for Coherent Nomenclature of Multicomponent Crystals. *Acta Cryst B* **2019**, *75* (1), 53–58. https://doi.org/10.1107/S2052520618015858.

(140) Aitipamula, S.; Banerjee, R.; Bansal, A. K.; Biradha, K.; Cheney, M. L.; Choudhury, A. R.; Desiraju, G. R.; Dikundwar, A. G.; Dubey, R.; Duggirala, N.; Ghogale, P. P.; Ghosh, S.; Goswami, P. K.; Goud, N. R.; Jetti, R. R. K. R.; Karpinski, P.; Kaushik, P.; Kumar, D.; Kumar, V.; Moulton, B.; Mukherjee, A.; Mukherjee, G.; Myerson, A. S.; Puri, V.; Ramanan, A.; Rajamannar, T.; Reddy, C. M.; Rodriguez-Hornedo, N.; Rogers, R. D.; Row, T. N. G.; Sanphui, P.; Shan, N.; Shete, G.; Singh, A.; Sun, C. C.; Swift, J. A.; Thaimattam, R.; Thakur, T. S.; Kumar Thaper, R.; Thomas, S. P.; Tothadi, S.; Vangala, V. R.; Variankaval, N.; Vishweshwar, P.; Weyna, D. R.; Zaworotko, M. J. Polymorphs, Salts, and Cocrystals: What's in a Name? *Crystal Growth & Design* **2012**, *12* (5), 2147–2152. https://doi.org/10.1021/cg3002948.

(141) Crassous, J.; Fuchter, M. J.; Freedman, D. E.; Kotov, N. A.; Moon, J.; Beard, M. C.; Feldmann, S. Materials for Chiral Light Control. *Nat Rev Mater* **2023**, *8* (6), 365–371. https://doi.org/10.1038/s41578-023-00543-3.

(142) Niu, X.; Zhao, R.; Yan, S.; Pang, Z.; Li, H.; Yang, X.; Wang, K. Chiral Materials: Progress, Applications, and Prospects. *Small* **2023**, *19* (38), 2303059. https://doi.org/10.1002/smll.202303059.

(143) Zhang, C.; Xiong, Y.; Jiao, F.; Wang, M.; Li, H. Redefining the Term of "Cocrystal" and Broadening Its Intention. *Crystal Growth & Design* **2019**, *19* (3), 1471–1478. https://doi.org/10.1021/acs.cgd.8b01537.

(144) Grothe, E.; Meekes, H.; Vlieg, E.; ter Horst, J. H.; de Gelder, R. Solvates, Salts, and Cocrystals: A Proposal for a Feasible Classification System. *Crystal Growth & Design* **2016**, *16* (6), 3237–3243. https://doi.org/10.1021/acs.cgd.6b00200.

(145) Gerard, C. J. J.; Pinetre, C.; Cercel, H.; Charpentier, M. D.; Sanselme, M.; Couvrat, N.; Brandel, C.; Cartigny, Y.; Dupray, V.; ter Horst, J. H. Phase Diagrams of Praziquantel and Vanillic Acid Cocrystals: Racemic Compound and Conglomerate System. *Crystal Growth & Design* **2024**. https://doi.org/10.1021/acs.cgd.4c00114.

(146) Rapeenun, P.; Gerard, C. J. J.; Pinètre, C.; Cartigny, Y.; Tinnemans, P.; de Gelder, R.; Flood, A. E.; ter Horst, J. H. Searching for Conglomerate Cocrystals of the Racemic Compound Praziquantel. *Crystal Growth & Design* **2024**, *24* (1), 480–490. https://doi.org/10.1021/acs.cgd.3c01158.

(147) *The IUPAC Compendium of Chemical Terminology: The Gold Book*, 4th ed.; Gold, V., Ed.; International Union of Pure and Applied Chemistry (IUPAC): Research Triangle Park, NC, 2019. https://doi.org/10.1351/goldbook.

(148) Tauvel, G.; Sanselme, M.; Coste-Leconte, S.; Petit, S.; Coquerel, G. Structural Studies of Several Solvated Potassium Salts of Tenatoprazole Crystallizing as Conglomerates. *Journal of Molecular Structure* **2009**, *936* (1), 60–66. https://doi.org/10.1016/j.molstruc.2009.07.014.

(149) Wacharine-Antar, S.; Levilain, G.; Dupray, V.; Coquerel, G. Resolution of (±)-Imeglimin-2,4-Dichlorophenylacetate Methanol Solvate by Preferential Crystallization. *Org. Process Res. Dev.* **2010**, *14* (6), 1358–1363. https://doi.org/10.1021/op100173r.

(150) Honer, K.; Kalfaoglu, E.; Pico, C.; McCann, J.; Baltrusaitis, J. Mechanosynthesis of Magnesium and Calcium Salt–Urea Ionic Cocrystal Fertilizer Materials for Improved Nitrogen Management. *ACS Sustainable Chem. Eng.* **2017**, *5* (10), 8546–8550. https://doi.org/10.1021/acssuschemeng.7b02621.

(151) Bennett, A. J.; Matzger, A. J. Progress in Predicting Ionic Cocrystal Formation: The Case of Ammonium Nitrate. *Chemistry – A European Journal* **2023**, *29* (27), e202300076. https://doi.org/10.1002/chem.202300076.

(152) Mbodji, A.; Gbabode, G.; Sanselme, M.; Couvrat, N.; Leeman, M.; Dupray, V.; Kellogg, R. M.; Coquerel, G. Family of Conglomerate-Forming Systems Composed of Chlocyphos and Alkyl-Amine. Assessment of Their Resolution Performances by Using Various Modes of Preferential Crystallization. *Crystal Growth & Design* **2019**, *19* (9), 5173–5183. https://doi.org/10.1021/acs.cgd.9b00568.

(153) Nayak, M.; Jana, A.; Fleck, M.; Hazra, S.; Mohanta, S. A Unique Example of a Three Component Cocrystal of Metal Complexes. *CrystEngComm* **2010**, *12* (5), 1416–1421. https://doi.org/10.1039/B919803B.

(154) Chu, Q.; Duncan, A. J. E.; Papaefstathiou, G. S.; Hamilton, T. D.; Atkinson, M. B. J.; Mariappan, S. V. S.; MacGillivray, L. R. Putting Cocrystal Stoichiometry to Work: A Reactive Hydrogen-Bonded "Superassembly" Enables Nanoscale Enlargement of a Metal–Organic Rhomboid via a Solid-State Photocycloaddition. *J. Am. Chem. Soc.* **2018**, *140* (14), 4940–4944. https://doi.org/10.1021/jacs.8b01775.

(155) Kulla, H.; Michalchuk, A. A. L.; Emmerling, F. Manipulating the Dynamics of Mechanochemical Ternary Cocrystal Formation. *Chem. Commun.* **2019**, *55* (66), 9793–9796. https://doi.org/10.1039/C9CC03034D.

(156) Song, L.; Robeyns, K.; Tumanov, N.; Wouters, J.; Leyssens, T. Combining API in a Dual-Drug Ternary Cocrystal Approach. *Chem. Commun.* **2020**, *56* (86), 13229–13232. https://doi.org/10.1039/D0CC05788F.

(157) Paul, M.; Desiraju, G. R. From a Binary to a Quaternary Cocrystal: An Unusual Supramolecular Synthon. *Angewandte Chemie* **2019**, *131* (35), 12155–12159. https://doi.org/10.1002/ange.201904339.

(158) Xu, Y.; Wang, Q.; Shen, C.; Lin, Q.; Wang, P.; Lu, M. A Series of Energetic Metal Pentazolate Hydrates. *Nature* **2017**, *549* (7670), 78–81. https://doi.org/10.1038/nature23662.

(159) Buffett, B. A. Clathrate Hydrates. *Annual Review of Earth and Planetary Sciences* **2000**, *28* (Volume 28, 2000), 477–507. https://doi.org/10.1146/annurev.earth.28.1.477.

(160) Veluswamy, H. P.; Kumar, A.; Seo, Y.; Lee, J. D.; Linga, P. A Review of Solidified Natural Gas (SNG) Technology for Gas Storage via Clathrate Hydrates. *Applied Energy* **2018**, *216*, 262–285. https://doi.org/10.1016/j.apenergy.2018.02.059.

(161) Ercicek, F.; Marchivie, M.; Nimod, L.; Cercel, H.; Brandel, C.; Ziri, I.; Cartigny, Y.; Monnier, O.; Marre, S.; Denux, D.; Subra-Paternault, P.; Harscoat-Schiavo, C. Unraveling a Unique Metastable Phase of a Proxyphylline Cocrystal Exclusively Produced by Compressed Carbon Dioxide. *Crystal Growth & Design* **2024**, *24* (11), 4630–4644. https://doi.org/10.1021/acs.cgd.4c00279.

(162) Hashimoto, T.; Oketani, R.; Nobuoka, M.; Seki, S.; Hisaki, I. Single Crystalline, Non-Stoichiometric Cocrystals of Hydrogen-Bonded Organic Frameworks. *Angewandte Chemie* **2023**, *135* (1), e202215836. https://doi.org/10.1002/ange.202215836.

(163) Kitaigorodsky, A. I. *Mixed Crystals*; Springer Science & Business Media, 2012.

(164) Pinètre, C.; Gendron, F.; Kuroda, R.; Oketani, R.; Aupetit, C.; Buffeteau, T.; Coquerel, G. Use of Conglomerate Mixed Crystals to Deracemize a Stable Racemic-Compound-Forming System. *Chemistry A European J* **2023**, e202300441. https://doi.org/10.1002/chem.202300441.

(165) Tamura, R.; Fujimoto, D.; Lepp, Z.; Misaki, K.; Miura, H.; Takahashi, H.; Ushio, T.; Nakai, T.; Hirotsu, K. Mechanism of Preferential Enrichment, an Unusual Enantiomeric Resolution Phenomenon Caused by Polymorphic Transition during Crystallization of Mixed Crystals Composed of Two Enantiomers. *J. Am. Chem. Soc.* **2002**, *124* (44), 13139–13153. https://doi.org/10.1021/ja020454r.

(166) Gonella, S.; Mahieux, J.; Sanselme, M.; Coquerel, G. Spotting a Conglomerate Is Just Halfway to Achieving a Preparative Resolution by Preferential Crystallization. *Org. Process Res. Dev.* **2012**, *16* (2), 286–293. https://doi.org/10.1021/op200092f.

(167) Drev, S.; Rečnik, A.; Daneu, N. Twinning and Epitaxial Growth of Taaffeite-Type Modulated Structures in BeO-Doped MgAl 2 O 4. *CrystEngComm* **2013**, *15* (14), 2640–2647. https://doi.org/10.1039/C3CE26997C.

(168) van Enckevort, W. J. P. On the Crystallization of Epitaxial Racemic Conglomerates. *J. Phys. Chem. C* **2010**, *114* (49), 21593–21604. https://doi.org/10.1021/jp108527h.

(169) Torbeev, V. Yu.; Lyssenko, K. A.; Kharybin, O. N.; Antipin, M. Yu.; Kostyanovsky, R. G. Lamellar Racemic Twinning as an Obstacle for the Resolution of Enantiomers by Crystallization: The Case of Me(All)N+(CH2Ph)Ph X- (X = Br, I) Salts. *J. Phys. Chem. B* **2003**, *107* (48), 13523–13531. https://doi.org/10.1021/jp035588l.

(170) Mbodji, A.; Gbabode, G.; Sanselme, M.; Cartigny, Y.; Couvrat, N.; Leeman, M.; Dupray, V.; Kellogg, R. M.; Coquerel, G. Evidence of Conglomerate with Partial Solid Solutions in Ethylammonium Chlocyphos. *Crystal Growth & Design* **2020**, *20* (4), 2562–2569. https://doi.org/10.1021/acs.cgd.9b01699.

(171) Renou, L.; Morelli, T.; Coste, S.; Petit, M.-N.; Berton, B.; Malandain, J.-J.; Coquerel, G. Chiral Discrimination at the Solid State of Methyl 2-(Diphenylmethylsulfinyl)Acetate. *Crystal Growth & Design* **2007**, *7* (9), 1599–1607. https://doi.org/10.1021/cg070075f.

(172) Zlokazov, M. V.; Pivnitsky, K. K. Lamellar Conglomerates. *Mendeleev Communications* **2020**, *30* (1), 1–6. https://doi.org/10.1016/j.mencom.2020.01.001.

(173) Gervais, C.; Beilles, S.; Cardinaël, P.; Petit, S.; Coquerel, G. Oscillating Crystallization in Solution between (+)- and (−)-5-Ethyl-5-Methylhydantoin under the Influence of Stirring. *J. Phys. Chem. B* **2002**, *106* (3), 646–652. https://doi.org/10.1021/jp012622s.

(174) Coquerel, G. Solubility of Chiral Species as Function of the Enantiomeric Excess. *Journal of Pharmacy and Pharmacology* **2015**, *67* (6), 869–878. https://doi.org/10.1111/jphp.12395.

(175) Srisanga, S.; ter Horst, J. H. Racemic Compound, Conglomerate, or Solid Solution: Phase Diagram Screening of Chiral Compounds. *Crystal Growth & Design* **2010**, *10* (4), 1808–1812. https://doi.org/10.1021/cg901483v.

(176) Simon, F.; Clevers, S.; Gbabode, G.; Couvrat, N.; Agasse-Peulon, V.; Sanselme, M.; Dupray, V.; Coquerel, G. Enhanced Second Harmonic Generation from an Organic Self-Assembled Eutectic Binary Mixture: A Case Study with 3-Nitrobenzoic and 3,5-Dinitrobenzoic Acids. *Crystal Growth & Design* **2015**, *15* (2), 946–960. https://doi.org/10.1021/cg5017565.

(177) Simon, F.; Clevers, S.; Dupray, V.; Coquerel, G. Relevance of the Second Harmonic Generation to Characterize Crystalline Samples. *Chem Eng & Technol* **2015**, *38* (6), 971–983. https://doi.org/10.1002/ceat.201400756.

(178) Clevers, S.; Coquerel, G. Kryptoracemic Compounds Hunting and Frequency in the Cambridge Structural Database. *CrystEngComm* **2018**, *20* (15), 2093–2101. https://doi.org/10.1039/C8CE00075A.

(179) Murti, Y. V. G. S.; Vijayan, C. Symmetry and Susceptibility Tensors. In *Physics of Nonlinear Optics*; Murti, Y. V. G. S., Vijayan, C., Eds.; Springer International Publishing: Cham, 2021; pp 27–48. https://doi.org/10.1007/978-3-030-73979-9_3.

(180) Galland, A.; Dupray, V.; Berton, B.; Morin-Grognet, S.; Sanselme, M.; Atmani, H.; Coquerel, G. Spotting Conglomerates by Second Harmonic Generation. *Crystal Growth & Design* **2009**, *9* (6), 2713–2718. https://doi.org/10.1021/cg801356m.

(181) Rekis, T. Crystallization of Chiral Molecular Compounds: What Can Be Learned from the Cambridge Structural Database? *Acta Crystallogr B Struct Sci Cryst Eng Mater* **2020**, *76* (3), 307–315. https://doi.org/10.1107/S2052520620003601.

(182) Gendron, F.-X. Contribution à La Discrimination Chirale à l'état Solide et Accès Aux Énantiomères Pures Par Cristallisation. These de doctorat, Normandie, 2018. https://theses.fr/2018NORMR032 (accessed 2024-09-20).

(183) Gendron, F.-X.; Mahieux, J.; Sanselme, M.; Coquerel, G. Resolution of Baclofenium Hydrogenomaleate By Using Preferential Crystallization. A First Case of Complete Solid Solution at High Temperature and a Large Miscibility Gap in the Solid State. *Crystal Growth & Design* **2019**, *19* (8), 4793–4801. https://doi.org/10.1021/acs.cgd.9b00665.

(184) Bredikhin, A. A.; Bredikhina, Z. A.; Novikona, V. G.; Pashagin, A. V.; Zacharychev, D. V.; Gubaidullin, A. T. Three Different Types of Chirality-Driven Crystallization within the Series of Uniformly Substituted Phenyl Glycerol Ethers. *Chirality* **2008**, *20*, 1092–1103. https://doi.org/10.1002/chir.20648.

(185) Qian, H.-L.; Xu, S.-T.; Yan, X.-P. Recent Advances in Separation and Analysis of Chiral Compounds. *Anal. Chem.* **2023**, *95* (1), 304–318. https://doi.org/10.1021/acs.analchem.2c04371.

(186) Teng, Y.; Gu, C.; Chen, Z.; Jiang, H.; Xiong, Y.; Liu, D.; Xiao, D. Advances and Applications of Chiral Resolution in Pharmaceutical Field. *Chirality* **2022**, *34* (8), 1094–1119. https://doi.org/10.1002/chir.23453.

(187) Tarafder, A.; Miller, L. Chiral Chromatography Method Screening Strategies: Past, Present and Future. *Journal of Chromatography A* **2021**, *1638*, 461878. https://doi.org/10.1016/j.chroma.2021.461878.

(188) De Saint Jores, C.; Brandel, C.; Vaccaro, M.; Gharbi, N.; Schmitz-Afonso, I.; Cardinael, P.; Tamura, R.; Coquerel, G. Reinvestigating the Preferential Enrichment of DL-Arginine Fumarate: New Thoughts on the Mechanism of This Far from Equilibrium Crystallization Phenomenon. *Molecules* **2022**, *27* (24), 8652. https://doi.org/10.3390/molecules27248652.

(189) Takahashi, H.; Numao, Y.; Motokawa, J.; Clevers, S.; Coquerel, G.; Tsue, H.; Tamura, R. A Novel Mechanism of Preferential Enrichment Phenomenon Observed for the Cocrystal of (*RS*)-2-{4-[(4-Chlorophenoxy)Methyl]Phenoxy}propionic Acid and Isonicotinamide. *Chem. Eur. J.* **2019**, *25* (71), 16405–16413. https://doi.org/10.1002/chem.201904130.

(190) Marchand, P.; Lefèbvre, L.; Querniard, F.; Cardinaël, P.; Perez, G.; Counioux, J.-J.; Coquerel, G. Diastereomeric Resolution Rationalized by Phase Diagrams under the Actual Conditions of the Experimental Process. *Tetrahedron: Asymmetry* **2004**, *15* (16), 2455–2465. https://doi.org/10.1016/j.tetasy.2004.06.044.

(191) Kaptein, B.; Elsenberg, H.; Grimbergen, R. F. P.; Broxterman, Q. B.; Hulshof, L. A.; Pouwer, K. L.; Vries, T. R. Dutch Resolution of Racemic 4-Hydroxy- and 4-¯uoro- Phenylglycine with Mixtures of Phenylglycine and (+)-10-Camphorsulfonic Acid. *Tetrahedron: Asymmetry* **2000**, 9.

(192) Kellogg, R. M.; Nieuwenhuijzen, J. W.; Pouwer, K.; Vries, T. R.; Broxterman, Q. B.; Grimbergen, R. F. P.; Kaptein, B.; Crois, R. M. L.; Wever, E. de; Zwaagstra, K.; Laan, A. C. van der. Dutch Resolution: Separation of Enantiomers with Families of Resolving Agents. A Status Report. *Synthesis* **2003**, *2003* (10), 1626–1638. https://doi.org/10.1055/s-2003-40508.

(193) Dalmolen, J.; Tiemersma-Wegman, T. D.; Nieuwenhuijzen, J. W.; van der Sluis, M.; van Echten, E.; Vries, T. R.; Kaptein, B.; Broxterman, Q. B.; Kellogg, R. M. The Dutch Resolution Variant of the Classical Resolution of Racemates by Formation of Diastereomeric Salts: Family Behaviour in Nucleation Inhibition. *Chemistry* **2005**, *11* (19), 5619–5624. https://doi.org/10.1002/chem.200500440.

(194) Dutch Resolution of Racemates and the Roles of Solid Solution Formation and Nucleation Inhibition. In *Novel Optical Resolution Technologies*; Kellogg, R. M., Kaptein, B., Ton R., V., Eds.; Topics in Current Chemistry; Springer Berlin Heidelberg: Berlin, Heidelberg, 2007; Vol. 269, pp 159–197. https://doi.org/10.1007/978-3-540-46320-7.

(195) Collet, A.; Brienne, M. J.; Jacques, J. Optical Resolution by Direct Crystallization of Enantiomer Mixtures. *Chem. Rev.* **1980**, *80* (3), 215–230. https://doi.org/10.1021/cr60325a001.

(196) Secor, R. M. Resolution of Optical Isomers by Crystallization Procedures. **1962**.

(197) Coquerel, G. Preferential Crystallization. In *Novel Optical Resolution Technologies*; Sakai, K., Hirayama, N., Tamura, R., Eds.; Springer: Berlin, Heidelberg, 2007; pp 1–51. https://doi.org/10.1007/128_2006_077.

(198) Levilain, G.; Coquerel, G. Pitfalls and Rewards of Preferential Crystallization. *CrystEngComm* **2010**, *12* (7), 1983–1992. https://doi.org/10.1039/C001895C.

(199) Mahieux, J.; Sanselme, M.; Harthong, S.; Melan, C.; Aronica, C.; Guy, L.; Coquerel, G. Preparative Resolution of (±)-Bis-Tetralone by Means of Autoseeded Preferential Crystallization Induced by Solvent Evaporation (ASPreCISE). *Crystal Growth & Design* **2013**, *13* (8), 3621–3631. https://doi.org/10.1021/cg400589u.

(200) Kovács, E. A.; Szilágyi, B. A Synthetic Machine Learning Framework for Complex Crystallization Processes: The Case Study of the Second-Order Asymmetric Transformation of Enantiomers. *Chemical Engineering Journal* **2023**, *465*, 142800. https://doi.org/10.1016/j.cej.2023.142800.

(201) Igarashi, K.; Fujimura, T. Efficient Optical Resolution of DL-Glutamate by Combining Enzymatic Racemization and Preferential Crystallization. *Journal of Chemical Engineering of Japan* **2023**, *56* (1), 2197012. https://doi.org/10.1080/00219592.2023.2197012.

(202) Wermester, N.; Aubin, E.; Pauchet, M.; Coste, S.; Coquerel, G. Preferential Crystallization in an Unusual Case of Conglomerate with Partial Solid Solutions. *Tetrahedron: Asymmetry* **2007**, *18* (7), 821–831. https://doi.org/10.1016/j.tetasy.2007.03.011.

(203) Weissbuch, I.; Lahav, M.; Leiserowitz, L. Toward Stereochemical Control, Monitoring, and Understanding of Crystal Nucleation. *Crystal Growth & Design* **2003**, *3* (2), 125–150. https://doi.org/10.1021/cg0200560.

(204) Clevers, S.; Simon, F.; Dupray, V.; Coquerel, G. Temperature Resolved Second Harmonic Generation to Probe the Structural Purity of M-Hydroxybenzoic Acid. *J Therm Anal Calorim* **2013**, *112* (1), 271–277. https://doi.org/10.1007/s10973-012-2763-y.

(205) Coquerel, G.; Hoquante, M. Spontaneous and Controlled Macroscopic Chiral Symmetry Breaking by Means of Crystallization. *Symmetry* **2020**, *12* (11), 1796. https://doi.org/10.3390/sym12111796.

(206) Bodák, B.; Breveglieri, F.; Mazzotti, M. Crystallization-Induced Deracemization: Experiments and Modeling. *Crystal Growth & Design* **2022**, *22* (2), 1427–1436. https://doi.org/10.1021/acs.cgd.1c01374.

(207) Bodák, B.; Breveglieri, F.; Mazzotti, M. On the Model-Based Design and Comparison of Crystallization-Based Deracemization Techniques. *Chemical Engineering Science* **2022**, *254*, 117595. https://doi.org/10.1016/j.ces.2022.117595.

(208) Bodák, B.; Maggioni, G. M.; Mazzotti, M. Effect of Initial Conditions on Solid-State Deracemization via Temperature Cycles: A Model-Based Study. *Crystal Growth & Design* **2019**, *19* (11), 6552–6559. https://doi.org/10.1021/acs.cgd.9b00988.

(209) Bodák, B.; Mazzotti, M. Solid-State Deracemization via Temperature Cycles in Continuous Operation: Model-Based Process Design. *Crystal Growth & Design* **2022**, *22* (3), 1846–1856. https://doi.org/10.1021/acs.cgd.1c01398.

(210) Breveglieri, F.; Mazzotti, M. Role of Racemization Kinetics in the Deracemization Process via Temperature Cycles. *Crystal Growth & Design* **2019**, *19* (6), 3551–3558. https://doi.org/10.1021/acs.cgd.9b00410.

(211) Deck, L.-T.; Hosseinalipour, M. S.; Mazzotti, M. Exact and Ubiquitous Condition for Solid-State Deracemization in Vitro and in Nature. *J. Am. Chem. Soc.* **2024**, *146* (6), 3872–3882. https://doi.org/10.1021/jacs.3c11332.

(212) Hosseinalipour, M. S.; Deck, L.-T.; Mazzotti, M. On Solute Recovery and Productivity in Chiral Resolution through Solid-State Deracemization by Temperature Cycling. *Crystal Growth & Design* **2024**, *24* (9), 3925–3932. https://doi.org/10.1021/acs.cgd.4c00233.

(213) Noorduin, W. L.; van Enckevort, W. J. P.; Meekes, H.; Kaptein, B.; Kellogg, R. M.; Tully, J. C.; McBride, J. M.; Vlieg, E. The Driving Mechanism Behind Attrition-Enhanced Deracemization. *Angewandte Chemie International Edition* **2010**, *49* (45), 8435–8438. https://doi.org/10.1002/anie.201002036.

(214) Noorduin, W. L.; Meekes, H.; Bode, A. A. C.; van Enckevort, W. J. P.; Kaptein, B.; Kellogg, R. M.; Vlieg, E. Explanation for the Emergence of a Single Chiral Solid State during Attrition-Enhanced Ostwald Ripening: Survival of the Fittest. *Crystal Growth & Design* **2008**, *8* (5), 1675–1681. https://doi.org/10.1021/cg701211a.

(215) Xiouras, C.; Ter Horst, J. H.; Van Gerven, T.; Stefanidis, G. D. Coupling Viedma Ripening with Racemic Crystal Transformations: Mechanism of Deracemization. *Crystal Growth & Design* **2017**, *17* (9), 4965–4976. https://doi.org/10.1021/acs.cgd.7b00908.

(216) Iggland, M.; Mazzotti, M. A Population Balance Model for Chiral Resolution via Viedma Ripening. *Crystal Growth & Design* **2011**, *11* (10), 4611–4622. https://doi.org/10.1021/cg2008599.

(217) Maeda, J.; Cardinael, P.; Flood, A.; Coquerel, G. Improved Experimental Yield of Temperature-Cycle-Induced Deracemization (TCID) with Cooling and Crystal Washing: Application of TCID for the Industrial Scale. *Crystals* **2024**, *14* (7), 588. https://doi.org/10.3390/cryst14070588.

(218) Bodák, B.; Maggioni, G. M.; Mazzotti, M. Population-Based Mathematical Model of Solid-State Deracemization via Temperature Cycles. *Crystal Growth & Design* **2018**, *18* (11), 7122–7131. https://doi.org/10.1021/acs.cgd.8b01292.

(219) Intaraboonrod, K.; Lerdwiriyanupap, T.; Hoquante, M.; Coquerel, G.; Flood, A. E. Temperature Cycle Induced Deracemization. *Mendeleev Communications* **2020**, *30* (4), 395–405. https://doi.org/10.1016/j.mencom.2020.07.002.

(220) Cameli, F.; Xiouras, C.; Stefanidis, G. D. Intensified Deracemization *via* Rapid Microwave-Assisted Temperature Cycling. *CrystEngComm* **2018**, *20* (21), 2897–2901. https://doi.org/10.1039/C8CE00575C.

(221) Iggland, M.; Fernández Ronco, M.; Senn, R.; Kluge, J.; Mazzotti, M. Complete Solid State Deracemization by High Pressure Homogenization. *Chemical Engineering Science* **2014**, *111*, 106–111. https://doi.org/10.1016/j.ces.2014.02.034.

(222) Xiouras, C.; Fytopoulos, A.; Jordens, J.; Boudouvis, A. G.; Van Gerven, T.; Stefanidis, G. D. Applications of Ultrasound to Chiral Crystallization, Resolution and Deracemization. *Ultrasonics Sonochemistry* **2018**, *43*, 184–192. https://doi.org/10.1016/j.ultsonch.2018.01.014.

(223) Dongen, S. W. van; Baglai, I.; Leeman, M.; Kellogg, R. M.; Kaptein, B.; Noorduin, W. L. Rapid Deracemization through Solvent Cycling: Proof-of-Concept Using a Racemizable Conglomerate Clopidogrel Precursor. *Chem. Commun.* **2023**, *59* (26), 3838–3841. https://doi.org/10.1039/D3CC00332A.

(224) van Dongen, S. W.; Ahlal, I.; Leeman, M.; Kaptein, B.; Kellogg, R. M.; Baglai, I.; Noorduin, W. L. Chiral Amplification through the Interplay of Racemizing Conditions and Asymmetric Crystal Growth. *J. Am. Chem. Soc.* **2023**, *145* (1), 436–442. https://doi.org/10.1021/jacs.2c10584.

(225) Lopes, C.; Cartigny, Y.; Brandel, C.; Dupray, V.; Body, C.; Shemchuk, O.; Leyssens, T. A Greener Pathway to Enantiopurity: Mechanochemical Deracemization through Abrasive Grinding. *Chemistry – A European Journal* **2023**, *29* (35), e202300585. https://doi.org/10.1002/chem.202300585.

CHAPTER II

SOLID-STATE DERACEMIZATION & NON-EQUILIBRIUM CONDITIONS

II.1 - Introduction

Despite substantial advancements in the enantiomeric separation of chiral compounds over the past decades,[1–4] accessing enantiopure materials remains a major scientific and economic challenge.[5–7] Among the various chiral resolution methods developed so far (*e.g.* asymmetric or chiral pool synthesis, preparative chromatography, biocatalysis etc),[8–15] the crystallization-based approaches, for instance solid-state deracemization, stand out as the most promising. Even though powerful, solid-state deracemization techniques have two major prerequisites: (i) self-sorting of enantiomers into enantiopure crystals and (ii) *in-situ* interconversion between enantiomers (*cf.* I.3.5.3). these conditions are concomitantly fulfilled by a limited fraction of chiral systems considering that only 5-10 % crystallizes as stable racemic conglomerates, of which a limited fraction are racemizable in solution.[16,17] As a consequence, many molecules of interest do not satisfy these criteria and cannot be deracemized. Nowadays, accessing stable racemic conglomerates from chiral substances crystallizing as racemic compounds is possible by using derivatization-routes (*cf.* I.3.3). However, this requires costly and time-consuming conglomerate screening procedures based on trial-and-error iterations (*e.g.* multi-components solid formation, reversible synthesis etc.), furthermore exhibiting the same 5-10% unfavourable outcome.

This chapter is therefore devoted to the development of new chiral resolution strategies adapted to systems unsuitable for solid-state deracemization (*i.e.* racemic compound-forming systems or non-racemizable molecules). In case of (i) hardly-racemizable molecules, we will explore the possibility of achieving chiral resolution through an out-of-equilibrium dissymmetric dissolution rate between enantiomers using 2-pivaloyl-1,2,3,6,7,11b-hexahydro-4H-pyrazino[2,1-a]isoquinolin-4-one as model compound, a conglomerate-forming system derived from Praziquantel (Figure II - 1, labelled **3u** in consistency with the following chapter). Despite crystallizing as a conglomerate, **3u** contains an asymmetric carbon bearing a weakly acidic proton, necessitating harsh conditions for racemization and thereby preventing any solid-state deracemization process in the absence of adapted equipment according to the prerequisite.[18,19] In the case of (ii) racemic compound-forming system, we investigate the concept of deracemizing a racemic compound through conglomerate mixed crystals. This is explored using a library based on the easily racemizable chiral core triazole

ketone (Figure II - 1, **1**),[20] a well-known case study in our lab, for which synthesis can exclusively be implemented in racemic form.

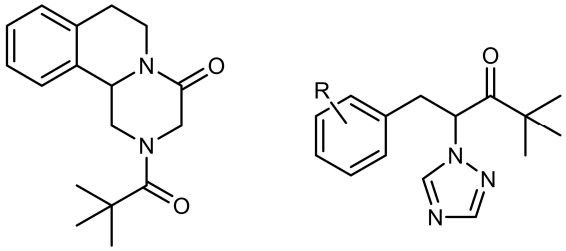

3u **1**

Figure II - 1. Molecular structures of the TAK chiral core (1) and the two conglomerates characterized from 1,3-dimethylxanthine-based chiral derivative library (2d) and the praziquantel derivative library (3u). Labels are consistent with previous chapters.

II.2 - Asymmetric dissolution of 3u

Kinetic asymmetries, for instance anisotropic crystal growths, variation in nucleation, dissolution and growth rates, are fundamental principles of crystallization shaping the size, structure and morphology of crystals as they evolve from disordered phases.[21–23] Therefore, we recognize that asymmetric dissolution kinetics of enantiomers crystallizing as a conglomerate-forming system under temperature variations may lead to sufficient chiral enrichment enabling a chiral resolution process. Supporting this idea, Noorduin *et al.* described the dissymmetric dissolution rate between enantiomers of a scalemic suspension of a conglomerate-forming system under abrasive condition, attributing the observed phenomena to the driving forces behind attrition-enhanced deracemization process (*i.e.* Viedma ripening).[24] Moreover, this attrition-enhanced dissymmetric dissolution has been already successfully used for the chiral resolution of non-racemizable chiral systems by exchanging the crystals-free solution of couple-batch vessels (Figure II - 2).[25–29]

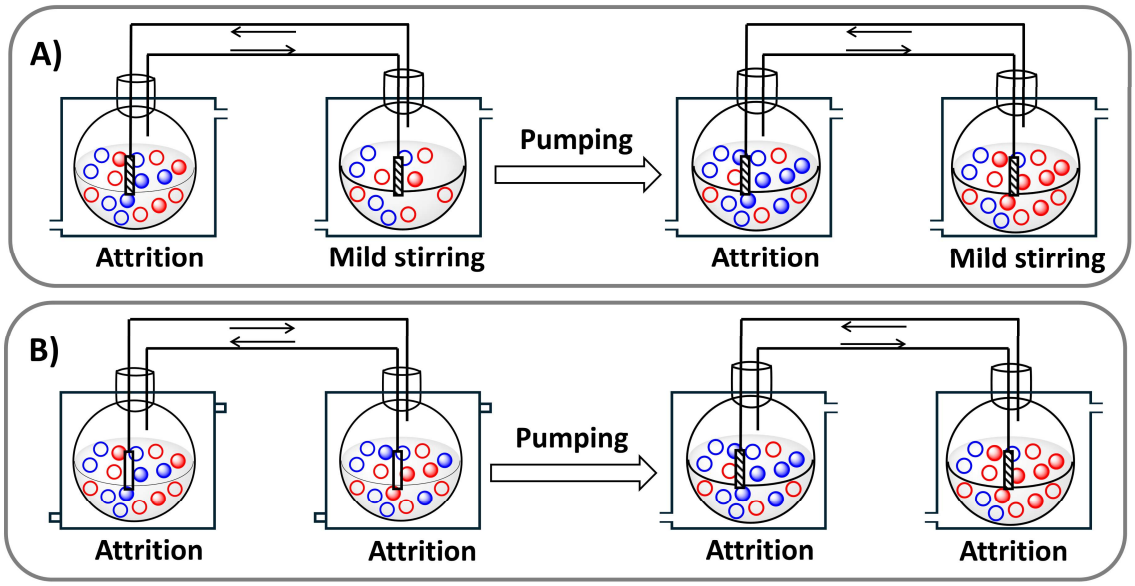

Figure II - 2. Resolution by crystal size-induced solubility difference developed by (A) Hein *et al.*[26] in a "Preferential crystallization-like" process and (C) Spix *et al.*[25] in an "attrition-enhance deracemization-like" process. The red and blue spheres represent a pair of enantiomers, where filled and empty spheres indicate the solid and solvated form respectively.

Notably, such studies received limited to no attention for the temperature cycling variation of solid-state deracemization (Temperature Cycling Induced Deracemization, TCID hereafter) and its possible impact on chiral resolution. This is what we decided to explore.

II.2.1 - Solubility measurements

Phase-transition may be induced by temperature changes. As a result, heating a scalemic suspension of a conglomerate-forming system could induce the complete dissolution of one enantiomer over the other at a certain temperature and result in an enantiopure suspension. It was therefore essential to accurately obtain the solubility data of **3u** in the working solvent to identify the phase boundaries prior to any dissolution experiments under temperature variations. This would enable us to correlate any observed deviations from thermodynamic equilibrium during the dissolution experiments.

Consequently, the temperature-dependent solubilities of racemic (Figure II - 3A, squares) and enantiopure (Figure II - 3A, triangles) **3u** in IPA were determined using the Crystal16 apparatus and fitted using Van't Hoff equation (*cf.* I.2.2.2 and Appendix A - I.3.2). Ternary isotherms relevant to our study can be constructed relying on these solubility data, assuming a thermodynamic ideality. To further support this analysis, the temperature-dependent solubility of an additional mixture of **3u** at 29 *e.e.*% was determined (Figure II - 3A, circles) and

also fitted using Van't Hoff equation. Figure II - 3B presents examples of such ternary isotherms, specifically at 15 °C; 20 °C and 30 °C. Moreover, the solubility curves are strait lines, which align with the (quasi-)ideal thermodynamic behaviour of this conglomerate-forming system.

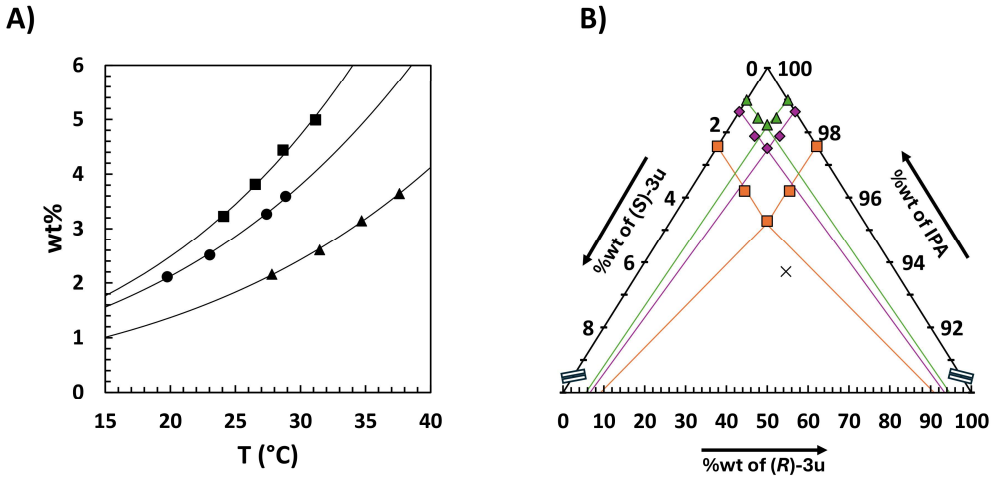

Figure II - 3. (A) Temperature-dependent solubility of (*R*)-3u (triangles), scalemic mixture of 3u at 29 *e.e.*% (circles) and (*RS*)-3u (squares). Lines are theoretical fits using Van't Hoff equation. (B) Isothermal sections of the ternary system (*R*)-3u / (*S*)-3u / IPA based on (A) at 15 °C (green triangles), 20 °C (purple diamonds) and 30 °C (orange squares) magnified in the IPA-rich part of the ternary solubility diagram. The black cross corresponds to the experimental mixtures used in the preferential dissolution experiments. Lines are guides for the eyes.

II.2.2 - Preferential dissolution under temperature variation

According to the above determined ternary isotherms (*i.e.* 15 °C, 20 °C and 30 °C), a scalemic mixtures of **3u** at 20 *e.e.*% was suspended in IPA (6.5 wt%), magnetically stirred at 300 rpm and subjected to different temperature programs (TP hereafter) over 3 completed cycles (Figure II - 4A). These TPs, typically used in TCID process, differ from each other by the highest temperature reached. Nonetheless, such suspension (*i.e.* 20 *e.e.*% at 6.5 wt%) remains within the triphasic domain, even at 30 °C (Figure II - 3B, black cross), meaning that the liquid phase should consistently remain racemic under thermodynamic equilibrium. Even though transient kinetic deviations may occur, they are expected to be short-lived. According to this statement, The low- and high- temperature isotherms last for 5 and 15 minutes respectively. The solid-phase and solution-phase *e.e.* is then monitored at the end of each isotherm and summarized in Table II - 1. An average of each solid and solution-phase monitoring is depicted as histograms to better visualize the change in *e.e.* during these experiments as function of the temperature program followed (Figure II - 4, B and C).

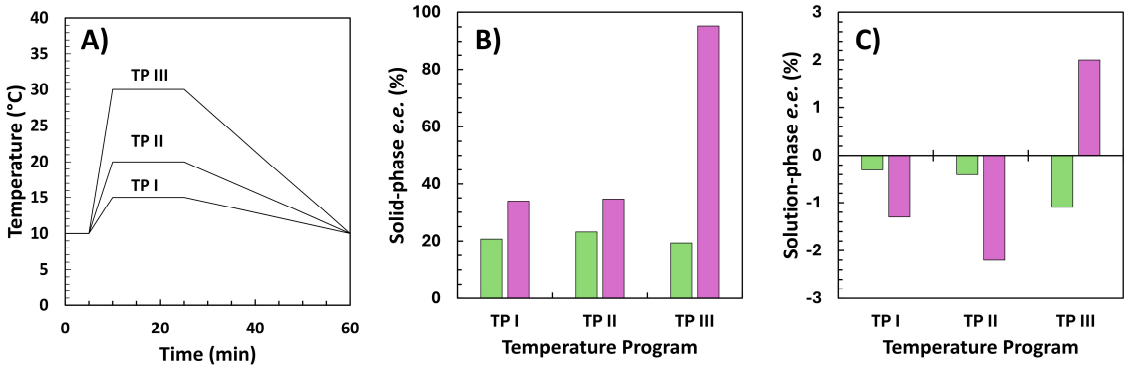

Figure II - 4. (A) Temperature program TP I, TP II and TP III. Monitoring of (B) the solid-phase *e.e.* (%) and (C) the solution-phase *e.e.* (%) as function of the temperature program highlighted in (A) of an initial 20 *e.e.*% solid mixtures suspended in IPA (6.5 wt%). The reported *e.e.*% values in (B) and (C) are an average of 3 different sampling performed at low temperature. Green bars represent the monitoring after the end of the low-temperature isotherm while purple bars represent the monitoring after the end of the high-temperature isotherm steps.

Table II - 1. Experimental solid-phase and solution-phase *e.e.* obtained for three successive cycles at the low and high temperatures of each temperature program. Each *e.e.* values are given with an uncertainty of ± 0.3 %.

Temperature program		**TP I**			**TP II**			**TP III**		
Repetition		1	2	3	1	2	3	1	2	3
Solid-phase e.e.	LT	28.1	24.4	9.5	21.4	19.3	28.8	23.5	13.4	21.4
(%)	HT	37	34.5	30.1	30.3	36.7	36.9	95.6	95.4	95
Solution-phase e.e.	LT	- 0.3	- 0.1	- 0.5	- 0.5	- 0.7	- 0.1	- 0.1	- 1.7	- 1.4
(%)	HT	- 1.3	- 1.1	- 1.6	- 2.3	- 2.2	- 2.1	1.4	2.2	2.5

Despite a slow cooling rate for each TP (*i.e.* < 0.6 k.min^{-1}), the solid-phase *e.e.* at low temperature remains unpredictable whatever the TPs applied to the system (Table II - 1). As the sampled volume is neglectable with respect to the total volume of the experiments (*i.e.* < 0.5% per sampling), this further demonstrates the asymmetry of the crystallization kinetics. However, the solid-phase *e.e.* consistently increases after the heating steps as theoretically expected from the tie-lines of the experimentally determined ternary isotherms (Figure II - 3B). This increase of the solid-phase *e.e.* is of similar magnitude for both TP I and II, reflecting the minor differences in solubility between these temperatures. As the temperature rises, the solid phase shows an enrichment of the major enantiomer, while the solution-phase *e.e.* in both experiments exhibits an enrichment of the minor enantiomer. Although TP I and TP II follow similar trends, the more pronounced decrease in the solution-phase *e.e.* in the case of TP II suggests that greater dissolution enhances the enantiomeric imbalance. It should be

noted that the quasi-racemic solution-phase *e.e.* after cooling in both experiments demonstrates the neglectable impact of attrition due to the magnetic stirring on the enantiomeric excess (Figure II - 4B and C).

By contrast, TP III consistently exhibits a quasi-enantiopure solid after each heating step (Table II - 1). More importantly, this is also associated with an enantiomeric enrichment of the solution-phase with enantiomers of the same handedness. Even though the solid mixture should belong to the triphasic domain at 30 °C, this enrichment of both the liquid and the solid phases indicates that this equilibrium is following a tie-line belonging to the biphasic domain (Figure II - 5).

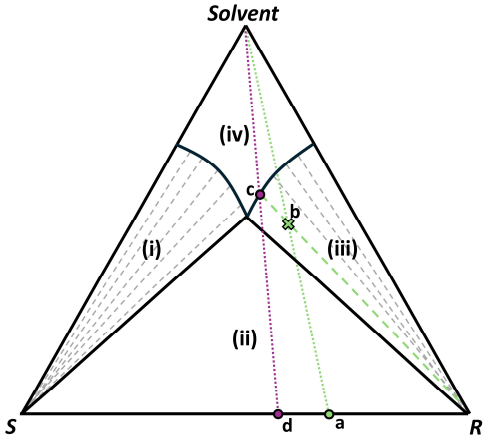

Figure II - 5. Schematic isoplethal ternary isotherm of a conglomerate-forming system / solvent highlighting the enrichment of the solution-phase with the major enantiomer for a mixture belonging to the biphasic domain b (green cross) starting from a scalemic mixture (a). The solution-phase composition is accessible by the projection of the tie-line associated with this composition (green dashed bar) up to the liquidus curve (point c). The projection of the point (c) to the composition axis (pink dotted line) gives the final solution-phase composition (d) under thermodynamic equilibrium. (i) <(*S*)> + *sat.sol.* (ii) <(*S*)> + <(*R*)> + *d.s.s.* (iii) <(*R*)> + *sat.sol.* (iv) *u.s.s.*

This could be due to experimental errors according to the proximity of this composition with the phase boundary, or to the presence of a partial solid-state miscibility between **3u** enantiomers that would slightly shift this phase boundary toward the racemic composition.[30,31] Furthermore, this would explain the quasi-enantiopure solid after each heating step. More importantly, an opposite enrichment of the liquid phase is also observed for TP III. By contrast with TP I and II, this enrichment occurs during cooling. This indicates that while preferential dissolution occurs when heating a scalemic suspension within the triphasic

domain, preferential crystallization takes place during cooling after reaching the biphasic domain (Figure II - 6).

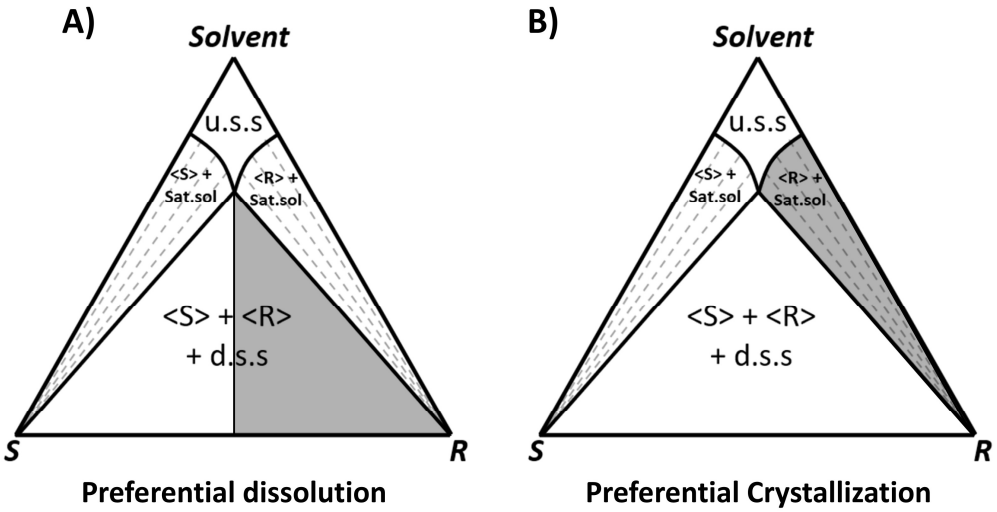

Figure II - 6. Schematic view of isothermal ternary solubility diagrams highlighting in grey the phases in which (A) preferential dissolution and (B) preferential crystallization occurs

Likewise attrition, even small temperature variations are sufficient to induce an out-of-equilibrium enantiomeric imbalance of comparable magnitude.[24] It should be noted that adding a racemizing agent would enhance this asymmetric dissolution by maintaining an identical supersaturation of both enantiomer throughout the process.

Even though asymmetric dissolution starting from scalemic mixtures under temperature variations is undeniable, one should wonder if this phenomenon also holds for a racemic mixture. To investigate this aspect, a racemic mixture of **3u** is suspended in IPA within a thermostated round-bottom flask in such a way that a slight suspension density remains at 40 °C based on the solubility data in Figure II - 3A. This system is submitted to three successive cycles of the following temperature program: an isotherm at -10 °C for 1 hour followed by a heating ramp at 4 $K.min^{-1}$ up to 40 °C. The solid phase is sampled after the isotherm at -10 °C and again after reaching 40 °C. The *e.e.* monitoring data are summarized in Table II - 2. It should be noted that the liquid phase is reinjected after sampling, preventing the system from being entirely dissolved, but hindering the monitoring of the solution-phase *e.e.*.

Table II - 2. Experimental solid-phase *e.e.* obtained at -10 °C and 40 °C 3u suspended in IPA for three successive cycles.

Cycles	**1**		**2**		**3**	
Temperature (°C)	- 10	40	- 10	40	-10	40
Solid-phase *e.e.* (%)	0.0	1.7	0.02	1.4	0.04	1.1

It can be seen that a slight enantiomeric imbalance in the solid-state occurs after heating, which is of the same magnitude of the solution-phase enrichment described above (*i.e.* > 1 *e.e.*%). This can reflect an initial enantiomeric imbalance of the starting material, even though undetectable from our HPLC measurements (*i.e.* < 0.1 *e.e.*%), which is further amplified by the temperature variation.

II.2.3 - Asymmetric dissolution-induced chiral resolution

This temperature variation-induced asymmetric dissolution might generate a sufficient enantiomeric imbalance for chiral resolution to be successful. For instance, this solution-phase enantiomeric imbalance could be introduced into another thermostated flask containing a symmetrical slurry of the substance to be resolved. Upon lowering the temperature, one would expect this enantiomeric imbalance of the solution-phase to crystallize into the later, inducing a chiral enrichment of the solid phase with enantiomers of the same handedness. Thereby, subsequent reheating of this slurry would therefore produce a symmetrical solution-phase enantiomeric imbalance, which could be reinjected into the initial thermostated flask. This process could be repeated in reverse, facilitating complete chiral resolution over successive cycles. Akin the chiral resolution of asparagine in a couple-batch grinding process by Spix *et al.*,[25] we setup two identical thermostated round-bottom flasks containing racemic **3u** suspended in IPA, for which the exchange of the crystal-free solution is ensured though a peristaltic pump connected to HPLC filters (Figure II - 7A).

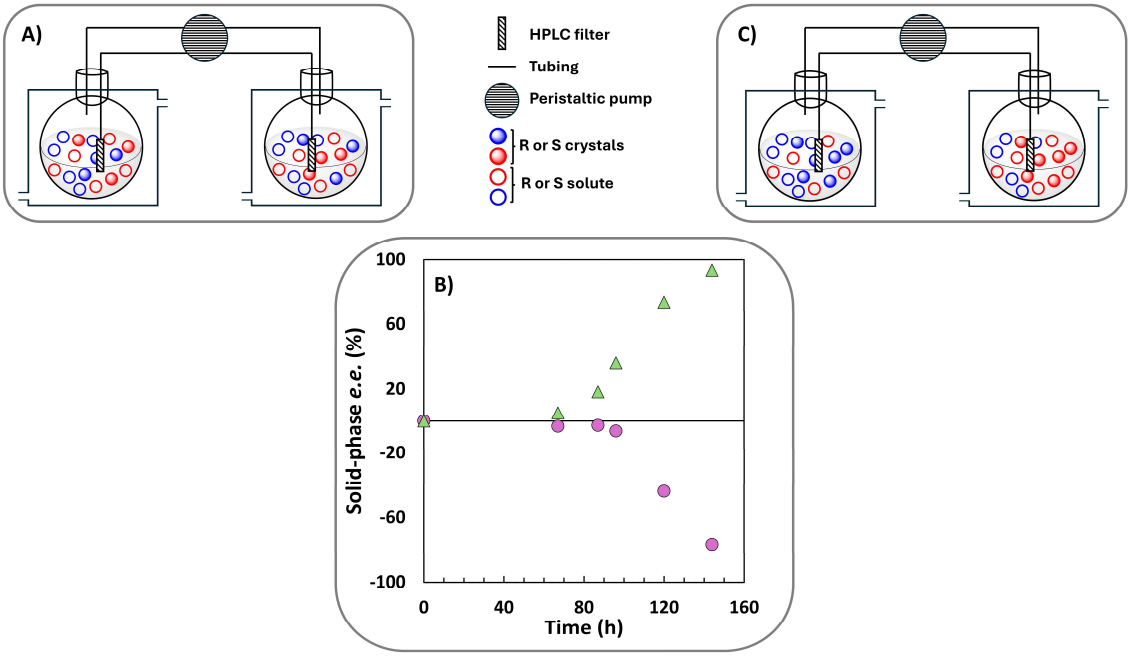

Figure II - 7. (A) illustration of the experimental setup combining two temperature-cycling experiment in coupled batch, for which the solutions are constantly exchanged using a peristaltic pump connected to HPLC filters. (B) Evolution of the solid-phase *e.e.* (%) in the two coupled batches as function of time starting from initially racemic and symmetrical suspensions. Positive *e.e.* is arbitrary attributed to the (*R*) enantiomer. (C) illustration of a completed temperature-cycling experiment in coupled batch.

Considering that classical TCID processes starting from a racemic composition reach enantiopurity over 80-100 hours, the solid-free solution is exchanged continuously for practical reason. These two thermostated round-bottom flasks are finally submitted to identical temperature variation following TP II (Figure II - 4A) and their solid-phase *e.e.* is monitored after the low temperature isotherms (Figure II - 7B).

As expected from above assumptions, the *e.e.* of the two thermostated flasks are evolving in opposite direction, demonstrating that such an out-of-equilibrium asymmetric dissolution is sufficient to drive a complete chiral resolution of a conglomerate-forming system throughout a kind of chiral segregation induced by simple temperature cycling. Intriguingly, the take-off is reached at ca. 80 hours, as commonly observed during TCID experiment from racemic composition, thus highlighting the similar effectiveness of such approach compared to classical resolution methods.

However, this setup suffers from a major drawback: the solid-free solution must be symmetrically exchanged during every step of the temperature program. Otherwise, the

change in solubility induced by the temperature variation would induce asymmetric slurry densities and, in the worst-case scenario, could lead to a complete dissolution of one system. It should be noted that enantiopurity could be reached for only one thermostated flask in our case (Figure II - 7B, green triangles) considering that a clear solution remains in the other flask after 150 hours of temperature cycling (Figure II - 7B, purple circles). Hence, this resolution method could be further improved by implementing exact inverse temperature variations between the two flasks and exchanging the solid-free liquid exclusively when the enantiomeric imbalance occurs. The process would then operate asynchronously, with one flask in the asymmetric dissolution regime while the other is in the crystallization regime.

Aside providing a practical way toward enantiopure materials for non-racemizable molecules, this asymmetric dissolution under temperature variation could also be used as a tool for evaluating the solid-state nature of newly synthesized molecules, which is a major issue of actual conglomerate screening. Indeed, the solid-state nature of the targeted compound can be readily distinguished from racemic mixtures by simply exchanging the solid-free mother liquor of symmetrical racemic slurries over several hours. It also demonstrates that simple temperature variations can induce a spontaneous chiral segregation.

II.3 - Mixed crystals deracemization

Conventional conglomerate screening processes ideally require the material to be available both at the racemic and enantiopure compositions (*cf.* I.3.4). Otherwise, SHG pre-screening methods or crystal structure resolution may be considered, provided that single crystals are available for the latter. This stands as a serious limitation for molecules solely accessible at the racemic composition. A notable example of this limitation is the library of triazole ketone derivatives previously investigated by Céline Rougeot, a former Ph.D. student from our lab, for which the synthesis of this library could exclusively be implemented in racemic form (Figure II - 1, **1**). Although this case study permitted the identification of a cluster of para-substituted conglomerate-forming systems by SC-XRD, the change of a single atom or substituting site led to the obtention of racemic compound-forming systems, emphasizing the unpredictable solid-state nature of chiral compound.[32]

Moreover, the use of chiral substances offers unique and innovative properties to several products, including optical and electrochemical sensors, molecular selectors, catalysts and

bioactive substances.[33,34] These excellent properties are often a result of chiral recognition phenomena, induced by the difference in affinity of two enantiomers with a chiral receptor.[35,36] For instance, this allows the development of highly selective chiral stationary phases, active pharmaceutical ingredients, asymmetric catalysts etc.[37–42] Therefore, we recognize that studying chemically related racemic derivatives might also open new route to reach chiral discrimination based on the opportunity to form mixed crystals between chemically related molecules, with one crystallizing as a conglomerate forming system.[43–46] Akin the chirality transfer-induced preferential crystallization,[47] we could make use of a highly discriminative chiral recognition phenomenon by introducing the substance to be deracemized (*i.e.* enantiomers of the racemic compound-forming systems) within the lattice sites of a conglomerate host structure, thus suitable for solid-state deracemization (Figure II - 8).[30,31,35,36]

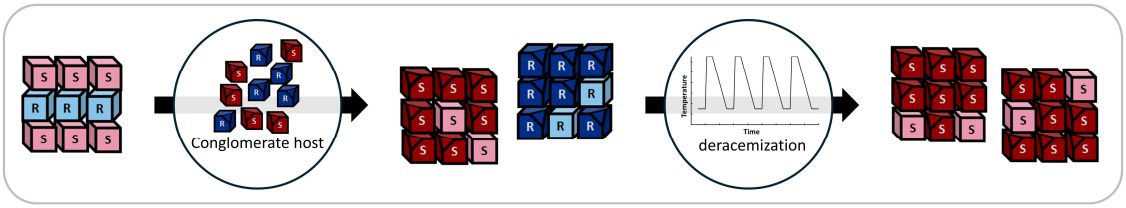

Figure II - 8. Schematic principle of the formation of conglomerate mixed crystal suitable for solid-state deracemization.

II.3.1 - History

Triazole ketone derivatives crystallizing as conglomerates were first introduced by Black *et al.*[20] Their attention was focused on the 1-(4-chlorophenyl)-4,4-dimethyl-2-(1H-1,2,4- triazol-1-yl)pentan-3-one (**1a**), a precursor of Paclobutrazol (Figure II - 9).

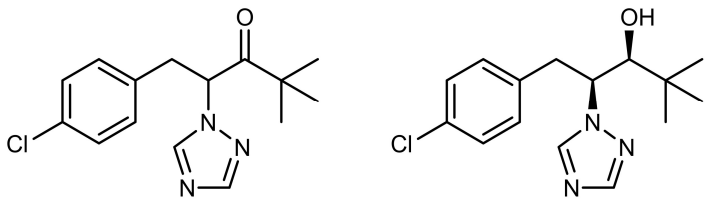

Figure II - 9. Molecular structure of 1a (left) and paclobutrazol (right).

Paclobutrazol, a plant growth inhibitor,[48,49] was previously obtained via diastereomeric salt resolution but the distomer remained difficult to recycle, hence leading to an expensive final product.[50] Black *et al.* introduced a new and attractive option for the preparation of enantiopure paclobutrazol using the conglomerate behaviour of **1a** to control the first

stereogenic centre by second order asymmetric transformation (SOAT).[20] The resulting (*S*)-**1a** could be thereby stereospecifically reduced using sodium borohydride to gives paclobutrazol (Figure II - 10).

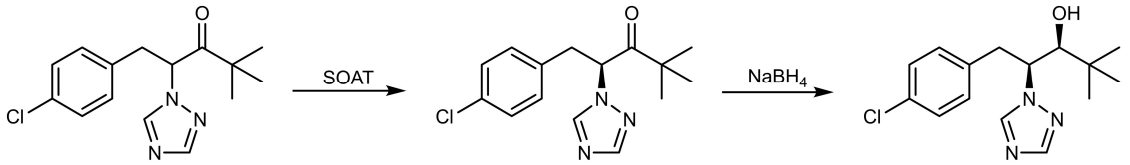

Figure II - 10. Synthesis path for paclobutrazol starting from 1a.

II.3.2 - Conglomerate cluster

Intriguingly, 1-(4-chloro-2-fluorophenyl)-4,4-dimethyl-2-(1H-1,2,4- triazol-1-yl)pentan-3-one, a chemically related derivative of **1a** for which the ortho position is substituted by a fluorine atom, also crystallizes as a conglomerate-forming system and shares strong crystal structures similarities.[51]

Based on this observation, Celine Rougeot studied the influence of the substitution of the aromatic group on crystal packing by synthesizing four other chemically related derivatives based on the chiral core triazole ketone (Figure II - 11). Among this study, the crystal structure of two additional para-substituted (p-Me and p-Br) and the unsubstituted compounds has been resolved, highlighting their conglomerate behaviour. Moreover, these Triazole ketone derivatives were successfully deracemized by Viedma ripening.

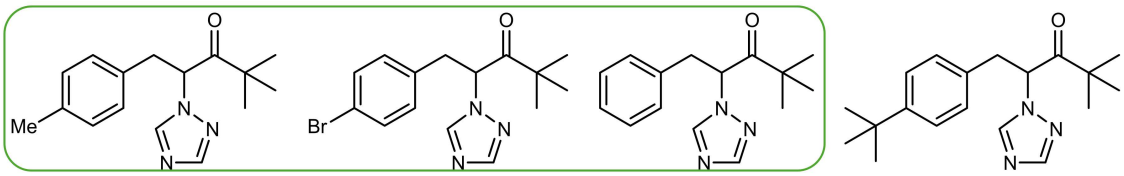

Figure II - 11. Conglomerate screening by library derivatization based the chiral core triazole ketone synthesised by Céline Rougeot. Successful conglomerate hits are highlighted in green.

More importantly, para-substituted derivatives all exhibit an isomorphous orthorhombic structure involving π-interaction in T shapes along [100] direction (Figure II - 12A). It can be seen from this crystal structure that the para-substituent has no influence on the PBC up to a certain steric hindrance (*e.g.* t-Bu).[32]

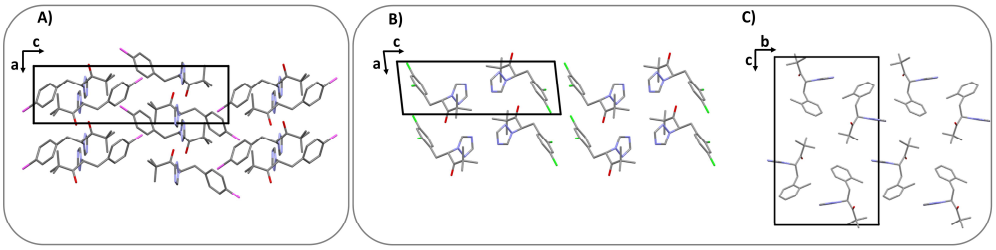

Figure II - 12. (A) Isomorphous crystal packing of para-substituted derivatives along [010] highlighting the large cavity in para position capable of accommodating a large variety of atoms. Atoms highlighted in purple correspond to either methyl, Chlorine or Bromine atom. (B) Crystal packing of 1b along [010]. (C) Crystal packing of 1d along [100]. Hydrogen atoms are omitted for clarity.

The influence of the substitution site was also investigated by synthesizing two additional compounds substituted in ortho-position (Figure II - 13). The single crystal resolution of these two compounds revealed their racemic compound behaviour. In contrast with para-substituted derivatives, an ortho substitution led to a completely different crystal packing even though their PBC are also ensured through planar or T-shaped π-interactions along [001] and [010] respectively (Figure II - 12, B and C). The steric hindrance induced by an ortho substituent appears to prevent the isomorphous orthorhombic structure, instead favouring more stable centrosymmetric crystalline arrangements.

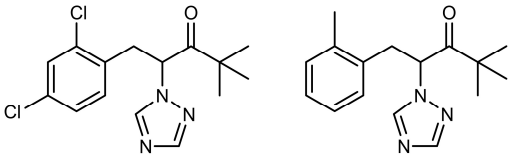

Figure II - 13. Ortho-substituted triazole ketone derivatives.

Despite crystallizing as racemic compounds, the ortho-substituted derivatives (Figure II - 14, **1b** and **1d**) share strong molecular similarities with para-substituted derivatives crystallizing as conglomerates (Figure II - 14, **1a** and **1c**). Based on this observation, chiral discrimination for **1b** and **1d** could be reached by using the opportunity to form mixed crystals with their chemically related conglomerate **1a** and **1c**, respectively, despite the structural differences between them.

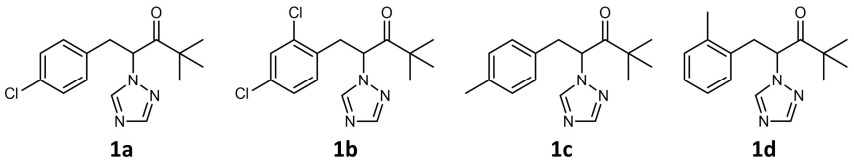

Figure II - 14. Molecular structure of the studied systems belonging to the family of triazole ketone derivation. 1a and 1c are conglomerate-forming system while 1c and 1d are racemic compound-forming system.

Supporting this idea, it was demonstrated that solid solutions between chemically related resolving agents of the same handedness improves the Pasteurian resolution, a process known as “Dutch resolution” (*cf.* I.3.5.1).[52–55] Moreover, there have been extensive reports in the literature of solid-state miscibility between chemically related molecules, but their application to chiral resolution has not been explored yet.[30,31,43–45,56]

II.3.3 - Heterogenous equilibria

It is first necessary to assess the feasibility of forming such conglomerate mixed crystals. To this end, the heterogenous equilibria between each structurally similar compound must be explored. The systems under investigation consist therefore of four independent components, which are thermodynamically described by a quaternary phase diagram. For simplicity, this four-order system can be represented through an extended T-X binary representation (Figure II - 15A), under the assumption of a perfect chiral recognition phenomenon, meaning that no diagonal interaction occurs (<S>$_{Cong}$ / <R>$_{RC}$ or <R>$_{Cong}$ / <S>$_{RC}$). Studying the racemic binary isopleth section (Figure II - 15B) allows for to the determination of the potential occurrence of solid-state miscibility and, in best case scenario, the limits of this solubility in the solid state.

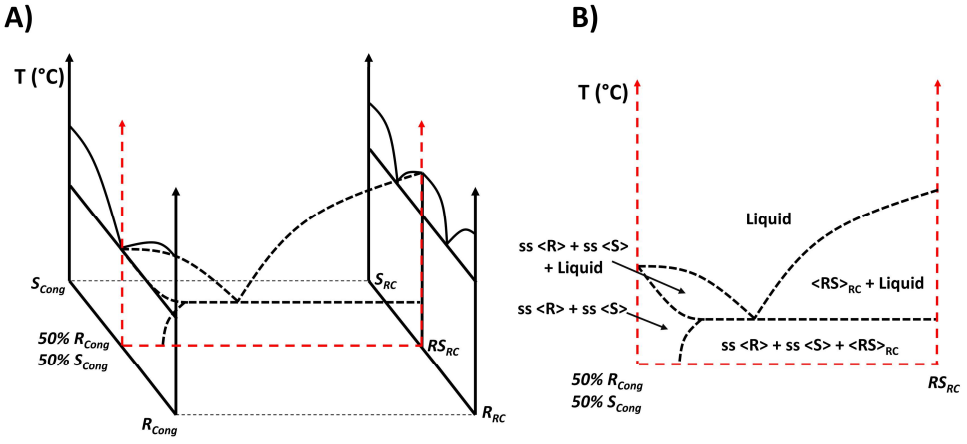

Figure II - 15. (A) Extended binary representation of a quaternary system racemic conglomerate / racemic compound and (B) its racemic binary isopleth section exhibiting a partial miscibility in the solid state. The subscripts “Cong” and “RC” stand for enantiomer crystallizing as conglomerate and racemic compound respectively.

The occurrence of partial solid solution on the systems (i) **1a** / **1b** and (ii) **1c** / **1d** will be investigated by the experimental determination of their racemic binary isoplethal sections, which will be described in mass fraction of the enantiomers of the racemic compound forming-systems x%-**1b** and x%-**1d** respectively.

II.3.3.1 - Racemic binary isoplethal section 1a / 1b

Different compositions of the system **1a** / **1b** are prepared by solvent evaporation in acetonitrile and hand-ground to ensure homogeneity. XRPD (Figure II - 16A) and DSC (Figure II - 16B) analyses are conducted on these samples.

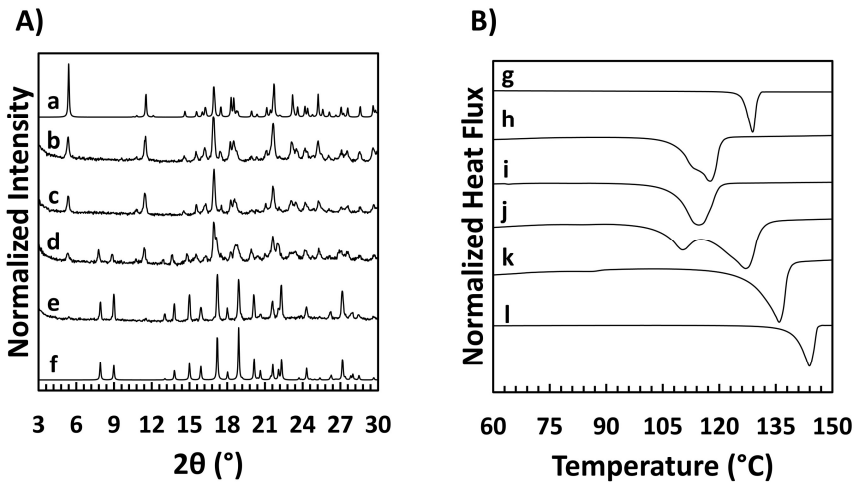

Figure II - 16. (A) XRPD patterns of selected racemic compositions between 1a and 1b obtained after recrystallization in acetonitrile or high energy milling: (a) 1 (b) 0.8 (c) 0.6 (d) 0.4 (e) 0.1 (f) 0. (B) DSC curves of selected racemic compositions between 1a and 1b: (g) 0 (h) 0.2 (i) 0.4 (j) 0.6 (k) 0.8 (l) 1.

It can be seen from Figure II - 16A that XRPD patterns are a juxtaposition of pure **1a** / **1b** patterns up to a composition of 60%-**1b**, indicating a complete discrimination between both solid phases below 60%-**1b**. Afterward, only the pattern of **1b** remains for composition ≥ 60%-**1b**, revealing a large solid-state miscibility of **1a** enantiomers into the racemic structure of **1b**. This is supported by the thermograms of compositions ≥ 60%-**1b** depicted in Figure II - 16B (j and k), in which three endothermic phenomena are observed. Thermal data of compositions < 60%-**1b** present an endothermic invariant at circa 110 °C, which are all concomitant to the liquidus endotherms, hindering the access of the eutectic enthalpies and preventing a possible Tammann plot. However, small shift of the diffraction peak observed at ca. 8 and 9 ° (2θ scale) could possibly be due to a small solid-state miscibility below 10%-**1b**.

Further XRPD analyses are conducted on compositions < 10%-**1b** using NaCl as an internal standard to ensure exact diffraction pick positions (Figure II - 17A). The diffractograms of these compositions display consistent patterns with this observed from **1a** up to 2.5%-**1b**, with noticeable peak shifts. Diffraction peaks corresponding to the presence of the racemic compound **1b** are detected from 5%-**1b**. Furthermore, DSC measurements of this composition

range showed that the eutectic invariant occurs for compositions ≥ 5%-**1b** while there is a single and decreasing endothermic signal up to 2.5%-**1b** (Figure II - 17B). This is consistent with a narrow domain of partial solid solution below 5%-**1b**. According to above investigations, the racemic isopleth section **1a** / **1b** is plotted in Figure II - 17C. This phase diagram shows that **1b** is miscible in the solid-state with **1a** within a small composition range (*i.e.* < 5 %mol). In contrast, the miscibility of **1a** in **1b**, which is strongly temperature dependent, is much larger.

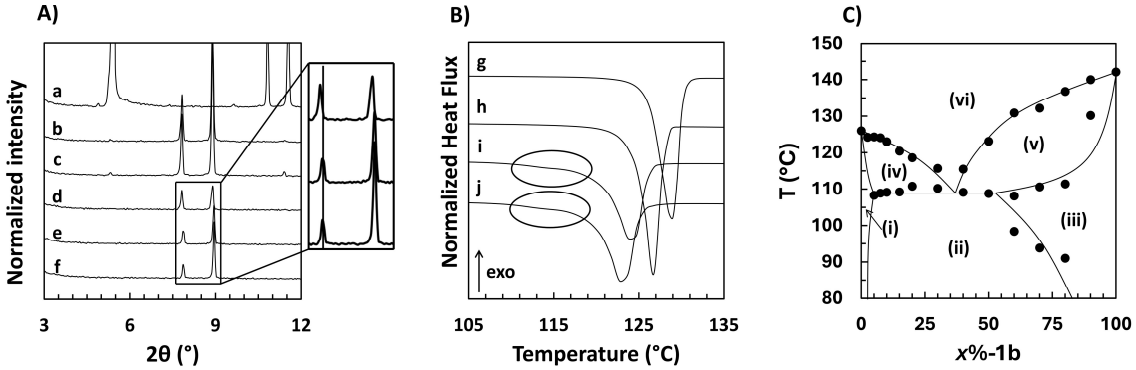

Figure II - 17. (A) XRPD patterns of additional compositions (a) 1 (b) 0.1 (c) 0.075 (d) 0.05 (e) 0.025 (f) 0 using sodium chloride as an internal standard. (B) DSC curves of additional compositions (g) 0 (h) 0.025 (i) 0.05 (j) 0.075. (C) Racemic binary isoplethal section between 1a and 1b supported by the above-mentioned investigations: (i) ss<(*R*)-1a> + ss<(*S*)-1a> (ii) ss<(*R*)-1a> + ss<(*S*)-1a> + ss<(*RS*)-1b> (iii) ss<(*RS*)-1b> (iv) ss<(*R*)-1a> + ss<(*S*)-1a> + liquid (v) ss<(*RS*)-1b> + liquid (vi) liquid

II.3.3.2 - Racemic binary isoplethal section 1c / 1d

Akin **1a** / **1b**, different compositions of the system **1c** / **1d** are prepared by solvent evaporation in acetonitrile, hand-ground to ensure homogeneity and analyzed by XPRD (Figure II - 18A) and DSC (Figure II - 18B). XRPD analyses of these compositions demonstrate the perfect juxtaposition of all diffraction patterns with that of pure **1c** / **1d** patterns, indicating a physical mixture of both phases between at least 10%-**1d** and 90%-**1d**. DSC measurements on the whole compositions range all presented two distinct phenomena: (i) an endothermic invariant around 61 °C and (ii) an endothermic signal varying between the melting point of pure components with a minimum at ca. 70%-**1d**. In this case, the widths of partial solid solutions are determined by plotting the enthalpy of the eutectic invariant for each composition (Figure II - 18C, Triangles). According to this Tammann graph (Figure II - 18C, triangles), this system must be a eutectic invariant with a eutectic point at around 76%-**1d** and partial solid solution domains below 9%-**1d** and above 96%-**1d.**

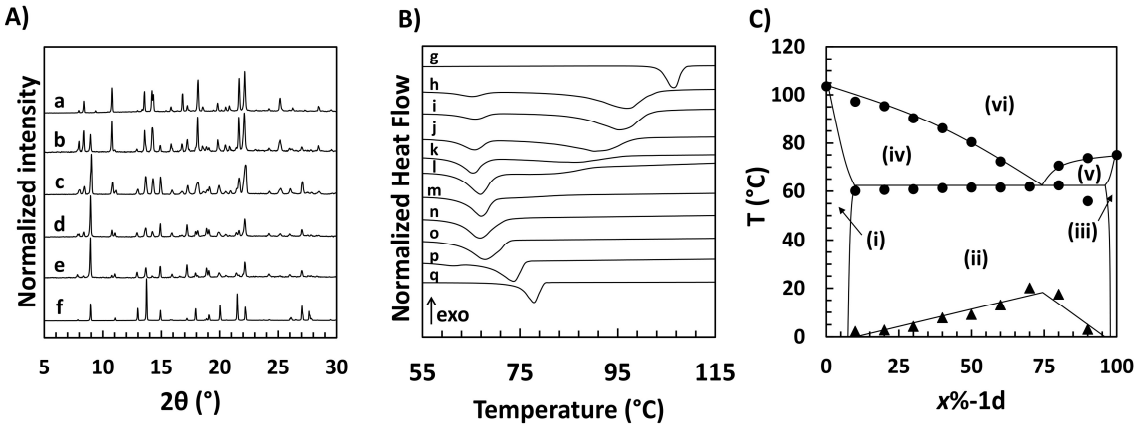

Figure II - 18. (A) XRPD patterns of selected racemic compositions between 1c and 1d obtained after recrystallization in acetonitrile: (a) 1 (b) 0.8 (c) 0.6 (d) 0.4 (e) 0.2 (f) 0. (B) DSC curves of the different racemic compositions between 1c and 2d: (g) 0 (h) 0.1 (i) 0.2 (j) 0.3 (k) 0.4 (l) 0.5 (m) 0.6 (n) 0.7 (o) 0.8 (p) 0.9 (q) 1. (C) Racemic binary isoplethal section (circles) and Tammann plot (triangles) between 1c and 1d supported by the above-mentioned investigations: (i) ss<(*R*)-1c> + ss<(*S*)-1c> (ii) ss<(*R*)-1c> + ss<(*S*)-1c> + ss<(*RS*)-1d> (iii) ss<(*RS*)-1d> (iv) ss<(*R*)-1c> + ss<(*S*)-1c> + liquid (v) ss<(*RS*)-1d> + liquid (vi) liquid.

Interestingly, the conglomerate mixed crystal miscibility limit can be extended via metastable incorporation up to ca. 30%-**1d** by using neat high energy milling, akin forced phases phenomenon in alloy.[57,58] This observation is supported by the perfect superimposition of the XRPD patterns (Figure II - 19) and the three different endotherms highlighted by DSC measurements of solid mixtures below 30%-**1d** (Figure II - 19g and h).

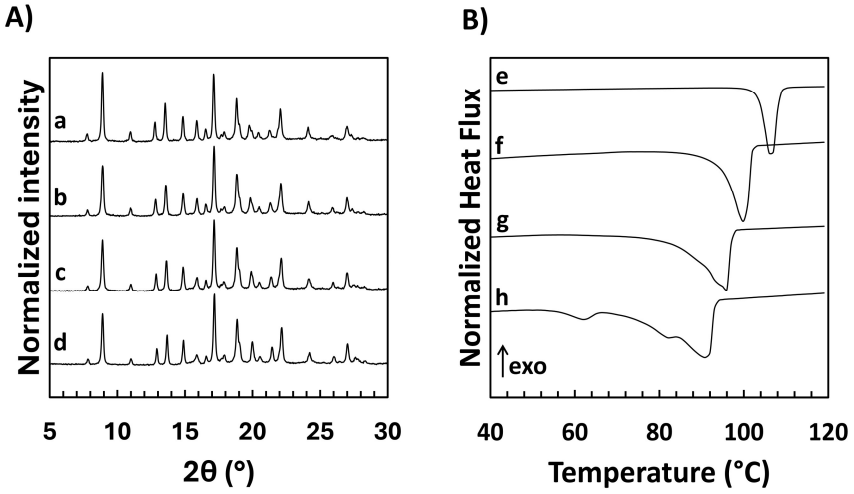

Figure II - 19. (A) XRPD patterns of racemic compositions between 1c and 1d obtained by high energy milling: (a) 0.3 (b) 0.2 (c) 0.1 (d) 0. (B) DSC of racemic compositions between 1c and 1d obtained by high energy milling: (e) 0 (f) 0.1 (g) 0.2 (h) 0.3.

New diffraction peaks are observed for composition > 30%-**1d**, indicative of a new solid phase (result not shown). However, plotting the thermal events on a racemic binary isopleth section

does not lead to an accurate explanation regarding the crystallographic data. Although the racemic binary isopleth section between **1c** and **1d** under high energy milling has not been precisely constructed, there is definitely a stable solid-state miscibility domain up to 9%-**1d** and a metastable solid-state miscibility domain up to 30%-**1d**.

II.3.4 - Temperature Cycling Induced Deracemization

The content of the present section has been published in Chemistry: a European Journal.[59] A narrow domain of stable partial miscibility in the solid state exists for both systems (**1a** / **1b**, **1c** / **1d**). Hence, TCID experiments within these domains must be performed to give proof-of-concept of the deracemization of a stable racemic compound through conglomerate mixed crystals. The experimental protocol will follow the successful solid-state deracemization by TCID of pure **1a** and **1c** already reported in the literature will be used: 2g of solid mixture, 0.2g of sodium hydroxide (racemizing agent) and a solvent mixture of methanol / water ($MeOH/H_2O$ hereafter).[60–64]

II.3.4.1 - Solubility measurements

The addition of a solvent adds an additional dimension to the deracemized system (c = 5, *cf.* Gibbs phase rule). In such scenarios, the initial conditions (*e.g.* solid composition and suspension density) play a crucial role in determining the phase in equilibrium. This concept is clearly illustrated by the schematic representation of the isoplethal ternary isotherm of a hypothetic system involving a racemic conglomerate, a racemic compound and a solvent with partial miscibility on the conglomerate side (Figure II - 20). Indeed, the composition of the mixed crystal in equilibrium with the doubly saturated solution is thermodynamically described by tie-lines (Figure II - 20, grey dashed lines). These tie-lines can vary significantly depending on either the starting solid composition (Figure II - 20, purple dotted lines) or suspension density (Figure II - 20, green dotted lines).

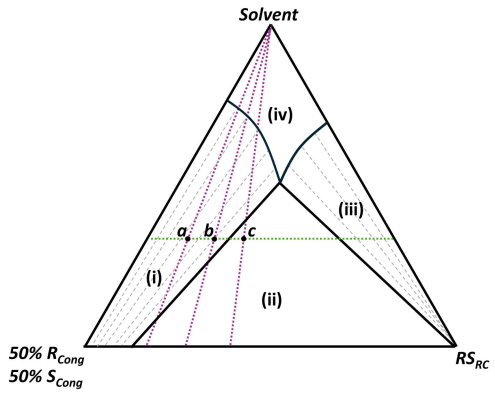

Figure II - 20. Schematic isoplethal ternary isotherm of a system racemic conglomerate / racemic compound / solvent exhibiting a partial miscibility on the conglomerate side and highlighting the importance of the starting composition (purple dotted lines) and suspension density (green dotted lines) on the phase in equilibrium: (i) ss<(*R*)$_{cong}$> + ss<(*S*)$_{cong}$> + d.s.s. (ii) ss<(*R*)$_{cong}$> + ss<(*S*)$_{cong}$> + ss<(*RS*)$_{RC}$> + t.s.s. (iii) ss<(*RS*)$_{RC}$> + sat. sol. (iv) u.s.s.. Points (a) and (b) belong to the mixed crystal phase domain (i) while point (c) belong to the quadriphasic domain (ii). Tie-lines are depicted as grey dashed lines.

By varying the solid composition while maintaining a constant solution density, the system can yield pure mirror-image mixed crystals (Figure II - 20, point a or b) or mirror-images mixed crystals containing centrosymmetric impurity that hinder the chiral discrimination (Figure II - 20, point c). It should be noted that point (*b*) is expected to be more enriched with the enantiomers forming the racemic compound compared to point (*a*), as indicated by the tie-lines.

In addition to these critical factors, the solubility of such composition must be carefully evaluated, as the solution may contain significant amounts of racemic solute, hence reducing the effectiveness of TCID. Therefore, it is essential to strike a balance between maximizing solute recovery while maintaining an optimal suspension density.

Bearing this in mind, the solubility of several compositions *x*%-**1b** and *x*%-**1d** above the maximum solid-state miscibility limit highlighted for both system in different MeOH / H_2O mixtures are determined by the gravimetric method and analyzed by XPRD after filtration to ensure the crystallization of the mirror-images mixed crystals. By coupling solubility measurements and crystallographic analyses, the solvent mixture MeOH/H_2O 85:15 (v/v) and 65:35 (v/v) stand out as the most promising for the deracemization of *x*%-**1b** and *x*%-**1d** respectively using ca. 15 wt% of solid. In these solvent mixtures, mirror-images mixed crystals remain up to ca. 5%-**1b** and 50%-**1d**. Their solubilities at 20 °C and 30 °C, along that of 20%-**1d** to exemplify the impact of the initial solid composition, are summarized in Table II - 3.

Table II - 3. Solubilities of *x*%-1b and *x*%-1d in MeOH/H2O 85:15 (v/v) and 65:35 (v/v) respectively.

	5%-1b		20%-1d		50%-1d	
Temperature (°C)	20	30	20	30	20	30
Solubility (wt%)	4.9	6.2	4.7	5.2	9.4	12.1

II.3.4.2 - Operative TCID experiments

TCID experiments using 5%-**1b**, 20%-**1d** and 50%-**1d** according to the abovementioned initial conditions are performed based on the temperature program reported by Suwannasang *et al*.[60]

For accurate analysis, the monitoring of the *e.e.* of both species of the solid mixtures must be accessible within a single measurement per sample. For *x*%-**1b**, optimal cHPLC condition is found using a Chiracel OD-H column (250 mm ×4.6mm×5 µm) with a UV detection at a wavelength of 220 nm, employing a mixture of isopropyl IPA / n-heptane (3:97, v/v) as eluent at a flow rate of 1 mL.min^{-1} (Figure II - 21A). In contrast, conventional cHPLC does not provide sufficient resolution for *x*%-**1d**, making 2D-cHPLC necessary. This 2D-cHPLC method involves Chiracel OD-H and AD-H columns (250 mm ×4.6mm×5 µm) with a UV detection at a wavelength of 220 nm using a mixture of isopropyl IPA / n-heptane / TFA (95:5:0.1, v/v/v) as eluent at a flow rate of 1 mL.min^{-1} (Figure II - 21B). The evolution of the solid-phase *e.e.* monitored using the abovementioned cHPLC conditions for each TCID experiments are depicted in Figure II - 22.

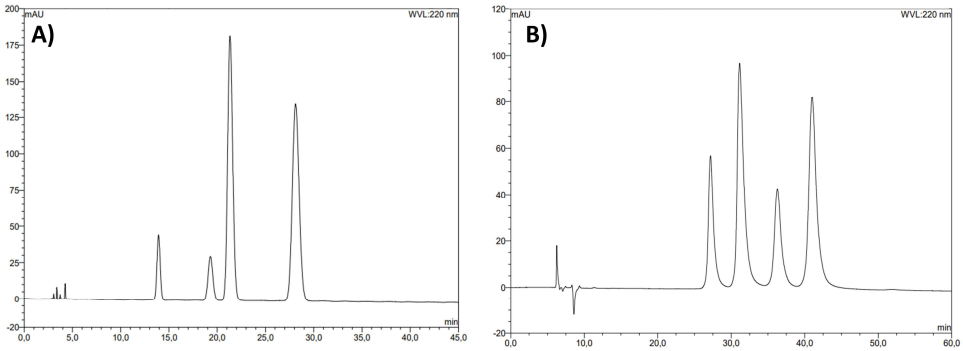

Figure II - 21. Typical chromatograms of (A) racemic *x*%-1b and (B) racemic *x*%-1d. Retention time (min) for (A) (*R*)-1a: 21.23 (*S*)-1a: 28.12 (*R*)-1b: 14.02 (*S*)-1b: 19.34 and (B) (*R*)-1c: 30.55 (*S*)-1c: 39.27 (*R*)-1b: 28.02 (*S*)-1b: 35.87.

It can be seen from this evolution that the increase in solid-phase *e.e.* of **1a** and **1c** (*i.e.* conglomerate-forming system) is followed by a similar and concomitant increase in solid-

phase *e.e.* of **1b** and **1d** (*i.e.* racemic compound-forming system). Moreover, a mixture of enantiopure mixed crystal *x*%-**1b** and *x*%-**1d** is obtained after 100 h of TCID, which is a deracemization time commonly observed for conventional TCID experiment starting from racemic composition. More importantly, this gives the proof-of-concept that deracemization can be extended to stable racemic compound-forming systems through a deracemizable conglomerate host.

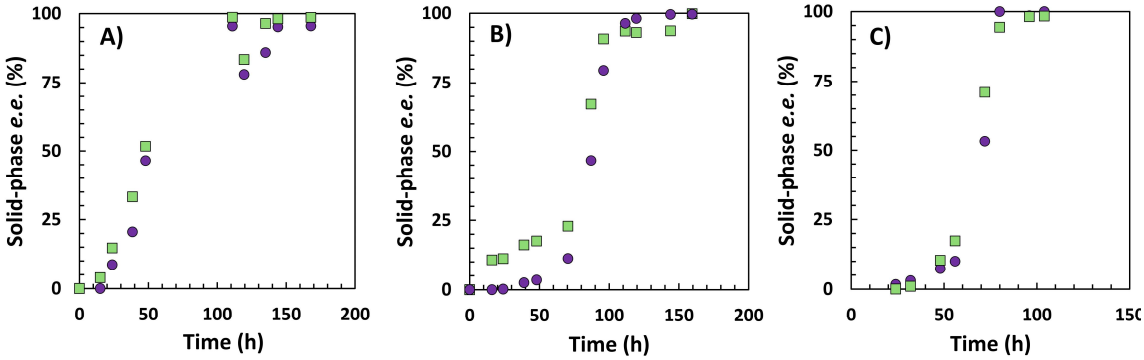

Figure II - 22. Evolution of the solid-phase *e.e.* versus time for the TCID experiments of (A) 5%-1b and (B) 20%-1d (B) 50%-1d. Green squares and purple circles stand for the enantiomers of the conglomerate-forming system and the racemic compounds respectively.

As expected from the tie-lines (Figure II - 20), the final deracemized mixed crystals are not composed of 5%-**1b**, 20%-**1d** and 50%-**1d** after TCID. According to the calibration curves in Figure II - 23, the deracemized solids are enantiopure mixed crystals 2.4%-**1b**, 3.4%-**1d** and 8.6%-**1d**, respectively, which are likely to be the stable solid-state miscibility limits for the homochiral enantiomer pairs.

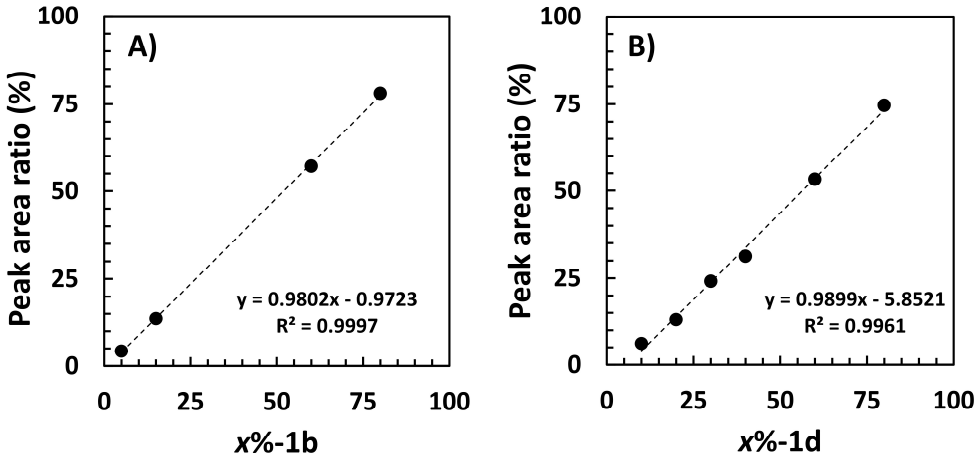

Figure II - 23. Calibration curves relating the solid composition to the HPLC percentage surface area of (A) *x*%-1b (B) *x*%-1d

It should be noted that the racemic binary isoplethal sections depicted in part II.3.3 are descriptive of the deracemized systems while no enantiomeric excesses are reached. Indeed, the solubility limits may evolve with the enantiomeric composition and could be therefore lower or higher compared to the racemic solid-state miscibility limits. The study of different compositions at different enantiomeric excess would improve understanding of this phenomenon. Although the deracemized solid are successfully separated by classical silicagel column due to their small molecular differences, enantiopure **1b** and **1d** could not be isolated in enough quantity to perform further experiments.

II.3.4.3 - Post-TCID Analyses

Further thermal analyses are performed on the final deracemized mixed crystal 3.4%-**1d** and 8.6%-**1d** (Figure II - 24A). It can be seen that only one endothermic phenomenon associated with a slight decrease of the melting point from the enantiopure **1c** to the enriched enantiopure mixed crystals 3.4%-**1d** and 8.6%-**1d** is observed on the thermograms. Those observations confirm that more material has been involved in the deracemization matrix. Moreover, crystallographic data are in line with this conclusion since only the pattern of **1c** is detected (Figure II - 24B).

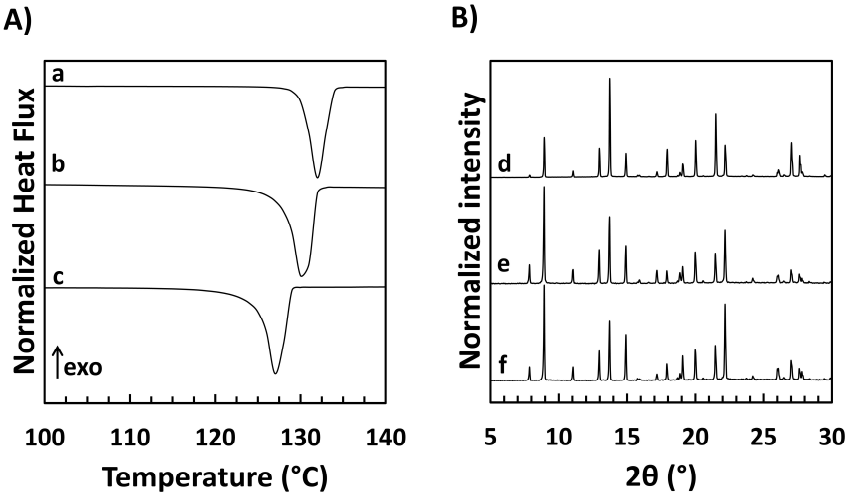

Figure II - 24. (A) DSC curves of deracemized (a) 1c (b) 3.4%-1d (c) 8.6%-1d. (B) XRPD patterns of (d) 8.6%-1d (e) 3.4%-1d (f) 1c.

The crystal habit of the final deracemized solids mixed crystals 3.4%-**1d** and 8.6%-**1d** are also observed by SEM and compared to SEM pictures of deracemized **1c** at three different magnifications (Figure II - 25). Although all deracemized solids present aggregates of prism-

like crystal, the crystal size distribution significantly decreased with variation in the composition of the mixed crystals. This observation may be a result of a crystal growth inhibition induced by the enrichment of the mixed crystal, acting as an impurity. According to the different theoretical models reported for the mechanism of solid-state deracemization,[65–69] this lowered crystal size distribution induced by the mixed crystal enrichment should enhance the agglomeration and clustering of enantiomer of the same handedness, and therefore, enhance the kinetic of deracemization. This is indeed observed in the case of 8.6%-**1d**, for which the *e.e.* take-off occurs 20 h earlier than 3.4%-**1d**.

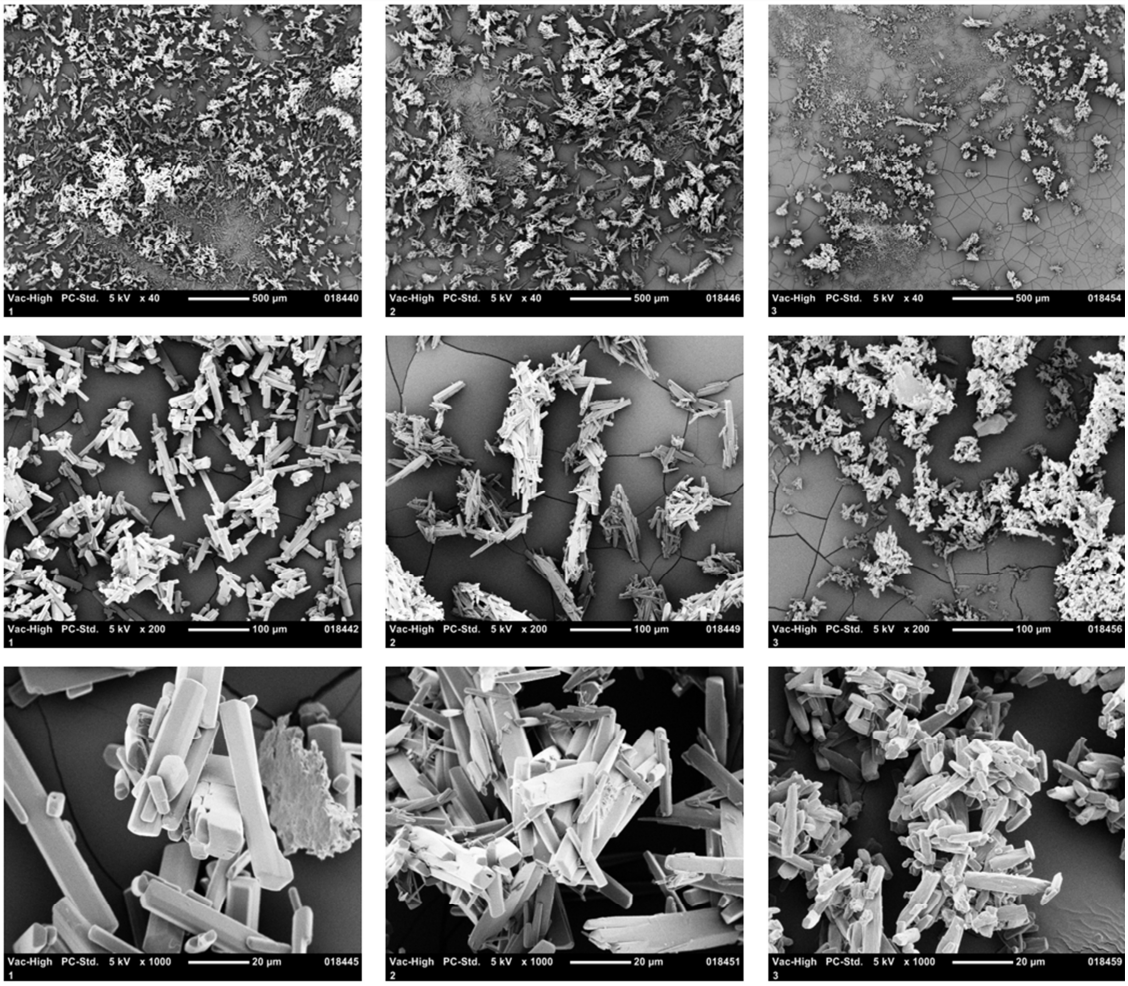

Figure II - 25 SEM pictures of deracemized 1c (left column), 3.4%-1d (middle column), and 8.6%-1d (right column). Magnification x40 (upper), x200 (middle), and x1000 (lower).

II.3.5 - Deracemization under high-energy milling

While the host conglomerate consistently provides chiral discrimination, the efficacy of this mixed crystal strategy is necessarily bounded by the stable solid-state miscibility of the guest

molecule inside the host structure (Figure II - 26A). For instance, TCID experiments performed with racemic 50%-**1d** consistently led to an enantiopure mixed crystal of 8.6%-**1d** composition, reflecting the maximum solid-state miscibility of **1d** within **1c**.[59] However, this solvent-mediated approach results in poor recovery since part of the target material remains racemized at the solvated state.[70]

Chrystal Lopes, a Ph.D. student from our lab, recently extended the scope of deracemization to mechanochemistry by giving the proof of concept of an almost solvent free method for deracemization under high energy milling (Figure II - 26B).[63] Additionally, we previously found that the solid-state miscibility between **1c** and **1d** is increased to roughly 30%-**1d** via metastable incorporation under high energy neat grinding (Figure II - 19). Therefore, we realize the benefit of coupling mixed crystals deracemization with mechanochemistry, thereby opening novel routes for the deracemization of metastable phases (Figure II - 26C).

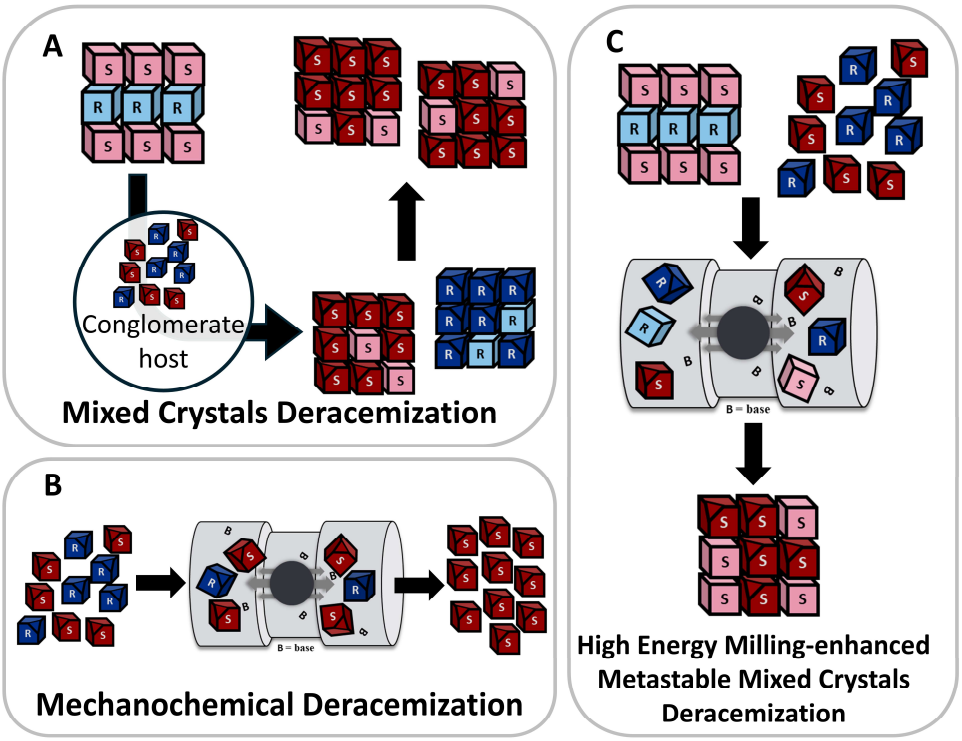

Figure II - 26. (A) Schematic principle of mixed crystal deracemization (B) Schematic principle of mechanochemical deracemization (C) Enlargement of the miscibility domain through high energy milling driven metastable equilibria.

Motivated by these insights, we here mill several *x*%-**1d** mixtures with sodium hydroxide as racemizing agent and sodium chloride as solid lubricant to ensure better homogeneity, for a maximum duration of 6h. After grinding, we collect the material and assess the final solid and

enantiomeric composition of both **1c** and **1d** by 2D-cHPLC (Figure II - 27, purple bars). The mechanochemical deracemization of 20%-**1d** and 30%-**1d** mixtures result in a complete enantioconversion of both compound (> 95 *e.e.*%) with a final solid composition above the stable solid-state miscibility (> 9%-**1d**, green dashed line in Figure II - 27). Deracemization of such mixtures by regular TCID using identical condition than the one described in II.3.4 (Figure II - 27, green bars) does not exceed this limit and only a maximum of 6%-**1d** is obtained as pure enantiomer mixed crystals. In contrast, high energy milling allows to reach 25%-**1d** consisting of a threefold increase with reference to the TCID process. This confirms the success of our deracemization strategy and further demonstrates the potential of extending solid-state miscibility under non-equilibrium conditions.

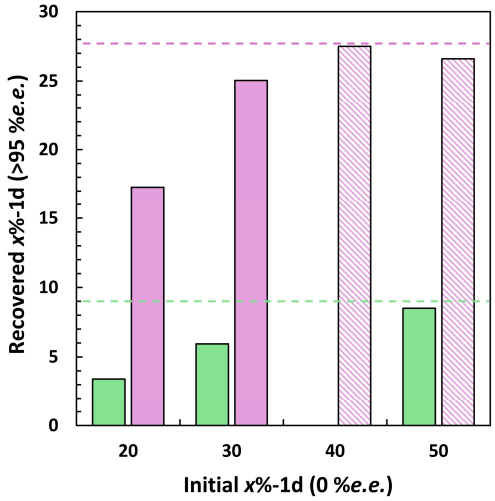

Figure II - 27. Proportion of enantiopure x%-1d as a function of the initial composition after: (green) TCID in methanol/water (65/35 v/v) (Green bars) and high energy milling (Purple bars). Dashed lines correspond to the maximum solid-state miscibility of racemic o-x%MeTAK according to either the stable (green) or the metastable (purple) equilibria. Dotted purple bars corresponds to the enantiopure fraction obtained after experiment exceeding the metastable miscibility domain.

To further investigate this high energy milling process, we perform experiments with mixtures above the metastable solid-state miscibility limit (Figure II - 27, purple dashed line), for instance 40%-**1d** and 50%-**1d**. We observe complete enantioconversion of **1c** (> 98 %*e.e.*) while the deracemization of **1d** remains partial, exhibiting an enantiomeric excess of 67 and 38 %*e.e.*, respectively. Here, the host conglomerate mixed crystal reaches saturation, the excess of **1d** remains as racemic crystals, thus explaining the lower optical purities. Considering the final solids to be composed of enantiopure *x*%-**1d** mixed crystals and racemic crystals of **1d** (Table II - 4), the final enantiopure mixed crystals consistently exhibit a

composition of ca. 27%-**1d** (Figure II - 27, dashed purple bars). By contrast, TCID of these mixtures once again resulted in solid compositions below the stable solid-state miscibility limit (Figure II - 27, green bars).

Table II - 4. Peak area collected by 2D-cHPLC after complete deracemization under high energy milling of different *x*%-1d mixtures. The composition of the racemic crystals is estimated considering the non-deracemized solids to be part of a racemic phase (either racemic conglomerate or racemic compound). The composition of the enantiopure crystals is therefore estimated by considering the deracemized solids to be part of an enantiopure mixed crystal phase.

Initial *x*%-**1d**			40%-**1d**	50%-**1d**
1c	Area (*a.u.*)	R	3.4	6.8
		S	236.7	250.1
	Area racemic mixture (*a.u.*)		6.8	13.6
	Area enantiopure crystal (*a.u.*)		233.3	250.1
1d	Area (*a.u.*)	R	16.2	51.5
		S	79.4	114.3
	Area racemic mixture (*a.u.*)		32.3	103.0
	Area enantiopure crystal (*a.u.*)		63.3	62.8
Peak area ratio of enantiopure crystals (%)			21.4	20.5
Recovered enantiopure mixed crystals *x*%-**1d** (%)			27.5	26.6

This maximum enantiopure mixed crystals composition must reflect the metastable solid-state miscibility limit under non-equilibrium conditions, which is in line with the solid-state miscibility estimated based on the thermochemical and crystallographic data (*cf.* II.3.3.2). More importantly, it consists of a threefold increase of the efficiency of this deracemization strategy based on the formation of conglomerate mixed crystals.

II.4 - Discussion & conclusion

This chapter described the use of unconventional strategies toward enantiopurity. The first strategy gets rid of the boundaries implied by thermodynamic considerations through the systematic use of fundamental kinetic asymmetries between enantiomers crystallizing as conglomerates. Intriguingly, our case study revealed a striking consistency in the out-of-equilibrium dissolution phenomenon and proportionality with respect to the temperature variation, even though such kinetic asymmetries are expected to depend on numerous parameters, which should therefore introduce inconsistencies between experiments. This

behaviour was also observed by applying a significant temperature variation to an initially racemic material, which may be the result of the amplification of an initial *e.e.* imbalance obtained after the synthesis. This initial *e.e.* imbalance may be inherent to the conglomerate nature of chiral systems.

Moreover, we demonstrated that this behaviour persists for at least 15 minutes despite expectations that it should be short-lived, raising the question of how long such an out-of-equilibrium phenomenon may actually last. By contrast, inconsistencies were characterized during the crystallization regime, even though the cooling steps operated at low cooling rate. Intriguingly, a preferential crystallization phenomenon occurs when the chiral system reaches enantiopurity upon heating (*i.e.* reaches the biphasic domain). Both preferential dissolution and crystallization phenomena may be a result of an Ostwald's ripening process, inducing the major enantiomer to growth at the expense of the minor enantiomer.

These observations under temperatures variation raise the question of the impact of a racemizing agent on such system. During the preferential dissolution regime, one would expect an enhancement of this phenomenon as it would keep an equal supersaturation of both enantiomer all along the process, therefore withdrawing any driving force for the reverse process to occur. Conversely, a racemization during the preferential crystallization regime would inhibit the asymmetric supersaturation of the targeted enantiomer upon cooling, thereby preventing the prevalence of a single-handed crystal population. This could explain the typical sigmoidal evolution of such solid-state deracemization processes: while the *e.e.* exponentially increase at the beginning of the process (preferential dissolution regime), it slows down at the end (self-defeating racemization of the targeted enantiomer).

More importantly, these out-of-equilibrium phenomena induce sufficient *e.e.* imbalance to drive a complete chiral resolution of a conglomerate-forming system throughout a kind of chiral segregation induced by simple temperature cycling. This chiral resolution process could also be included in conventional conglomerate screening process from racemic mixture for straightforward identification of conglomerate-forming system. This could be done by simply monitoring the evolution of the *e.e.* while exchanging the solid-free liquid between two symmetrical racemic slurries under temperature variations. A deviation from the racemic composition would be indicative of a conglomerate-forming system.

The second strategy is to make use of a highly discriminative chiral recognition phenomenon, akin chirality transfer and Dutch resolution processes, to engineer a conglomerate host-guest mixed crystal structure. Interestingly, such conglomerate mixed crystals were systematically characterized for our two model systems although exhibiting different solid-state miscibility limit, raising the question of how this chiral recognition phenomenon does extend to other system, being either chemically related or unrelated. Additionally, this work is echoing the well know natural library of chemically related derivative that are the proteogenic amino acids: since some of them crystallize as conglomerate (*e.g.* threonine, asparagine monohydrate etc.), one may imagine that such complex conglomerate mixed crystal could arise and evolve toward the homochirality that we observe nowadays.

More precisely, it is possible to direct the complete symmetry breaking towards a single handedness for a racemic-compound-forming system by using a solid solution with a chemically related racemizable conglomerate through conventional deracemization routes (*e.g.* TCID). However, the comprehensive widespread use of this strategy requires a good knowledge of the heterogenous equilibria between all involved component to ensure the evolution of the system towards enantiopurity. Moreover, a clear example of a forced extension of the conglomerate mixed crystal domain under neat high-energy milling was characterized, in which operative deracemization condition is successfully implemented. Among the two successful examples, we could deracemize up to 25 wt% of the racemic compound inside the conglomerate matrix. Although the solid-state miscibility limits could be extended through non-equilibrium forced extension, the effectiveness of this deracemization strategy remains limited by this phase boundary. More importantly, we demonstrate that high energy inputs provide sufficient far-from-equilibrium conditions for accessing metastable structures with efficient chiral discrimination capabilities, thereby underlining the tremendous potential of mechanochemistry in the field of chiral resolution.

This chapter described the benefit of studying libraries of chemically related derivatives and the potential of performing crystallization process under far-from-equilibrium conditions. It remains to know how much far-from-equilibrium conditions could overcome the thermodynamic boundaries usually stated as limitation.

References

(1) Qian, H.-L.; Xu, S.-T.; Yan, X.-P. Recent Advances in Separation and Analysis of Chiral Compounds. *Anal. Chem.* **2023**, *95* (1), 304–318. https://doi.org/10.1021/acs.analchem.2c04371.

(2) Ward, T. J.; Ward, K. D. Chiral Separations: A Review of Current Topics and Trends. *Anal. Chem.* **2012**, *84* (2), 626–635. https://doi.org/10.1021/ac202892w.

(3) Zhu, Q.; Cai, Z.; Zhou, P.; Sun, X.; Xu, J. Recent Progress of Membrane Technology for Chiral Separation: A Comprehensive Review. *Separation and Purification Technology* **2023**, *309*, 123077. https://doi.org/10.1016/j.seppur.2022.123077.

(4) Sui, J.; Wang, N.; Wang, J.; Huang, X.; Wang, T.; Zhou, L.; Hao, H. Strategies for Chiral Separation: From Racemate to Enantiomer. *Chem. Sci.* **2023**, *14* (43), 11955–12003. https://doi.org/10.1039/D3SC01630G.

(5) Maier, N. M.; Franco, P.; Lindner, W. Separation of Enantiomers: Needs, Challenges, Perspectives. *Journal of Chromatography A* **2001**, *906* (1), 3–33. https://doi.org/10.1016/S0021-9673(00)00532-X.

(6) Shen, J.; Okamoto, Y. Efficient Separation of Enantiomers Using Stereoregular Chiral Polymers. *Chem. Rev.* **2016**, *116* (3), 1094–1138. https://doi.org/10.1021/acs.chemrev.5b00317.

(7) Ward, T. J.; Ward, K. D. Chiral Separations: Fundamental Review 2010. *Anal. Chem.* **2010**, *82* (12), 4712–4722. https://doi.org/10.1021/ac1010926.

(8) Borowiecki, P.; Paprocki, D.; Dudzik, A.; Plenkiewicz, J. Chemoenzymatic Synthesis of Proxyphylline Enantiomers. *J. Org. Chem.* **2016**, *81* (2), 380–395. https://doi.org/10.1021/acs.joc.5b01840.

(9) Brill, Z. G.; Condakes, M. L.; Ting, C. P.; Maimone, T. J. Navigating the Chiral Pool in the Total Synthesis of Complex Terpene Natural Products. *Chem. Rev.* **2017**, *117* (18), 11753–11795. https://doi.org/10.1021/acs.chemrev.6b00834.

(10) Alezra, V.; Kawabata, T. Recent Progress in Memory Of Chirality (MOC): An Advanced Chiral Pool. *Synthesis* **2016**, *48*, 2997–3016. https://doi.org/10.1055/s-0035-1562441.

(11) Blaser, H. U. The Chiral Pool as a Source of Enantioselective Catalysts and Auxiliaries. *Chem. Rev.* **1992**, *92* (5), 935–952. https://doi.org/10.1021/cr00013a009.

(12) Speybrouck, D.; Howsam, M.; Lipka, E. Recent Developments in Preparative-Scale Supercritical Fluid- and Liquid Chromatography for Chiral Separations. *TrAC Trends in Analytical Chemistry* **2020**, *133*, 116090. https://doi.org/10.1016/j.trac.2020.116090.

(13) Kumar, V.; Lenhoff, A. M. Mechanistic Modeling of Preparative Column Chromatography for Biotherapeutics. *Annual Review of Chemical and Biomolecular Engineering* **2020**, *11* (Volume 11, 2020), 235–255. https://doi.org/10.1146/annurev-chembioeng-102419-125430.

(14) Wu, S.; Snajdrova, R.; Moore, J. C.; Baldenius, K.; Bornscheuer, U. T. Biocatalysis: Enzymatic Synthesis for Industrial Applications. *Angewandte Chemie International Edition* **2021**, *60* (1), 88–119. https://doi.org/10.1002/anie.202006648.

(15) Hall, M. Enzymatic Strategies for Asymmetric Synthesis. *RSC Chemical Biology* **2021**, *2* (4), 958–989. https://doi.org/10.1039/D1CB00080B.

(16) Jacques, J.; Collet, A.; Wilen, S. H. *Enantiomers, Racemates, and Resolutions*; Krieger Publishing Company: Malabar, 1994.

(17) Otero-de-la-Roza, A.; Hein, J. E.; Johnson, E. R. Reevaluating the Stability and Prevalence of Conglomerates: Implications for Preferential Crystallization. *Crystal Growth & Design* **2016**, *16* (10), 6055–6059. https://doi.org/10.1021/acs.cgd.6b01088.

(18) Valenti, G.; Tinnemans, P.; Baglai, I.; Noorduin, W. L.; Kaptein, B.; Leeman, M.; ter Horst, J. H.; Kellogg, R. M. Combining Incompatible Processes for Deracemization of a Praziquantel Derivative under Flow Conditions. *Angew. Chem.* **2021**, *133* (10), 5339–5342. https://doi.org/10.1002/ange.202013502.

(19) Buhse, T.; Cruz, J.-M.; Noble-Terán, M. E.; Hochberg, D.; Ribó, J. M.; Crusats, J.; Micheau, J.-C. Spontaneous Deracemizations. *Chem. Rev.* **2021**, *121* (4), 2147–2229. https://doi.org/10.1021/acs.chemrev.0c00819.

(20) Black, S. N.; Williams, L. J.; Davey, R. J.; Moffatt, F.; Jones, R. V. H.; McEwan, D. M.; Sadler, D. E. The Preparation of Enantiomers of Paclobutrazol: A Crystal Chemistry Approach. *Tetrahedron* **1989**, *45* (9), 2677–2682. https://doi.org/10.1016/S0040-4020(01)80097-1.

(21) Fytopoulos, A. A.; Kavousanakis, M. E.; Van Gerven, T.; Boudouvis, A. G.; Stefanidis, G. D.; Xiouras, C. Crystal Growth, Dissolution, and Agglomeration Kinetics of Sodium Chlorate. *Ind. Eng. Chem. Res.* **2021**, *60* (19), 7367–7384. https://doi.org/10.1021/acs.iecr.1c00595.

(22) Snyder, R. C.; Doherty, M. F. Faceted Crystal Shape Evolution during Dissolution or Growth. *AIChE Journal* **2007**, *53* (5), 1337–1348. https://doi.org/10.1002/aic.11132.

(23) Sacchi, P.; Wright, S. E.; Neoptolemou, P.; Lampronti, G. I.; Rajagopalan, A. K.; Kras, W.; Evans, C. L.; Hodgkinson, P.; Cruz-Cabeza, A. J. Crystal Size, Shape, and Conformational Changes Drive Both the

Disappearance and Reappearance of Ritonavir Polymorphs in the Mill. *Proceedings of the National Academy of Sciences* **2024**, *121* (15), e2319127121. https://doi.org/10.1073/pnas.2319127121.

(24) Noorduin, W. L.; van Enckevort, W. J. P.; Meekes, H.; Kaptein, B.; Kellogg, R. M.; Tully, J. C.; McBride, J. M.; Vlieg, E. The Driving Mechanism Behind Attrition-Enhanced Deracemization. *Angewandte Chemie International Edition* **2010**, *49* (45), 8435–8438. https://doi.org/10.1002/anie.201002036.

(25) Spix, L.; Van Enckevort, W. J. P.; Van Der Wal, L. J. M.; Meekes, H.; Vlieg, E. Resolution of Asparagine in a Coupled Batch Grinding Process: Experiments and Modelling. *CrystEngComm* **2016**, *18* (48), 9252–9259. https://doi.org/10.1039/C6CE02043G.

(26) Hein, J. E.; Huynh Cao, B.; Viedma, C.; Kellogg, R. M.; Blackmond, D. G. Pasteur's Tweezers Revisited: On the Mechanism of Attrition-Enhanced Deracemization and Resolution of Chiral Conglomerate Solids. *J. Am. Chem. Soc.* **2012**, *134* (30), 12629–12636. https://doi.org/10.1021/ja303566g.

(27) Elsner, M. P.; Ziomek, G.; Seidel-Morgenstern, A. Simultaneous Preferential Crystallization in a Coupled Batch Operation Mode. Part II: Experimental Study and Model Refinement. *Chemical Engineering Science* **2011**, *66* (6), 1269–1284. https://doi.org/10.1016/j.ces.2010.12.035.

(28) Elsner, M. P.; Ziomek, G.; Seidel-Morgenstern, A. Simultaneous Preferential Crystallization in a Coupled, Batch Operation Mode—Part I: Theoretical Analysis and Optimization. *Chemical Engineering Science* **2007**, *62* (17), 4760–4769. https://doi.org/10.1016/j.ces.2007.05.035.

(29) Svang-Ariyaskul, A.; Koros, W. J.; Rousseau, R. W. Chiral Separation Using a Novel Combination of Cooling Crystallization and a Membrane Barrier: Resolution of DL-Glutamic Acid. *Chemical Engineering Science* **2009**, *64* (9), 1980–1984. https://doi.org/10.1016/j.ces.2008.12.024.

(30) Brandel, C.; Petit, S.; Cartigny, Y.; Coquerel, G. Structural Aspects of Solid Solutions of Enantiomers. *CPD* **2016**, *22* (32), 4929–4941. https://doi.org/10.2174/1381612822666160720164230.

(31) Rekis, T.; Agris, B. On the Structural Aspects of Solid Solutions of Enantiomers: An Intriguing Case Study of Enantiomer Recognition in the Solid State. *CrystEngComm*. 2018, pp 6909–6918.

(32) Rougeot, C. Deracemisation of Active Compound Precursors by Physical Treatments, UNIVERSITÉ DE TOULOUSE, 2012. http://thesesups.ups-tlse.fr/3095/1/2012TOU30316.pdf.

(33) Crassous, J.; Fuchter, M. J.; Freedman, D. E.; Kotov, N. A.; Moon, J.; Beard, M. C.; Feldmann, S. Materials for Chiral Light Control. *Nat Rev Mater* **2023**, *8* (6), 365–371. https://doi.org/10.1038/s41578-023-00543-3.

(34) Niu, X.; Zhao, R.; Yan, S.; Pang, Z.; Li, H.; Yang, X.; Wang, K. Chiral Materials: Progress, Applications, and Prospects. *Small* **2023**, *19* (38), 2303059. https://doi.org/10.1002/smll.202303059.

(35) Peluso, P.; Chankvetadze, B. Recognition in the Domain of Molecular Chirality: From Noncovalent Interactions to Separation of Enantiomers. *Chem. Rev.* **2022**, *122* (16), 13235–13400. https://doi.org/10.1021/acs.chemrev.1c00846.

(36) Xu, W.; Cheng, M.; Zhang, S.; Wu, Q.; Liu, Z.; Dhinakaran, M. K.; Liang, F.; Kovaleva, E. G.; Li, H. Recent Advances in Chiral Discrimination on Host–Guest Functionalized Interfaces. *Chem. Commun.* **2021**, *57* (61), 7480–7492. https://doi.org/10.1039/D1CC01501J.

(37) Scriba, G. K. E. Update on Chiral Recognition Mechanisms in Separation Science. *Journal of Separation Science* **2024**, *47* (9–10), 2400148. https://doi.org/10.1002/jssc.202400148.

(38) Zhang, J.-H.; Xie, S.-M.; Yuan, L.-M. Recent Progress in the Development of Chiral Stationary Phases for High-Performance Liquid Chromatography. *Journal of Separation Science* **2022**, *45* (1), 51–77. https://doi.org/10.1002/jssc.202100593.

(39) Kandula, J. S.; Rayala, V. P. K.; Pullapanthula, R. Chirality: An Inescapable Concept for the Pharmaceutical, Bio-Pharmaceutical, Food, and Cosmetic Industries. *SEPARATION SCIENCE PLUS* **2023**, *6* (4), 2200131. https://doi.org/10.1002/sscp.202200131.

(40) Hu, M.; Feng, H.-T.; Yuan, Y.-X.; Zheng, Y.-S.; Tang, B. Z. Chiral AIEgens – Chiral Recognition, CPL Materials and Other Chiral Applications. *Coordination Chemistry Reviews* **2020**, *416*, 213329. https://doi.org/10.1016/j.ccr.2020.213329.

(41) Arnold, F. H. Directed Evolution: Bringing New Chemistry to Life. *Angewandte Chemie International Edition* **2018**, *57* (16), 4143–4148. https://doi.org/10.1002/anie.201708408.

(42) Leveson-Gower, R. B.; Mayer, C.; Roelfes, G. The Importance of Catalytic Promiscuity for Enzyme Design and Evolution. *Nat Rev Chem* **2019**, *3* (12), 687–705. https://doi.org/10.1038/s41570-019-0143-x.

(43) Saršūns, K.; Bērziņš, A.; Rekis, T. Solid Solutions in the Xanthone–Thioxanthone Binary System: How Well Are Similar Molecules Discriminated in the Solid State? *Crystal Growth & Design* **2020**, *20* (12), 7997–8004. https://doi.org/10.1021/acs.cgd.0c01241.

(44) Mohajerani, S. S.; Paolello, M.; Linehan, B.; Ricci, F.; Capellades, G.; Nordstrom, F. L. Thermodynamic Stability Transitions and Coexistence of Two Polymorphs via Crystalline Solid Solutions: The T-X Phase

Diagram of Salicylic Acid and 2,3-Dihydroxybenzoic Acid. *Crystal Growth & Design* **2024**, *24* (11), 4847–4861. https://doi.org/10.1021/acs.cgd.4c00503.

(45) Paolello, M.; Mohajerani, S. S.; Linehan, B.; Ricci, F.; Capellades, G.; Nordstrom, F. L. Polymorphic Stability Shifts, Co-Crystals, and Crystalline Solid Solutions: The T-X Phase Diagram of Salicylic Acid–Salicylamide. *Crystal Growth & Design* **2024**, *24* (5), 2188–2201. https://doi.org/10.1021/acs.cgd.3c01501.

(46) Bolla, G.; Sarma, B.; Nangia, A. K. Crystal Engineering of Pharmaceutical Cocrystals in the Discovery and Development of Improved Drugs. *Chem. Rev.* **2022**, *122* (13), 11514–11603. https://doi.org/10.1021/acs.chemrev.1c00987.

(47) Hoquante, M. Homochiral vs. Heterochiral Crystal Packing Dilemma. Interplay between Intrinsic Chirality and Supramolecular Chirality, Rouen, 2021.

(48) Wiggins, T. E.; Baldwin, B. C. Binding of Azole Fungicides Related to Diclobutrazol to Cytochrome P-450. *Pestic. Sci.* **1984**, *15* (2), 206–209. https://doi.org/10.1002/ps.2780150212.

(49) Desta, B.; Amare, G. Paclobutrazol as a Plant Growth Regulator. *Chem. Biol. Technol. Agric.* **2021**, *8* (1), 1. https://doi.org/10.1186/s40538-020-00199-z.

(50) Balasubramanyan, S.; Shephard, M. C. Fungicidal Compounds. US4243405A, January 6, 1981. https://patents.google.com/patent/US4243405A/en (accessed 2024-09-01).

(51) Branch, S. K.; Nowell, I. W. Structure of 1-(4-Chloro-2-Fluorophenyl)-4,4-Dimethyl-2-(1H-1,2,4-Triazol-1-Yl)-3-Pentanone. *Acta Crystallogr C Cryst Struct Commun* **1986**, *42* (4), 440–442. https://doi.org/10.1107/S0108270186095860.

(52) Dalmolen, J.; Tiemersma-Wegman, T. D.; Nieuwenhuijzen, J. W.; van der Sluis, M.; van Echten, E.; Vries, T. R.; Kaptein, B.; Broxterman, Q. B.; Kellogg, R. M. The Dutch Resolution Variant of the Classical Resolution of Racemates by Formation of Diastereomeric Salts: Family Behaviour in Nucleation Inhibition. *Chemistry* **2005**, *11* (19), 5619–5624. https://doi.org/10.1002/chem.200500440.

(53) Kaptein, B.; Elsenberg, H.; Grimbergen, R. F. P.; Broxterman, Q. B.; Hulshof, L. A.; Pouwer, K. L.; Vries, T. R. Dutch Resolution of Racemic 4-Hydroxy- and 4-¯uoro- Phenylglycine with Mixtures of Phenylglycine and (+)-10-Camphorsulfonic Acid. *Tetrahedron: Asymmetry* **2000**, 9.

(54) Dutch Resolution of Racemates and the Roles of Solid Solution Formation and Nucleation Inhibition. In *Novel Optical Resolution Technologies*; Kellogg, R. M., Kaptein, B., Ton R., V., Eds.; Topics in Current Chemistry; Springer Berlin Heidelberg: Berlin, Heidelberg, 2007; Vol. 269, pp 159–197. https://doi.org/10.1007/978-3-540-46320-7.

(55) Kellogg, R. M.; Nieuwenhuijzen, J. W.; Pouwer, K.; Vries, T. R.; Broxterman, Q. B.; Grimbergen, R. F. P.; Kaptein, B.; Crois, R. M. L.; Wever, E. de; Zwaagstra, K.; Laan, A. C. van der. Dutch Resolution: Separation of Enantiomers with Families of Resolving Agents. A Status Report. *Synthesis* **2003**, *2003* (10), 1626–1638. https://doi.org/10.1055/s-2003-40508.

(56) Saršūns, K.; Kons, A.; Leduskrasts, K.; Karziņins, A.; Krūkle-Bērziņa, K.; Bobrovs, R.; Noohinejad, L.; Bērziņš, A.; Rekis, T. Fifteen Solid Solutions of Four Thioxanthone Halogen Derivatives: Structures, Miscibility Limits, and Luminescence. *Crystal Growth & Design* **2024**. https://doi.org/10.1021/acs.cgd.4c00969.

(57) Chaffron, L.; Le Bouar, Y.; Saint-Ayes, G.; Martin, G. Driven Phase Transformations in Forced Alloys. *Rev. Met. Paris* **2003**, *100* (2), 183–192. https://doi.org/10.1051/metal:2003100.

(58) Pochet, P.; Bellon, P.; Boulanger, L.; Chaffron, L.; Martin, G. Phase Transformations under Ball Milling. *MSF* **1998**, *269–272*, 655–664. https://doi.org/10.4028/www.scientific.net/MSF.269-272.655.

(59) Pinètre, C.; Gendron, F.; Kuroda, R.; Oketani, R.; Aupetit, C.; Buffeteau, T.; Coquerel, G. Use of Conglomerate Mixed Crystals to Deracemize a Stable Racemic-Compound-Forming System. *Chemistry A European J* **2023**, e202300441. https://doi.org/10.1002/chem.202300441.

(60) Suwannasang, K.; Flood, A. E.; Rougeot, C.; Coquerel, G. Using Programmed Heating–Cooling Cycles with Racemization in Solution for Complete Symmetry Breaking of a Conglomerate Forming System. *Crystal Growth & Design* **2013**, *13* (8), 3498–3504. https://doi.org/10.1021/cg400436r.

(61) Rougeot, C.; Guillen, F.; Plaquevent, J.-C.; Coquerel, G. Ultrasound-Enhanced Deracemization: Toward the Existence of Agonist Effects in the Interpretation of Spontaneous Symmetry Breaking. *Crystal Growth & Design* **2015**, *15* (5), 2151–2155. https://doi.org/10.1021/cg501765g.

(62) Maeda, J.; Cardinael, P.; Flood, A.; Coquerel, G. Improved Experimental Yield of Temperature-Cycle-Induced Deracemization (TCID) with Cooling and Crystal Washing: Application of TCID for the Industrial Scale. *Crystals* **2024**, *14* (7), 588. https://doi.org/10.3390/cryst14070588.

(63) Lopes, C.; Cartigny, Y.; Brandel, C.; Dupray, V.; Body, C.; Shemchuk, O.; Leyssens, T. A Greener Pathway to Enantiopurity: Mechanochemical Deracemization through Abrasive Grinding. *Chemistry – A European Journal* **2023**, *29* (35), e202300585. https://doi.org/10.1002/chem.202300585.

(64) Suwannasang, K.; Flood, A. E.; Rougeot, C.; Coquerel, G. Use of Programmed Damped Temperature Cycles for the Deracemization of a Racemic Suspension of a Conglomerate Forming System. *Org. Process Res. Dev.* **2017**, *21* (4), 623–630. https://doi.org/10.1021/acs.oprd.7b00028.

(65) Bodák, B.; Breveglieri, F.; Mazzotti, M. Crystallization-Induced Deracemization: Experiments and Modeling. *Crystal Growth & Design* **2022**, *22* (2), 1427–1436. https://doi.org/10.1021/acs.cgd.1c01374.

(66) Bodák, B.; Breveglieri, F.; Mazzotti, M. On the Model-Based Design and Comparison of Crystallization-Based Deracemization Techniques. *Chemical Engineering Science* **2022**, *254*, 117595. https://doi.org/10.1016/j.ces.2022.117595.

(67) Bodák, B.; Maggioni, G. M.; Mazzotti, M. Population-Based Mathematical Model of Solid-State Deracemization via Temperature Cycles. *Crystal Growth & Design* **2018**, *18* (11), 7122–7131. https://doi.org/10.1021/acs.cgd.8b01292.

(68) Iggland, M.; Mazzotti, M. A Population Balance Model for Chiral Resolution via Viedma Ripening. *Crystal Growth & Design* **2011**, *11* (10), 4611–4622. https://doi.org/10.1021/cg2008599.

(69) Bodák, B.; Maggioni, G. M.; Mazzotti, M. Effect of Initial Conditions on Solid-State Deracemization via Temperature Cycles: A Model-Based Study. *Crystal Growth & Design* **2019**, *19* (11), 6552–6559. https://doi.org/10.1021/acs.cgd.9b00988.

(70) Hosseinalipour, M. S.; Deck, L.-T.; Mazzotti, M. On Solute Recovery and Productivity in Chiral Resolution through Solid-State Deracemization by Temperature Cycling. *Crystal Growth & Design* **2024**, *24* (9), 3925–3932. https://doi.org/10.1021/acs.cgd.4c00233.

CHAPTER III

ENANTIOPURITY BY DIRECTED EVOLUTIONARY DESIGN: THE CASE OF PRAZIQUANTEL

III.1 - Introduction

2-(cyclohexanecarbonyl)-1,2,3,6,7,11b-hexahydro-4H-pyrazino[2,1-a]isoquinolin-4-one is a chiral anthelminthic drug, commonly known as Praziquantel (Figure III - 1), use to treat parasitic flat worms infection schistosomiasis.[1–3] Although it is listed in the WHO Model List of Essential Drugs,[4] its poor water solubility and resulting low bioavailability necessitate a high dosage to achieve the desired therapeutic effect.[5–8] Moreover, Praziquantel is commercialized and administrated as a racemate whereas the pharmacological activity is exclusively attributed to the (*R*) enantiomer.[9–11] Even though the (S) enantiomer is generally safe and well tolerated by human metabolism, it can still cause side effects such as nausea or abdominal pain for instance. Therefore, this has sparked significant interest in isolating the bioactive (*R*) enantiomer, which could potentially allow for dose reduction or side effects lowering.[12,13] Unfortunately, Praziquantel crystallizes as a racemic compound, hence hindering the vast majority of crystallization-enhanced chiral resolution or deracemization methods.[14]

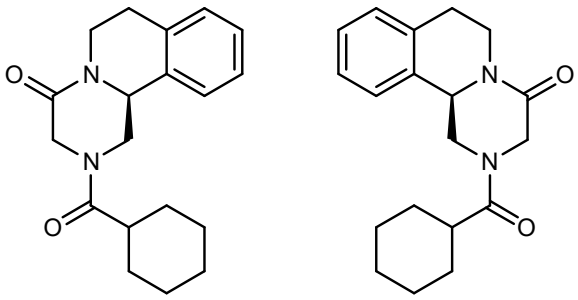

Figure III - 1. Chemical structures of (S)-Praziquantel (left) and (R)-Praziquantel (right)

However, many successful chiral resolution procedures were reported since the last decades, for instance the diastereomeric salt resolution by forming either diastereomeric pairs between Praziquantel and Malic Acid (Figure III - 2A) or between a Praziquantel precursor (*i.e.* Praziquanamine) with a Tartaric Acid derivative (L-DBTA hereafter) (Figure III - 2B).[15,16] More recently, Valenti *et al.* reported the efficient chiral resolution of Praziquantel through a chemical derivative crystallizing as a conglomerate by the temperature induced variation of Viedma ripening coupled with an *ex-situ* racemization via reversible hydrogenation over Pd/C packed column. This illustrates that reversible chemical modifications of the target compound can induce the formation of a conglomerate with possible route toward enantiomeric

resolution (Figure III - 2C).[17] Although promising, spotting conglomerate by this derivatization approach requires the reversible synthesis of numerous derivatives which are randomly selected since the occurrence of a stable conglomerate remains unpredictable.[18–21]

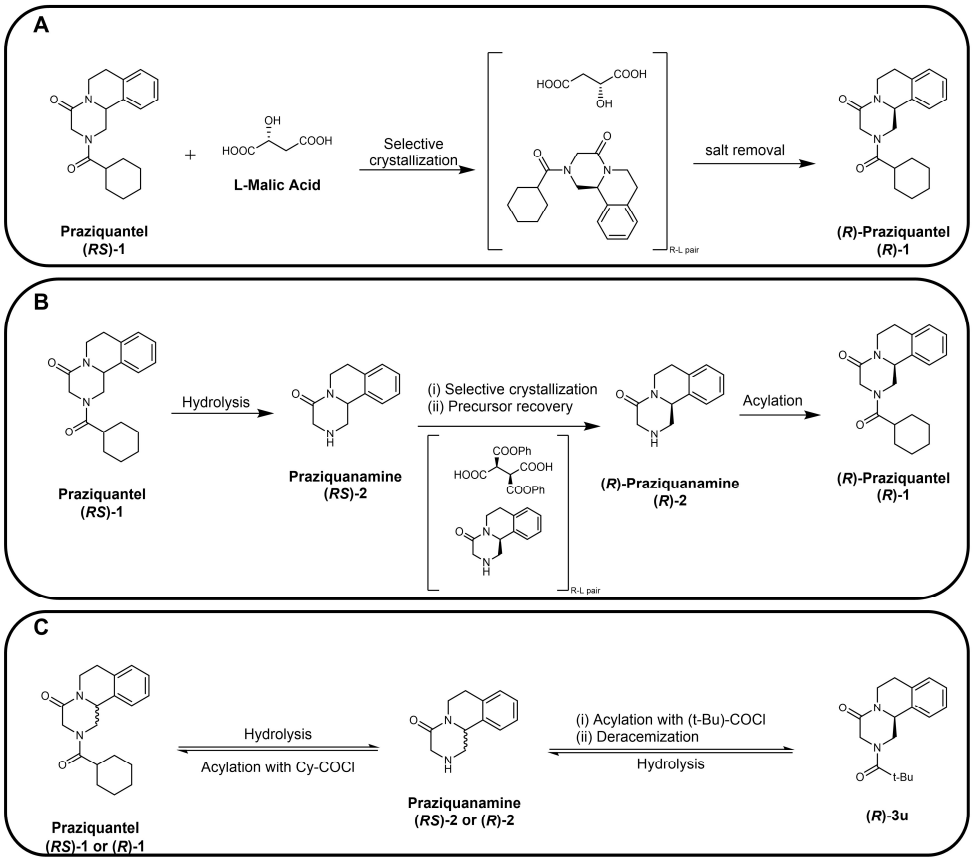

Figure III - 2. Reported resolution routes of Praziquantel via its diastereomeric salt resolution (a) with L-malic acid or (b) through its precursor with L-dibenzoyl-tartaric acid and (c) reversible synthesis of conglomerate derivatives subsequently deracemized.

Moreover, no systematic approach has been developed so far to overcome this random experimental design, leading to low outcomes. Indeed, up to now, identifying conglomerates within libraries lacks theoretical guidance and is therefore based on trial and error with a binary outcome that has unfavourable odds: either a library entry forms a stable racemic compound or a stable conglomerate with only a 5-10% chance of finding the coveted conglomerate (5-10%).[22–24] This challenge will be addressed in this chapter under collaborative effort with the Symeres company (M. Leeman and R.M. Kellogg), AMOF (S.W. van Dongen and W.L. Noorduin) and Radboud University (P.T. Tinnemans).

III.2 - Praziquantel derivative library

III.2.1 - Presentation of the praziquantel derivatives

The possibility to access conglomerate-forming systems through the reversible synthesis of chemically related derivatives has already been demonstrated in the literature.[25–28] In this route, a library of crystalline derivatives of Praziquantel was first introduced by Valenti *et al.* in 2020 by substituting the 6 membered cyclohexyl ring of the amide function by several substituents (Figure III - 3, **3a-3ad)**. In this library, only the pivaloyl derivative was characterized as a stable conglomerate-forming system, leading to a devaluated conglomerate frequency (< 4%) compared to what is commonly expected (5-10%).

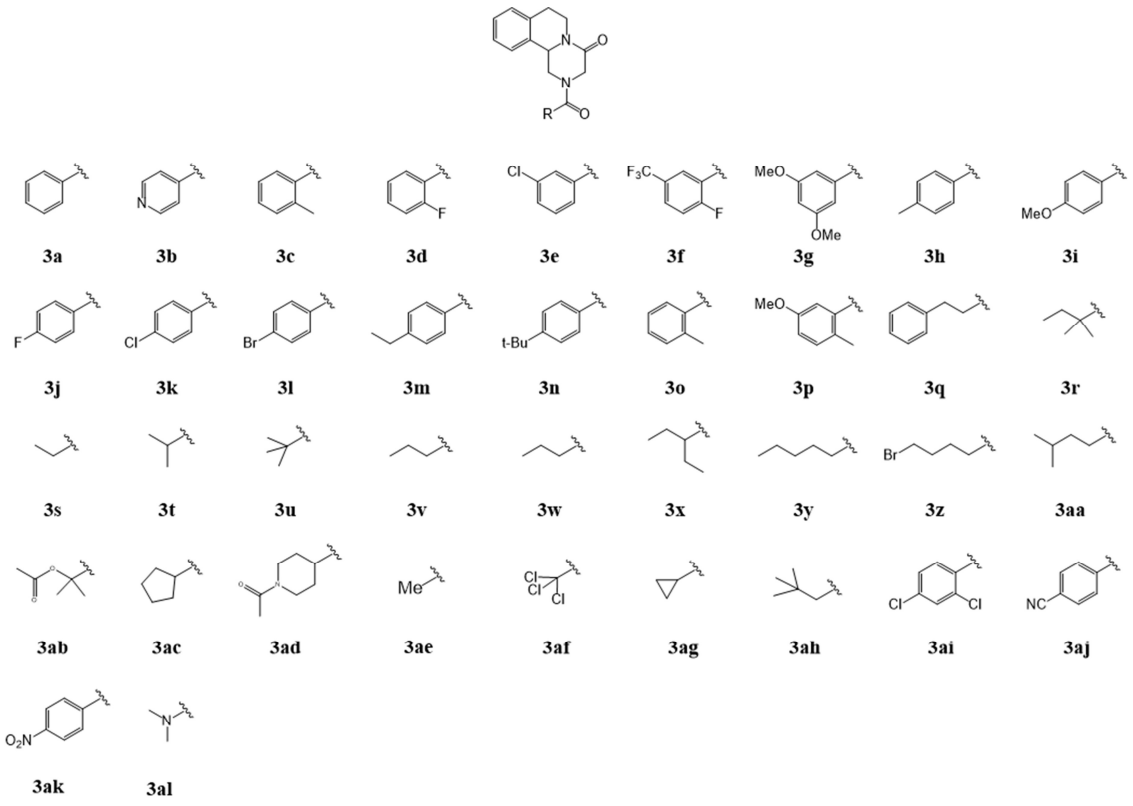

Figure III - 3. Library of the synthesized derivatives of Praziquantel. Compounds 3a-ad were synthesized through a collaboration with Symeres.

Akin Valenti's synthesis procedure (Figure III - 4), numerous enantiopure and racemic Praziquantel chemical derivatives were synthesized with the aims of identifying new scientific guidelines for conglomerate formation and bringing theoretical guidance toward chiral resolution through the study of chemically related derivatives.

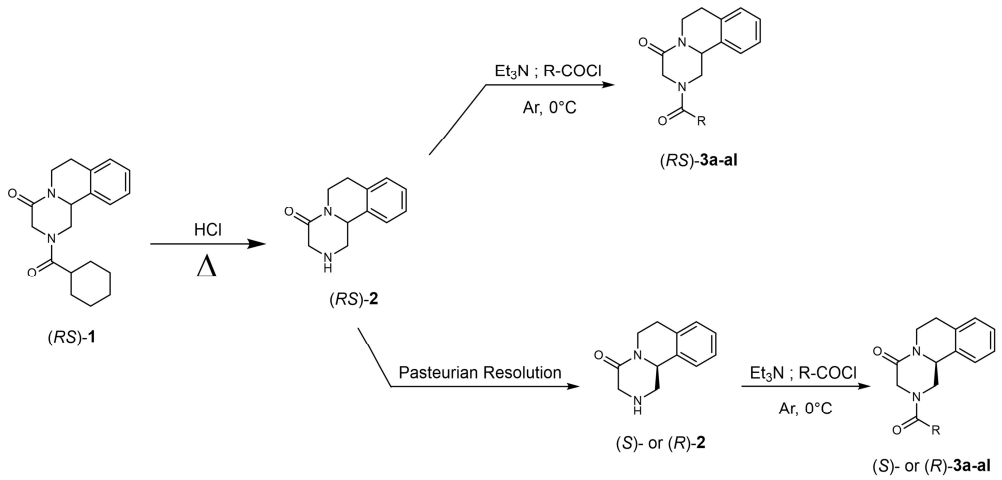

Figure III - 4. Derivatization route of praziquantel for generating a library of compound 3.

In addition to the 30 derivatives already introduced, 8 other derivatives are synthesized in this study, increasing the number of studied systems up to 38 chemically related derivatives (Figure III - 3, **3ae-3al).** Among these derivatives, three of them did not crystallize neither at the racemic nor at the enantiopure compositions despite several attempts (Figure III - 3, **3g-p-q**). For some systems, only the characterization of the racemic mixture could be performed as their corresponding pure enantiomer did not crystallize (Figure III - 3, **3v-3ab**, **3ad-ah-al**).

III.2.2 - Optimization and rationalization of the chiral resolution of (*RS)*-2

Supporting our Praziquantel derivatization strategy necessitates a substantial amount of (*RS*)-**2** (*i.e.* Praziquanamine) but also (*R*)-**2** or (*S*)-**2**, we focused on optimizing the Pasteurian resolution of (*RS*)-**2** that Woelfle *et al.* recently reported using L-DBTA as chiral resolving agent.[16,29] This method involves the crystallization of an equimolar mixture of (*RS*)-**2** and L-DBTA in an isopropanol / water (IPA/H_2O Hereafter) solvent mixture (80/20 ; v/v) but requires an additional recrystallization step to reach enantiopurity**,** leading to the recovery of 66% of the targeted enantiomer. However, such high yield was never reached during this study. This part will focus therefore on achieving enantiopurity of **2** in a single crystallization step, enabling a time-efficient cyclic resolution process of (*R*)-**2** or (*S*)-**2** by performing symmetrical Pasteurian resolution on the recovered enantioenriched material from the mother liquor.

In such system, one must consider the number of independent components involved in this resolution process (c = 5) that lead to a possible 6-phase equilibria under isobaric condition

(*cf.* I.3.2.1), underlining the complexity of this resolution. Accurate knowledge of the corresponding heterogenous equilibria under operative conditions was lacking.

Prior to any optimization of this chiral resolution process, it was essential to assess the solid-state nature of the recovered enantiopure salt. Hence, enantiopure salt is recovered by performing small scale Pasteurian resolution following the reported procedure and subsequent TGA-DSC measurements is conducted (Figure III - 5A).

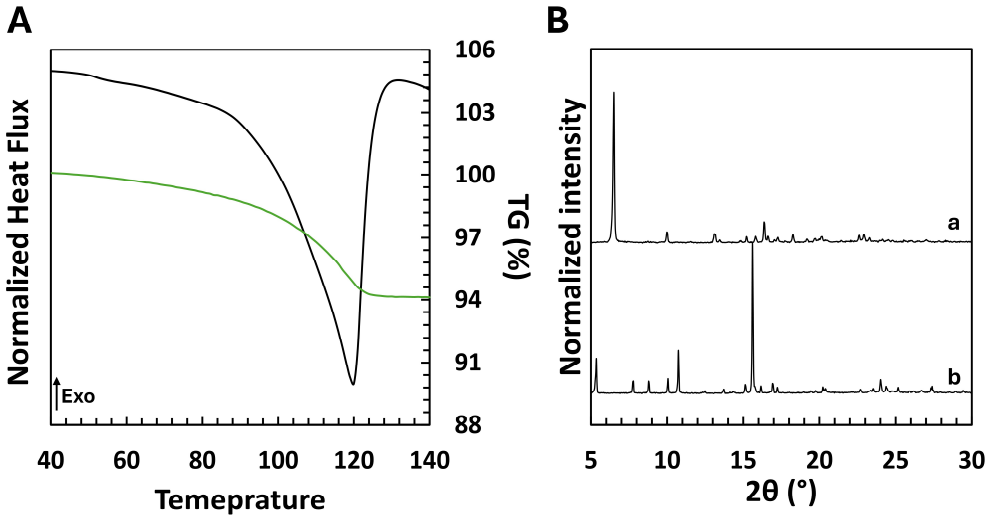

Figure III - 5. (A) TGA-DSC of the recovered enantiopure diastereomeric salt [(R)-2:L-DBTA].2H_2O. TGA and DSC curves are depicted in green and black respectively. (B) X-ray powder diffraction patterns of (a) [(S)-2:L-DBTA] (b) [(R)-2:L-DBTA].

This reveals a single endothermic event at ca. 100 °C associated with a mass loss of 6.06% resulting from water removal (green curve in Figure III - 5, confirmed by mass spectrometry, data not shown), which is coherent with a dihydrated salt: [(*R*)-**2**: L-DBTA].2H_2O. No other thermal phenomenon is observed after the dehydration, denoting a destructive dehydration mechanism (confirmed by HSM).[30] According to the poor thermal stability of (*R*)-**2** above its melting point, which has been reported elsewhere and confirmed by our own DSC measurement of (*R*)-**2** (T_m = 122.1°C),[31] this destructive dehydration mechanism precludes the crystallization of any anhydrous salt. However, since the operational conditions do not exceed these high temperatures, [(*R*)-**2**: L-DBTA].2H_2O can be used as a solid-form reference whose XRPD pattern is displayed in Figure III - 5B. It should be noted that the enantiopurity of the salt is confirmed by HPLC via small scale isolation of (*R*)-**2** before any measurements. Furthermore, pure (*S*)-**2** is obtained by performing a symmetrical Pasteurian resolution process (*i.e.*

involving D-DBTA instead of L-DBTA) and subsequently crystallized with L-DBTA. The resulting counter salt could be only crystallized as its anhydrous form [(*S*)-**2**:*L*-DBTA] whose XRPD pattern is display in Figure III - 5A.

Thereupon, the crystallization pathway under operative conditions is assessed using the InSituX prototype,[32] allowing *in-situ* X-ray diffraction analysis (*cf.* Appendix A - I.2.5), for which compiled *in-situ* XRPD patterns are displayed in Figure III - 6A. A first solid phase is observed from 60 °C to 40°C, labelled φ_1 (Black patterns in Figure III - 6A). Unfortunately, the poor quality of these patterns, denoting a low suspension density, preclude the identification of this solid phase although new diffraction peaks, for instance at *ca.* 30° (2θ), are definitely observed. φ_1 does not correspond to our solid-form reference [(*R*)-**2**:*L*-DBTA].2H_2O and could therefore be either a single or a mixture of uncharacterized phases. Below 30 °C, a second solid phase is observed and labelled φ_2 (red curves in Figure III - 6A). Alike φ_1, this new phase does not match the XRPD pattern of our reference [(*R*)-**2**:*L*-DBTA].2H_2O.

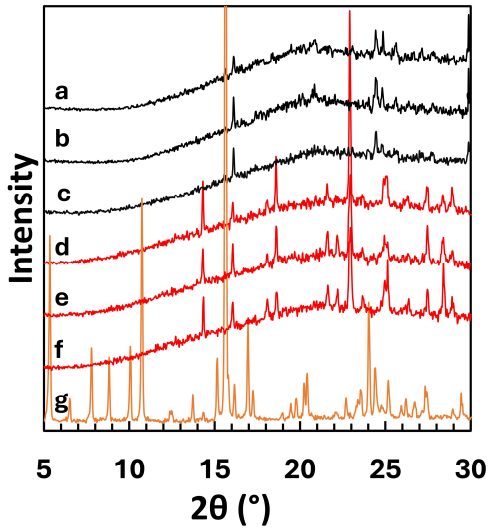

Figure III - 6. In-Situ X-ray powder diffraction patterns of a mixture between (RS)-2 and L-DBTA under reported Pasteurian resolution conditions upon cooling and holding for 10 h at (a) 60 °C (b) 50 °C (c) 40 °C (d) 30 °C (e) 20 °C (f) 10 °C and (g) after filtration.

Interestingly, another XRPD pattern is obtained after filtration of either φ_1 or φ_2 (Orange curve in Figure III - 6A), most likely indicating cases of efflorescent solvates (heterosolvate, solvated double salt, IPA solvate or hydrate with different stoichiometries etc.). This filtrated solid form strongly matches the XRPD patterns of the enantiopure dihydrated salt [(*R*)-**2**:*L*-

DBTA].2H_2O although additional peak corresponding to the anhydrous counter salt [(*S*)-**2**:*L*-DBTA] are detected (Figure III - 7). This indicates that φ_1 or φ_2 are efflorescent solvated solid phases composed of the two handedness and should therefore be avoided during the chiral resolution process. Furthermore, small scale isolation of **2** highlighted an enantiomeric purity of 79 %*e.e.* only.

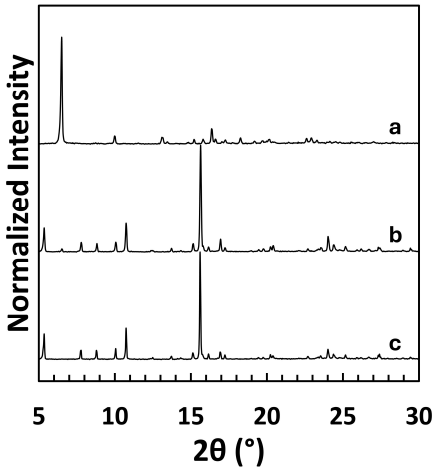

Figure III - 7. X-ray powder diffraction patterns of (a) [(S)-2:L-DBTA] (b) φ_1 or φ_2 after filtration and (c) [(R)-2:L-DBTA].2H_2O.

Similar investigations using enantiopure (*R*)-**2** rather than racemic **2** evidence the perfect matching between the XRPD patterns of the crystallizing phase with the one of [(*R*)-**2**:*L*-DBTA].2H_2O (Figure III - 8). More importantly, it is likely indicating a case of an efflorescent double salt solvate as φ_2 does not exist at the enantiopure composition.

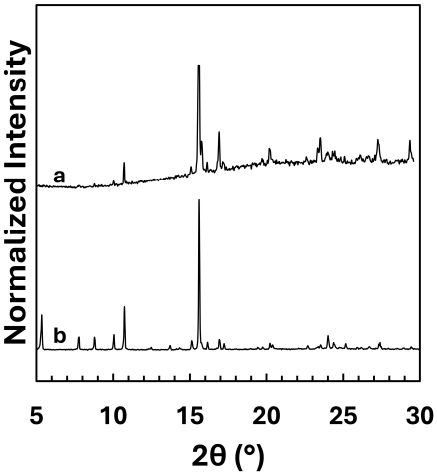

Figure III - 8. X-ray powder diffraction patterns of (a) a mixture between (R)-2 and L-DBTA under reported Pasteurian resolution conditions and (b) [(R)-2:L-DBTA].2H_2O.

Achieving enantiopurity in a single step requires therefore favouring [(*R*)-**2**:*L*-DBTA].2H_2O over either φ_1 or φ_2. While the crystallization of φ_1 is easily avoided by maintaining the crystallization temperature below 30°C, the uncertain solid-state nature of φ_2 presents different potential optimisation route. Assuming φ_2 to be an efflorescent double salt solvate, two optimization routes to access pure [(*R*)-**2**:L-DBTA].2H_2O from racemic **2** are explored:

- Pasteurian resolution with a reduced suspension density compared to the reported procedure: this may enable the access of pure [(*R*)-**2**:L-DBTA].2H_2O in case of an non-congruent solubility of φ_2
- Pasteurian resolution using higher proportions of H_2O than in the reported procedure: this may enable the access of pure [(*R*)-**2**: L-DBTA].2H_2O assuming φ_2 as an efflorescent double salt solvate of IPA

Figure III - 9 displays various *in* situ XRPD patterns following the first optimization route, however, these efforts were unsuccessful and yielded exclusively to the formation of φ_2, mostly indicating a congruent solubility for φ_2 in these conditions. Consequently, we explored the second optimization route whose results of these experiments are summarized in Table III - 1.

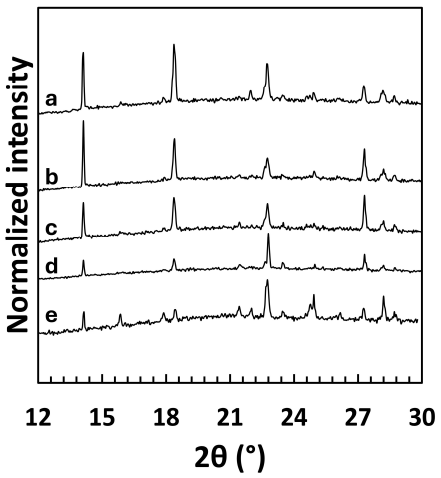

Figure III - 9. In-Situ X-ray powder diffraction patterns of a mixture between (RS)-2 and L-DBTA in an 80/20 v/v IPA / H_2O solvent mixtures at (a) 5.69 wt% (b) 4.6 wt% (c) 3.33 wt% (d) 2.93 wt%. (e) In-Situ X-ray powder diffraction patterns of φ_2.

Table III - 1. Yield comparison between the different operative conditions tested for the Pasteurian resolution of (RS)-2

Entry	IPA / H_2O ratio (v/v)	Crystallization temperature (°C)	Yield[(a)] (%)	Enantiomeric excess[(b)] (%*e.e.*)	Reference
1	4:1	20	78	79	[16]
3	1:1	20	44	96	This work
4	0:1	20	42	<10	This work

[(a)] Based on the maximum amount of pure enantiomer (*i.e.* 50% of the initial mass of (*RS*)-**2**).

[(b)] Determined by polarimetry:[16] $[\alpha]_D^{20°C} = \pm 306°$

It clearly shows that enantiopurity is improved within a single step by increasing the ratio of H_2O (entry 3 in Table III - 1). However, the use of an excess of H_2O in the solvent mixture led to a drastic drop in enantiopurity, reflecting the necessity of a compromise between enantiopurity and productivity, which is provided by conditions in entry 3. A potential explanation of this behaviour is schematically depicted in Figure III - 10 (considering φ_2 as an efflorescent double salt solvate):

- The presence of φ_2, which exhibits a congruent solubility in a 80/20 *v/v* IPA/H_2O solvent mixture, eliminates any possibility of forming an enantiopure solid starting from racemic **2**.
- Adding an excess of H_2O results in the enlargement of the crystallization domain of <[(*R*)-**2**: L-DBTA].2H_2O> at the expense of φ_2. The ternary isopleth at 50/50 *v/v* IPA/H_2O solvent mixture illustrates a theoretical scenario in which φ_2 no longer exists under these conditions, facilitating the representation.
- In contrast, the exclusive use of H_2O as solvent result in a significant decrease in solubility, thereby reducing the working window of this resolution process and explaining the experimental drop in enantiopurity using this condition. Although enantiopure <[(*R*)-**2**: L-DBTA].2H_2O> should theoretically be accessible from racemic **2**, this approach would be less efficient.

These results highlight the importance of *in situ* characterization of such processes to better understand the crystallization pathway for subsequent optimization.

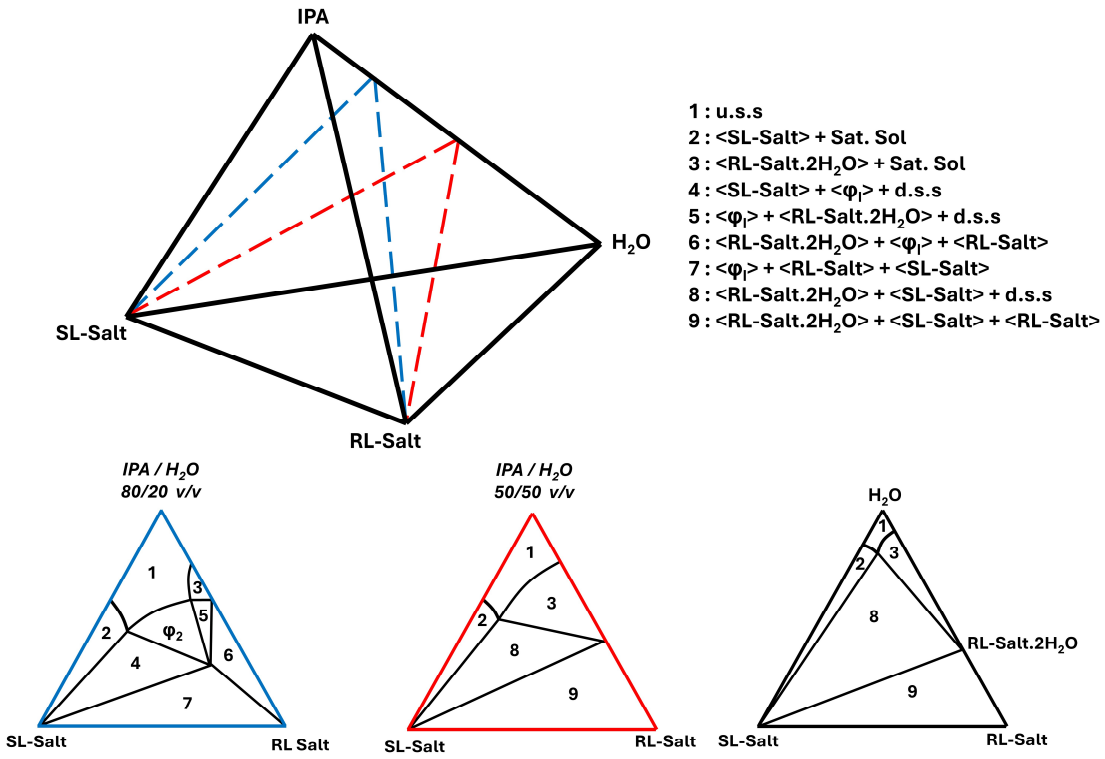

Figure III - 10. Schematic ternary isoplethal section under operative conditions.

Almost enantiopure material is obtained in a single step with a global yield of 44% using operative condition in entry 3. Although the recovery could be further improved, this single step operational condition already facilitates the potential of a cyclic resolution process of (*R*)-**2** or (*S*)-**2**. By performing symmetrical Pasteurian resolution on the recovered enantioenriched material from the mother liquor, we can significantly enhance productivity. Indeed, this approach enables us to recover nearly 90% of enantiopure (*R*)-**2** or (*S*)-**2** from the initial racemic mixture of **2**, thereby supporting our derivatizing strategy all along this research.

III.2.3 - Crystallization behaviour of the Praziquantel derivatives

After synthesis of the different derivatives depicted in Figure III - 3 (as racemic mixtures and pure enantiomers), it is important to first determine the crystallization behaviour of all the systems (*i.e.* solid-state landscape and racemate classification). Hence, a systematic workflow is applied to all synthesized couples (Figure III - 11), which involves SHG, XRPD and DSC measurements, as well as crystal structure resolution and *d.s.p.c* determination (*cf.* I.3.3.1).

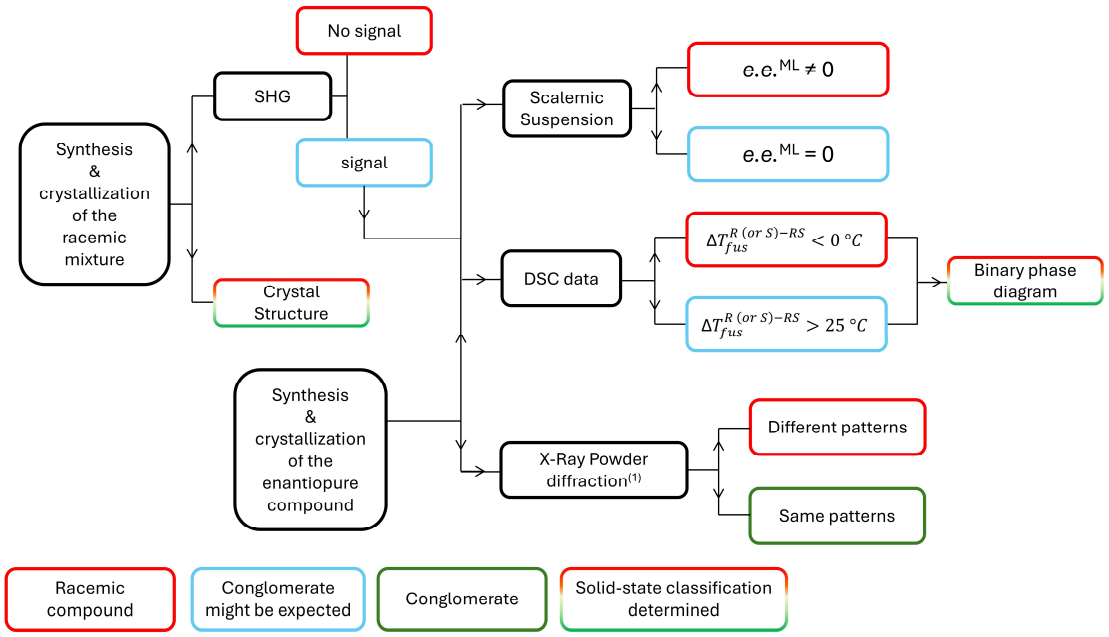

Figure III - 11. Conglomerate screening workflow. (1) Crystallization conditions must be identical.

A SHG analysis is performed on all the synthesized racemate derivatives and compared with the previously reported data (Table III - 2). The number of potential conglomerates extracted from these analyses, *i.e.* SHG positive racemate, is of 10 derivatives. One can note that some SHG intensities differ from those reported by Valenti *et al.*[17] (*e.g.* **3j**, **3k**, **3l**, **3n**). However, the SHG analysis is highly sensitive to PSD and impurities even at the ppm scale. The consequence is that SHG intensity < 10 %quartz cannot be considered as positive signal. Thus, the results align with the reported SHG intensity.

Regarding the newly synthesized derivatives (*i.e.* **3ae-3al**), only derivative **3ae** exhibits an SHG signal, *i.e.* potential conglomerate. The chemical similarities between the reported conglomerate **3u** and the derivative **3ae** should be underlined (Figure III - 3).

Table III - 2. SHG intensity recorded for SHG positive derivative and comparison with already previously reported data.

ID	3h	3j	3k	3l	3n	3r	3t	3u	3ac	3ae
From ref [17]	S	S	S	W	W	W	N	S	N	n/a
SHG intensities (%quartz)	590	11	33	221	3	29	6	157	10	173

Nomenclature used by Valenti *et al.*[17]: N = no SHG signal ; W = "weak" SHG signal ; S = "strong" SHG signal

The solid-state classification of the SHG positive derivatives is then clarified through the partial determination of a ternary phase diagram between the two enantiomers and a solvent. From a thermodynamic point of view, a scalemic suspension of a conglomerate-forming system must be in thermodynamic equilibrium with its racemic saturated solution due to its symmetrical solubility behaviour. By contrast, the mother liquor of a scalemic suspension of a racemic compound-forming system cannot be racemic under any circumstances. Therefore, the determination of the doubly saturated point composition (*d.s.p.c*) can be used to identify the solid-state classification of the studied system, provided that enantiopure or at least scalemic material is available (*cf.* I.3.2.4).

A scalemic mixture of each derivative (ca. 20 %ee) is suspended in Toluene for 9 days to reach thermodynamic equilibrium. The composition of both the mother liquor and the suspended solid is analyzed by chiral HPLC and the results regarding the SHG positive derivative are summarized in Table III - 3. The vast majority of the studied systems have a scalemic mother liquor (*i.e.* racemic compound). Nevertheless, 3 SHG positive systems belonging to the class of alkyl-substituted derivatives resulted in a mother liquor close to the racemic composition (**3r**-**u**-**ae**). Further examination of the suspended solid excluded **3r** from the list of potential conglomerates as it also exhibits a racemic suspended solid, which does not align with the requirements for a conglomerate-forming system.

Table III - 3. Enantiomeric composition of the solid and mother liquor measured by cHPLC after equilibrating the suspensions in toluene for 9h.

ID		3h	3j	3k	3l	3r	3u	3ae
% *e.e.*	**Solid**	8.0	5.7	22.4	19.6	0.3	57.9	40.5
	Mother liquor	54.4	65.4	19.7	16.6	6.0	0.8	12.5

Although certain systems are promising, different XRPD patterns between enantiopure and their associate racemate solid forms are detected for all the studied systems, confirming their racemic-compound classification. More importantly, this statement also applies to the derivative **3u**, which was used as model compound in part II.2 and previously reported as a conglomerate-forming system and successfully deracemized.[17] In addition to these meaningful outcomes, four interesting cases are noteworthy (i) **3ag** (ii) **3ae** (iii) **3u** (iv) **3t**.

III.2.4 - Case study of derivative 3ag

Derivative **3ag**, for which the six-membered cyclohexyl ring of praziquantel has been substituted by a three-membered ring, exhibits an unusual solid-state behaviour for which the identification of the solid-state nature of each solid form and their thermochemical properties will be used further in the manuscript. The content of this section has been published in *Organic Process Research & Design*.[33]

III.2.4.1 - Crystallization of racemic and enantiopure 3ag

After synthesis and purification, samples of racemic and enantiopure **3ag** are separately analyzed by XRPD, revealing the pattern shown in Figure III - 12a and b and confirming the crystallinity of the materials. While a single solid phase melting at T_m = 149.1 °C for (*R*)-**3ag** is detected, indicating the presence of a single enantiopure solid form, the DSC analyses of the racemic sample reproducibly gave the thermogram shown in Figure III - 12e: upon heating at 2 K.min^{-1}, a first endothermic phenomenon is observed at T_m = 126.4 °C rapidly followed by an exothermic peak at T_{peak} = 133.2 °C. A second endothermic event occurs at T_m = 144.5 °C, once again followed by an exothermic event at T_{peak} = 147.0 °C. Then, a third endothermic event is detected at a peak temperature T_{peak} =149.4 °C (no onset temperature could be reliably measured for this event). No thermal event is detected upon cooling the melt whereas a subsequent re-heating of the SCM at 2 K.min^{-1} results in an exothermic event at *ca.* 50 °C, associated to crystallization (Figure III - 12f). This is followed by a slightly visible wide exothermic phenomenon from 70 °C to 90 °C and two endothermic events (at T_m = 143.9 °C and T_m = 144.5 °C). TGA-DSC measurements show that no detectable mass loss occurs upon heating (result not shown) which reveal that none of the thermal events can be associate to desolvation. The thermogram in Figure III - 12e can therefore be interpreted as a succession of melting of a less stable polymorph and crystallization of a higher melting polymorph.

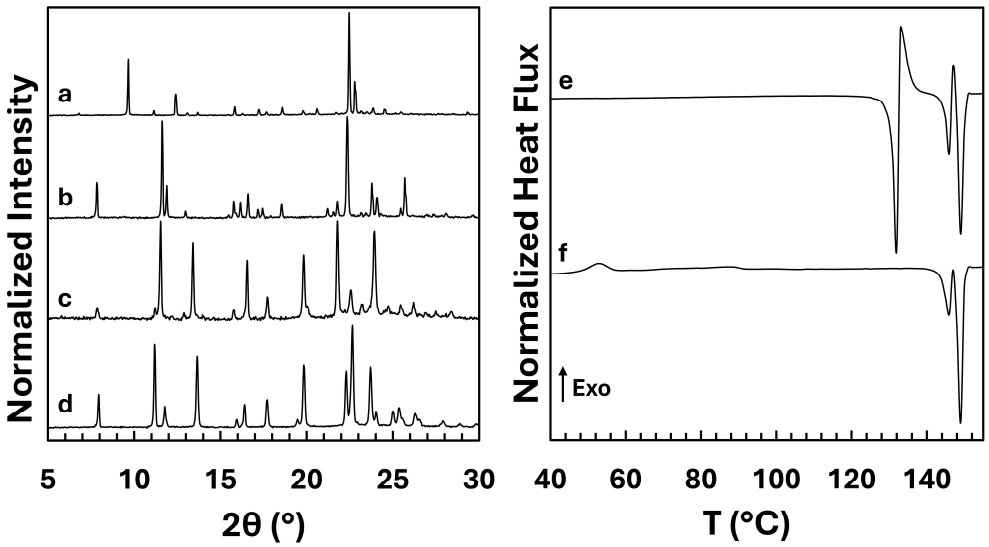

Figure III - 12. XRPD patterns of (a) (R)-3ag, (b) (RS-I)-3ag and (c) (RS-II)-3ag. (d) (RS-III)-3ag. Typical DSC thermogram obtained by heating at 2 K.min^{-1} from 40 to 155 °C: (e) (RS-III)-3ag and (f) the SCM.

These interpretations are confirmed by hot stage microscopy experiments which highlight that a sample of initial crystals (Figure III - 13a) undergoes a melting and crystallization event at *ca.* 126°C (Figure III - 13b), which is followed by a second melting-crystallization event at ca. 146°C (Figure III - 13c)

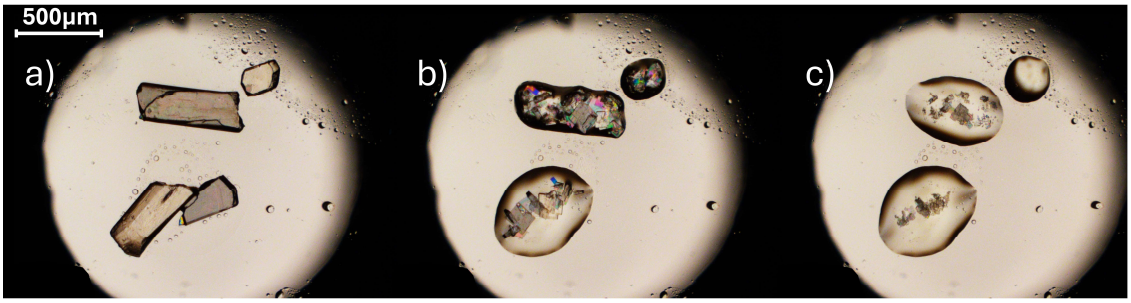

Figure III - 13. Selected pictures of Hot-stage Microscopy observation performed on (RS-I)-3ag single crystals heated at 1 K.min^{-1} from 25 to 150 °C (a) 125°C (b) 140°C (c) 146°C.

To confirm the existence of new polymorphs at higher temperature, **3ag** is annealed at 135°C and 147°C for 15 minutes prior to XRPD analyses at room temperature. The detection of new XRPD patterns (Figure III - 12c and d) confirms that (*RS*)-**3ag** can exist as three polymorphic forms, hereafter labelled (*RS-I*)-**3ag** (low temperature form), (*RS-II*)-**3ag** (mid-temperature form) and (*RS-III*)-**3ag** (high temperature form). The solid-solid phase transitions are sufficiently slow at room temperature so that it is possible to store and manipulate the crystal

without crystallographic transformation. In fact, no solid-solid phase conversion was observed after more than a year.

By contrast, cross seeding experiments performed in ethanol and acetone at 20°C systematically results in solvent mediated polymorphic transitions of (*RS-II*)-**3ag** and (*RS-III*)-**3ag** into (*RS-I*)-**3ag**, thus confirming that (*RS-I*)-**3ag** is the thermodynamically stable polymorph at room temperature. The stability relationships between the three phases at higher temperature could not be unambiguously determined from DSC data since the lower temperature phases melt prior to recrystallization of the higher temperature phases (*i.e.* the heat of fusion rule cannot be applied).[34]

III.2.4.2 - Construction of the binary phase diagram of 3ag

To further elucidate the stability relationships between the different phases of **3ag**, the binary phase diagram between (*S*)- and (*R*)-**3ag** enantiomers is constructed using DSC measurements. Thus, (*R*)-**3ag** is mixed separately with the different polymorphic forms of (*RS*)-**3ag** and ground with a mortar and pestle to afford the different compositions listed in Table III - 4, described in molar fraction of (*S*)-**3ag** ($X_{(S)}$). The mixtures are analyzed in DSC by heating from 25 to 160 °C at 2 K.min^{-1} (Figure III - 14).

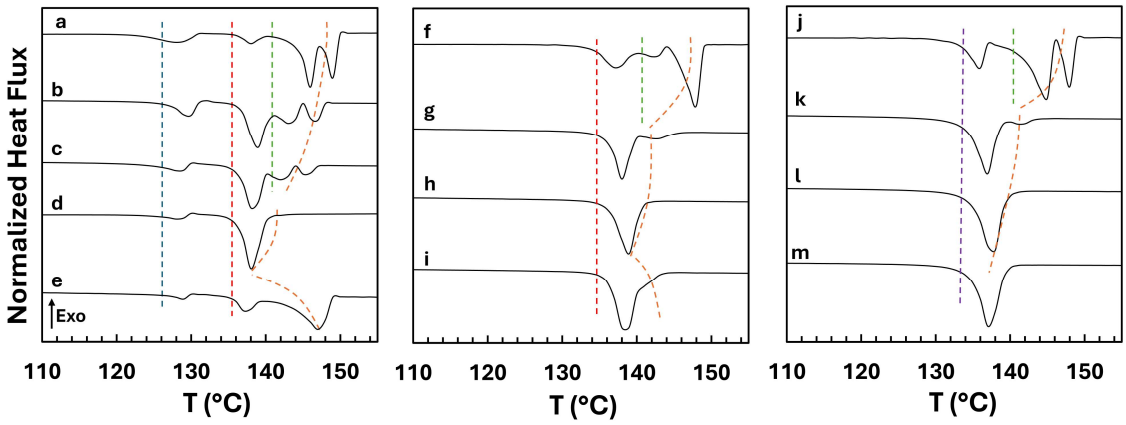

Figure III - 14. DSC thermograms measured at 2 K.min^{-1} for the different mixtures involving (RS-I)-3ag at $X_{(S)}$ = (a) 0.45 (b) 0.35 (c) 0.33 (d) 0.25 (e) 0.05, (RS-II)-3ag at $X_{(S)}$ = (f) 0.40 (g) 0.28 (h) 0.20 (i) 0.15 and (RS-III)-3ag at $X_{(S)}$ = (j) 0.40, (k) 0.28, (l) 0.24, (m) 0.22. Dotted lines are guide for the eyes (Blue, Red, Green, violet: invariant temperatures; Orange: liquidus temperature).

A liquidus and four invariant phenomena are observed :

- The lower temperature invariant at *ca.* 124 °C (Figure III - 14, blue dotted line) only occurs for mixtures involving (*RS-I*)-**3ag** and is compensated by an exotherm.
- The second invariant at *ca.* 133 °C (Figure III - 14, purple dotted line) only occurs for mixtures involving (*RS-III*)-**3ag**.
- By contrast, the third invariant at *ca.* 136 °C (Figure III - 14, red dotted lines) is observed for mixtures involving (*RS-I*)-**3ag** and (*RS-II*)-**3ag.**
- The last invariant at *ca.* 142 °C (Figure III - 14, green dotted lines) occurs whatever the initial polymorph used. However, this invariant is observed for a limited composition range $X_{(s)} > 0.3$.
- Finally, another endothermic signal whose temperature varies between the melting point of pure (*R)*-**3ag** and (*RS-III*)-**3ag** is detected, corresponding to liquidus temperatures (Figure III - 14, orange dotted lines). The discontinuity of this liquidus curve should be underlined.

It can therefore be concluded that:

(i) The event at *ca.* 124 °C results from an equilibrium involving the disappearance of the (*RS-I*)-**3ag** phase upon heating. Considering that the polymorphic transition (*RS-I*)→ (*RS-II*) occurs through a melting and crystallization process rather than solid-solid phase transition (Figure III - 13), the invariant at 124°C must therefore be associated to the metastable eutectic invariant occurring between (*RS-I*)-**3ag** and (*R*)-**3ag**, which is further supported by temperature resolved X-ray diffraction experiment shown in Figure III - 15.

(ii) The invariant at 133°C corresponds to the eutectic invariant between (*RS-III*)-**3ag** and (*R*)-**3ag**. This invariant occurs 3°C below the eutectic invariant involving (*RS-II*)-**3ag**, confirming its metastability at this temperature

(iii) The invariant at 136°C corresponds to the eutectic invariant between (*RS-II*)-**3ag** and (*R*)-**3ag**, with a eutectic point composition estimated at *ca.* $X_{(S)} = 0.2$.

(iv) The invariant at 142 °C is attributed to the polymorphic transition invariant (*RS-II*)-**3ag** →(*RS-III*)-**3ag**, considering the concordance of this invariant and the slope change of

the liquidus. More importantly, it demonstrates the enantiotropic relationship between these two polymorphs.

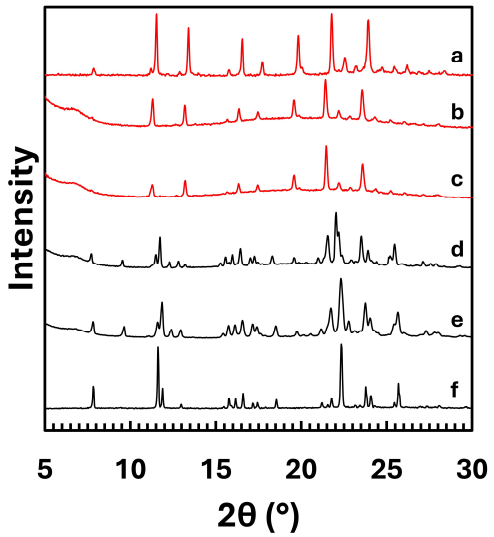

Figure III - 15. TR-XRPD of a (R)-3ag / (RS-I)-3ag mixture at $X_{(S)}$ = 0.4 at (b) 24 °C (c) 118 °C (d) 123 °C (e) 133 °C. XRPD patterns (a) and (f) correspond to the simulated diffractograms of (RS-I)-3ag (black) and (RS-I)-3ag (red) respectively.

All temperature data are gathered in Table III - 4. The accuracy of these data allows us to estimate the melting enthalpy of (*RS-I*)-**3ag** ($\Delta H_m = 20.7\ \mathrm{kJ.mol^{-1}}$) and (*RS-II*)-**3ag** ($\Delta H_m = 41.1\ \mathrm{kJ.mol^{-1}}$) based on the Schröeder-van Laar and Prigogine-Defay simplified equations using the measured eutectic temperatures and compositions.[24,35]

Table III - 4. Thermochemical data measured for the different (R)-3ag / (RS)-3ag mixtures using (RS-I)-3ag, (RS-II)-3ag or (RS-III)-3ag The used colours are consistent with those used in the following figures.

	(RS-I)-3ag					(RS-II)-3ag				(RS-III)-3ag			
$X_{(S)}$	0.45	0.35	0.33	0.25	0.05	0.40	0.28	0.20	0.15	0.40	0.28	0.24	0.22
$T^{I}_{Eutectic}$	122.5	127.0	124.2	124.4	126.8	-	-	-	-	-	-	-	-
$T^{II}_{Eutectic}$	136.1	136.6	136.1	136.1	135.6	136.4	136.9	136.2	134.3	-	-	-	-
$T^{III}_{Eutectic}$	-	-	-	-	-	-	-	-	-	133.1	133.6	133.6	133.9
$T^{II \rightarrow III}_{Transition}$	143.4	143.2	142.5	-	-	142.3	142.6	-	-	141.5	142.9	-	-
$T^{Liquidus}$	148.8	146.7	145.4	142.5	147.3	147.8	-	-	141.4	147.9	-	135.9	-

The binary phase diagram between enantiomers of **3ag**, resulting from the above investigations and computation using Schröeder-van Laar and Prigogine-Defay simplified equations, is therefore shown in Figure III - 16. Since phase diagram between enantiomers are

symmetrical with respect to the racemic composition (*i.e.* $X_{(S)}$ = 0.5), the equilibria obtained in the restricted composition range 0 < X(*s*) < 0.5 can be reproduced for composition X(S) > 0.5. It should be underlined that the true (*RS-I*)-**3ag** to (*RS-II*)-**3ag** polymorphic transition temperature cannot be unambiguously determined from our data. More importantly, cross-seeding experiments and the intersection of the liquidus curves of (*RS-II*)-**3ag** and (*RS-III*)-**3ag** indicate that the three racemic polymorphs are enantiotropically related, further emphasizing how phase diagram determinations are an efficient tool for assessing the stability relationship between polymorphs.

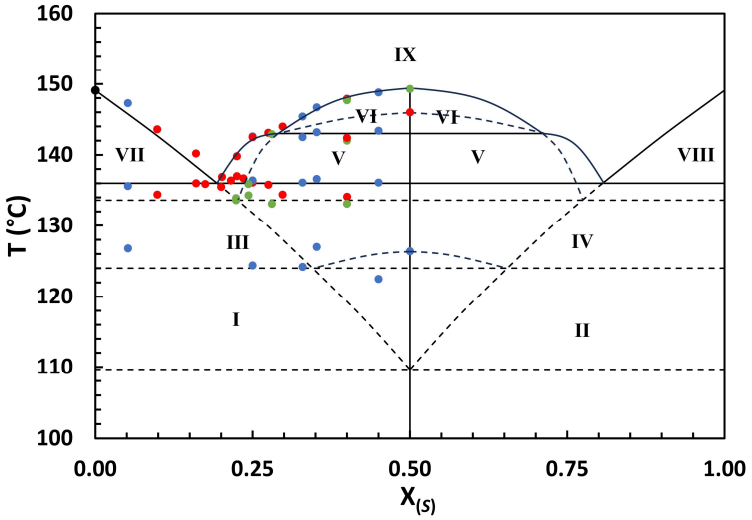

Figure III - 16. Melting phase diagram of 3ag. Blue, red and green circles stand for experimental data obtained using (RS-I)-3ag, (RS-II)-3ag and (RS-III)-3ag respectively. I: <R> + <RS-I>; II: <S> + <RS-I>; III: <R> + <RS-II>; IV: <S> + <RS-II>; V: <RS-II> + Liquid; VI: <RS-III> + Liquid; VII: <R> + Liquid; VIII: <S> + Liquid; IX: Liquid. Bolded lines and dashed lines are respectively for stable and metastable equilibria (guides for the eyes).

III.2.4.3 - Crystal structure resolution

To better understand the enantiotropic relationship of the different **3ag** phases, single crystals of (*RS-I*)-**3ag** and (*R*)-**3ag** are prepared via the classical solvent evaporation method while single crystals of sufficient quality of (*RS-II*)-**3ag** and (*RS-III*)-**3ag** are grown simultaneously by sublimation in an evacuated quartz tube in a tube furnace at 140 °C with (*RS-I*)-**3ag** as starting material. The single crystals thus formed are collected and analyzed by SC-XRD. The main crystallographic data collected are summarized in Table III - 5.

Table III - 5. Crystallographic data of the different 3ag phases.

	(*R*)- **3ag**	(*RS-I*)-**3ag**	(*RS-II*)-**3ag**	(*RS-III*)-**3ag**
Crystal System	Orthorhombic	Triclinic	Orthorhombic	Monoclinic
Space Group	$P2_12_12$	*P*-1	*P*bca	$P2_1/c$
Z, Z'	8, 2	2, 1	8, 1	4, 1
a (Å)	15.7980(2)	7.5008(3)	8.0294(3)	7.8666(3)
b (Å)	22.3286(2)	7.8947(4)	15.2124(6)	22.1616(8)
c (Å)	7.9349(1)	11.8256(5)	22.4180(9)	7.8146(2)
α (°)	90	107.1998(16)	90	90
β (°)	90	100.8463(17)	90	90.2443(12)
γ (°)	90	90.0477(16)	90	90
V (Å^3)	2799.01(6)	656.85(5)	2738.28(18)	1362.36(8)
Calculated Density (g.cm^{-3})	1.283	1.367	1.311	1.318
Measured data	5921	4333	3403	3381
Observed data (F_0>4.0 σ(F_0))	5836	3926	2906	3262
No. Restraints/params	0/362	0/181	0/181	0/182
Goodness-on-fit on F2	0.945	1.042	1.240	1.084
R1/wR2 (F_0>4.0 σ(F_0))	0.0384/0.1192	0.0395/0.1063	0.0953/0.2129	0.0400/0.1100
R1 (all data)	0.0386	0.0436	0.1103	0.0413
Largest diff peak and hole (e$^-$.Å^{-3})	0.222/-0.147	0.414/-0.198	0.382/-0.335	0.350/-0.198

All three racemic forms crystallize in a centrosymmetric non-Sohncke space group $P\bar{1}$, *P*bca and $P2_1/c$ (*i.e.* non-enantiomorphic), respectively, confirming the racemic compound nature of each polymorph. These three space groups are adopted by the vast majority, about 83%, of the characterized racemic compound-forming systems.[22,23]

These structures feature a single molecule in the asymmetric unit. Although (*RS-II*)-**3ag** and (*RS-III*)-**3ag** display strong conformational similarities with an almost planar octahydrophenanthrene moiety (torsion angles of 39.3 ° and 34.6 ° respectively), (*RS-I*)-**3ag** exhibits a different conformation, with an almost right-angled octahydrophenanthrene moiety (torsion angle of 69.9 °) (Figure III - 17).

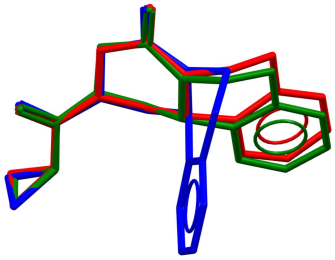

Figure III - 17. Molecular conformation comparison of the (RS-I)-3ag, (RS-II)-3ag and (RS-III)-3ag polymorphs (blue, red and green, respectively). Hydrogen atoms are omitted for clarity.

This conformational difference of (*RS-I*)-**3ag** led to alternating layers of *R* and *S* enantiomers in the [001] direction, while chirality is maintained along the [100] and [010] directions (Figure III - 18). The PBC connecting the enantiopure slices in the [100] direction is ensured through weak van der Waals interactions, mainly between the lactam functional group of two molecules of opposite chirality in the [001] direction (3.74 Å). Although the aromatic rings are stacked parallel along the [010] direction within the enantiopure slice, they are not overlapping each other and their interplanar distance is too far apart for π-π stacking to be considered (4.12 Å, Figure III - 18 dashed line).

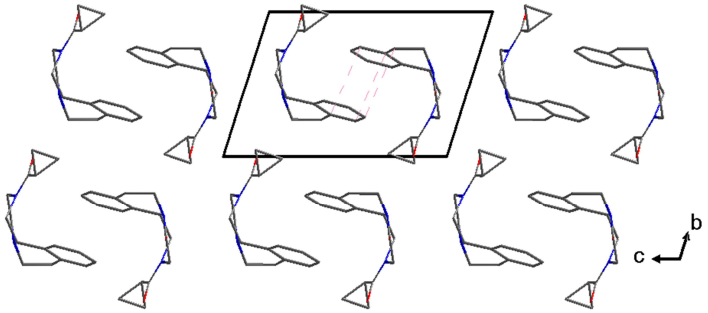

Figure III - 18. View along the [100] direction of the (RS-I)-3ag crystal structure in which enantiopure slices are stacked with an alternating chirality along the [001] direction. Dashed lines represent the closest distance between the aromatic rings. Hydrogen atoms are omitted for clarity.

(*RS-II*)-**3ag** has a heterochiral PBCs in which *R* and *S* molecules are stacked in an alternating fashion in the [010] and [001] directions. Chirality is maintained only in the [100] direction, giving rise to alternating homochiral columns spreading in the *bc*-plane (Figure III - 19a). The three glide mirrors lead to alternating layers of opposite torsion angle of the octahydrophenanthrene moiety (*i.e.* +39.3 ° and -39.3 °) stacked along the [010] direction (Figure III - 19b), resulting in greater distances between the closest aromatic rings compared

(*RS-I*)-**3ag** (4.73 Å). Thus, connectivity is again ensured by weak van der Waals interactions, mainly between the amide function of two molecules of opposite chirality in the [100] direction (3.86 Å). The crystal structure of (*RS-II*)-**3ag** is denser than (*RS-I*)-**3ag**, leading to closer distances between molecules in the crystal structures and then, qualitatively stronger van der Waals interactions which could explain the difference in relative stability between these two polymorphs as function of the temperature and their enantiotropic relationship.

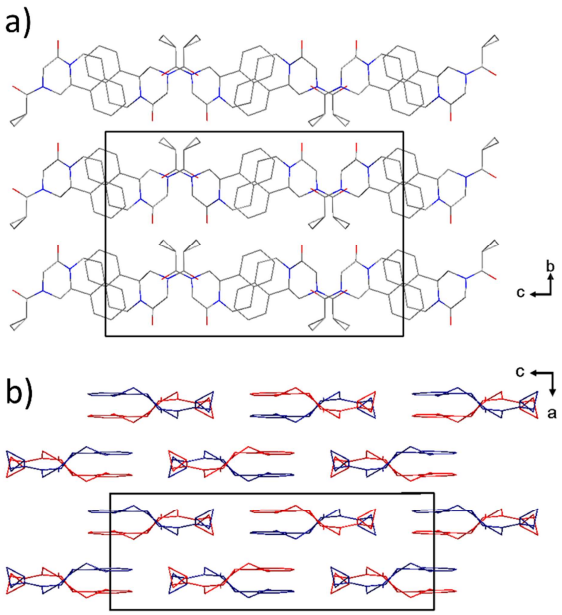

Figure III - 19. View along the (a) [100] and (b) [010] directions of the (RS-II)-3ag crystal structure. Red and blue molecules correspond to two different layers of the PBC. Hydrogen atoms are omitted for clarity.

The crystal structure of (*RS-III*)-**3ag** is strongly related to that of (*RS-II*)-**3ag**. However, the loss of symmetry induces the PBC to be composed of homochiral layers in the *ab*-plane (Figure III - 20b), with an alternated chirality in the [001] direction (Figure III - 20a). Despite an interplanar distance of the aromatic rings too far apart for π-π stacking to be considered (4.55 Å), it remains closer compared to (*RS-II*)-**3ag**. Considering that the same van der Waals interactions are involved with regard to (*RS-II*)-**3ag**, these shorter distances may explain the small increase in relative stability ($\Delta T_{Fus}^{III-II} = 3.3$ °C). Even if these two structures share similarities, a solid-solid transition from (*RS-II*)-**3ag** to (*RS-III*)-**3ag** would involve shifting of layers and rotation of molecules, explaining that the transition only occurs from the metastable melting of the less stable polymorph (*i.e.* (*RS-II*)-**3ag**).

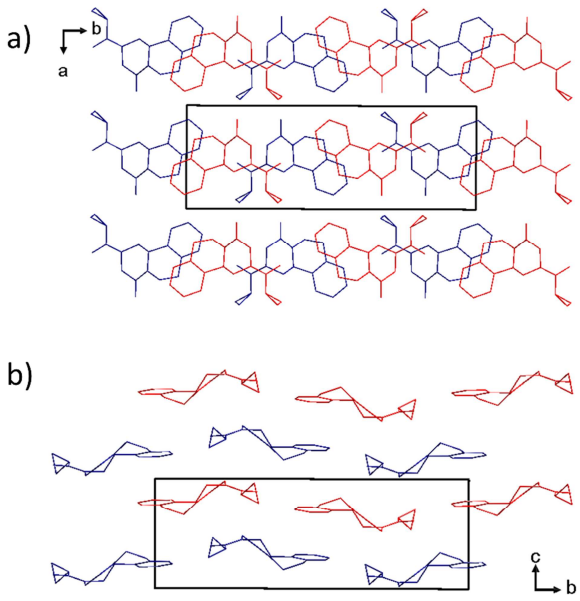

Figure III - 20. View along the (a) [001] and (b) [100] directions of the (RS-III)-3ag crystal structure. R and S enantiomers are highlighted in blue and red respectively. Hydrogen atoms are omitted for clarity.

By contrast, (*R*)-**3ag** crystallizes in the Sohncke space group $P2_12_12$ (*i.e.,* enantiomorphic), which is adopted by 2% of the reported enantiopure structures of small organic molecules.[22,23] The asymmetric unit is composed of two independent molecules with slightly different torsion angle of the amide moiety (ΔAngle = 18.07 °). The PBC is ensured by weak van der Waals interactions, mainly established by the amide function of two adjacent molecules (3.3 Å) along the [100] direction (Figure III - 21). The PBCs are regenerated in the *bc*-plane by mean of the remaining 2_1 screw axes and 2 axes along [010] and [001] directions respectively. Remarkably, it should be noted that homochiral layers of (*RS-III*)-**3ag** are superimposable to the [100] PBC of (*R*)-**3ag**.

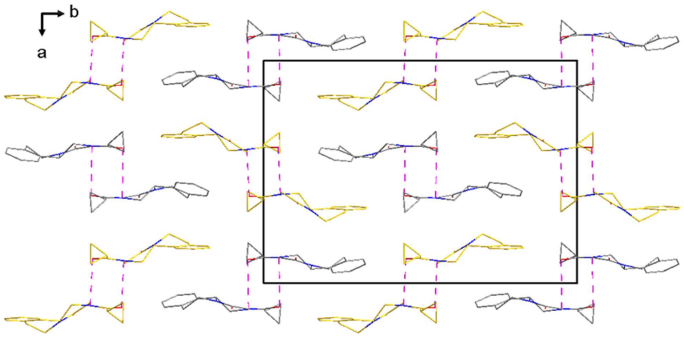

Figure III - 21. View along the [001] directions of the (R)-3ag crystal structure. The two molecules of the asymmetric unit are highlighted in yellow and grey. Dashed lines represent the VdW interactions between the amide function of two identical molecules of the asymmetric unit. Hydrogen atoms are omitted for clarity.

Additionally to the identification of the solid-state classification of each solid phase, this case study permits the determination of their thermodynamic data (Melting enthalpy and temperature), which are important data to be considered further in the manuscript.

III.2.5 - Case study of derivative 3t

After synthesis and purification, samples of racemic and enantiopure **3t** are separately analyzed by XRPD (Figure III - 22a and c). This analysis highlighted the racemic compound behaviour of this system, which was further confirmed by resolving the crystal structure of this racemic phase crystallizing in the space group *P*bca (crystallographic data in Appendix A-II). Although crystallizing as a stable racemic compound, another solid phase could be grown and isolated from the racemic mixture of this derivative. XRPD analysis of this solid phase demonstrated its perfect match with the XRPD pattern of its enantiopure counterpart (*R*)-**3t**, indicating its conglomerate behaviour (Figure III - 22b). Interestingly, the nucleation of the racemic conglomerate is favoured under stagnant conditions in several solvents, either by temperature lowering or solvent evaporation, and can be reproducibly isolated. However, few hours of stirring induced the conversion of this conglomerate phase to (*RS*)-**3t**. These observations are therefore in line with the Ostwald's rule of stages[36] and confirm the metastable nature of the conglomerate in this temperature range.

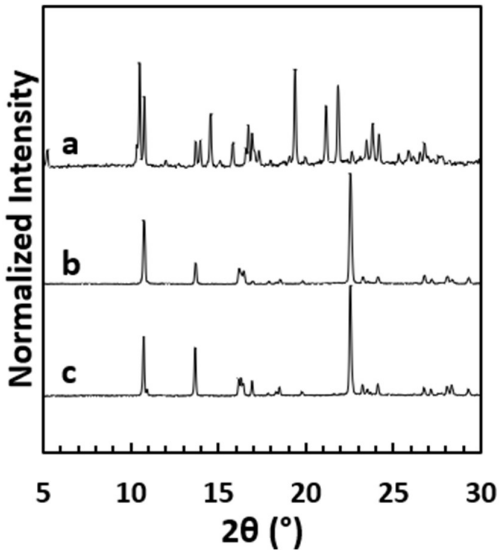

Figure III - 22. XRPD patterns of (a) (RS)-3t (b) 3t racemic conglomerate (c) (R)-3t.

III.2.6 - Case study of derivatives 3ae and 3u

Despite a positive SHG signal for derivatives **3ae**, it exhibits an interesting crystallization behaviour as two different XRPD patterns that do not match the XRPD pattern of the enantiopure crystals is identified from the racemate (Figure III - 23). The crystal structure resolution of the two forms indicates two polymorphic forms of the racemic compound : (*RS-I*)-**3ae** crystallizing in the non-centrosymmetric space group *I*ba2 (*i.e.* SHG positive racemic compound) and (*RS-II*)-**3ae** crystallizing in the most common space group $P2_1/c$ (Table III - 6, SHG negative material).[22,23] Surprisingly, (*R*)-**3ae** crystallizes in the space group $P4_12_12$ which is one of the space group that should not exhibit positive SHG signal according to the Kleinman Symmetry rules. Hence, the SHG signal observed on the racemate of this derivative must be due to the presence of (*RS-I*)-**3ae** in our analyzed sample (Table III - 2).

Further investigations are conducted on the derivative **3ae** to evidence its solid-state behaviour and the stability relationship between the different phases obtained. The thermochemical data of the two polymorphic forms (*i.e.* (*RS-I*)-**3ae** and (*RS-II*)-**3ae**) are depicted in the right part of Figure III - 23. It shows that (*RS-II*)-**3ae** ($T_m = 148.2°\mathrm{C}, \Delta H_m = 22.4\ \mathrm{kJ.mol^{-1}}$) is the most thermodynamically stable form at high temperature compared to (*RS-I*)-**3ae** ($T_m = 143.6°\mathrm{C}, \Delta H_m = 27.6\ \mathrm{kJ.mol^{-1}}$). Although the heat of fusion rule would predict an enantiotropic relationship,[34] slurry experiments in IPA consisting of pure (*RS-I*)-**3ae**

at ambient and sub-ambient temperature (*e.g.* -10 °C and -30 °C) resulted in the formation of (*RS-II*)-**3ae**, the two polymorphic forms are therefore monotropically related in the considered temperature range (-30 °C to 148 °C). Despite several attempts, the racemic conglomerate of **3ae** could only be obtained by manually grinding a racemic mixture of enantiopure crystals. DSC measurement of this manually prepared conglomerate (Figure III - 23d) indicates that it melts 2.4 ± 0.2 °C lower than (*RS-I*)-**3ae** (Figure III - 23e), highlighting its metastable behaviour.

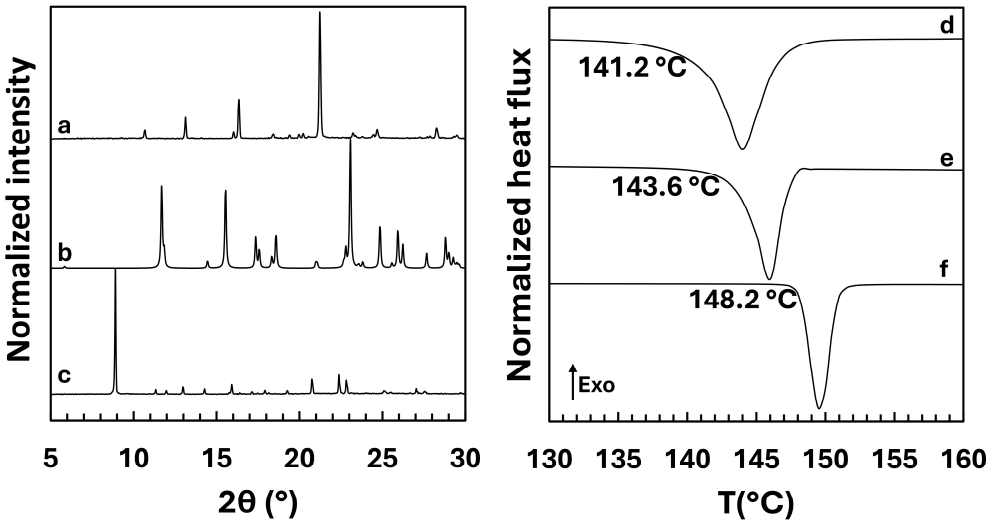

Figure III - 23. XRPD patterns of (a) (R)-3ae, (b) (RS-I)-3ae and (c) (RS-II)-3ae. DSC curves of (d) 3ae racemic conglomerate, (e) (RS-I)-3ae and (f) (RS-II)-3ae. Onset temperatures are depicted alongside the melting endotherms.

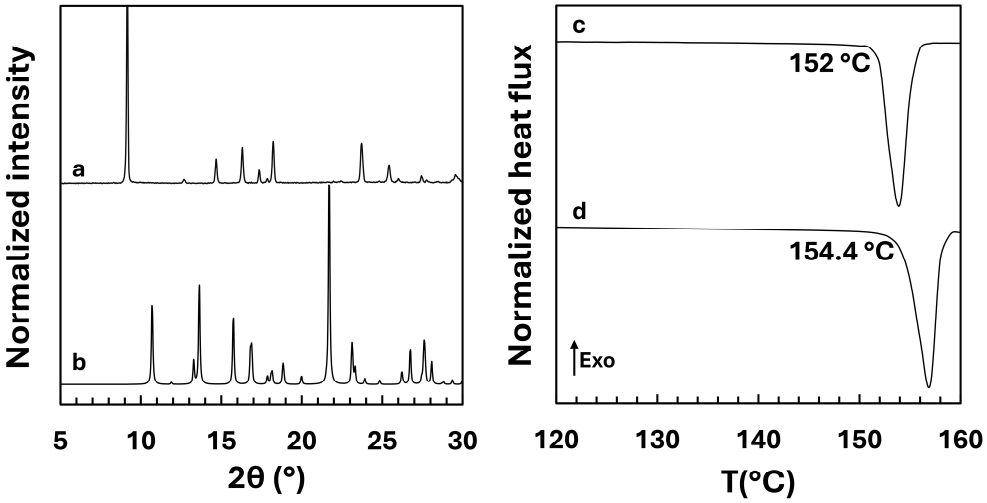

Figure III - 24. XRPD patterns of (a) (R)-3u (b) (RS)-3u. DSC curves of (c) 3u racemic conglomerate and (d) (RS)-3u. Onset temperatures are depicted alongside the melting endotherms.

Similar investigations are conducted on derivative **3u**. Interestingly, a new XRPD pattern is identified after the synthesis of the racemate of this derivative, although it was reported as a stable conglomerate (Figure III - 24).[17] Moreover, the single crystal structure resolution of this new solid form shows that it crystallizes in the non-centrosymmetric space group *Cc* (*i.e.* SHG positive racemic compound) and will be labelled (*RS*)-**3u** (Table III - 6).

Table III - 6 Crystallographic data of the different 3ae and 3u phases.

	3ae			**3u**	
	R	***RS-I***	***RS-II***	***R* (EKIGUD)[17]**	***RS***
Crystal System	tetragonal	orthorhombic	monoclinic	orthorhombic	monoclinic
Space Group	$P4_12_12_1$	*I*ba2	$P2_1/c$	$P2_12_12_1$	*Cc*
Z, Z'	8, 1	8, 1	4, 1	4, 1	4,1
a (Å)	7.92120(10)	30.2497(7)	10.1013(5)	10.4900(2)	20.4600(6)
b (Å)	7.92120(10)	7.7046(2)	16.7164(8)	10.5410(2)	7.4268(2)
c (Å)	39.4724(4)	10.2061(2)	7.8110(3)	13.3225(2)	10.5016(3)
α (°)	90	90	90	90	90
β (°)	90	90	109.9810(10)	90	108.0277(11)
γ (°)	90	90	90	90	90
V ($Å^3$)	2476.71(7)	2378.65(9)	1239.55(10)	1473.14(5)	1517.40(7)
Calculated Density ($g.cm^{-3}$)	1.310	1.364	1.309	1.291	1.254
Measured data	2635	2952	3762	5619	5741
Observed data ($F_0>4.0\ \sigma(F_0)$)	2635	2848	2967	5213	5621
No. Restraints/params	0/165	0/164	0/164	0/193	2/193
Goodness-on-fit on F2	1.089	1.162	1.122	1.049	1.038
R1/wR2 ($F_0>4.0\ \sigma(F_0)$)	0.0397/0.1027	0.0398/0.0956	0.0556/0.1923	0.0376/0.0958	0.0312/0.0875
R1 (all data)	0.0403	0.0398	0.072	0.0416	0.0317
Largest diff peak and hole ($e^-.Å^{-3}$)	0.246/-0.217	0.260/-0.210	0.350/-0.397	0.307/-0.247	0.388/-0.211

The stability relationship between the racemic conglomerate **3u** and (*RS*)-**3u** is established by further DSC measurements of the two solid forms (Figure III - 24). It indicates that (*RS*)-**3u**

melts 2.4 ± 0.2 °C higher than the reported conglomerate and thus, is the most thermodynamically stable form at high temperature. These results indicates that the racemic conglomerate could become a case of "disappearing conglomerate" if the crystallization of the racemic compound (*RS*)-**3u** prevail.[37] However, despite its thermal stability, slurry experiment consisting of pure (*RS*)-**3u** at room temperature in various solvents led to the formation of the racemic conglomerate after 2h, indicating that the racemic conglomerate remains more stable at room temperature than (*RS*)-**3u** and that an eutectoid transition <(*R*)-**3u**> + <(*S*)-**3u**> → <(*RS*)-**3u**> must occur at elevated temperatures. This eutectoid transition is roughly estimated by measuring the solubility of both crystal forms using the Crystal16 (Figure III - 25). First, an interesting information extracted from these experiments is the lower solubility in this temperature range of the racemic conglomerate **3u,** confirming its higher stability than (*RS*)-**3u**.

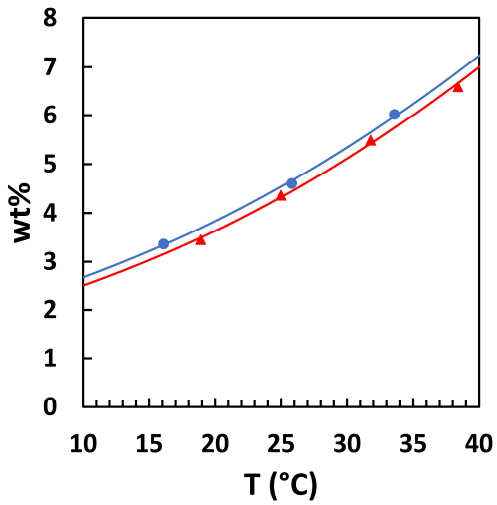

Figure III - 25. Solubility curves in toluene as function of the temperature of the racemic conglomerate 3u (red) and (RS)-3u (blue). The curves represent the Van't Hoff fitting based on the experimental point (blue circles and red triangles).

Then, a fitting based on the experimental solubility points using the Van't Hoff equation (Eq. III - 1) remained necessary to identify the transition temperature, that is characterized by the temperature for which both solubilities are equals.

$$\ln(x) = -\frac{\Delta_{dis}H}{R}\frac{1}{T} + \frac{\Delta_{dis}S}{R} \qquad \text{Eq. III - 1}$$

According to the thermodynamic data obtained via the Van't Hoff plots (Eq. III - 1), it is estimated that the racemic compound (*RS*)-**3u** becomes more stable above ca. 83°C as its solubility equals that of the racemic conglomerate **3u** at this temperature**.** However, this transition temperature remains a rough estimation and was not confirmed experimentally since the solubilities of (*RS*)-**3u** at temperature greater than 40 °C resulted in non-reliable measurements due to parasitic phase transitions occurring before reaching the experimental clear points. Moreover, slurry experiment in toluene above 80°C resulted in the degradation of the molecule, hindering the experimental confirmation of this transition temperature.

Table III - 7. Dissolution enthalpy and entropy extracted from the Van't Hoff plot $ln(x) = f\left(\frac{1}{T}\right)$ of the racemic conglomerate 3u and (RS)-3u in toluene.

Solid forms	$\Delta_{dis}H$ (J.mol^{-1})	$\Delta_{dis}S$ (J.mol^{-1}.K^{-1})
Racemic conglomerate **3u**	381.36	2.02
(*RS*)-**3u**	370.04	1.76

In addition to the chemical similarities between derivatives **3u** and **3ae**, common structural features are also highlighted for the two non-centrosymmetric racemic compounds (*RS*)-**3u** and (*RS-I*)-**3ae** (Figure III - 26). The PBC of these two structures is ensured by weak van der Waals interactions between the aromatic ring and the lactam function of two molecules of opposite chirality spreading along the [010] (3.6 Å and 3.8 Å for (*RS*)-**3u** and (*RS-I*)-**3ae** respectively). The lower steric hindrance of the methyl function (**3ae**) compared to the ter-butyl function (**3u**) increases the molecular flexibility of the amide moiety. This molecular flexibility induces a wider amide torsion angle of 151° in the case of (*RS-I*)-**3ae**, allowing two amide moieties to face each other and leading to alternating homochiral dimers in the [100] direction whereas the chirality is spreading in an alternating fashion in the ab-plane for (*RS*)-**3u** due to the almost planar amide torsion angle (168°).

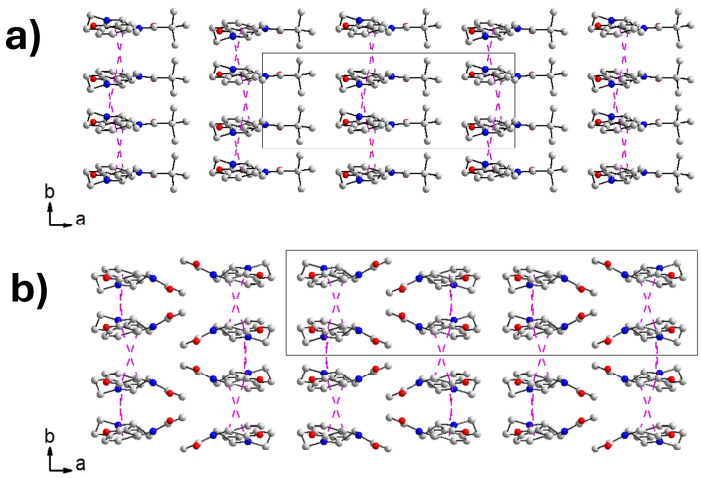

Figure III - 26. Crystal structures comparison between (a) (RS)-3u and (b) (RS-I)-3ae.

Although (*RS-I*)-**3ae** share similarities with (*RS*)-**3u** (*e.g.* similar crystal structures and melting temperature difference with their respective racemic conglomerate), its lower steric hindrance and higher molecular flexibility permits the existence of a more stable racemic compound (*i.e.* (*RS-II*)-**3ae**), exhibiting a denser crystal packing and stronger intermolecular interactions. For instance, T-shaped π - π (4.5 Å), π - lactam (5 Å) and amide - amide (3.4 Å) interactions (Figure III - 27).[38–42]

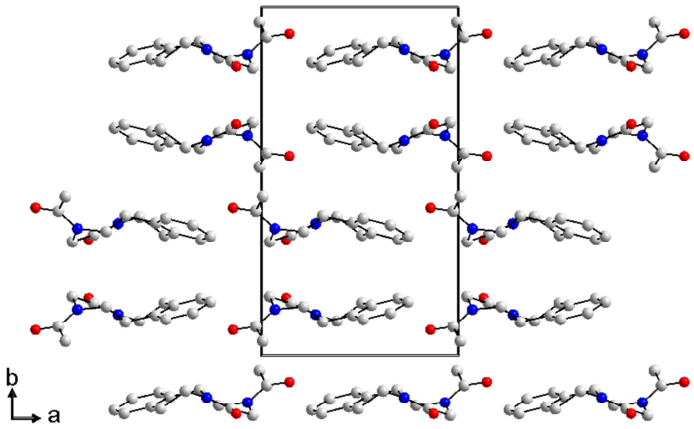

Figure III - 27. Crystal structures of (RS-II)-3ae.

More importantly, it emphasizes how a small chemical modification may drastically change the crystallization behaviour, for instance stable conglomerate or stable racemic compound, and further demonstrating the potential complexity of crystal structure predictions in such cases, even when the considered molecules are closely related.[43,44]

III.3 - Thermodynamic stability of racemic compounds

The above-mentioned conglomerate screening clearly illustrates the poor outcomes resulting from such random derivatization strategy. Indeed, only one entry out of the 38 studied derivatives crystallizes as a stable conglomerate, which furthermore becomes metastable at elevated temperature and the rest result in racemic compounds. From a resolution point of view, this would be considered as a screening failure.

However, this approach only evaluates the success of the conglomerate screening based on the nature of the most thermodynamically stable phase: if a stable racemic compound is detected, the candidate is automatically dismissed. This approach overlooks the inherent out-of-equilibrium nature of crystallization: While racemic crystals do represent the minimum free energy of racemic compound-forming system, other metastable solid forms may exist as local minima. The presence of a metastable conglomerates can thus always be envisaged and such phase may also be brought to crystallize by modulating the crystallization conditions (Figure III - 28).[45,46] Regular screening strategies overlook the wide field of possibilities offered by playing on the kinetic of crystallization.

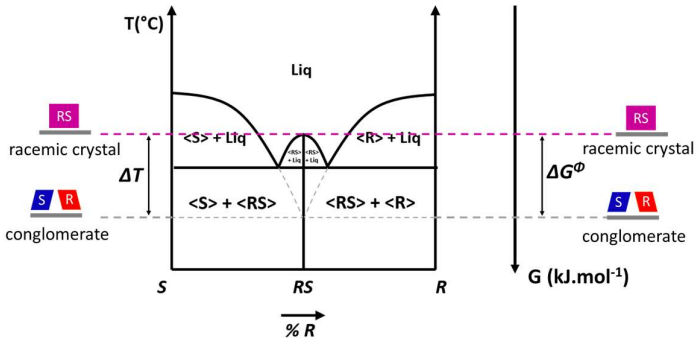

Figure III - 28. Conceptual representation of the relative stability of racemic compounds-forming systems and the difference in the Gibb's free energy ΔG^{Φ} with their associated metastable racemic conglomerate.

We thus suggest that the scope of crystallization-based resolution procedures can be enlarged by exploring non-equilibrium conditions. Under non-equilibrium conditions, nucleation and crystal growth rates, instead of thermodynamic stabilities alone, may determine which crystalline phase dominates, akin to phenomena in polymorphism.[47,48] This would open the potential to exploit non-equilibrium conditions for favouring enantiopure crystals at the cost of thermodynamically stable racemic compounds.

Supporting this idea, there have already been reports of racemic compounds converting into enantiopure crystals under far-from equilibrium conditions, for instance the preferential crystallization of 1,3-dimethylxanthine-based chiral derivatives crystallizing as racemic compounds.[37,49–54] Although promising, it remains unclear if such cases are incidental reports on systems with specific trades, or if there are general guidelines that can be exploited to extend these principles for systematic isolation of enantiomers by crystallization.[55] Motivated by these insights, two analyses based on thermochemical data are conducted on the data collected for the derivatives of Praziquantel.

- A systematic study of the melting point differences $\Delta T_m^{RS-R} = T_m^{RS} - T_m^R$ to to compare the relative stability of the racemic compound with respect to their associate pure enantiomers.
- Another thermodynamic approach based on the difference in the Gibb's free energy ΔG^{Φ} between racemates and their racemic conglomerate accessible via Eq. II - 1 and Eq. II - 2.[56]

$$\Delta G_1^{\phi} = \Delta H_m^{RS}\left(\frac{T_m^R}{T_m^{RS}} - 1\right) - T_m^R R ln2 \qquad \text{For } T_m^R < T_m^{RS} \qquad \text{Eq. II - 1}$$

$$\Delta G_2^{\phi} = \Delta H_m^{R}\left(1 - \frac{T_m^{RS}}{T_m^{R}}\right) - T_m^{RS} R ln2 \qquad \text{For } T_m^R > T_m^{RS} \qquad \text{Eq. II - 2}$$

III.3.1 - Melting point difference

The relative stability difference based on the melting point is first assessed by plotting $T_m^R = f(T_m^{RS})$ (Figure III - 29A). An initial observation of this plot is that derivatives are evenly distributed with respect to the straight line $T_m^R = T_m^{RS}$ (Figure III - 29A, black dotted line). Moreover, conglomerates **3u** (stable), **3t** and **3ae** (metastable) are characterized for $\Delta T_m^{RS-R} \leq$ - 30 °C, aligning with the commonly admitted rule of thumb for the minimum ΔT_m^{RS-R} of a conglomerate-forming system (Figure III - 29A red line).[24] However, a better understanding of the distribution of the meting point differences is observed by plotting these data as a cumulative probability distribution (Figure III - 26B), giving the probability of the variable ΔT_m^{RS-R} to take a value less than or equal to x (Eq. II - 3).

$$f_{\Delta T_m^{RS-R}}(x) = P(\Delta T_m^{RS-R} \leq x) \qquad \text{Eq. II - 3}$$

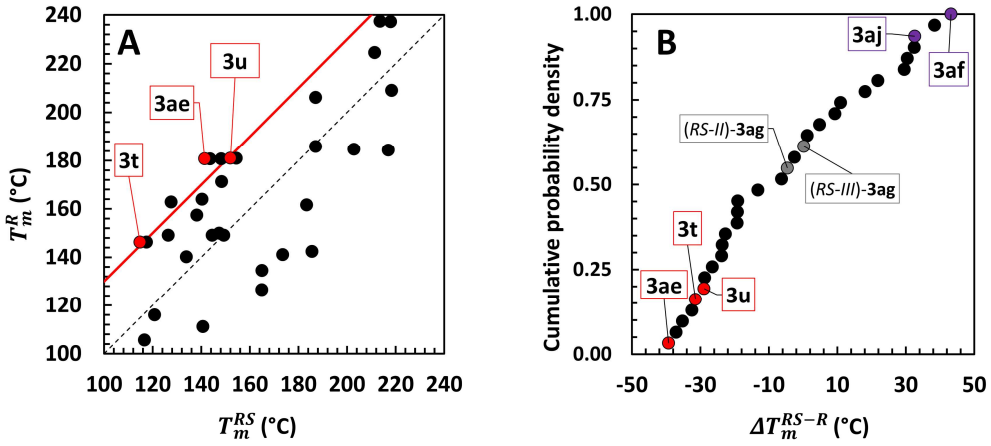

Figure III - 29. (A) Plot of $T_m^R = f(T_m^{RS})$ of the 25 crystalline derivatives. Characterized conglomerates are highlighted by red circles, full red line corresponds to Tpure = Trac + 30 and dotted line corresponds to $T_m^R = T_m^{RS}$. (B) Cumulative probability distribution of the melting points difference ΔT_m^{RS-R}.

Even within this small library, we already obtain a broad distribution of ΔT_m^{RS-R}, ranging from -40 °C (*i.e.* metastable or slightly stable racemic compound) to +40 °C (*i.e.* relatively stable racemic compound). This indicates that the modification of even a single atom can drastically change the stability of a crystal phase, hence complexifying the rationalization of such approach. However, derivatives **3t**, **3u** and **3ae**, all belonging to the alkyl's chemical class and sharing similar racemic crystal structures, are clustering together in the same ΔT_m^{RS-R} range. Moreover, structural similarities are also observed for polymorphs of derivative **3ag** whose crystal structures are described in section III.2.4.3 and two other derivative that are —to a large extent— chemically unrelated derivatives: **3af** and **3aj** (Figure III - 29B). Indeed, despite their molecular differences, commonalities in their crystal structures are observed (Figure III - 30).

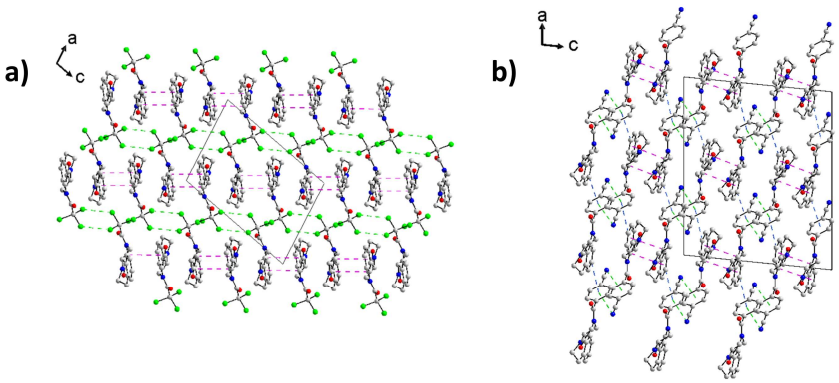

Figure III - 30. Crystal structures comparison between (a) 3af and (b) 3aj.

The PBC of these two molecules is composed of two distinct layers spreading along [101] and [001] directions for derivatives **3af** and **3aj** respectively. The first layer is composed of the octahydrophenanthrene moiety, in which the cohesion is ensure by weak van der Waals interactions, mainly between the aromatic ring and the electrophilic carbon in-between the lactam and the amide functions, that are distant of 3.7 Å and 3.9 Å for derivatives **3af** and **3aj** respectively. The chirality is spreading in an alternating fashion in the *ac*-plane, leading to the regeneration of the PBC along the [010] direction with larger distance of 4.1 Å and 4.2 Å for derivatives **3af** and **3aj** respectively. Although the amide moiety is different for derivatives **3af** and **3aj**, the same crystal packing is also identified for the second layer, but different type of interactions is involved. The PBC is ensured by chlorine-chlorine bonding with Cl-Cl distances of 3.6 Å in the case of **3af**,[57–60] whereas it is π-π interaction between the nitrile function and the aromatic ring in the case of **3aj** (3.4 Å).[40,41] It should be noted that these two crystal structures are not isomorphous and the main difference is that derivative **3aj** has the possibility to form π-π interactions in t-shape between the two aromatic rings of the amide moiety and the octahydrophenanthrene moiety (3.4 Å), connecting the two layers together. These striking observations led us to a systematic analysis of ΔG^{Φ} between racemic crystal phases and their enantiopure counterparts for structurally related compounds.

III.3.2 - Gibb's Free Energy differences ΔG^{Φ}

We recognize that the conversion from racemic crystal phases into their enantiopure counterparts may be feasible when the energy difference ΔG^{Φ} between both phases is small. Indeed, it is commonly accepted for polymorphic transformations that thermodynamically

stable solid phases may be converted into kinetic solid phases when ΔG^{Φ} < 2.1 kJ.mol^{-1}.[61,62] Already, ΔG^{Φ} has been analyzed for many chiral compounds, and has been used as indicator for identifying thermodynamically stable racemic conglomerates.[63–66] However, the distribution of ΔG^{Φ} of molecules with the same chiral centre has not been investigated. Such analysis might not only enable the systematic discovery of chiral system that can be thermodynamically or kinetically resolved but may also guide rational experimental design to systematically exploit non-equilibrium conditions for destabilizing racemic compounds into their kinetic conglomerate counterparts. To assess the potential of such an evolutionary approach to molecular design, we took advantage of the 25 synthesized derivatives that group into four distinct modification classes (Figure III - 31): alkyls (dark green); carbocycles (light green); aromatic alkyls (orange), aromatic halides and other substituted aromatics (light blue), as well as three unclassified derivatives (grey).

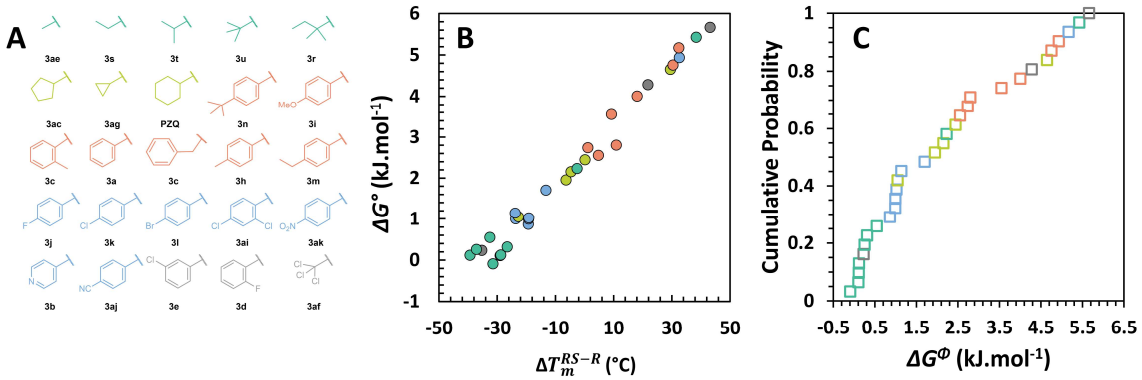

Figure III - 31. (A) derivative synthesized both at racemic and enantiopure compositions, classified as alkyls (dark green), carbocycle (light green), aromatic alkyls (orange), halogen and other substituted aromatics (light blue), non-classified (grey). (B) Plot of ΔG$^{\Phi}$ as function of the melting temperature difference of the derivatives. (C) Cumulative probability distribution of free energy differences.

Thus, we determined and plot $\Delta G^{\Phi} = f(\Delta T_m^{RS-R})$ (Figure III - 31B) and the cumulative probability density distribution of ΔG^{Φ} (Figure III - 31C) and found, with few exceptions, that library entries cluster along ΔG^{Φ} according to the pre-determined modification classes, enabling to propose an **evolutionary strategy for library design**. Specifically, starting with only four entries (one per modification class) as the first generation, the alkyl derivative can be immediately identified as most promising, since that entry shows the lowest ΔG^{Φ}. Subsequently preparing a second generation of four additional alkyl derivatives already yields

the stable conglomerate 3u. Hence, rather than preparing 25 quasi-arbitrary derivatives, we can find conglomerates and low ΔG^{Φ} entries within just two generations and with less than a third of the total number of library entries (8 instead of 25), showing the potential of library design through directed evolution.

III.4 - Preferential crystallization of derivative 3t and 3ae

The clustering of chemical classes not only enables library design through directed evolution but may also group racemic compounds within the ΔG^{Φ} distribution that are suitable for isolating enantiopure crystals. To investigate this idea, we explore whether racemic compounds-forming systems **3t** and **3ae**, which are situated in the same low ΔG^{Φ} region as the known stable conglomerate **3u**, can be isolated as enantiopure crystals using far-from equilibrium conditions, for instance preferential crystallization, which is an ideal resolution method in these scenarios.

Classical preferential crystallization of stable conglomerate forming-system is an out-of-equilibrium method that relies on the kinetically favoured nucleation and growth of an enantiopure solid over its antipode (*cf.* I.3.5.2).[24,67–70] In case of racemic compound-forming systems, such as derivatives **3t** and **3ae**, the kinetic nucleation and growth of the enantiopure solid competes with an additional solid phase: a more stable racemic compound.[71] Therefore, the choice of the crystallization parameters is of paramount importance (*e.g.* solvent, stirring rate, seed properties, temperature program etc.).

III.4.1 - Solvent selection

In case of racemic compound-forming systems, the solubility of the racemic crystals is always lower than that of its associated racemic conglomerate, implying that a supersaturation of the metastable racemic conglomerate would induce an even higher supersaturation of the racemic crystals. The goal of this solvent selection is to find a solvent in which the solubility difference between the stable racemic compound and the metastable racemic conglomerate is minimal. A way to assess this difference in solubility is to determine the invariant *d.s.p.c.*: the lower *e.e.* of this invariant (*i.e.* the closer to the racemic composition), the lower the solubility difference between the two crystal forms, and therefore the smaller the difference in supersaturation. Akin to conglomerate screening procedure, scalemic mixtures of

derivatives **3t** and **3ae** (ca. 20 *e.e.*%) are suspended in IPA for 9 days to reach thermodynamic equilibrium. The composition of both the mother liquor and the suspended solid is analyzed by chiral HPLC on a Chiracel OD-H column (4.6 x 250 mm, 5µm) with a mobile phase consisting of n-heptane and 2-propanol (85/15 and 60/40 v:v respectively) at flow rate of 1 $mL.min^{-1}$ with a UV detection at 220 nm (Figure III - 32). The results are summarized in Table III - 8 and compared with previously obtained *d.s.p.c.* in toluene. It should be noted that IPA was tested due to the rather high induction time for spontaneous crystallization of the considered derivatives in this solvent (this will be demonstrated in Figure III - 35).

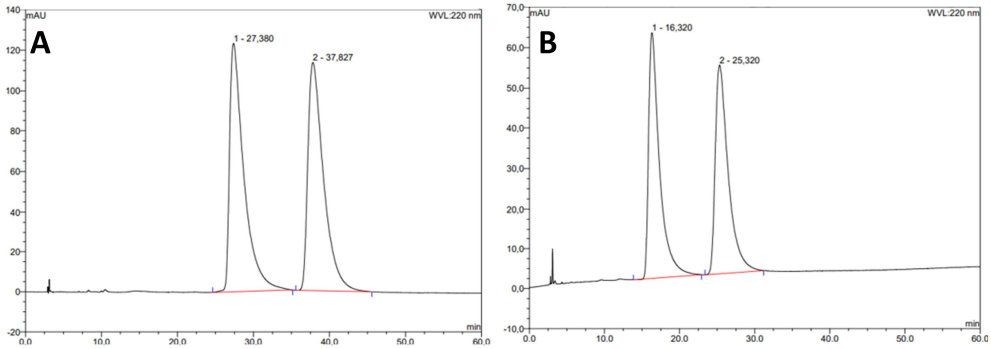

Figure III - 32. Typical chromatogram for racemic 3t (A) and racemic 3ae (B). Retention time (min) for 3t: (R)-3t: 27.38 (S)-3t: 37.83 and 2c: (R)-3ae: 16.32 (S)-3ae: 25.32.

Table III - 8. Composition of the resulting mother liquor and solid of scalemic suspensions (d.s.p.c.) of derivative 3t and 3ae in toluene and 2-propanol at 20°C.

		3t		**3ae**	
		Toluene	IPA	Toluene	IPA
e.e. (%)	Solid	36.4	85.8	40.5	30.1
	Mother Liquor	5.5	4.8	12.2	1.2

A striking observation of this analysis is the drastic decrease in *e.e.* of the invariant point using IPA instead of Toluene in case of the derivative **3ae**, highlighting the difference in solid-liquid interactions of the different solid phases and these solvents. It further emphasizes the importance of the choice of the working solvent for such resolution methods. These observations raise the question about how close it is possible to get to the racemic composition by simply changing the solvent, and therefore to which extent the racemic

conglomerate can be favoured at the expense of the racemic compound. However, with the aim of achieving a straightforward procedure of chiral resolution, we limited ourselves to these two solvents.

According to the *d.s.p.c.* results, the temperature dependent solubility of the two derivatives in the most promising solvent (*i.e.* IPA) are determined using the Crystal16 apparatus (Figure III - 33). It should be noted that the crystallizing solid was stirred for 5h before the determination of the clear point to avoid any remaining parasitic metastable phases that could have kinetically crystallized along the different cycles of the temperature program (Figure III - 33, see Appendix A - I.3.2).

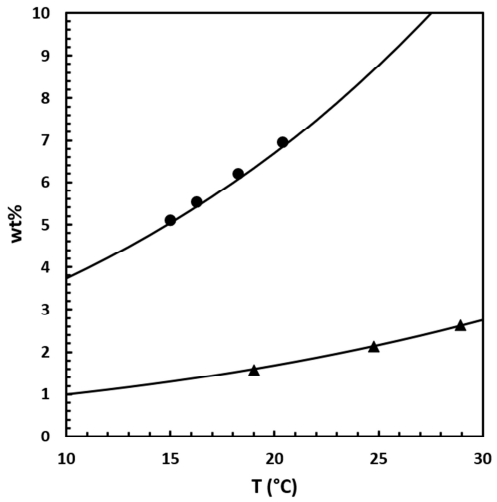

Figure III - 33. Temperature dependent solubility of (RS)-3t (circle) and (RS)-3ae (triangle) in IPA from 10 °C to 30°C. Solubility lines are theoretical modelling using Van't Hoff equation.

III.4.2 - SIPC method

Although other parameters are of interest (*e.g.* temperature profile, stirring mode, seed properties etc.), attempts to perform preferential crystallization using the SIPC method were performed based on the solubility data. Table III - 9 summarizes the starting conditions for the SIPC implementation of both **3t** and **3ae** in IPA.

Table III - 9. Starting conditions for the implementation of the successful preferential crystallization experiments using the SIPC mode.

	3t	**3ae**
Volume of IPA (mL)	10.0	30.0
Mass of racemic **3** (mg)	834.3	805.4
Mass of enantiopure seed (mg)	40.1	39.8
Stirring mode and shape	Cross-shaped PTFE magnetic bar	
Stirring speed (rpm)	700	
Working temperature (°C)	15	20
Supersaturation (β)[a]	2	

[a]Calculated with respect to the solubility of the racemic crystals

The supersaturated solutions are obtained by heating the initial slurry over the clear point until a clear solution is observed. These clear solutions are then filtered through 0.22 µm syringe filter to avoid any parasitic solid impurities that may affect the crystallization behaviour of our system,[72] cooled to reach a supersaturation β = 2 and seeded with pure enantiomer to trigger the crystallization of the desired enantiomer. These chiral resolutions are monitored by sampling the slurry from the crystallization flask at different times from which the solid and liquid phases are isolated and analyzed by enantioselective HPLC. The crystallized mass is obtained by (i) weighing the total amount of enantiopure solid recovered or (ii) determining the concentration of the solute based on the calibration curve. The evolution of the crystallized mass and its associated enantiomeric excess are summarized in Table III - 10.

The evolution of the *e.e.* of the mother liquor is indicative of a preferred crystallization of the targeted enantiomer induced by seeding while the high solid enantiopurities (>94 %*e.e.*) confirm the success of these chiral resolutions. Moreover, these high enantiopurities persist for 30 min and 120 min in the case of derivative **3t** and **3ae** respectively, indicating that these systems remain far-from-equilibrium for an extended period of time. If the racemic crystals had crystallized (*i.e.* return to equilibrium), a significant decrease in the solid-phase *e.e.* would have occurred. This prolonged non-equilibrium state provides therefore ample opportunity to further optimize and enhance this process.

Although the crystallized mass of the derivative **3t** drastically increased after 30 minutes, this is accompanied by a significant decrease in solid *e.e.* (Figure III - 34). This change in the solubility regime associated with this decrease in enantiopurity evidenced a return to equilibrium (*i.e.* crystallization of either the undesired antipode or racemic crystals). However, preferential crystallization is nearly complete within 15 minutes, underscoring the efficiency of this method and the strong kinetic favourability towards the formation of the enantiopure crystal (Table III - 10).

Table III - 10. SIPC monitoring result of compounds 3t and 3ae giving the crystallized mass (mass of initial seed already deducted) and the enantiomeric excess of both the solid and liquid phases. The e.e. positive sign is arbitrary attributed to the (R) enantiomer.

	3t			**3ae**		
Sampling time	Crystallized mass	*e.e.* (%)		Crystallized mass	*e.e.* (%)	
(min)	(mg)	Solid	liquid	(mg)	Solid	liquid
5	43.6	95.7	- 6.3	14.8	99.4	- 0.9
15	131.1	98.7	- 6.6	46.9	98.4	- 1.2
30	151.4	95.6	-7.6	77.0	98.9	- 1.5
60	260.5	54.4	-3.3	87.1	97.2	- 1.9
120	242.0	18.8	-2.5	96.8	94.0	- 2.4

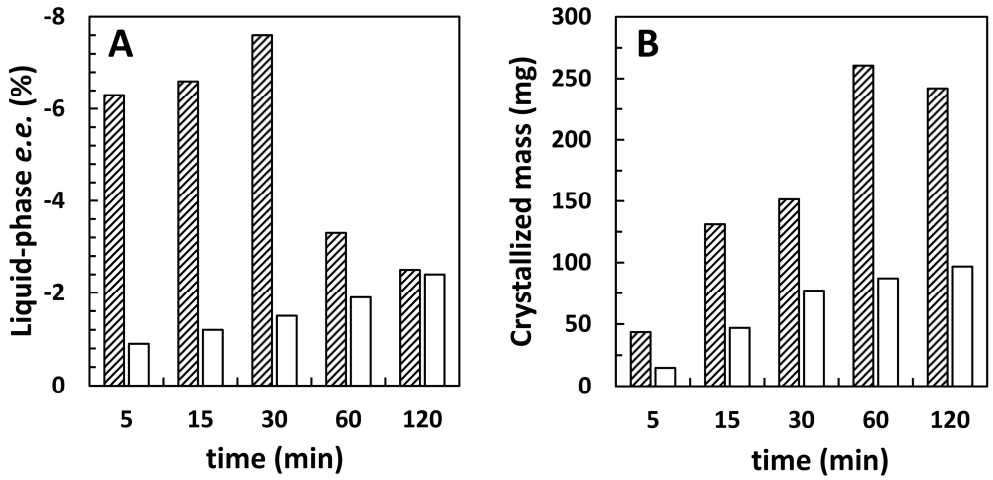

Figure III - 34. Evolution of (A) the solution-phase e.e. (%) and (B) the crystallized mass as function of the time during SIPC experiments of compounds 3t (dashed bars) and 3ae (blank bars).

These results show that the possible straightforward isolation of enantiopure crystal despite the presence of a more stable racemic compound, moreover in good yield, is not a specific trend observed for chiral derivative of theophylline[51–53,73] but may be rationalized by using ΔG^{Φ} as a diagnostic tool. It demonstrates the potential of such evolutionary design which is not only capable of reaching conglomerates within few iterations, but also find racemic compound-forming systems suitable for chiral resolution under far from equilibrium conditions. Although these two successful preferential crystallizations on racemic compound-forming systems exhibiting a low ΔG^{Φ} (< 0.8 kJ.mol^{-1}) confirm the goal of our approach, it does not stand as an unbreachable boundary. This approach may also work for systems with higher ΔG^{Φ}, provided that suitable non-equilibrium conditions are found.

III.4.3 - Nucleation rate measurement

SIPC of derivatives **3t** and **3ae** using Toluene or Ethanol as working solvent were also attempted several times but resulted in an instant crystallization of the racemic compounds (result not shown). Although further investigations may have helped in finding suitable conditions in these solvents, it demonstrates the various nucleation behaviours observed from different solvents. We already found that the difference in solubility of the metastable racemic conglomerate and the stable racemic compound are minimal in both cases according to our *d.s.p.c.* measurements (< 5 *e.e.*%). Therefore, assessing the crystal nucleation rate and properties of the racemic and enantiopure phases from the two derivatives in IPA are of interest. These data may be accessible from the measurements of their induction time distribution based on equations from the Classical Nucleation Theory (CNT) assuming a heterogenous nucleation mechanism.[74–78] Indeed, the nucleation rate *J* at different supersaturation ratio can be extracted from such distribution of induction time using Eq. II - 4 and further implemented into Eq. II - 5 to determine the kinetic factor A (Eq. II - 6) and the thermodynamic factor B (Eq. II - 7) of nucleation by plotting $\ln\left(\frac{J}{S}\right) = f(\ln^{-2} S)$.

$$P(t) = 1 - \exp\left(-JV\left(t - t_g\right)\right)$$ with *J*: Nucleation rate (m^{-3}.s^{-1}); V: Sample volume (m^{-3}); t: Nucleation time (s); t_g : Growth time (s) — Eq. II - 4

$$J = AS \exp\left(-\frac{B}{\ln^2 \beta}\right)$$ with J: Nucleation rate ($m^{-3}.s^{-1}$); β: Supersaturation ratio; A: Kinetic factor ($m^{-3}.s^{-1}$); B: Thermodynamic factor — Eq. II - 5

$$A = \frac{z f^* C_0}{\beta}$$ with A: Kinetic factor ($m^{-3}.s^{-1}$); z: Zeldovich factor; f^*: Attachment frequency (s^{-1}); C_0: Nucleus site concentration (m^{-3}); β: Supersaturation ratio — Eq. II - 6

$$B = \frac{4c^3 v^3 \gamma_{ef}}{27(k_b T)^3} = \frac{W^* \ln^2 \beta}{k_b T}$$ with B: Thermodynamic factor; c: Shape factor[a]; v: molecular volume (m^3); γ_{ef}: Interfacial energies ($J.m^{-2}$); k_b: Boltzmann constant ($J.K^{-1}$); T: Temperature (K); β: Supersaturation ratio; W^*: Nucleation work (J) — Eq. II - 7

[a] $c = (36\pi)^{\frac{1}{3}}$ for spherical particles

To compare the nucleation parameters of our two systems, nucleation rate measurement at different supersaturations using the Crystal16 at 15 °C and 20 °C in IPA for derivative **3t** and **3ag** respectively (*i.e.* at the respective temperatures used for operative preferential crystallizations) are conducted, plotted and fitted following Eq. II - 4 (Figure III - 35).

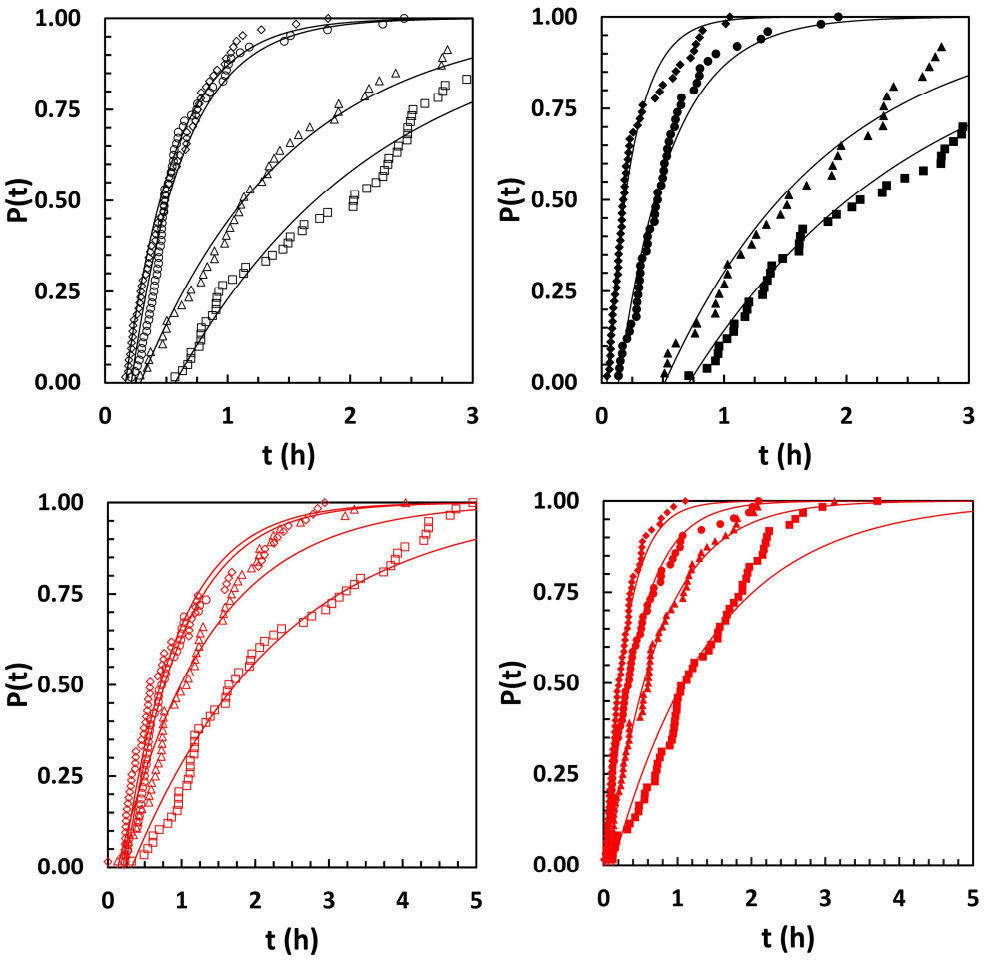

Figure III - 35. Experimental induction time probability distributions of (RS)-3t (empty red), (R)-3t (full red) at 15°C and (RS)-3ae (empty black) and (R)-3ae (full black) at 20°C in IPA at different supersaturation ration S: 2.3 (red squares), 2.6 (red triangles), 2.9 (red circles) and 3.2 (red diamond) for derivative 3t; 2.4 (black squares); 2.7 (black triangles); 3.0 (black circles) and 3.3 (black diamond) for derivative 3ae.

It can be seen from these distributions that the lower the supersaturation, the broader the distributions. Indeed, a lower supersaturation induces a lower driving force for nucleation, hence decreasing the nucleation rate *J* and increasing the growth time t_g. The fitted values of the nucleation rate *J* at different supersaturations for both **3t** and **3ae** are summarized in Table III - 11. Clearly, enantiopure (*R*)-**3t** grows faster and has a higher nucleation rate than racemic (*RS*)-**3t** under the same conditions whatever the supersaturation ratio. By contrast, two regimes are observed for **3ae**: while racemic (*RS*)-**3ae** dominates in term of growth time and nucleation rate at low supersaturation (≤ 2.7), the reverse is observed at higher supersaturation (≥ 3.0).

Table III - 11. Values of the nucleation rate J and growth time t_g determined from the fit of Eq. II - 4 to the experimental induction time probability distribution of derivative 3t and 3ae in IPA. The error in the fit is lower than 5%.

	3t					**3ae**			
	(*RS*)-**3t**		(*R*)-**3t**			(*RS*)-**3ae**		(*R*)-**3ae**	
β	*J* ($m^{-3}.s^{-1}$)	t_g (s)	*J* ($m^{-3}.s^{-1}$)	t_g (s)	β	*J* ($m^{-3}.s^{-1}$)	t_g (s)	*J* ($m^{-3}.s^{-1}$)	t_g (s)
2.3	136.7	1155	203.1	447	**2.4**	168.2	2050	148.1	2561
2.6	362.1	843	402.1	227	**2.7**	227.9	1032	205.4	1849
2.9	380.4	736	639.1	97	**3**	644.1	768	649.6	492
3.2	225.6	474	941.6	9	**3.3**	684.0	598	1317.3	155

Thereafter, the kinetic pre-exponential factor A and the thermodynamic exponential factor B are obtained by plotting the experimental $\ln\left(\frac{J}{\beta}\right) = f(\ln^{-2}\beta)$ based on Eq. II - 5 (Figure III - 36). It can be seen that experimental data appear, to a certain extent, to be aligned in straight lines. Therefore, the values of variables A and B are extracted and summarized in Table III - 12.

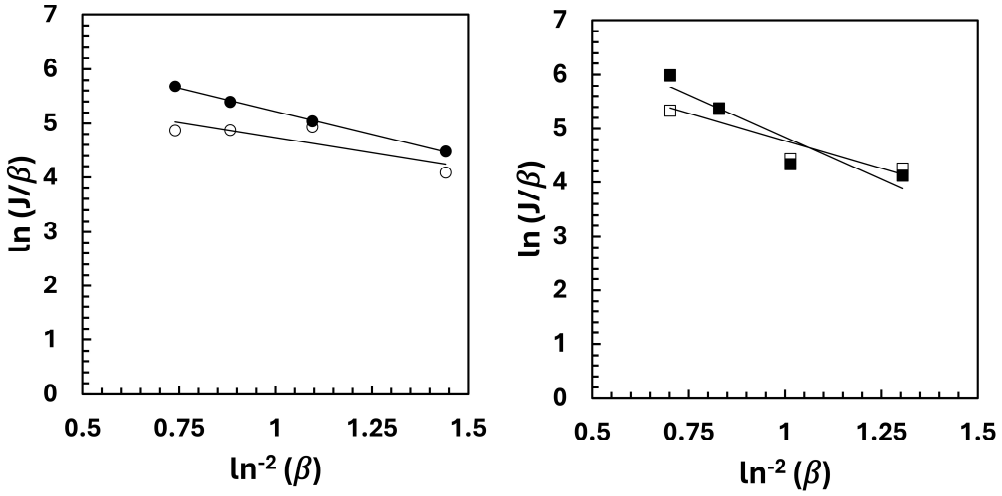

Figure III - 36. Experimental nucleation rate from (RS)-3t (empty circles), (R)-3t (full circles), (RS)-3ae (empty squares) and (R)-3ae (full squares) in IPA plotted as $ln\left(\frac{J}{S}\right) = f(ln^{-2}S)$ following Eq. II - 5.

Table III - 12. Values for the pre-exponential kinetic factor A, the thermodynamic factor B and the effective interfacial energy γ_{ef} calculated for derivatives 3t and 3ae in IPA from the nucleation rate measurements.

	3t		**3ae**	
	(*RS*)-**3t**	(*R*)-**3t**	(*RS*)-**3ae**	(*R*)-**3ae**
A ($m^{-3}.s^{-1}$)	349	1005	918	2875
B	1.12	1.70	2.05	3.13
γ_{ef} ($J.m^{-2}$)[a]	3.20	3.68	4.43	5.09

[a]calculated assuming $\nu = 358.10^{-30}$ m^{-3} for derivative **3t** and $\nu = 306.10^{-30}$ m^{-3} for derivative **3ae** based on crystallographic data

The two derivatives exhibit the same nucleation trends: while the enantiopure phase is thermodynamically disfavoured as $B^{(RS)} < B^{(R)}$ (*i.e.* lower energy barrier for nucleation in case of racemic crystals), the enantiopure phase is kinetically favoured ($A^{(R)} > A^{(RS)}$).

The exponential factor B is related to the effective interfacial energy γ_{ef}, which is a balance between the three interfacial energies (*i.e.* nucleus-solvent, nucleus-heterogeneous particles, solution-heterogeneous particle). This data is calculated following Eq. II - 7 and reported in Table III - 12. It shows that γ_{ef} for enantiopure crystal in IPA is always higher than the racemic crystals, indicating a more energy-intensive nucleation of enantiopure crystals. By contrast, the pre-exponential factor A is about three times higher in case of the nucleation of enantiopure crystals, further emphasizing how enantiopure crystals may be kinetically favored at the expense of more stable racemic crystals and therefore kinetically resolved using out-of-equilibrium methods.

Although the difference exponential factor *ΔB* is of similar order of magnitude (0.58 and 1.08 for **3t** and **3ae** respectively), its implication in an exponential term induce a higher impact on the nucleation behaviour of **3ae**. It may explain the higher efficiency of the preferential crystallization of **3t** compared to **3ae**. However, these results must be interpreted with caution when comparing them to operational preferential crystallization: under operative conditions, the seed crystals are in equilibrium with an initial racemic solution, whereas in these nucleation rate measurements, the seed crystals are in equilibrium with an enantiopure solution. It would be of interest to compare these data in other solvents

III.4.4 - Generality assessment

The chemical core of our library is large and stiff without possibilities for H-bonding. However, comparing the distribution of ΔG^{Φ} of another library based on the chemical core Phenylglycine Amide provided by S.W. van Dongen (AMOLF), which is small and flexible and can form H-bonding[33,79,80] highlighted a strikingly similar distribution in ΔG^{Φ} despite the difference in molecular structure (Figure III - 37A). Also, we shown for both libraries that it is possible to straightforwardly isolate enantiopure crystals from racemic compounds when ΔG^{Φ} < 0.8 kJ.mol^{-1}.[49,68]

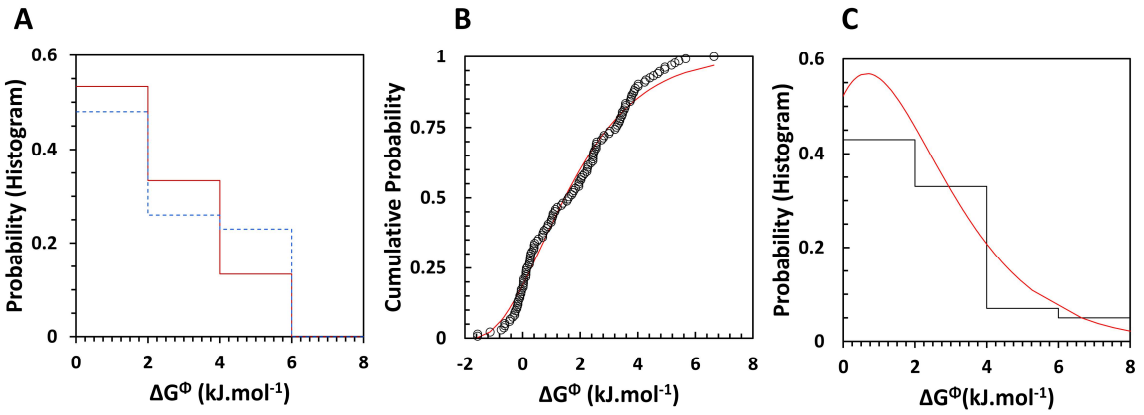

Figure III - 37. (A) Probability histogram of free energy differences ΔG^{Φ} of the praziquantel library (dashed blue histogram) and the phenylglycinamide library (solid red line) (B) Cumulative probability distribution of free energy differences ΔG^{Φ} of the literature dataset (black circle) fitted with an adapted gamma-distribution (red line). (C) Probability histogram of free energy differences ΔG^{Φ} of the literature dataset (black histogram) and its associated gamma-distribution represented as a probability density function.

These commonalities prompt the question of how general these trends are. To address this question, we collect thermodynamic data for more than a hundred chiral organic racemic compounds that have been previously investigated.[24,63,81] This literature catalogue of molecules is very diverse, ranging from salts to molecules with multiple chiral centres and covering a wide breadth of functional groups featuring several heteroatoms (S, N, O). Moreover, in contrast to our library, the entries in the literature set are, to a large extent, structurally not related, thus forming a representative reference set for assessing generality. We find that the literature data are well-described by a gamma distribution (Figure III - 37B red line). A statistical comparison (Kolmogorov-Smirnov test) shows that the two libraries follow the same gamma-distribution (Figure III - 37C). These similarities suggest that the

trends for this library can be generalized to a large diverse set of unrelated chiral organic molecules.

Based on this analysis, we assess the potential of non-equilibrium conditions to kinetically stabilize enantiopure crystals by identifying three racemic compounds (diprophylline, aspartic acid, proxyphylline) that have previously been kinetically converted to enantiopure crystals,[50,50–52] calculate their ΔG^{Φ} (1.00, 1.88, and 2.01 kJ.mol^{-1} respectively. We realize that all three conversions require crystallization conditions that favour kinetic phases, suggesting that far-from-equilibrium conditions are essential.

Consistent with this idea, ΔG^{Φ} of these compounds is close to the thermal energy $k_B T$ (2.48 kJ.mol^{-1}) at room temperature, which suggests that transitions between crystal phases with such energy differences are kinetically probable. Indeed, polymorphic transitions between crystal phases are routinely observed for energy differences below 2.5 kJ.mol^{-1},[61,82] such as caffeine (ΔG^{Φ} = 2.09 kJ.mol^{-1})[83] and tolfenamic acid (TFA, ΔG^{Φ} = 2.30 kJ.mol^{-1}).[84] For some reported transformations the energy differences are even much larger, as exemplified by the archetypical polymorphic system known as ROY, with a ΔG^{Φ} as large as 7.11 kJ.mol^{-1}.[62,85] Hence, we estimate that 40-50% of thermodynamically stable racemic compounds ($\Delta G^{\Phi} \leq 2.1$ kJ.mol^{-1}) can likely be kinetically converted to enantiopure crystals (Figure III - 37C). Additionally, 5-10% of chiral molecules are already stable conglomerates. Consequently, we predict that 45-60% of all chiral molecules can be isolated as desired enantiomers through crystallization under non-equilibrium conditions.

III.5 - Discussion & conclusion

Conventional conglomerate screening apply to our derivatives clearly illustrates the poor outcomes resulting from such random derivatization strategy. Indeed, only one entry out of the 38 studied derivatives crystallizes as a stable conglomerate (*i.e.* **3u**), which furthermore becomes metastable at elevated temperature. In worst-case scenario, **3u** might have been mischaracterized as a stable racemic compound and discarded, potentially missing its eutectoid transition. Conversely, despite being a stable racemic compound, the conglomerate form of the derivative **3t** could still be obtained.

It definitely demonstrates the importance of a careful investigation of the solid-state behaviour of each newly engineer solid form, which is also well illustrated by the case study of derivative **3ag**. This derivative exhibits a very rare crystallization behaviour with no less than three enantiotropic polymorphs of the racemic compound, evidenced by the construction of the complex binary phase diagram despite the absence of solid-solid transition, further emphasizing how phase diagram determinations are an efficient tool for assessing the stability relationship between polymorphs. Moreover, the analysis of the crystal structures of all solid forms revealed that their crystal packings rely on comparable weak van der Waals interactions. However, interaction distances are shortened from (*RS-I*)-**3ag** to (*RS-III*)-**3ag**, aligning with their respective relative stability. Despite sharing similar structures, the solid-solid transition from (*RS-II*)-**3ag** to (*RS-III*)-**3ag** requires overcoming a high energy barrier due to the shifting of layers and rotation of molecules.

More importantly, this chapter disclosed a new approach compared to conventional binary conglomerate screening (*i.e.* either conglomerate or racemic compound) by considering the continuous evolution of the energetic difference ΔG^{Φ} occurring between stable racemic compounds and their associate metastable conglomerates. Intriguingly, more than half of the chiral systems studied exhibit a ΔG^{Φ} close to the thermal energy k_BT (*i.e.* < 2.1 kJ.mol^{-1}), which suggests that transitions between crystal phases with such energy differences are kinetically probable. Moreover, the distribution of ΔG^{Φ} within a library based on a single chemical core demonstrated the striking clustering of similar derivatives, further exhibiting strong crystal structure similarities although non-isomorphous, enabling methodological library design. Analogous to directed evolution in catalysis,[86–88] a rational derivatization strategy may be implemented by synthesizing a small library with very diverse entries that are ranked according to ΔG^{Φ} as a fitness parameter, after which the most favourable entry is selected for synthesis of the next generation of entries. This evolutionary strategy prevents that only unfavourable zones with high ΔG^{Φ} are screened, and instead iterate within only a few cycles towards favourable low ΔG^{Φ}. We foresee that making informed design choices may be further aided by integrating Crystal Structure Prediction (CSP) methodologies. Ultimately, combining advanced machine learning, CSP methods, and our directed evolution strategy may enable the rapid discovery of (kinetic) conglomerates.

Moreover, this thermal energy k_BT does not stand as an unbreachable boundary as this approach may also work for systems with higher ΔG^{Φ}, provided that suitable non-equilibrium conditions are found. Supporting this idea, ΔG^{Φ} does only describe the energy difference at the melting temperature of this higher-melting solid form, hence occulting any impact of temperature on crystal stability. Therefore, the determination of the *d.s.p.c* serves as a valuable tool for assessing the relative stability of the different solid forms in the working conditions. More specifically, this *d.s.p.c.* value also includes the impact of the solvent on both crystal forms, as demonstration by the large variation in *e.e.* of this value in case of the derivative **3ae** in toluene or IPA.

More importantly, we here show that enantiopure crystals can successfully be kinetically isolated from racemic mixtures by applying suitable non-equilibrium conditions, for instance in the case of the successful preferential crystallizations of derivatives **3t** and **3ae**. These successful preferential crystallization experiments demonstrate that the straightforward isolation of enantiopure crystal despite the presence of a more stable racemic compound, moreover in good yield, is not a specific trend observed for chiral derivative of 1,3-dimethylxanthine-based chiral derivatives. Instead, it may be rationalized by using ΔG^{Φ} as a diagnostic tool. The key next step is to systematically exploit non-equilibrium conditions under which crystallization rates, instead of thermodynamic stabilities alone, determine which crystalline phase is favoured such that for instance, the favoured kinetic conglomerate grows faster than the unfavoured racemic compound. Alternatively, specific non-equilibrium conditions can be exploited to supress the nucleation and growth rate of stable racemic compound crystals, such that the desired enantiopure crystals can be isolated. The crystallization process offers a large parameter space that can be exploited to achieve these favourable rates of nucleation and growth, ranging from choice of solvent, confinements such as microdroplets, and (chiral) additives to temperature gradients and mechanochemistry.[89–95]

Assessing the crystal nucleation rate and properties of the racemic and enantiopure phases from derivatives **3t** and **3ae** in IPA based on equations from the Classical Nucleation Theory (CNT) assuming a heterogenous nucleation mechanism[74–78] shows that γ_{ef}, which is a balance between the three interfacial energies (*i.e.* nucleus-solvent, nucleus-heterogeneous particles, solution-heterogeneous particle) is always higher for enantiopure crystal in IPA than the

racemic crystals, indicating a more energy-intensive nucleation of enantiopure crystals. By contrast, the pre-exponential factor A is about three times higher in case of the nucleation of enantiopure crystals, further emphasizing how enantiopure crystals may be kinetically favoured at the expense of more stable racemic crystals and therefore kinetically resolved using out-of-equilibrium methods. Although the difference of the exponential factor ΔB is of similar order of magnitude (0.58 and 1.08 for **3t** and **3ae** respectively), its implication in an exponential term induce a higher impact on the nucleation behaviour of **3ae**. It may explain the higher efficiency of the preferential crystallization of **3t** compared to **3ae**. However, these results must be interpreted with caution when comparing them to operational preferential crystallization: under operative conditions, the seed crystals are in equilibrium with an initial racemic solution, whereas in these nucleation rate measurements, the crystals are in equilibrium with an enantiopure solution. It would be of interest to compare this data in other solvents.

References

(1) Cioli, D.; Pica-Mattoccia, L. Praziquantel. *Parasitol Res* **2003**, *90* (S1), S3–S9. https://doi.org/10.1007/s00436-002-0751-z.

(2) Cioli, D.; Pica-Mattoccia, L.; Basso, A.; Guidi, A. Schistosomiasis Control: Praziquantel Forever? *Mol Biochem Parasitol* **2014**, *195* (1), 23–29. https://doi.org/10.1016/j.molbiopara.2014.06.002.

(3) Dömling, A.; Khoury, K. Praziquantel and Schistosomiasis. *ChemMedChem* **2010**, *5* (9), 1420–1434. https://doi.org/10.1002/cmdc.201000202.

(4) Lindenberg, M.; Kopp, S.; Dressman, J. B. Classification of Orally Administered Drugs on the World Health Organization Model List of Essential Medicines According to the Biopharmaceutics Classification System. *European Journal of Pharmaceutics and Biopharmaceutics* **2004**, *58* (2), 265–278. https://doi.org/10.1016/j.ejpb.2004.03.001.

(5) D'Abbrunzo, I.; Procida, G.; Perissutti, B. Praziquantel Fifty Years on: A Comprehensive Overview of Its Solid State. *Pharmaceutics* **2023**, *16* (1), 27. https://doi.org/10.3390/pharmaceutics16010027.

(6) Dinora, G.-E.; Julio, R.; Nelly, C.; Lilian, Y.-M.; Cook, H. J. In Vitro Characterization of Some Biopharmaceutical Properties of Praziquantel. *International Journal of Pharmaceutics* **2005**, *295* (1), 93–99. https://doi.org/10.1016/j.ijpharm.2005.01.033.

(7) Jung-Cook, H. Pharmacokinetic Variability of Anthelmintics: Implications for the Treatment of Neurocysticercosis. *Expert Review of Clinical Pharmacology* **2012**, *5* (1), 21–30. https://doi.org/10.1586/ecp.11.72.

(8) Bagchus, W. M.; Bezuidenhout, D.; Harrison-Moench, E.; Kourany-Lefoll, E.; Wolna, P.; Yalkinoglu, O. Relative Bioavailability of Orally Dispersible Tablet Formulations of Levo- and Racemic Praziquantel: Two Phase I Studies. *Clinical and Translational Science* **2019**, *12* (1), 66–76. https://doi.org/10.1111/cts.12601.

(9) Kovač, J.; Vargas, M.; Keiser, J. In Vitro and in Vivo Activity of R- and S- Praziquantel Enantiomers and the Main Human Metabolite Trans-4-Hydroxy-Praziquantel against Schistosoma Haematobium. *Parasites Vectors* **2017**, *10* (1), 365. https://doi.org/10.1186/s13071-017-2293-3.

(10) Shu-Hua, X.; Catto, B. A. Comparative in Vitro and in Vivo Activity of Racemic Praziquantel and Its Levorotated Isomer on Schistosoma Mansoni. *The Journal of Infectious Diseases* **1989**, *159* (3), 589–592. https://doi.org/10.1093/infdis/159.3.589.

(11) Meister, I.; Ingram-Sieber, K.; Cowan, N.; Todd, M.; Robertson, M. N.; Meli, C.; Patra, M.; Gasser, G.; Keiser, J. Activity of Praziquantel Enantiomers and Main Metabolites against Schistosoma Mansoni. *Antimicrob Agents Chemother* **2014**, *58* (9), 5466–5472. https://doi.org/10.1128/AAC.02741-14.

(12) Gerard, C. J. J.; Pinetre, C.; Cercel, H.; Charpentier, M. D.; Sanselme, M.; Couvrat, N.; Brandel, C.; Cartigny, Y.; Dupray, V.; ter Horst, J. H. Phase Diagrams of Praziquantel and Vanillic Acid Cocrystals: Racemic Compound and Conglomerate System. *Crystal Growth & Design* **2024**. https://doi.org/10.1021/acs.cgd.4c00114.

(13) Rapeenun, P.; Gerard, C. J. J.; Pinètre, C.; Cartigny, Y.; Tinnemans, P.; de Gelder, R.; Flood, A. E.; ter Horst, J. H. Searching for Conglomerate Cocrystals of the Racemic Compound Praziquantel. *Crystal Growth & Design* **2024**, *24* (1), 480–490. https://doi.org/10.1021/acs.cgd.3c01158.

(14) El-Arini, S. K.; Giron, D.; Leuenberger, H. Solubility Properties of Racemic Praziquantel and Its Enantiomers. *Pharmaceutical Development and Technology* **1998**, *3* (4), 557–564. https://doi.org/10.3109/10837459809028638.

(15) Buol, X.; Caro Garrido, C.; Robeyns, K.; Tumanov, N.; Collard, L.; Wouters, J.; Leyssens, T. Chiral Resolution of Mandelic Acid through Preferential Cocrystallization with Nefiracetam. *Crystal Growth & Design* **2020**, *20* (12), 7979–7988. https://doi.org/10.1021/acs.cgd.0c01236.

(16) Woelfle, M.; Seerden, J.-P.; de Gooijer, J.; Pouwer, K.; Olliaro, P.; Todd, M. H. Resolution of Praziquantel. *PLoS Negl Trop Dis* **2011**, *5* (9), e1260. https://doi.org/10.1371/journal.pntd.0001260.

(17) Valenti, G.; Tinnemans, P.; Baglai, I.; Noorduin, W. L.; Kaptein, B.; Leeman, M.; ter Horst, J. H.; Kellogg, R. M. Combining Incompatible Processes for Deracemization of a Praziquantel Derivative under Flow Conditions. *Angew. Chem.* **2021**, *133* (10), 5339–5342. https://doi.org/10.1002/ange.202013502.

(18) Agranat, I.; Wainschtein, S. R.; Zusman, E. Z. The Predicated Demise of Racemic New Molecular Entities Is an Exaggeration. *Nat Rev Drug Discov* **2012**, *11* (12), 972–973. https://doi.org/10.1038/nrd3657-c1.

(19) Otero-de-la-Roza, A.; Cao, B. H.; Price, I. K.; Hein, J. E.; Johnson, E. R. Predicting the Relative Solubilities of Racemic and EnantiopureCrystals by Density-Functional Theory. *Angew. Chem. Int. Ed.* **2014**, *53* (30), 7879–7882. https://doi.org/10.1002/anie.201403541.

(20) Zheng, Y.; Wang, X.; Wu, Z. Machine Learning Modeling and Predictive Control of the Batch Crystallization Process. *Ind. Eng. Chem. Res.* **2022**, *61* (16), 5578–5592. https://doi.org/10.1021/acs.iecr.2c00026.
(21) Lu, M.; Rao, S.; Yue, H.; Han, J.; Wang, J. Recent Advances in the Application of Machine Learning to Crystal Behavior and Crystallization Process Control. *Crystal Growth & Design* **2024**. https://doi.org/10.1021/acs.cgd.3c01251.
(22) Clevers, S.; Coquerel, G. Kryptoracemic Compounds Hunting and Frequency in the Cambridge Structural Database. *CrystEngComm* **2018**, *20* (15), 2093–2101. https://doi.org/10.1039/C8CE00075A.
(23) Rekis, T. Crystallization of Chiral Molecular Compounds: What Can Be Learned from the Cambridge Structural Database? *Acta Crystallogr B Struct Sci Cryst Eng Mater* **2020**, *76* (3), 307–315. https://doi.org/10.1107/S2052520620003601.
(24) Jacques, J.; Collet, A.; Wilen, S. H. *Enantiomers, Racemates, and Resolutions*; Krieger Publishing Company: Malabar, 1994.
(25) Baglai, I.; Leeman, M.; Kellogg, R. M.; Noorduin, W. L. A Viedma Ripening Route to an Enantiopure Building Block for Levetiracetam and Brivaracetam. *Org. Biomol. Chem.* **2018**, *17* (1), 35–38. https://doi.org/10.1039/C8OB02660B.
(26) van der Meijden, M. W.; Leeman, M.; Gelens, E.; Noorduin, W. L.; Meekes, H.; van Enckevort, W. J. P.; Kaptein, B.; Vlieg, E.; Kellogg, R. M. Attrition-Enhanced Deracemization in the Synthesis of Clopidogrel - A Practical Application of a New Discovery. *Org. Process Res. Dev.* **2009**, *13* (6), 1195–1198. https://doi.org/10.1021/op900243c.
(27) Wilmink, P.; Rougeot, C.; Wurst, K.; Sanselme, M.; Van Der Meijden, M.; Saletra, W.; Coquerel, G.; Kellogg, R. M. Attrition Induced Deracemisation of 2-Fluorophenylglycine. *Org. Process Res. Dev.* **2015**, *19* (1), 302–308. https://doi.org/10.1021/op500352m.
(28) Baglai, I.; Leeman, M.; Wurst, K.; Kaptein, B.; Kellogg, R. M.; Noorduin, W. L. The Strecker Reaction Coupled to Viedma Ripening: A Simple Route to Highly Hindered Enantiomerically Pure Amino Acids. *Chem. Commun.* **2018**, *54* (77), 10832–10834. https://doi.org/10.1039/C8CC06658B.
(29) Marchand, P.; Lefèbvre, L.; Querniard, F.; Cardinaël, P.; Perez, G.; Counioux, J.-J.; Coquerel, G. Diastereomeric Resolution Rationalized by Phase Diagrams under the Actual Conditions of the Experimental Process. *Tetrahedron: Asymmetry* **2004**, *15* (16), 2455–2465. https://doi.org/10.1016/j.tetasy.2004.06.044.
(30) Petit, S.; Coquerel, G. Mechanism of Several Solid−Solid Transformations between Dihydrated and Anhydrous Copper(II) 8-Hydroxyquinolinates. Proposition for a Unified Model for the Dehydration of Molecular Crystals. *Chem. Mater.* **1996**, *8* (9), 2247–2258. https://doi.org/10.1021/cm9600438.
(31) Cedillo–Cruz, A.; Villalobos–López, D. C.; Aguilar, M. I.; Trejo–Soto, P. J.; Hernández–Campos, A.; Jung–Cook, H. Praziquanamine Enantiomers: Crystal Structure, Hirshfeld Surface Analysis, and Quantum Chemical Studies. *Journal of Molecular Structure* **2023**, *1283*, 135343. https://doi.org/10.1016/j.molstruc.2023.135343.
(32) Coquerel, G.; Sanselme, M.; Lafontaine, A. Method of Measuring Scattering of X-Rays, Its Applications and Implementation Device. WO2012/136921, October 11, 2012.
(33) Pinètre, C.; Ritou, L.; Gerard, C. J. J.; Cercel, H.; Leeman, M.; Kellogg, R. M.; Tinnemans, P.; Sanselme, M.; Brandel, C.; Dupray, V.; ter Horst, J. H. Rare Case of Polymorphism in the Binary System of Enantiomers of a Praziquantel Derivative. *Org. Process Res. Dev.* **2024**. https://doi.org/10.1021/acs.oprd.4c00035.
(34) Burger, A.; Ramberger, R. On the Polymorphism of Pharmaceuticals and Other Molecular Crystals. I. *Mikrochim Acta* **1979**, *72* (3–4), 259–271. https://doi.org/10.1007/BF01197379.
(35) Prigogine, I.; Defay, R. Chemical Thermodynamics. **1958**.
(36) Threlfall, T. Structural and Thermodynamic Explanations of Ostwald's Rule. *Org. Process Res. Dev.* **2003**, *7* (6), 1017–1027. https://doi.org/10.1021/op030026l.
(37) Hoquante, M.; Sanselme, M.; Rietveld, I. B.; Coquerel, G. Disappearing Conglomerates, Assessment of the Threat. *Crystal Growth & Design* **2019**, *19* (12), 7396–7401. https://doi.org/10.1021/acs.cgd.9b01316.
(38) A. Hunter, C.; R. Lawson, K.; Perkins, J.; J. Urch, C. Aromatic Interactions. *Journal of the Chemical Society, Perkin Transactions 2* **2001**, *0* (5), 651–669. https://doi.org/10.1039/B008495F.
(39) Dunitz, J. D. Weak Interactions in Molecular Crystals. In *Implications of Molecular and Materials Structure for New Technologies*; Howard, J. A. K., Allen, F. H., Shields, G. P., Eds.; Springer Netherlands: Dordrecht, 1999; pp 175–184. https://doi.org/10.1007/978-94-011-4653-1_12.
(40) Hunter, C. A.; Sanders, J. K. M. The Nature of .Pi.-.Pi. Interactions. *J. Am. Chem. Soc.* **1990**, *112* (14), 5525–5534. https://doi.org/10.1021/ja00170a016.

(41) Kruszynski, R.; Sierański, T. Can Stacking Interactions Exist Beyond the Commonly Accepted Limits? *Crystal Growth & Design* **2016**, *16* (2), 587–595. https://doi.org/10.1021/acs.cgd.5b00852.
(42) Steiner, T.; Desiraju, G. R. Distinction between the Weak Hydrogen Bond and the van Der Waals Interaction. *Chemical Communications* **1998**, *0* (8), 891–892. https://doi.org/10.1039/A708099I.
(43) Carpenter, J. E.; Grünwald, M. Pre-Nucleation Clusters Predict Crystal Structures in Models of Chiral Molecules. *J. Am. Chem. Soc.* **2021**, *143* (51), 21580–21593. https://doi.org/10.1021/jacs.1c09321.
(44) Goodall, R. E. A.; Lee, A. A. Predicting Materials Properties without Crystal Structure: Deep Representation Learning from Stoichiometry. *Nat Commun* **2020**, *11* (1), 6280. https://doi.org/10.1038/s41467-020-19964-7.
(45) Ricci, J. E. The Phase Rule and Heterogeneous Equilibrium. In *The Phase Rule and Heterogeneous Equilibrium*; Dover: New York, 1951.
(46) Gibbs, J. W. (Josiah W.; Tyndall, J.; Connecticut Academy of Arts and Sciences; Burndy Library, donor D. *On the Equilibrium of Heterogeneous Substances*; [New Haven : Published by the Academy], 1874.
(47) Kocevska, S.; Burcham, C. L.; Nordstrom, F.; Maggioni, G. M. A Changing Paradigm in Industrial Pharmaceutical Crystallization. *Nat Chem Eng* **2024**, *1* (5), 327–329. https://doi.org/10.1038/s44286-024-00068-8.
(48) Sacchi, P.; Wright, S. E.; Neoptolemou, P.; Lampronti, G. I.; Rajagopalan, A. K.; Kras, W.; Evans, C. L.; Hodgkinson, P.; Cruz-Cabeza, A. J. Crystal Size, Shape, and Conformational Changes Drive Both the Disappearance and Reappearance of Ritonavir Polymorphs in the Mill. *Proceedings of the National Academy of Sciences* **2024**, *121* (15), e2319127121. https://doi.org/10.1073/pnas.2319127121.
(49) Engwerda, A. H. J.; Meekes, H.; Kaptein, B.; Rutjes, F. P. J. T.; Vlieg, E. Speeding up Viedma Ripening. *Chem. Commun.* **2016**, *52* (81), 12048–12051. https://doi.org/10.1039/C6CC06766B.
(50) Spix, L.; Meekes, H.; Blaauw, R. H.; van Enckevort, W. J. P.; Vlieg, E. Complete Deracemization of Proteinogenic Glutamic Acid Using Viedma Ripening on a Metastable Conglomerate. *Crystal Growth & Design* **2012**, *12* (11), 5796–5799. https://doi.org/10.1021/cg301343a.
(51) Harfouche, L. C.; Brandel, C.; Cartigny, Y.; ter Horst, J. H.; Coquerel, G.; Petit, S. Enabling Direct Preferential Crystallization in a Stable Racemic Compound System. *Mol. Pharmaceutics* **2019**, *16* (11), 4670–4676. https://doi.org/10.1021/acs.molpharmaceut.9b00805.
(52) Brandel, C.; Amharar, Y.; Rollinger, J. M.; Griesser, U. J.; Cartigny, Y.; Petit, S.; Coquerel, G. Impact of Molecular Flexibility on Double Polymorphism, Solid Solutions and Chiral Discrimination during Crystallization of Diprophylline Enantiomers. *Mol. Pharmaceutics* **2013**, *10* (10), 3850–3861. https://doi.org/10.1021/mp400308u.
(53) Brandel, C.; Cartigny, Y.; Coquerel, G.; ter Horst, J. H.; Petit, S. Prenucleation Self-Assembly and Chiral Discrimination Mechanisms during Solution Crystallisation of Racemic Diprophylline. *Chemistry—A European Journal* **2016**, *22* (45), 16103–16112. https://doi.org/10.1002/chem.201602707.
(54) He, Q.; Rohani, S.; Zhu, J.; Gomaa, H. Crystallization of the Racemic Compound and Conglomerate of (RS)-2-Chloromandelic Acid. *Crystal Growth & Design* **2010**, *10* (12), 5136–5145. https://doi.org/10.1021/cg100879p.
(55) Gavezzotti, A.; Rizzato, S. Are Racemic Crystals Favored over Homochiral Crystals by Higher Stability or by Kinetics? Insights from Comparative Studies of Crystalline Stereoisomers. *J. Org. Chem.* **2014**, *79* (11), 4809–4816. https://doi.org/10.1021/jo500528k.
(56) Leclercq, M.; Collet, A.; Jacques, J. Etude Des Melanges d'antipodes Optiques—XII: Mesure de La Stabilite Des Racemiques Vrais. *Tetrahedron* **1976**, *32* (7), 821–828. https://doi.org/10.1016/0040-4020(76)80007-5.
(57) Brammer, L.; Bruton, E. A.; Sherwood, P. Understanding the Behavior of Halogens as Hydrogen Bond Acceptors. *Crystal Growth & Design* **2001**, *1* (4), 277–290. https://doi.org/10.1021/cg015522k.
(58) Csöregh, I.; Brehmer, T.; Bombicz, P.; Weber, E. Halogen···halogen versus OH···O Supramolecular Interactions in the Crystal Structures of a Series of Halogen and Methyl Substituted Cis-9,10-Diphenyl-9,10-Dihydroanthracene-9,10-Diols. *Crystal Engineering* **2001**, *4* (4), 343–357. https://doi.org/10.1016/S1463-0184(01)00026-0.
(59) Desiraju, P. The Nature of Halogen...Halogen Interactions: Are Short Halogen Contacts Due to Specific Attractive Forces or Due to Close Packing of Non Spherical Atoms.
(60) Politzer, P.; Lane, P.; Concha, M. C.; Ma, Y.; Murray, J. S. An Overview of Halogen Bonding. *J Mol Model* **2007**, *13* (2), 305–311. https://doi.org/10.1007/s00894-006-0154-7.
(61) Borchardt-Setter, K. A.; Yu, L. Assessing the Potential for Chiral Separation by Crystallization Using Crystal Energies. *Crystal Growth & Design* **2023**, *23* (5), 3615–3622. https://doi.org/10.1021/acs.cgd.3c00077.

(62) Beran, G. J. O.; Sugden, I. J.; Greenwell, C.; Bowskill, D. H.; Pantelides, C. C.; Adjiman, C. S. How Many More Polymorphs of ROY Remain Undiscovered. *Chem. Sci.* **2022**, *13* (5), 1288–1297. https://doi.org/10.1039/D1SC06074K.
(63) Li, Z. J.; Zell, M. T.; Munson, E. J.; Grant, D. J. W. Characterization of Racemic Species of Chiral Drugs Using Thermal Analysis, Thermodynamic Calculation, and Structural Studies. *Journal of Pharmaceutical Sciences* **1999**, *88* (3), 337–346. https://doi.org/10.1021/js980205u.
(64) Collet, A.; Ziminski, L.; Garcia, C.; Vigné-Maeder, F. Chiral Discrimination in Crystalline Enantiomer Systems: Facts, Interpretations, and Speculations. In *Supramolecular Stereochemistry*; Siegel, J. S., Ed.; Springer Netherlands: Dordrecht, 1995; pp 91–110. https://doi.org/10.1007/978-94-011-0353-4_12.
(65) Wang, Y.; Chen, A. M. Enantioenrichment by Crystallization. *Org. Process Res. Dev.* **2008**, *12* (2), 282–290. https://doi.org/10.1021/op700239a.
(66) Bredikhin, A. A.; Bredikhina, Z. A.; Novikona, V. G.; Pashagin, A. V.; Zacharychev, D. V.; Gubaidullin, A. T. Three Different Types of Chirality-Driven Crystallization within the Series of Uniformly Substituted Phenyl Glycerol Ethers. *Chirality* **2008**, *20*, 1092–1103. https://doi.org/10.1002/chir.20648.
(67) Coquerel, G. Preferential Crystallization. In *Novel Optical Resolution Technologies*; Sakai, K., Hirayama, N., Tamura, R., Eds.; Springer: Berlin, Heidelberg, 2007; pp 1–51. https://doi.org/10.1007/128_2006_077.
(68) Kaptein, B.; Noorduin, W. L.; Meekes, H.; van Enckevort, W. J. P.; Kellogg, R. M.; Vlieg, E. Attrition-Enhanced Deracemization of an Amino Acid Derivative That Forms an Epitaxial Racemic Conglomerate. *Angewandte Chemie International Edition* **2008**, *47* (38), 7226–7229. https://doi.org/10.1002/anie.200802468.
(69) van Enckevort, W. J. P. On the Crystallization of Epitaxial Racemic Conglomerates. *J. Phys. Chem. C* **2010**, *114* (49), 21593–21604. https://doi.org/10.1021/jp108527h.
(70) Wermester, N.; Aubin, E.; Pauchet, M.; Coste, S.; Coquerel, G. Preferential Crystallization in an Unusual Case of Conglomerate with Partial Solid Solutions. *Tetrahedron: Asymmetry* **2007**, *18* (7), 821–831. https://doi.org/10.1016/j.tetasy.2007.03.011.
(71) Levilain, G.; Coquerel, G. Pitfalls and Rewards of Preferential Crystallization. *CrystEngComm* **2010**, *12* (7), 1983–1992. https://doi.org/10.1039/C001895C.
(72) Xu, S.; Cao, D.; Liu, Y.; Wang, Y. Role of Additives in Crystal Nucleation from Solutions: A Review. *Crystal Growth & Design* **2022**, *22* (3), 2001–2022. https://doi.org/10.1021/acs.cgd.1c00776.
(73) Pinetre, C.; Harfouche, L.; Brandel, C.; Bendeif, E.-E.; Sanselme, M.; Cartigny, Y.; Couvrat, N.; Dupray, V. Investigation of the Binary System of Proxyphylline Enantiomers: Structural Resolution and Phase Diagram Determination. *Mol. Pharmaceutics* **2024**, *21* (2), 845–853. https://doi.org/10.1021/acs.molpharmaceut.3c00922.
(74) Brandel, C.; ter Horst, J. H. Measuring Induction Times and Crystal Nucleation Rates. *Faraday Discuss.* **2015**, *179*, 199–214. https://doi.org/10.1039/C4FD00230J.
(75) Sullivan, R. A.; Davey, R. J.; Sadiq, G.; Dent, G.; Back, K. R.; ter Horst, J. H.; Toroz, D.; Hammond, R. B. Revealing the Roles of Desolvation and Molecular Self-Assembly in Crystal Nucleation from Solution: Benzoic and p-Aminobenzoic Acids. *Crystal Growth & Design* **2014**, *14* (5), 2689–2696. https://doi.org/10.1021/cg500441g.
(76) Auer, S.; Frenkel, D. Prediction of Absolute Crystal-Nucleation Rate in Hard-Sphere Colloids. *Nature* **2001**, *409* (6823), 1020–1023. https://doi.org/10.1038/35059035.
(77) Kashchiev, D. *Nucleation Basic Theory with Applications*; Butterworth-Heinemann: Oxford, 2000.
(78) Liu, X. Y. Heterogeneous Nucleation or Homogeneous Nucleation? *The Journal of Chemical Physics* **2000**, *112* (22), 9949–9955. https://doi.org/10.1063/1.481644.
(79) George, F.; Norberg, B.; Wouters, J.; Leyssens, T. Structural Investigation of Substituent Effect on Hydrogen Bonding in (S)-Phenylglycine Amide Benzaldimines. *Crystal Growth & Design* **2015**, *15* (8), 4005–4019. https://doi.org/10.1021/acs.cgd.5b00621.
(80) Borrego-Sánchez, A.; Viseras, C.; Aguzzi, C.; Sainz-Díaz, C. I. Molecular and Crystal Structure of Praziquantel. Spectroscopic Properties and Crystal Polymorphism. *European Journal of Pharmaceutical Sciences* **2016**, *92*, 266–275. https://doi.org/10.1016/j.ejps.2016.04.023.
(81) Charpentier, M. D. Crystallization in Multicomponent Chiral Systems: Thermodynamic Characterization and Guidelines for Chiral Resolution of Racemic Compounds with Cocrystallization, University of Strathclyde, 2023. https://stax.strath.ac.uk/concern/theses/6q182k65j.
(82) Nyman, J.; Day, G. M. Static and Lattice Vibrational Energy Differences between Polymorphs. *CrystEngComm* **2015**, *17* (28), 5154–5165. https://doi.org/10.1039/C5CE00045A.

(83) Pinto, S. S.; Diogo, H. P. Thermochemical Study of Two Anhydrous Polymorphs of Caffeine. *The Journal of Chemical Thermodynamics* **2006**, *38* (12), 1515–1522. https://doi.org/10.1016/j.jct.2006.04.008.
(84) Sacchi, P.; Neoptolemou, P.; J. Davey, R.; M. Reutzel-Edens, S.; J. Cruz-Cabeza, A. Do Metastable Polymorphs Always Grow Faster? Measuring and Comparing Growth Kinetics of Three Polymorphs of Tolfenamic Acid. *Chemical Science* **2023**, *14* (42), 11775–11789. https://doi.org/10.1039/D3SC02040A.
(85) Lévesque, A.; Maris, T.; Wuest, J. D. ROY Reclaims Its Crown: New Ways To Increase Polymorphic Diversity. *J. Am. Chem. Soc.* **2020**, *142* (27), 11873–11883. https://doi.org/10.1021/jacs.0c04434.
(86) Arnold, F. H. Directed Evolution: Bringing New Chemistry to Life. *Angewandte Chemie International Edition* **2018**, *57* (16), 4143–4148. https://doi.org/10.1002/anie.201708408.
(87) Yang, K. K.; Wu, Z.; Arnold, F. H. Machine-Learning-Guided Directed Evolution for Protein Engineering. *Nat Methods* **2019**, *16* (8), 687–694. https://doi.org/10.1038/s41592-019-0496-6.
(88) Romero, P. A.; Arnold, F. H. Exploring Protein Fitness Landscapes by Directed Evolution. *Nat Rev Mol Cell Biol* **2009**, *10* (12), 866–876. https://doi.org/10.1038/nrm2805.
(89) Candoni, N.; Grossier, R.; Lagaize, M.; Veesler, S. Advances in the Use of Microfluidics to Study Crystallization Fundamentals. *Annual Review of Chemical and Biomolecular Engineering* **2019**, *10* (Volume 10, 2019), 59–83. https://doi.org/10.1146/annurev-chembioeng-060718-030312.
(90) Gu, C. H.; Young, V.; Grant, D. J. Polymorph Screening: Influence of Solvents on the Rate of Solvent-Mediated Polymorphic Transformation. *J Pharm Sci* **2001**, *90* (11), 1878–1890. https://doi.org/10.1002/jps.1137.
(91) Belenguer, A. M.; Lampronti, G. I.; De Mitri, N.; Driver, M.; Hunter, C. A.; Sanders, J. K. M. Understanding the Influence of Surface Solvation and Structure on Polymorph Stability: A Combined Mechanochemical and Theoretical Approach. *J. Am. Chem. Soc.* **2018**, *140* (49), 17051–17059. https://doi.org/10.1021/jacs.8b08549.
(92) Linberg, K.; C. Sander, P.; Emmerling, F.; L. Michalchuk, A. A. In Situ Investigation of Controlled Polymorphism in Mechanochemistry at Elevated Temperature. *RSC Mechanochemistry* **2024**, *1* (1), 43–49. https://doi.org/10.1039/D3MR00019B.
(93) M. Belenguer, A.; I. Lampronti, G.; J. Cruz-Cabeza, A.; A. Hunter, C.; M. Sanders, J. K. Solvation and Surface Effects on Polymorph Stabilities at the Nanoscale. *Chemical Science* **2016**, *7* (11), 6617–6627. https://doi.org/10.1039/C6SC03457H.
(94) Yeom, J.; Yeom, B.; Chan, H.; Smith, K. W.; Dominguez-Medina, S.; Bahng, J. H.; Zhao, G.; Chang, W.-S.; Chang, S.-J.; Chuvilin, A.; Melnikau, D.; Rogach, A. L.; Zhang, P.; Link, S.; Král, P.; Kotov, N. A. Chiral Templating of Self-Assembling Nanostructures by Circularly Polarized Light. *Nature Mater* **2015**, *14* (1), 66–72. https://doi.org/10.1038/nmat4125.
(95) Weissbuch, I.; Lahav, M. Crystalline Architectures as Templates of Relevance to the Origins of Homochirality. *Chem. Rev.* **2011**, *111* (5), 3236–3267. https://doi.org/10.1021/cr1002479.

CHAPTER IV

TOWARD A GENERALIZED DIRECTED EVOLUTION: THE CASE OF PROXYPHYLLINE

IV.1 - Introduction

The previous chapter presented a robust directed evolution strategy based on the ΔG^{Φ} ranking of molecular derivatives that mostly form racemic compounds. We have shown that chemically related chiral molecules often clusters into families with similar ΔG^{Φ} values and similar structural features. It gives general hints to identify chiral systems whose energy difference between racemic and enantiopure phases is low and for which chiral resolution can be envisaged by playing with kinetics, despite the quasi-systematic presence of stable racemic compounds. Although this process could be further enhanced by Crystal Structure Prediction (CSP) and machine-learning methodologies, the identification of specific molecular features favouring the crystallization of enantiopure crystals could enhance the accuracy and rationality of design choices. Among the reported systems assessing the generality of our directed evolution strategy in the previous chapter (Figure III - 37), two are 1,3-dimethylxanthine-based chiral APIs derived from theophylline (TPH, Figure IV - 1A) used for the treatment of obstructive airway diseases:[1–3] diprophylline (Figure IV - 1B, DPL hereafter, ΔG^{Φ} = 1.00 kJ.mol^{-1}) and proxyphylline (Figure IV - 1C, PXL hereafter, ΔG^{Φ} = 2.01 kJ.mol^{-1}). It is worth noting that PXL and DPL share significant molecular similarities, echoing our derivatization strategy involving a single chemical core.

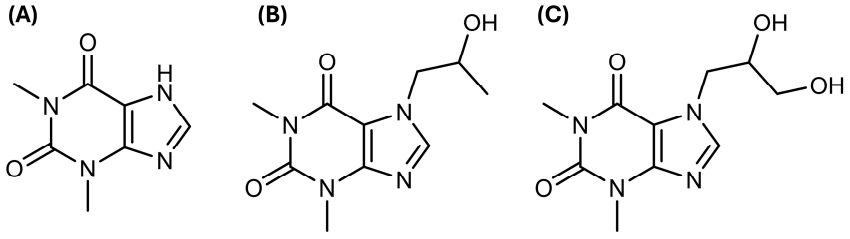

Figure IV - 1. Chemical structure of (A) theophylline, (B) proxyphylline and (C) diprophylline.

Brandel *et al*.[4,5] described the complex crystallization behaviour of DPL and demonstrated the significant impact of the molecular flexibility associated to the diisopropyl moiety on the crystallization outcomes. This molecular flexibility results in a very versatile crystallization behaviour and the binary phase diagram between DPL enantiomers exhibits no less than a stable racemic compound, two metastable solid solutions and a metastable conglomerate.[6] The conformational diversity of DPL enantiomers also gives rise to several type of self-associations at the solvated state that can be modulated by changing the solvent, resulting in

different crystallization behaviours. For instance, some solvents triggered the fast crystallization of one of the solid solutions, whereas other solvents markedly inhibited the spontaneous nucleation of any solid phases. Such specific nucleation behaviour provided ideal non-equilibrium conditions for chiral resolution and DPL enantiomers have already been resolved by preferential crystallization despite the existence of many unselective phases in this system.[6]

PXL is another chiral derivative of TPH which shows some degree of molecular flexibility. The mixture of PXL enantiomers was also known to crystallize as a stable racemic compound.[7] Based on the same assumption that preferential crystallization could be performed if the crystallization of the racemic compound is delayed by a suitable choice of solvent, a screening of solvent was performed by Harfouche *et al.*[8] The target was to evidence conditions in which spontaneous nucleation of that racemic compound was inhibited to the benefit of enantiopure seeding, without the need to evidence any metastable conglomerate. With this methodology, PXL enantiomers could be successfully resolved by preferential crystallization,[8,9] although the efficacy of that process was lower compared to that of DPL due to less favourable kinetics, involving the recrystallization of the racemic compound. In addition, let us note that the solid-state landscape of the system of PXL enantiomers and associated crystal structures was unknown.[8,9]

These notorious, yet isolated, case studies exhibiting similar trends prompt the question about how much the flexibility and increased H-bonding capacity of the flexible moieties of these TPH derivatives is responsible for nucleation inhibition and, in turn, to preferential crystallization success. Since it is shown that DPL is more efficiently resolved than PXL by using preferential crystallization, would the nucleation of another TPH derivative with a more flexible moiety be easier to inhibit? Also, we can wonder if a moiety bearing more H-bond donors would give rise to better odds regarding our approach to preferential crystallization. Would such chemical modifications be also accompanied by a lowering of ΔG^{Φ}? Or even better, to the formation of a stable conglomerate?

In this chapter, we will first establish a clearer picture of the solid-state landscape between PXL enantiomers. This was a missing point when the present work was engaged, and such knowledge needed to be obtained. Then, we will take another step with reference to our

directed evolution strategy presented in chapter 3: several chiral derivatives of TPH will be synthesized with a logical increase in H-bonding capacity associated to the flexible moiety. Thus, the derivation strategy is conducted by correlating the thermodynamic aspects and ΔG^{Φ} calculations along with a rational design regarding the structural modification themselves. This approach would permit a better understanding of the molecular origins that favour the existence of crystallization conditions that are suitable for preferential crystallization and could help to understand the molecular origin of conglomerate formation.

IV.2 - Establishing the solid-state landscape between PXL enantiomers

The content of the present section has been published in the Molecular Pharmaceutics journal.[10] The phase behaviour of racemic PXL was previously investigated by Griesser *et al*.[7] in 2000, by using DSC, FTIR, Raman spectroscopy and Hot Stage Microscopy. This study highlighted the presence of three different racemic solid phases (labelled "Modifications" by the authors): Mod. I (melting at 133.5 °C), Mod. II (melting at 113.5 °C) and Mod. III (melting at 82-85 °C). Their solid-state behaviour with regards to the packing of enantiomers (*i.e.* racemic compound, conglomerate or solid solution) were unknown. Harfouche *et al.* evidenced the existence of a stable racemic compound but many aspects of the binary system between PXL enantiomers was unknown.

IV.2.1- Crystallization behaviour of enantiopure PXL

After the synthesis, crystallization from ethanol of the pure enantiomer of PXL, *i.e.* (*R*)-PXL, resulted in the isolation of a single solid phase. Indeed, changing the crystallization solvent (limited to polar protic solvents) or crystallization conditions (*i.e.* evaporation, cooling or antisolvent) had no impact on the solid form produced. The solid form, labelled EI in consistency with the phase labels of DPL,[4] is analyzed by DSC, revealing a single melting endotherm at T_m^{EI} = 148.3 °C with a melting enthalpy of ΔH_m^{EI} = 25.6 kJ.mol^{-1} (Figure IV - 2c). No mass loss is recorded upon heating, indicating the absence of any solvated crystal structure. The XRPD pattern of EI is shown in Figure IV - 2a.

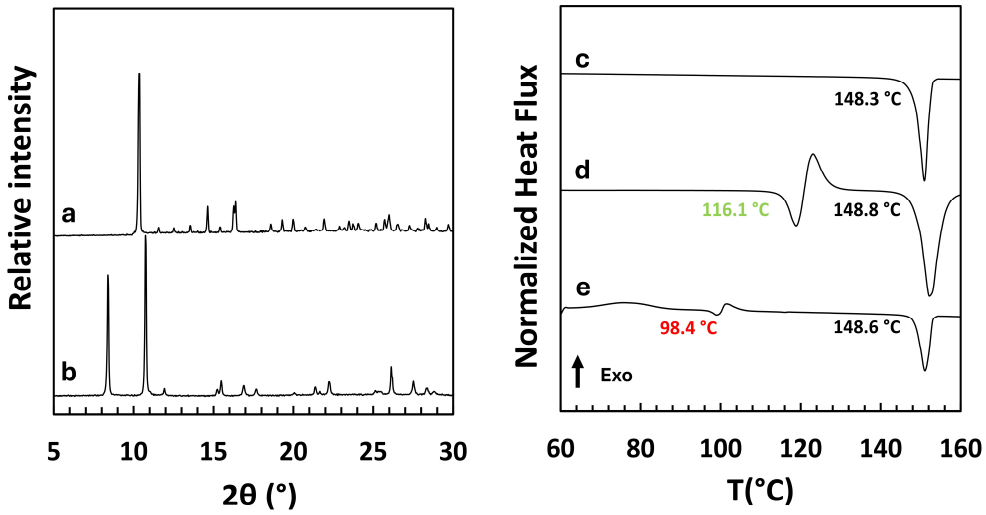

Figure IV - 2. XRPD patterns of (a) EI (b) EII. DSC thermograms obtained upon heating: (c) EI at 5 K.min^{-1}, (d) the SCM annealed at 80°C for 30min before heating at 20 K.min^{-1}, (e) the SCM at 10 K.min^{-1}.

The absence of detectable thermal degradation in this temperature range prompted us to explore the crystallization of (*R*)-PXL from the supercooled melt (SCM).[11] After melting (*R*)-PXL and rapid cooling to room temperature, storing the SCM at 20 °C for several hours results in the crystallization of EI (confirmed by both XRPD and DSC measurements, data not shown). However, a different solid phase is obtained by annealing the SCM at 80 °C for 30 minutes, as indicated by the measured XRPD pattern (Figure IV - 2b). Upon heating at 20 K.min^{-1}, the DSC analysis (Figure IV - 2d) shows: (i) an endotherm at 116.1 °C compensated by (ii) an exotherm at ca. 123 °C and (iii) a second endotherm at 148.8 °C, corresponding to the melting temperature of EI. This suggests that a new crystal form of (*R*)-PXL, labelled EII, crystallizes from the SCM in these conditions. Upon heating, its melting occurs at T_m^{EII} = 116.1 °C (Table IV - 1) but is calorimetrically compensated by the concomitant crystallization of EI.

Table IV - 1. Thermochemical data collected by DSC for the different forms of PXL pure enantiomer. The melting enthalpies of EII and EIII could not be experimentally measured.

Forms	Preparation	T_{fus}^{onset} (°C)	ΔH_{fus} (kJ.mol^{-1})
EI	SC[a]	148.3	25.6
EII	SCMA[b]	116.1	n/a
EIII	SCM[c]	98.4	n/a

[a]Solvent crystallization. [b]SuperCooled Melt annealing (at 80°C for 30min).[c] Heating the SuperCooled Melt at 10K.min^{-1}.

Slower or faster heating rate (1 or 50 K.min^{-1}, data not shown) did not allow to deconvolute these two events. As a result, the melting enthalpy of EII could not be reliably measured.

Hot Stage Microscopy (HSM) observations are performed to support these interpretations. EI is first melted at 150°C between two microscopy glass cover slides, quenched at 25°C and the obtained SCM is annealed at 80°C. During this annealing process, the formation of snowflake-shaped crystals is observed after a single minute although complete crystallization occurred after 45 minutes (Figure IV - 3a). Upon subsequent heating at 20 K.min^{-1}, the snowflake-shaped crystals melt at ca. 115 °C while another population of irregular-shaped spherulite crystals simultaneously crystallizes from the bulk (Figure IV - 3b and c) and melt at ca. 149°C. This observation aligns with the DSC data, confirming that the SCM crystallization of (*R*)-PXL results in the crystallization of a metastable polymorph, EII, which melts prior to the crystallization of the most stable form, EI. It also underlines that the phase transition from EII to EI does not proceed by solid-solid transformation.

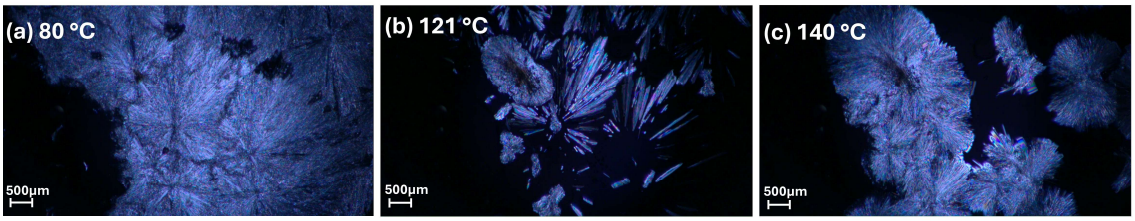

Figure IV - 3. Polarized light microscopy images of the crystallization of PXL pure enantiomers upon heating the SCM from 80 °C to 160°C at 20 K.min^{-1} (a) after annealing at 80 °C for 60min (b) 121°C (c) 140°C.

In addition, a different thermogram is observed upon heating the SCM from 25 to 160 °C at 10 K.min^{-1} (Figure IV - 2e): a crystallization is detected at ca. 75 °C prior to another melting event at 98.4 °C. Once again, this melting endotherm is calorimetrically compensated by the crystallization of EI, as evidenced by the detection of the melting endotherm of this form at 148.1 °C. Numerous attempts to replicate this experiment outside the DSC oven (or even by HSM) resulted in the crystallization of EI. The melting event detected at 98.4 °C is putatively attributed to the melting of a third polymorph of (*R*)-PXL, labelled EIII (Figure IV - 2). However, achieving a reproducible preparation protocol was not possible due to the high metastability of this phase.

IV.2.2- Crystallization Behaviour of Racemic PXL

Based on the data published by Griesser et al.,[7] a polymorph screening involving solvent crystallization (either by evaporation, cooling or antisolvent addition) as well as SCM crystallization, grinding, or sublimation of racemic PXL is performed. Most crystallization attempts resulted in a single solid phase that is analyzed by DSC (Figure IV - 4d), revealing a single melting endotherm at T_m^{RI}= 134.0 °C without any detectable mass loss. This confirms the absence of thermal degradation upon heating and indicates that no solvated phase is formed. This solid phase, identified by its XRPD pattern (Figure IV - 4a), corresponds to the phase Mod. I reported by Griesser *et al.*[7] and to the racemic compound, RC-PXL, reported by Harfouche *et al.*[8,9] In consistency with the phase labels of DPL forms,[4] this phase will be labelled RI in this manuscript.

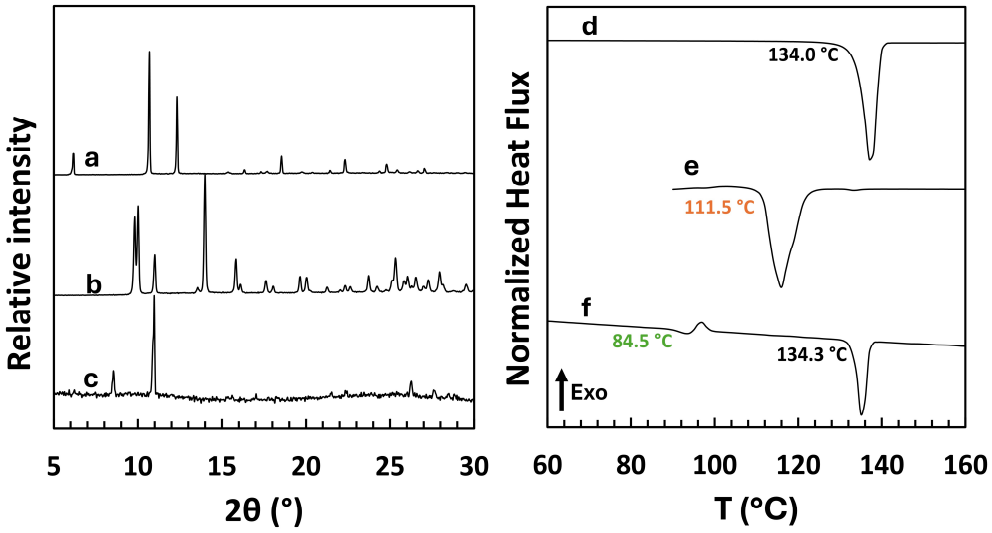

Figure IV - 4. XRPD patterns of (a) RI (b) RII (c) cEII. DSC curves obtained by heating: (d) RI at 5 K.min^{-1}, (e) the SCM annealed at 80 °C for 30 min before heating at 20 K.min^{-1}, (f) the SCM annealed at 80 °C for 10 min before heating at 10 K.min^{-1}.

After melting RI, we observe that annealing the SCM at 80°C for 30 minutes results in the crystallization of a different solid form. This phase displays a broad melting endotherm at T_m = 111.5 °C (without mass loss, Figure IV - 4e) and is identified by a different XRPD pattern (Figure IV - 4b). It corresponds to the phase Mod. II reported by Griesser *et al.*[7] and will be referred to as RII in this manuscript. The phase Mod. III was reported to crystallize by annealing the racemic SCM at 55-65 °C for several hours.[7] In this work, this form could only be obtained by annealing at 80 °C for 10 min. The DSC analysis of Mod. III reveals a melting endotherm at

$T_m^{Mod.\ III}$ = 84.5 °C which, alike EII and EIII, is calorimetrically compensated by the crystallization of RI, thus underlining its metastability (Figure IV - 4f). The XRPD pattern of Mod. III was not previously reported and is shown in Figure IV - 4c. It should be noted that it is superimposable to the XRPD pattern of EII (Figure IV - 5) which suggests that Mod. III is a racemic mixture of EII particles (*i.e.* a racemic conglomerate) that will be labelled cEII hereafter.

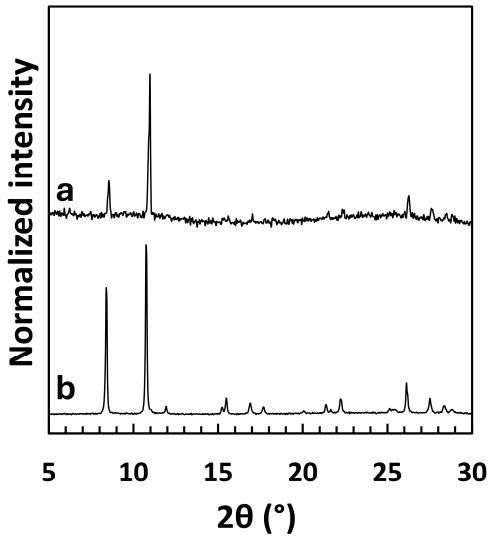

Figure IV - 5. XRPD patterns of (a) cEII and (b) EII.

All thermochemical data have been gathered in Table IV - 2. It should be underlined that, according to the heat of fusion rule, RII is metastable and monotropically related to the thermodynamically stable form RI. It is likely that cEII is of even lower stability. This is confirmed experimentally by cross seeding experiments at 20 °C (in Acetonitrile, Methanol, Tetrahydrofuran, data not shown). RII is more stable than cEII and the sequence of SCM crystallization at 80 °C is in accordance with the Ostwald's rule of stages.[12]

Table IV - 2. Thermochemical data collected by DSC analyses of the different racemic forms of PXL. The melting enthalpy cEII could not be experimentally measured.

Forms	Preparation	T_{fus}^{onset} (°C)	ΔH_{fus} (kJ.mol^{-1})
RI	SC[a]	134.0	22.4
RII	SCMA[b] (30 min at 80°C)	111.5	15.2
cEII	SCMA[b] (10 min at 80°C)	84.5	n/a

[a]Solvent crystallization
[b]SuperCooled Melt annealing

IV.2.3 - Crystal structures determination of the PXL phases

The study of DPL crystal structures showed that crystal phase diversity was correlated to conformational flexibility since each crystal form was made from a different conformer.[6] A major missing point in the characterization of the PXL system was the crystal structures of the different solid forms. EI single crystals have been rather easily obtained by slow evaporation in methanol. However, attempts to prepare single crystals of racemic PXL remained unsuccessful for a long time. A large array of method, either by using slow cooling of supersaturated solutions, melt crystallization, or even gels failed. PXL being an API with high water solubility,[13] the choice of solvent was actually limited to water and light alcohols (methanol, ethanol, n-propanol and isopropanol) which also limited the chance of success. It was however possible to grow very elongated particles of the thermodynamically stable form RI by sublimation of a few mg of racemic PXL loaded in a 3 mL vial covered with a glass slide and stored onto a hot plate at 100 °C for a week. The small needle shaped crystals that formed on the glass slides were analyzed with a higher resolution diffractometer due to their lower quality.[1] The high metastability of EII prevented the formation of well faceted crystals of this phase and RII could not be grown as satisfactory particles, despite numerous attempts and their crystal structures remains unknown to date. The main crystallographic data collected for RI and EI are summarized in Table IV - 3.

EI crystallizes in the non-centrosymmetric space group $P2_12_12_1$ (Table IV - 3), the most common Sohncke space group for organic compounds.[14,15] The two independents PXL molecules, A and B, in the asymmetric unit of EI (Figure IV - 6a) have their 1,3-dimethylxanthine moiety almost parallel (with an interplanar distance of about 3.4 Å and are not linked by H-bonds. The conformation of these two molecules differs strongly by means of the C4-N1-C3-C2 and N1-C3-C2-C1 torsion angles (Table IV - 4), actually underlining the conformational variability of the PXL molecule, as in the case of DPL.[4]

[1] Crystallographic data obtained by Dr. El-Eulmi Bendeif, Université de Lorraine, CNRS CRM2, F-54000, Nancy, France

Table IV - 3. Crystallographic data of RI and EI.

	RI	**EI (*S*)**
Crystal System	Trigonal	Orthorhombic
Space Group	*P*3c1	$P2_12_12_1$
Z, Z'	6, 1	8, 2
a (Å)	28.48746(16)	7.7763(1)
b (Å)	28.48746(16)	17.133(3)
c (Å)	7.16020(5)	17.171(3)
α (°)	90	90
β (°)	90	90
γ (°)	120	90
V (Å^3)	5032.2	2287.7
Calculated Density (g.cm^{-3})	1.417	1.383
Measured data	128921	18337
Observed data (F_0>4σ(F_0))	7027	4666
No. Restraints/params	1/473	315
Goodness-on-fit on F2	1.049	0.957
R1/wR2 (F_0>4σ(F_0))	0.0305/0.0847	0.0612/0.1173
R1 (all data)	0.0309	0.1529
Largest diff peak and hole (e$^-$.Å^{-3})	0.582, -0.213	0.155, -0.157

The main H-bonds, O1-H…N2 and O1-H…O3 (shown in Figure IV - 6 and summarized in Table IV - 4), form a corrugated arrangement of PXL molecules as a result of the 2_1 screw axis along [100] direction, giving rise to a periodic bond chain (PBC) spreading along the [100] direction (Figure IV - 6b). These PBCs are regenerated in the *bc*-plan by means of the two remaining 2_1 axes, as shown in Figure IV - 6c and interact by means of C-H…O contacts (Table IV - 4) and weaker van der Waals interactions.

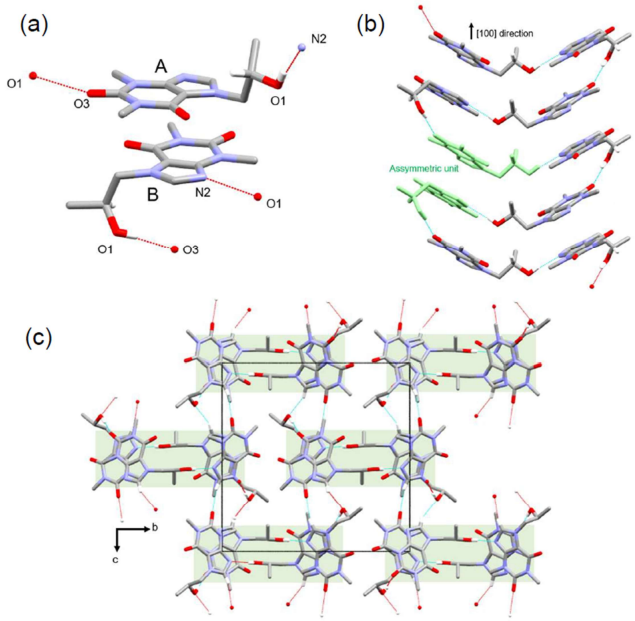

Figure IV - 6. (a) View of the two PXL molecules A and B of the asymmetric unit of EI. (b) View of the PBC spreading along [100] (the asymmetric unit is highlighted in green). (c) View of the crystal packing along the [100] direction. The green rectangles highlight the PBC. H-bonds are shown in blue (or red, if hanging). Non-H-bonding hydrogen atoms have been removed for clarity.

Table IV - 4. Summary of the isopropyl torsion angles (°) of the different PXL molecules in the asymmetric unit of EI and RI, and main D…A H-bond distances (Å) and D-H…A angles (°) within the crystal structures of EI and RI. The distances given for RI are averaged over the three molecules of the asymmetric unit

	EI		**RI**		
Torsion Angle	A	B	1	2	3
C4-N1-C3-C2	98.2	104.4	104.6	108.4	-104.7
N1-C3-C2-C1	-172.6	-62.3	-178.2	-179.6	179.5
H-Bonds	D···A	D-H···A	D···A		D-H···A
O1-H…N2	2.841(5)	169.9	/		/
O1-H…O3	2.756(5)	170.4	/		/
O1-H…O2	/	/	2.785 ± 0.008		169.5 ± 8.0
C4-H…O3	3.277(3)	157.5	3.140 ± 0.040		144.8 ± 8.0
C4-H…O1	3.356(5)	156.6	/		/

By contrast, RI crystallizes in the space group *P*3c1 (Table IV - 3, described here using the hexagonal conventional coordinate system), a non-centrosymmetric non-Sohncke space group adopted by less than 0.3% of the reported crystal structures of organic molecules.[14,15]

This confirms the racemic compound nature of RI. The asymmetric unit is shown in Figure IV - 7a and contains three independent PXL molecules (labelled 1, 2 and 3). Molecules 1 and 2 correspond to the (*R*) enantiomer, molecule 3 is the (*S*) enantiomer. Molecules 1 and 2 are linked by a C4-H…O3 contact (Table IV - 4). Unlike EI, it can be seen from Table IV - 4 that molecules 1 and 2 have the same isopropyl conformations but molecule 3 has opposite C4-N1-C3-C2 and N1-C3-C2-C1 torsion angle values. The main H-bond existing in this structure consists of a O1-H…O2 interaction (Table IV - 4) which gives rise to a unidimensional PBC in which the enantiomers are packed along the [001] direction in an alternating fashion (Figure IV - 7). These heterochiral PBCs are arranged in the *ab* plane and linked by a C4-H…O3 contact and weaker van der Walls interactions. Figure IV - 7c highlights the 3-fold symmetry of the crystal packing.

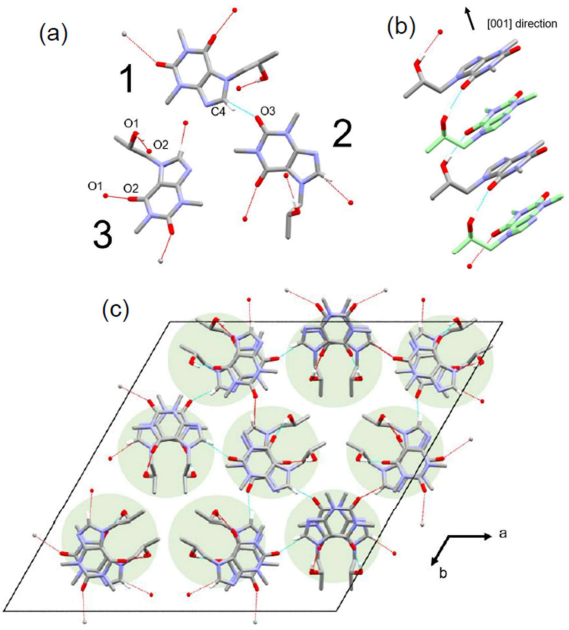

Figure IV - 7. (a) View of the three PXL molecules 1, 2 and 3 of the asymmetric unit of RI. (b) View of the PBC spreading along [001] (the R enantiomer is shown in green). (c) View of the crystal packing along the [001] direction. The green circles highlight the PBC. H-bonds are shown in blue (or red, if hanging). Non-H-bonding hydrogen atoms have been removed for clarity.

From the analysis of the crystal structures of RI and EI, it is worth noting that: (i) the isopropyl moiety of the PXL molecule can adopt several conformations, (ii) the crystal packings of these two phases are primarily governed by H-bonds being established by the hydroxyl function bear by the isopropanol moiety. It can be therefore envisaged that the flexibility of the H-bond

donor moiety of the molecule is the main factor contributing to the diversity of solid phases observed in the case of PXL.[16,17] By analogy with the situation observed for DPL,[4–6] where the conformational variability of the molecule at the solvated state was found responsible for nucleation hindrances of the racemic compounds, this feature may also account for the rather long induction times reported for the crystallization of RI in several solvents, which allowed Harfouche *et al.* to perform preferential crystallization by managing the metastable equilibria of the conglomerate cEI.[8,9] However, as stated in the introduction of this chapter, it should be noted that the efficiency of the preferential crystallization process was better in the case of DPL compared to PXL, both in terms of productivity and optical purity.

IV.2.4 - Determination of the binary phase diagram

To further confirm the solid-state nature of each solid phase and their thermodynamic properties, the binary phase diagram between (*S*)- and (*R*)-PXL enantiomers is constructed using DSC measurements

IV.3.1 - Stable equilibrium between RI and EI

To gather experimental data for this equilibrium, physical mixtures of the stable forms RI and EI are prepared and analyzed by DSC. The thermograms obtained for $0.5 < X_{(R)} < 1$ mixtures are shown in Figure IV - 8, alongside those of pure RI and EI. Two thermal events are detected: (i) an endothermic invariant at ca. 131 °C, corresponding to the eutectic temperature and (ii) another endothermic signal whose temperature varies between the melting points of pure RI and EI, corresponding to the liquidus line,[18] with a minimum near to the $X_{(R)} = 0.65$ composition, corresponding to the eutectic point.

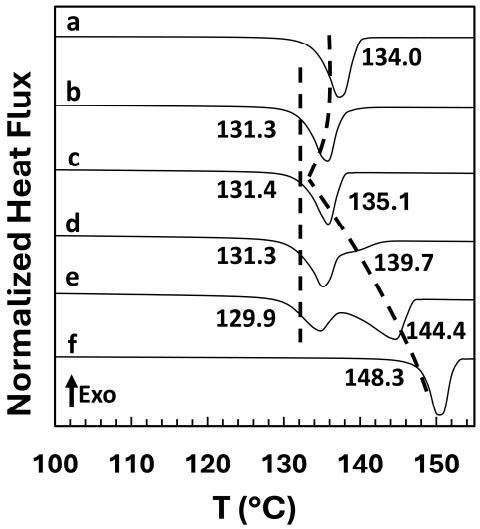

Figure IV - 8. DSC curves of RI and EI mixtures (X(R)) (a) RI (b) 0.6 (c) 0.7 (d) 0.8 (e) 0.9 (f) EI. Dotted lines are guide for the eyes.

Using the measured melting enthalpies for the different solid forms (Table IV - 1 and Table IV - 2), the equilibrium between the stable forms RI and EI can be estimated using the Schroeder Van-Laar (SVL hereafter, for EI) and Prigogine Defay (PD hereafter, for RI) simplified equations.[19,20] Table IV - 5 reports that the predicted eutectic temperature of this equilibrium is at T_m^{eut} = 128.6 °C. The agreement between predicted (T_m^{eut} = 128.6 °C) and measured (T_m^{eut} = 131.0 °C) eutectic temperature is satisfactory (Table IV - 5) although suggesting a slight deviation from thermodynamic ideality.

Table IV - 5. Summary of the predicted, measured and recalculated invariant temperatures between the different solid phases in the binary system of PXL enantiomers. Invariants temperature for RI/EII and RII/EII have been recalculated based on a theoretical value of the EII melting enthalpy.

Equilibrium	Invariant Temperature (°C)		
	Predicted	Measured by DSC	Recalculated
RI / EI	128.6	131.0	n/a
(*R*)PXL / (*S*)PXL (cEI)	111.2	120.4	n/a
RI / EII	n/a	n/a	111.9
RII / EII	n/a	n/a	100.6

IV.3.2- Metastable equilibrium of racemic conglomerate (cEI & cEII)

The metastable conglomerate cEI is characterized by mixing an equimolar mixture of (*R*)-PXL and (*S*)-PXL (crystallized as EI crystals of opposite chirality), which is analyzed by DSC at 20 K.min^{-1} (Figure IV - 9a). A single and wide endotherm, typical of a eutectic invariant for such "manually prepared" conglomerate (hereafter labelled cEI),[4] is detected at T_m^{cEI} = 120.4 °C with a melting enthalpy of ΔH_m^{cEI} = 20.4 kJ.mol-1 (Table IV - 6). This eutectic temperature is further confirmed by analysing a second sample with a non-racemic composition of $X_{(R)}$ = 0.84, for which the onset of melting was detected at 120.5°C (result not shown). The metastable invariant corresponding to the conglomerate cEI is also estimated using the SVL equation, giving an invariant temperature at T_m^{eut} = 111.2 °C.

The agreement between the predicted (T_m^{eut} = 111.2 °C) and measured (T_m^{eut} = 120.4 °C) eutectic temperatures of cEI is rather poor, suggesting that the melting of this racemic conglomerate presents a non-ideal behaviour. Indeed, the calculated entropy of mixing in the liquid state based on the experimental data obtained from the DSC experiments gives ΔS_{exp}^{mix} = - 3.5 J.mol^{-1}.k^{-1},[20–24] thus further confirming the non-ideal behaviour of this system (ΔS_{ideal}^{mix} = - 5.76 J.mol^{-1}.k^{-1}).

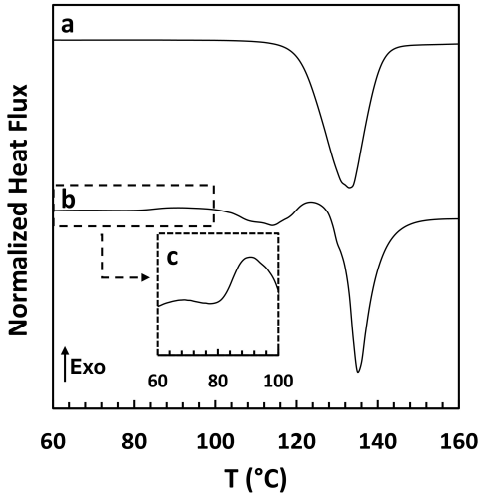

Figure IV - 9. DSC curves obtained by heating: (a) the equimolar physical mixtures of EI at 20 K.min^{-1} (b) the equimolar physical mixtures of EII at 50 K.min^{-1} and (c) a magnification of the temperature range 60-100 °C.

Table IV - 6. Thermochemical data collected by DSC analyses of the different manually prepared racemic conglomerate of PXL.

Forms	Preparation of the sample	T_{fus}^{eut} (°C)	ΔH_{fus} (kJ.mol^{-1})
cEI	mixing EI	120.4	20.4
cEII	mixing EII	81.2	n/a

Thereafter, the metastable conglomerate cEII is characterized by analysing an equimolar mixture of EII crystals of opposite chirality (isolated after SCM annealing) by DSC, which gives rise to a wide endotherm starting at ca. T_m^{eut} = 81.2 °C (Figure IV - 9b and c) followed by two other endotherms at ca. 100 °C and 130 °C, attributed to the melting of more stable forms (for instance RII and RI). Considering the high metastability of this preparation, a minimum of 50 K.min^{-1} heating rate is required to detect the melting onset of cEII (T_m^{eut} = 81.2 °C), which explains the discrepancy with the melting temperature measured for this form prepared by SCM crystallization (T_m^{eut} = 84.5 °C, Table IV - 2). It is worth noting that cEI is of lower thermodynamic stability compared to RI since it melts ca. 15 °C lower but is more stable than RII (T_m^{RII} = 111.5 °C) and cEII (T_m^{cEII} = 81.2 °C).

IV.3.3- Other metastable equilibria and phase diagram

According to the above investigations, the binary phase diagram based on experimental data and theoretical computation is shown in Figure IV - 10. RI/EI and cEI equilibria are shown as black full lines (for the stable equilibrium) and blue dashed lines (for the metastable equilibrium). Additionally, using the measured eutectic temperature of cEII (T_m^{eut} = 81.2 °C) and the melting temperature of pure EII (T_m^{EII} = 116.1 °C), the melting enthalpy of EII is estimated by using the SVL equation, assuming an ideal thermodynamic behaviour (Table IV - 6). This gives an estimated ΔH_m^{EII} value of 22.8 kJ.mol^{-1} and allowed the theoretical liquidus of EII to be recalculated, which is shown as green dashed lines in Figure IV - 10. The melting point of RII (T_m^{RII} = 111.5 °C) being too close to the invariant temperature of cEI (T_m^{cEI}= 111.2 °C), the RII/EI invariant temperature is not predicted although it should lie between 111.5 and 111.2 °C. Nevertheless, the estimated melting enthalpy of EII permits to predict two other metastable invariant temperatures using SVL and PD equations: RI/EII and RII/EII equilibria, listed in Table IV - 5. The corresponding equilibria are shown as red and orange dashed lines, respectively, in Figure IV - 10. However, due to the too high metastability of RII and EII, it was

not feasible to confirm these calculated temperatures experimentally since the physical mixtures prepared with these phases consistently resulted in the crystallization of more stable phases prior to DSC analyses.

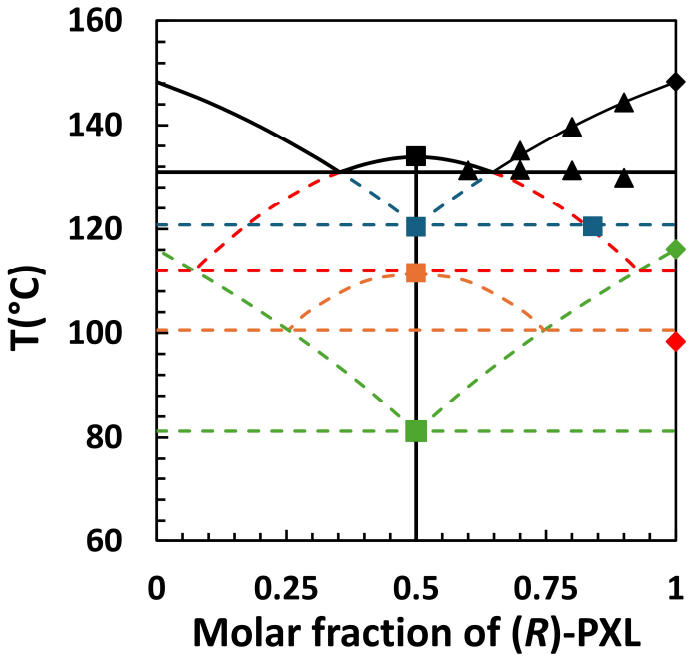

Figure IV - 10. Binary phase diagram between PXL enantiomers. Black full lines correspond to the stable equilibria measured experimentally (▲). Red, orange and green dashed lines correspond to the metastable equilibria predicted by SVL and PD equations. Blue dashed lines correspond to the metastable equilibria fitted with the experimental points. Some experimental points are also shown: (■) melting of RI, (◆) melting of EI, (■) cEI invariant, (■) melting of RII, (■) cEII invariant (◆) melting of EII (◆) melting of EIII.

Consequently, two different racemic compounds (*i.e.* RI and RII) and two mixtures of enantiopure crystals (*i.e.* racemic conglomerates cEI and cEII) are highlighted at the racemic mixture of PXL from the above investigations. The melting temperatures of RI, RII and cEII are in good agreement with the three "modifications" reported by Griesser *et al.* (Table IV - 7).[7] Concerning the pure enantiomer of PXL, three crystal forms are reported and characterized: EI, EII and EIII. It should be underlined that another racemic mixture of enantiopure crystals cEIII must exist but could not be experimentally characterized. These results confirm the versatility of the crystallization behaviour observed in the series of theophylline derivatives to which DPL also belongs.[4]

Table IV - 7. Thermochemical data comparison.

Griesser *et al.*		This study			
Racemic		Racemic		Enantiopure	
ID	**T (°C)**	**ID**	**T (°C)**	**ID**	**T (°C)**
Mod. I	133.5	RI	134.0	EI	148.3
n/a	n/a	cEI	120.4	EII	116.1
Mod. II	113.5	RII	111.5	EIII	98.4
Mod. III	82-85	cEII	81.2		

IV.3 - Modulating H-bonding propensity

Combined with the data observed for DPL, the study on PXL further emphasizes that factors beyond thermodynamic, such as the molecular flexibility, hydrogen bonding interactions, or specific crystallization conditions, may play a more significant role in favouring the nucleation and growth of enantiopure crystals and therefore determining the efficiency of crystallization-based chiral resolution routes under non-equilibrium conditions.

Indeed, the molecular flexibility of the H-bond donor moiety of 1,3-dimethylxanthine-based chiral derivatives likely plays a substantial role in explaining their versatile phase behaviour. This observation suggests that both molecular flexibility and hydrogen bonding interactions are crucial factors enabling the possibility of a preferential crystallization process in conditions where the spontaneous nucleation of stable racemic phases is hindered. Consequently, this allows the system to evolve through metastable equilibria, such as metastable conglomerates. Therefore, we aim to prepare and investigate more members of the 1,3-dimethylxanthine-based family exhibiting different H-bonding propensity by substituting the hydroxyl group(s) of PXL and DPL with different chemical functions: namely acetoxyl (Figure IV - 11, **1a** and **2a)**, methoxyl (Figure IV - 11, **1b** and **2b**), amino (Figure IV - 11, **1c** and **2c**) and amino-alcohol (Figure IV - 11, **2d**).

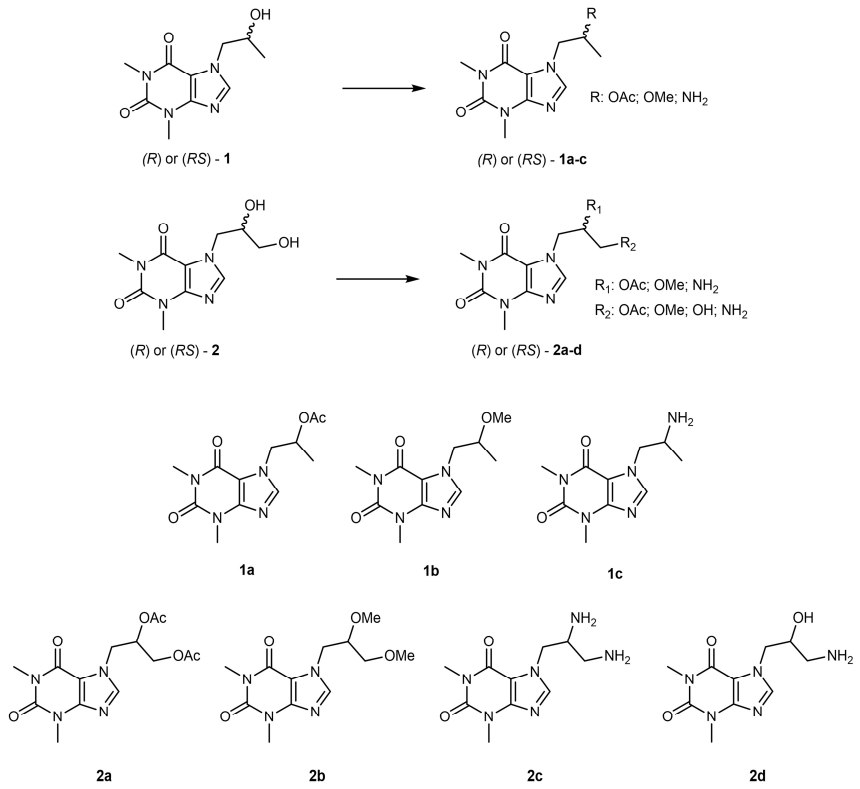

Figure IV - 11. List of the targeted 1,3-dimethylxanthine-based derivatives

Access to the molecules listed in Figure IV - 11 could be elaborated by organic synthesis using either racemic or enantiopure PXL and DPL as starting material. Although racemic proxyphylline and diprophylline are commercially available, access to enantiopure materials necessitates the use of chiral pool syntheses following published procedures with slight modification, especially the equivalence of propylene oxide in the case of proxyphylline (Figure IV - 12).[5,13]

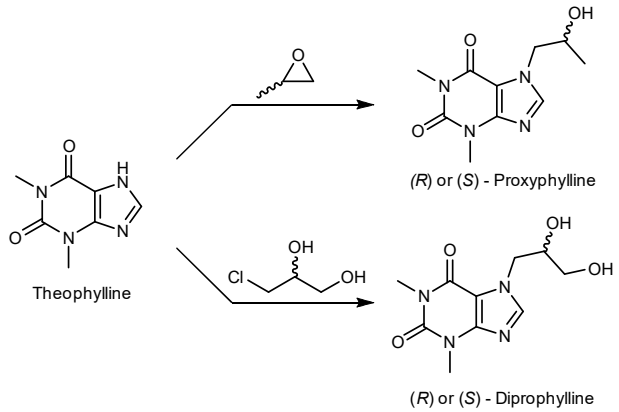

Figure IV - 12. Synthesis path used for the synthesis of enantiopure PXL and DPL.

IV.3.2.1- 1,3-dimethylxanthine-based derivatives: Acetoxyl chemical function

Acetylation of hydroxyl function is a well-documented chemical reaction.[25–27] More specifically, Conelly-Espinosa *et al.* reported a synthesis route of **2a** using acetic anhydride,[28] whose procedure is repeated in the present work using either racemic and enantiopure DPL as starting material to isolate either (*RS*)-**2a** and (*R*)-**2a** in good yield (≥ 85 %). It should be noted that the crystallization of this chiral system as racemic compound was already highlighted by the resolution of its racemic crystal structure ($P\bar{1}$) by Conelly-Espinosa *et al.* (Figure IV - 13a, CSD refcode: ROXWEI).

After synthesis and purification, the crystallization from ethanol of (*RS*)-**2a** resulted in the isolation of the reported racemic solid phase (labelled (*RS-I*)-**2a** hereafter) whose XRPD pattern is displayed in Figure IV - 13b. Intriguingly, DSC measurement of this solid phase revealed a shouldered endotherm at $T_m^{(RS-I)-\mathbf{2a}}$ = 141.5 °C (Figure IV - 13e, $\Delta H_m^{(RS-I)-\mathbf{2a}}$= 38.9 kJ.mol^{-1}). Indeed, a subsequent heating of the SCM triggered the crystallization of a more stable solid phase (labelled (*RS-II*)-**2a** hereafter), as illustrated by the exothermic event at ca. 90 °C in Figure IV - 13f and the higher melting point $T_m^{(RS-II)-\mathbf{2a}}$ = 147.0 °C ($\Delta H_m^{(RS-II)-\mathbf{2a}}$ = 34.4 kJ.mol^{-1}). It should be noted that a small endotherm is observed prior to the final melting in Figure IV - 13f, which could be indicative of the presence of remaining (*RS-I*)-**2a** particles. More importantly, this new solid phase is isolated out of the DSC oven by annealing the SCM at 100 °C for 30 minutes and analyzed by XRPD (Figure IV - 13c), underlining its structural differences compared to (*RS-I*)-**2a**. Although attempts for growing single crystals of this solid phase remain unfruitful, it must be a polymorphic form of the racemic compound as it melts higher ($T_m^{(R)-\mathbf{2a}}$ = 134.4 °C, $\Delta H_m^{(R)-\mathbf{2a}}$ = 35.6 kJ.mol^{-1}, Figure IV - 13f) and has a different XRPD pattern than its pure enantiomer (*R*)-**2a** (Figure IV - 13g).

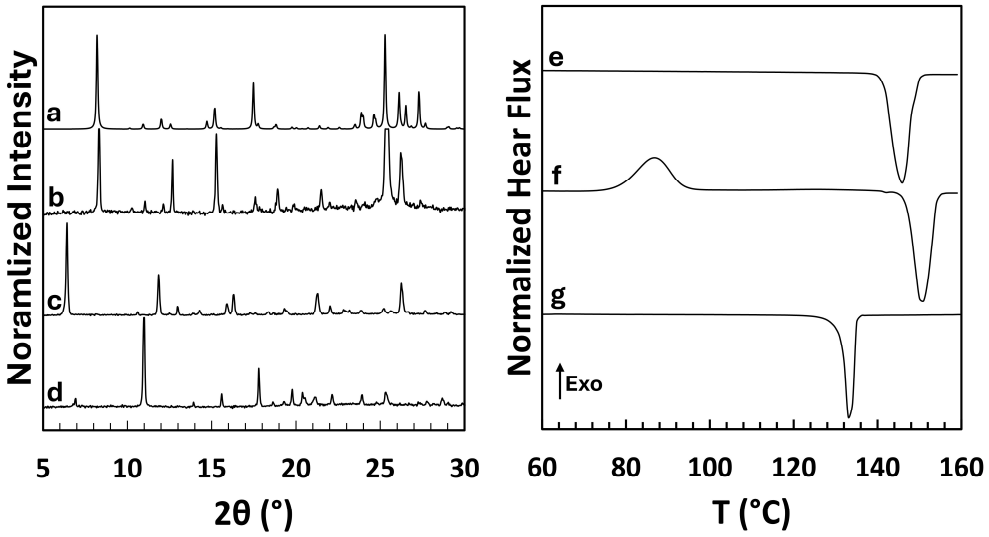

Figure IV - 13. XRPD patterns of (a) ROXWEI (b) (*RS*)-2a after 30min of SCM annealing at 100°C (c) (*RS*)-2a after stirring in ethanol at room temperature (d) (*R*)-2a. DSC curves at 5 k.min^{-1} of (e) (*RS*)-2a after stirring in ethanol at room temperature (f) reheating the SCM from 20 °C to 160 °C (g) (*R*)-2a. Preferential orientation of the [201] (25.3° 2θ) was observed for (b), its intensity has been limited to 1000 counts for better comparison.

According to the heat-of-fusion rule,[29] one would predict an enantiotropic relationship between (*RS-I*)-**2a** and (*RS-II*)-**2a**. This behaviour is confirmed by cross-seeding experiments, which demonstrate the thermodynamic stability of (*RS-I*)-**2a** at room temperature despite its lower melting point. Although the solid-solid transition could not be experimentally observed, the polymorphic transition is estimated by constructing the phase diagram between **2a** enantiomers (Figure IV - 14). The stable equilibrium is first characterized by DSC analysis of various mixtures consisting of enantiopure **2a** and (*RS-II*)-**2a** (Figure IV - 14, triangles). The quasi-perfect alignment of the experimental points with the predicted liquidus of (*RS-II*)-**2a** using PG simplified equation underlines the validity of such prediction in the present case study (Figure IV - 14, black lines). Consequently, a similar prediction is computed for (*RS-I*)-**2a** and extrapolated until it intersects the predicted liquidus of (*RS-II*)-**2a**, estimating therefore the solid-solid polymorphic transition at 123 °C. Additionally, the eutectic temperature associated to the metastable racemic conglomerate is also estimated by predicting the liquidus of (*R*)-**2a** using SVL simplified equation, emphasizing the substantial relative stability of the racemic crystals.

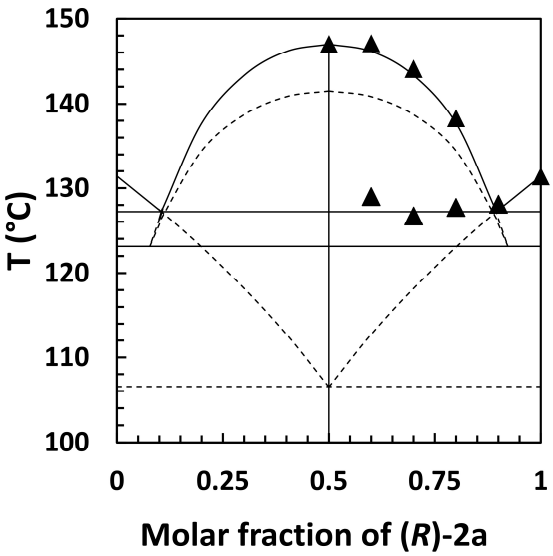

Figure IV - 14. Binary phase diagram between 2a enantiomers. Black full lines correspond to the stable equilibria predicted by SVL and PD equations alongside experimental points measure by DSC (▲). Dashed lines correspond to the metastable equilibria predicted by SVL and PD simplified equations.

Despite the absence of H-bond donors in case of derivative **2a**, at the exception of weakly polarized C-H bonds,[30–32] the ability of this system to crystallize as different polymorphic forms remains. Akin DPL and PXL, the crystal structure of (*RS-I*)-**2a** demonstrate the key role of the acetoxy moiety in the crystal packing. Indeed, the PBC is ensured by C-H…O contacts involving the polarized methyl function of the 1,3-dimethylxantine moiety and the oxygen of the acetoxy moiety (≈ 3 Å) along the *bc* plan. It can therefore be assumed that the molecular flexibility of **2a** and the polar behaviour of the acetoxy function are factors enabling this polymorphic behaviour.[16,17]

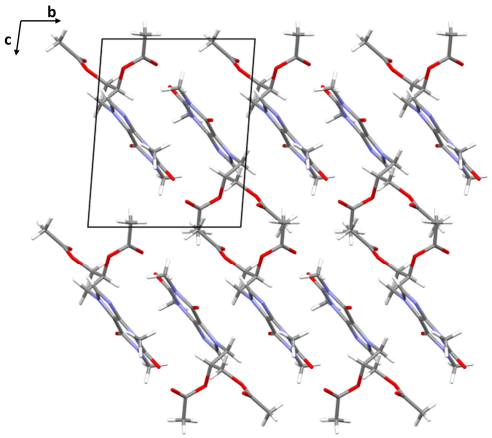

Figure IV - 15. View of the crystal packing of (*RS-I*)-2a along the [010] direction (CSD refcode: ROXWEI).

Thereafter, derivative **1a** is synthesized using the same procedure using racemic or enantiopure PXL as starting material instead of DPL. Although similar investigations are conducted on **1a**, only a single solid phase could be isolated either at the enantiopure ($T_m^{(S)-\mathbf{1a}}$ = 103.8 °C, $\Delta H_m^{(S)-\mathbf{1a}}$ = 23.1 kJ.mol^{-1}, Figure IV - 16a) or at the racemic composition ($T_m^{(RS)-\mathbf{1a}}$ = 89.7 °C, $\Delta H_m^{(RS)-\mathbf{1a}}$ = 20.8 kJ.mol^{-1}, Figure IV - 16b) exhibiting different XRPD patterns (Figure IV - 16c and d).

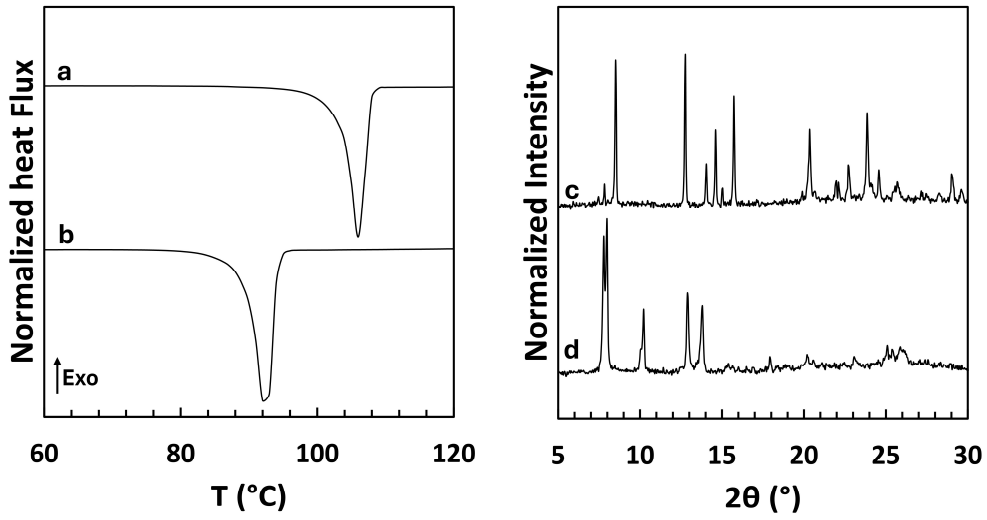

Figure IV - 16. DSC curves at 5 k.min^{-1} of (a) (*S*)-1a (b) (*RS*)-1a. XRPD patterns of (c) (*S*)-1a (d) (*RS*)-1a.

It can be seen that the acetylation of PXL lowered substantially the melting temperature of ca. 50 °C although the melting temperature difference of **1a** is comparable to PXL (ΔT^{R-RS} = 14.1 °C) (Figure IV - 17). Although the common adage "*in general, the number of forms known for a compound is proportional to the time and money spent in its research*" is often verified,[33–35] no polymorphic form could be identified from this system. This could be a result of the reduced molecular flexibility and H-bond propensity of **1a** compared to PXL and **2a**. A structural study could help understanding this behaviour, however, any attempt to grow single crystals remained unfruitful.

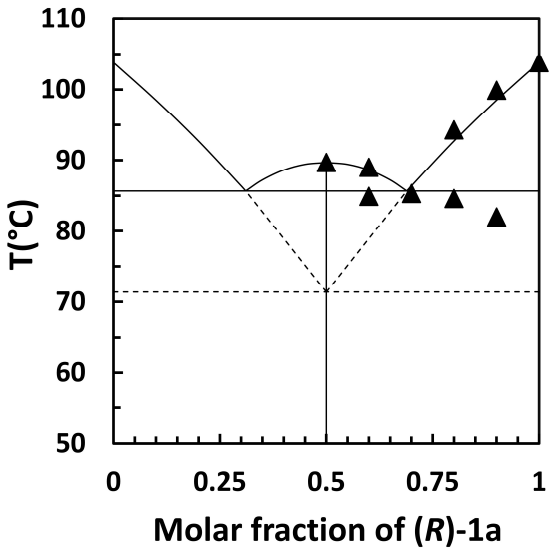

Figure IV - 17. Binary phase diagram between 1a enantiomers. Black full lines correspond to the stable equilibria predicted by SVL and PD equations alongside experimental points measure by DSC (▲). Dashed lines correspond to the metastable equilibria predicted by SVL and PD simplified equations.

IV.3.2.2- 1,3-dimethylxanthine-based derivatives: Methoxyl chemical function

Alike the well-documented acetylation of hydroxyl function, their methylation is also extensively described in the literature.[36–38] In our study, methoxyl groups are formed by reacting either enantiopure or racemic PXL or DPL with methyl iodide, a potent alkylating agent, in presence of sodium hydride, a strong but non-nucleophilic base, under dry and inert conditions. These procedures afford derivatives **1b** and **2b** in decent yield (≥ 50 %) for both racemic and enantiopure compositions.

After several purification steps and crystallization from dichloromethane, the two derivatives could be crystallized as a single enantiopure solid form and a single racemic form, exhibiting different XRPD patterns (Figure IV - 18), whose thermochemical data are summarized in Table IV - 8. Their respective binary phase diagrams are drawn in Figure IV - 19, underlining the quasi-perfect alignment of the experimental data with SVL and PD predictions.

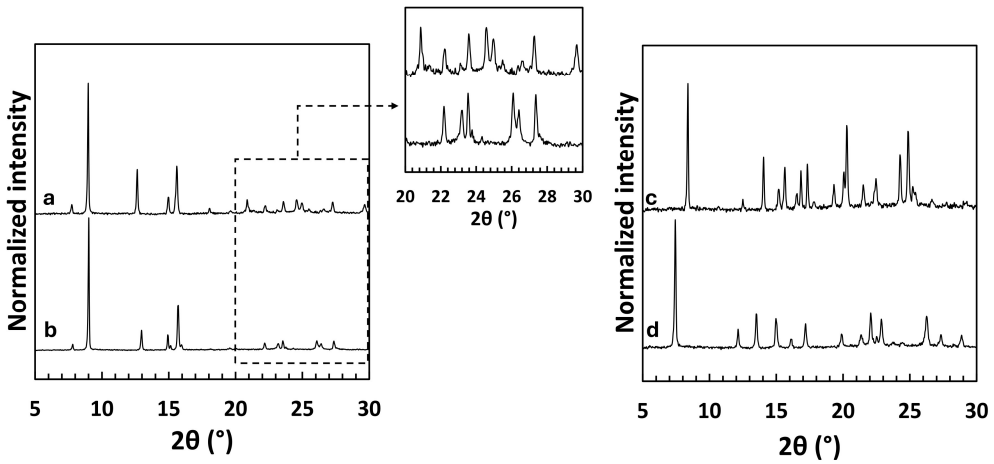

Figure IV - 18. XRPD patterns of (a) (*S*)-1b (b) (*RS*)-1b (c) (*R*)-2b and (d) (*RS*)-2b. A magnification of (a) and (b) in the 20-30 2θ range for better comparison.

Table IV - 8. Thermochemical data of derivative 1b and 2b.

	1b		2b	
	(*RS*)-1b	(*R*)-1b	(*RS*)-2b	(*R*)-2b
T_{fus}^{onset} (°C)	100.5	77.3	98.1	80.4
ΔH_{fus} (kJ.mol^{-1})	25.4	19.8	29.2	24.6

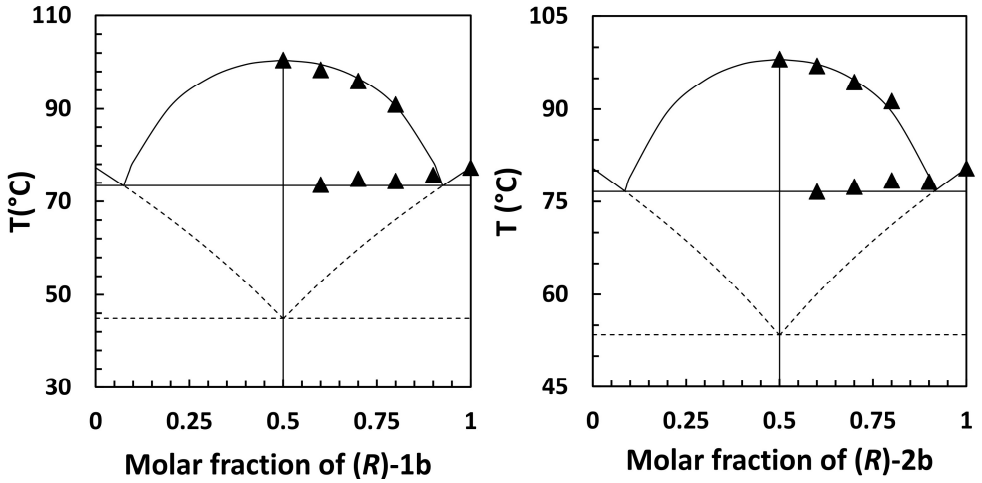

Figure IV - 19. Binary phase diagram between 1b enantiomers (left) and 2b enantiomers (right). Black full lines correspond to the stable equilibria predicted by SVL and PD simplified equations alongside experimental points measure by DSC (▲). Dashed lines correspond to the metastable equilibria predicted by SVL simplified equation.

More importantly, both systems exhibit a quasi-similar thermal behaviour as function of the enantiomeric composition. Interestingly, the melting temperatures of these systems is

drastically decreased compared to their respective hydroxylated molecules. It can be concluded that suppressing the H-bond propensity as well as reducing the polarity of the isopropyl moiety drastically decrease the intermolecular interactions at the solid-state. Moreover, the racemic compound is all the more thermodynamically favoured in this case. Although a structural study could help understanding this behaviour, any attempt to grow single crystals remains unfruitful.

IV.3.2.3- 1,3-dimethylxanthine-based derivatives: Amino chemical function

The access to derivatives **1c**, **2c** and **2d** requires the implementation of a multistep synthesis involving a tosylation (*i.e.* formation of a nucleofuge), an azidation, whose protocols are extensively described in the literature due to its relevance for click-chemistry,[39–41] and a Staudinger reduction (Figure IV - 20).[42–44] This synthesis procedure afford the derivative **1c** in good yield at the racemic composition. Unfortunately, applying the same synthesis procedure to access enantiopure **1c** yield an oil, hindering therefore the characterization of its solid-state.

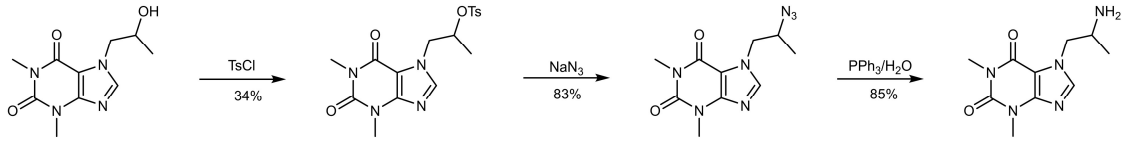

Figure IV - 20. Synthesis path of derivative 1c.

However, further TGA-DSC-MS examination of the racemic (*RS*)-**1c** highlighted its hydrated behaviour whose associated mass change is coherent with a monohydrated solid phase (Figure IV - 21). Despite several attempts, access to anhydrous (*RS*)-**1c** remains unfeasible. Although interesting, these data cannot be included in our study since it does not reflect the impact on the crystal packing of the amino function itself.

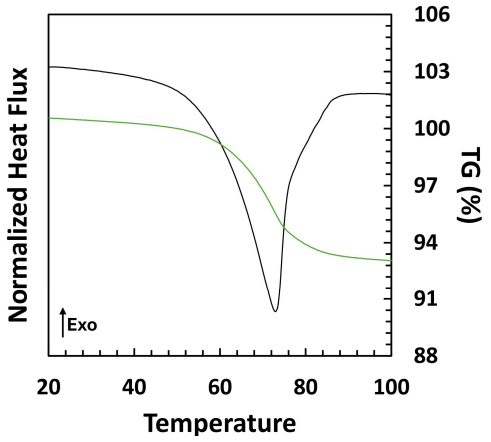

Figure IV - 21. TG-DSC measurements of (*RS*)-1c. A mass loss of 7.57% is detected (green curve)

Derivatives **2c** and **2d** are obtained using the same synthesis procedure.[45] Moreover, both tosylated intermediates are accessible in one pot by controlling the addition rate and the equivalence of tosyle chloride and easily isolated by silica gel column chromatography (Figure IV - 22). Similar to **1c**, derivatives **2c** and **2d** yield an oil after complete synthesis and purification, suggesting that the protic function strongly inhibit the nucleation of 1,3-dimethylxantine-based derivatives.

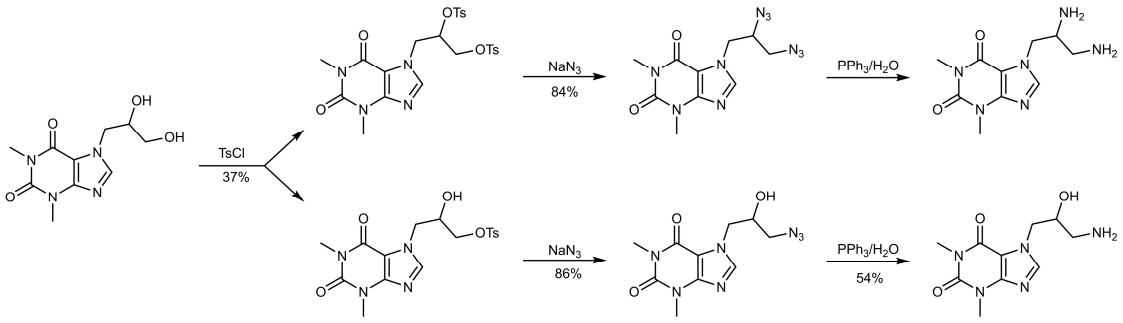

Figure IV - 22. synthesis path of derivative 2c and 2d.

Even though derivative **2c** could not be crystallized in either its racemic or enantiopure composition, derivative **2d** is successfully isolated after several crystallization trials (evaporation in several solvent, temperature cooling, antisolvent, evaporation under reduce pressure), both as pure enantiomer and racemic mixture. More importantly, XRPD analyses of the two isolated solid phases demonstrate the perfect superimposition of their XRPD pattern (Figure IV - 23a and b), indicating that (*RS*)-**2d** is a racemic mixture of enantiopure crystals: **2d** is therefore a conglomerate-forming system. This affirmation is further supported by SHG

microscopy observations of the racemic solid (Figure IV - 24b) showing the presence of an SHG emission for these crystals and confirming that the associated crystal structure is non-centrosymmetric.

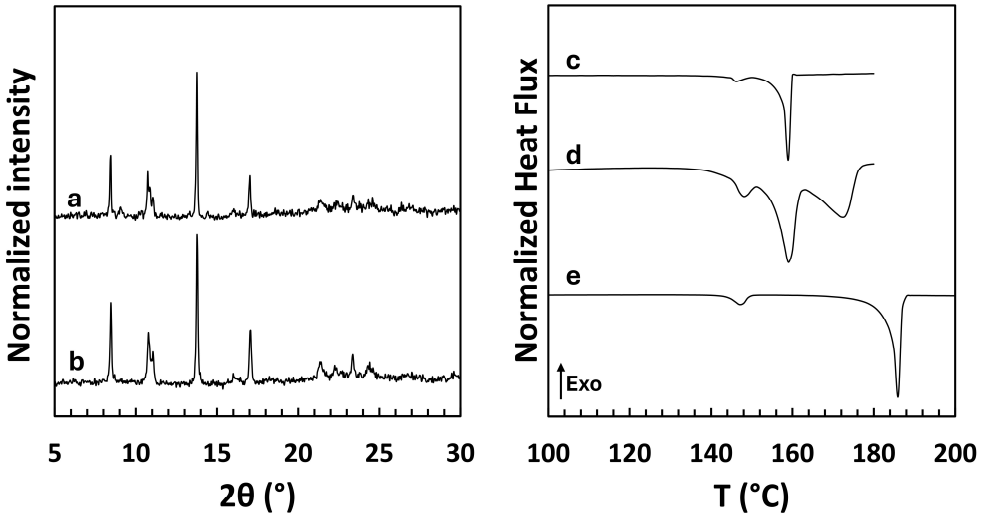

Figure IV - 23. XRPD patterns of (a) (*S*)-2d (b) (R*S*)-2d and DSC curves of (c) (*RS*)-2d and (d) 2d at 50 *e.e.*% (d) (*S*)-2d.

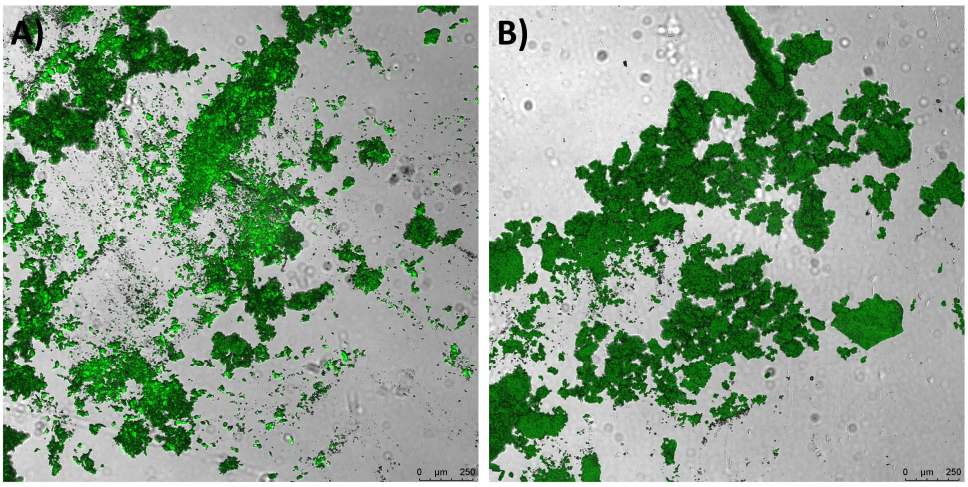

Figure IV - 24. SHGM analysis of (a) (*S*)-2d (b) (R*S*)-2d. Green pixels denote a SHG positive signal.

The DSC measurements of (*S*)-**2d** (Figure IV - 23e) revealed two endotherms at T_{endo}^{onset} = 143.9 °C and T_{endo}^{onset} = 184.5 °C. This first endotherm may indicate the presence of a polymorphic form or a deviation in enantiopurity resulting from the various steps of the chiral pool synthesis, which would suggest a eutectic invariant. Interestingly, DSC analysis of (*RS*)-**2d** at 0.5 K.min^{-1} (Figure IV - 23c) shows an identical behaviour with an endotherm at T_{endo}^{onset} = 144.5 and a second endotherm associated to the eutectic invariant at T_{eut}^{onset} = 153.9 °C. Considering

the versatile crystallization behaviour of PXL and DPL, it can be envisioned that this endotherm T_{endo}^{onset} = 143.9 °C is due to a solid-solid transition. Supporting this hypothesis, temperature-resolved SHG (Figure IV - 25A) and XRPD (Figure IV - 25B) measurements was performed and demonstrate the structural change occurring at ca. 143 °C. However, this structural change seems to be rather small as indicated by the apparent similarities of both XRPD patterns (Figure IV - 25B, d and e), mostly indicating an order-disorder transition or polymorphic forms sharing strong structural similarities. In absence of hard evidence regarding the nature of the two solid forms, the low and high temperature solid phases will be labelled **2d$_\alpha$** and **2d$_\beta$**, respectively.

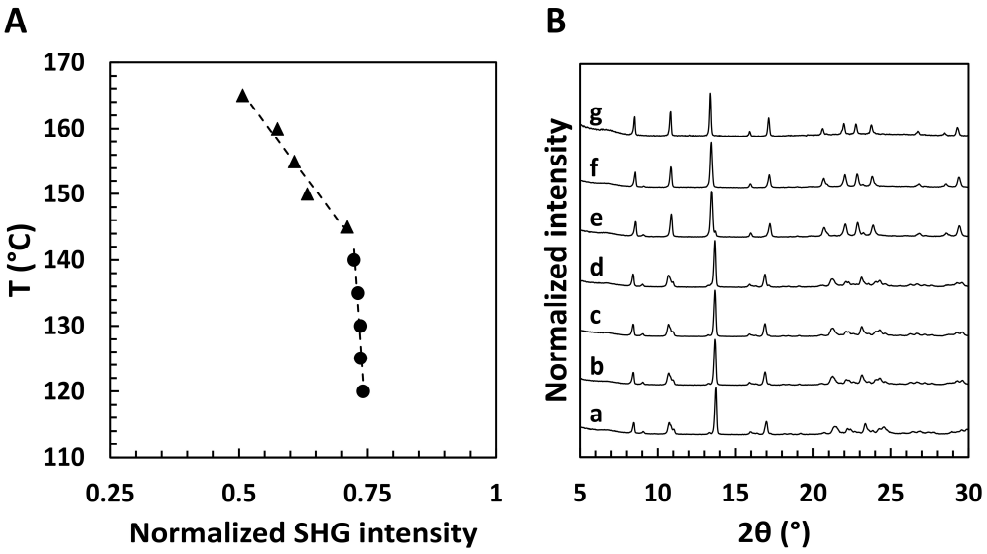

Figure IV - 25. Evolution of (A) the SHG signal and (B) XRPD as function of the temperature of (*S*)-2d. (A) black circles represent the low temperature form while black triangles represent the high temperature form. (B) (a) 21 °C (b) 133 °C (c) 138 °C (d) 143 °C (e) 153 °C (f) 158 °C (g) 163 °C.

Moreover, the agreement between the predicted equilibria using SVL simplified equation (T_m^{eut} = 151.8 °C) and measured (T_m^{eut} = 153.9 °C) eutectic temperatures is rather good (Figure IV - 26). Additionally, DSC measurement on an enantioenriched **2d** sample (Figure IV - 23d) confirms the two invariant transitions and fit the predicted equilibria using SVL simplified equation (Figure IV - 26).

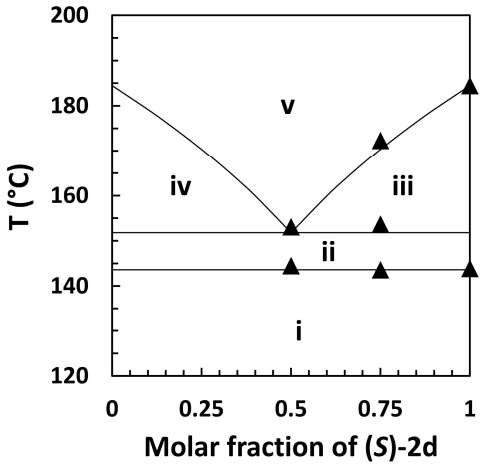

Figure IV - 26. Binary phase diagram between 2d enantiomers. Black full lines (liquidus and eutectic invariant) correspond to the stable equilibria predicted by SVL simplified equation alongside experimental points measure by DSC (▲). (i) <(*S*)-2d$_\alpha$> + <(*R*)-2d$_\alpha$> ; (ii) <(*S*)-2d$_\beta$> + <(*R*)-2d$_\beta$> ; (iii) <(*S*)-2d$_\alpha$> + sat.sol. ; (iv) <(*R*)-2d$_\alpha$> + sat.sol. ; (v) u.s.s.

IV.3.2.4– Ranking the Gibb's free energy ΔG^{Φ} of the THP derivatives

Consistently with the idea of a directed evolutionary design based on ΔG^{Φ} measurements, we computed this data for the different 1,3-dimethylxanthine-based derivatives (Table IV - 9). It can be seen that, at the exception of **1a**, derivatives are evolving toward low ΔG^{Φ} as function of the increase H-bond propensity and polarity of the molecule. It demonstrates a powerful example of an informed and rational directed evolution strategy enabling the identification of kinetically accessible conglomerate, but also stable conglomerate-forming system.

Table IV - 9. ΔG^{Φ} value for the different 1,3-dimethylxanthine-based derivatives.

	Acetoxyl			Methoxyl		Hydroxyl		Amino
	1a		2a	1b	2b	PXL	DPL	2d
ΔG^{Φ}(kJ.mol^{-1})	1.23	3.01	3.38	3.59	3.42	2.01	1.00	0.17

IV.4 – Discussion & conclusion

The crystallization behaviour of racemic and enantiopure PXL was investigated by using several crystallization methods and this study highlighted, similarly to DPL, the benefit of using melt crystallization to access a number of phases inaccessible by solvent crystallization. This study shows a very rich binary phase diagram between PXL enantiomers with no less than three polymorphs of the pure enantiomer (*i.e.* EI, EII, EIII) and two polymorphs of the racemic compound (*i.e.* RI and RII) in monotropic relationships. Mixtures of PXL enantiomers can also

crystallize into three metastable conglomerates, one of which was experimentally obtained via SCM thermal treatment, echoing the impact of non-equilibrium condition to reach chiral discrimination.

The crystallization behaviour of PXL was further explored through the analysis of the crystal structures of the most stable phases, RI and EI, leading to the conclusion that the molecular flexibility of the H-bond donor moiety likely plays a significant role in explaining the versatility of PXL phase behaviour. This observation is similar to the reported case of DPL, suggesting that molecular flexibility and hydrogen bonding interactions are crucial factors enabling the possibility of preferential crystallization in conditions where the spontaneous nucleation of stable racemic phases is hindered, allowing the system to evolve through metastable equilibria (*i.e.* metastable conglomerates).

Combined with the data observed for DPL, the present work suggests that other factors, such as the molecular flexibility, hydrogen bonding interactions, or specific crystallization conditions, may play a significant role in determining the efficiency of preferential crystallization performed with metastable conglomerate. The synthesis of other 1,3-dimethylxantine-based derivatives exhibiting a gradient of H-bonding propensity support this hypothesis. Specifically, a drastic decrease in thermal stability is observed for the methoxylated derivatives **1b** and **2b**, which are furthermore associated with the highest ΔG^{Φ} values among the studied derivatives. Moreover, the lowest ΔG^{Φ} value is obtained for the amino alcohol derivative **2d**, which exhibits the chemical function with the highest proticity, and which was isolated as crystalline particles in the present study. More importantly, the nucleation of the racemic compound is sufficiently unfavourable in this case for its enantiopure counterpart to becomes thermodynamically stable.

Intermediate case is observed for acetoxylated derivatives **2a**, where weak C-H…O interactions remain possible as demonstrated by the crystal structure of (*RS-I*)-**2a**, leading to an increase in the stability of the racemic compound compared to DPL while keeping a versatile crystallisation behaviour. Interestingly, the acetoxylated derivative **1a** does not follow the same trends as its ΔG^{Φ} value is even lower than PXL, it would be interesting to further explore this chiral system to understand the underlying factor(s) responsible of this

behaviour and to check whether preferential crystallization by enantiopure seeding would proceed without recrystallization of the racemic compound.

The identification of key factors hindering the nucleation of the racemic compound, as in the case of DPL, helps inform our directed evolution strategy by targeting the right way to proceed derivatization. However, such factors hindering the nucleation of the racemic compound could also hinder the nucleation of any solid phase, as demonstrated by derivatives **1c** and **2c**. Consequently, this approach is a compromise between destabilizing the racemic compound to low values of ΔG^{Φ} while retaining the enantiopure counterpart.

More importantly, our insights can directly be implemented for the rational, almost predictive discovery of chiral compounds that crystallize as stable conglomerates, provided that peculiar molecular features favouring the enantiopure phase are uncovered.

References

(1) Boylan, P. M.; Abdalla, M.; Bissell, B.; Malesker, M. A.; Santibañez, M.; Smith, Z. Theophylline for the Management of Respiratory Disorders in Adults in the 21st Century: A Scoping Review from the American College of Clinical Pharmacy Pulmonary Practice and Research Network. Pharmacotherapy: The Journal of Human Pharmacology and Drug Therapy 2023, 43 (9), 963–990. https://doi.org/10.1002/phar.2843.

(2) Montaño, L. M.; Sommer, B.; Gomez-Verjan, J. C.; Morales-Paoli, G. S.; Ramírez-Salinas, G. L.; Solís-Chagoyán, H.; Sanchez-Florentino, Z. A.; Calixto, E.; Pérez-Figueroa, G. E.; Carter, R.; Jaimez-Melgoza, R.; Romero-Martínez, B. S.; Flores-Soto, E. Theophylline: Old Drug in a New Light, Application in COVID-19 through Computational Studies. International Journal of Molecular Sciences 2022, 23 (8), 4167. https://doi.org/10.3390/ijms23084167.

(3) Selvig, K. Pharmacokinetics of Proxyphylline in Adults after Intravenous and Oral Administration. Eur J Clin Pharmacol 1981, 19 (2), 149–155. https://doi.org/10.1007/BF00568402.

(4) Brandel, C.; Amharar, Y.; Rollinger, J. M.; Griesser, U. J.; Cartigny, Y.; Petit, S.; Coquerel, G. Impact of Molecular Flexibility on Double Polymorphism, Solid Solutions and Chiral Discrimination during Crystallization of Diprophylline Enantiomers. Mol. Pharmaceutics 2013, 10 (10), 3850–3861. https://doi.org/10.1021/mp400308u.

(5) Brandel, C. Structural Purity and Solid-Solid Transitions in Molecular Crystals. PhD Manuscript, Université de Rouen, 2014.

(6) Brandel, C.; Cartigny, Y.; Coquerel, G.; ter Horst, J. H.; Petit, S. Prenucleation Self-Assembly and Chiral Discrimination Mechanisms during Solution Crystallisation of Racemic Diprophylline. Chemistry—A European Journal 2016, 22 (45), 16103–16112. https://doi.org/10.1002/chem.201602707.

(7) Griesser, U. J.; Auer, M. E.; Burger, A. Micro-Thermal Analysis, FTIR- and Raman-Microscopy of (R,S)-Proxyphylline Crystal Forms. Microchemical Journal 2000, 65, 283–292. https://doi.org/10.1016/S0026-265X(00)00124-7.

(8) Harfouche, L. C.; Brandel, C.; Cartigny, Y.; ter Horst, J. H.; Coquerel, G.; Petit, S. Enabling Direct Preferential Crystallization in a Stable Racemic Compound System. Mol. Pharmaceutics 2019, 16 (11), 4670–4676. https://doi.org/10.1021/acs.molpharmaceut.9b00805.

(9) Harfouche, L. Non-Classical Studies for Cyclic Preferential Crystallization of a Stable Racemic Compound. phdthesis, Normandie Université, 2020. https://theses.hal.science/tel-03238187 (accessed 2024-08-07).

(10) Pinetre, C.; Harfouche, L.; Brandel, C.; Bendeif, E.-E.; Sanselme, M.; Cartigny, Y.; Couvrat, N.; Dupray, V. Investigation of the Binary System of Proxyphylline Enantiomers: Structural Resolution and Phase Diagram Determination. Mol. Pharmaceutics 2024, 21 (2), 845–853. https://doi.org/10.1021/acs.molpharmaceut.3c00922.

(11) Lemercier, A.; Viel, Q.; Brandel, C.; Cartigny, Y.; Dargent, E.; Petit, S.; Coquerel, G. Optimization of Experimental Conditions for the Monitoring of Nucleation and Growth of Racemic Diprophylline from the Supercooled Melt. Journal of Crystal Growth 2017, 472, 11–17. https://doi.org/10.1016/j.jcrysgro.2017.03.034.

(12) Threlfall, T. Structural and Thermodynamic Explanations of Ostwald's Rule. Org. Process Res. Dev. 2003, 7 (6), 1017–1027. https://doi.org/10.1021/op030026l.

(13) Borowiecki, P.; Paprocki, D.; Dudzik, A.; Plenkiewicz, J. Chemoenzymatic Synthesis of Proxyphylline Enantiomers. J. Org. Chem. 2016, 81 (2), 380–395. https://doi.org/10.1021/acs.joc.5b01840.

(14) Rekis, T. Crystallization of Chiral Molecular Compounds: What Can Be Learned from the Cambridge Structural Database? Acta Crystallogr B Struct Sci Cryst Eng Mater 2020, 76 (3), 307–315. https://doi.org/10.1107/S2052520620003601.

(15) Clevers, S.; Coquerel, G. Kryptoracemic Compounds Hunting and Frequency in the Cambridge Structural Database. CrystEngComm 2018, 20 (15), 2093–2101. https://doi.org/10.1039/C8CE00075A.

(16) Bernstein, J.; Hagler, A. T. Conformational Polymorphism. The Influence of Crystal Structure on Molecular Conformation. J. Am. Chem. Soc. 1978, 100 (3), 673–681. https://doi.org/10.1021/ja00471a001.

(17) Cruz-Cabeza, A. J.; Bernstein, J. Conformational Polymorphism. Chem. Rev. 2014, 114 (4), 2170–2191. https://doi.org/10.1021/cr400249d.

(18) Ricci, J. E. The Phase Rule and Heterogeneous Equilibrium. In The Phase Rule and Heterogeneous Equilibrium; Dover: New York, 1951.

(19) Prigogine, I.; Defay, R. Chemical Thermodynamics. 1958.

(20) Jacques, J.; Collet, A.; Wilen, S. H. Enantiomers, Racemates, and Resolutions; Krieger Publishing Company: Malabar, 1994.

(21) Collet, A.; Ziminski, L.; Garcia, C.; Vigné-Maeder, F. Chiral Discrimination in Crystalline Enantiomer Systems: Facts, Interpretations, and Speculations. In Supramolecular Stereochemistry; Siegel, J. S., Ed.; Springer Netherlands: Dordrecht, 1995; pp 91–110. https://doi.org/10.1007/978-94-011-0353-4_12.
(22) Leclercq, M.; Collet, A.; Jacques, J. Etude Des Melanges d'antipodes Optiques—XII: Mesure de La Stabilite Des Racemiques Vrais. Tetrahedron 1976, 32 (7), 821–828. https://doi.org/10.1016/0040-4020(76)80007-5.
(23) Bredikhin, A. A.; Bredikhina, Z. A.; Novikona, V. G.; Pashagin, A. V.; Zacharychev, D. V.; Gubaidullin, A. T. Three Different Types of Chirality-Driven Crystallization within the Series of Uniformly Substituted Phenyl Glycerol Ethers. Chirality 2008, 20, 1092–1103. https://doi.org/10.1002/chir.20648.
(24) Li, Z. J.; Zell, M. T.; Munson, E. J.; Grant, D. J. W. Characterization of Racemic Species of Chiral Drugs Using Thermal Analysis, Thermodynamic Calculation, and Structural Studies. Journal of Pharmaceutical Sciences 1999, 88 (3), 337–346. https://doi.org/10.1021/js980205u.
(25) Drazic, A.; Myklebust, L. M.; Ree, R.; Arnesen, T. The World of Protein Acetylation. Biochimica et Biophysica Acta (BBA) - Proteins and Proteomics 2016, 1864 (10), 1372–1401. https://doi.org/10.1016/j.bbapap.2016.06.007.
(26) Okoye, P. U.; Hameed, B. H. Review on Recent Progress in Catalytic Carboxylation and Acetylation of Glycerol as a Byproduct of Biodiesel Production. Renewable and Sustainable Energy Reviews 2016, 53, 558–574. https://doi.org/10.1016/j.rser.2015.08.064.
(27) Wang, X.; Wang, Z.; Shen, M.; Yi, C.; Yu, Q.; Chen, X.; Xie, J.; Xie, M. Acetylated Polysaccharides: Synthesis, Physicochemical Properties, Bioactivities, and Food Applications. Critical Reviews in Food Science and Nutrition 2024, 64 (15), 4849–4864. https://doi.org/10.1080/10408398.2022.2146046.
(28) Conelly-Espinosa, P.; Toscano, R. A.; Morales-Morales, D. Synthesis and Characterization of Hydrophilic Theophylline Base Compounds and Their Use as Ligands in the Microwave Assisted Suzuki–Miyaura Couplings of Halopyridines in Water. Tetrahedron Letters 2014, 55 (42), 5841–5845. https://doi.org/10.1016/j.tetlet.2014.08.103.
(29) Burger, A.; Ramberger, R. On the Polymorphism of Pharmaceuticals and Other Molecular Crystals. I. Mikrochim Acta 1979, 72 (3–4), 259–271. https://doi.org/10.1007/BF01197379.
(30) Van Den Berg, J.-A.; Seddon, K. R. Critical Evaluation of C−H···X Hydrogen Bonding in the Crystalline State. Crystal Growth & Design 2003, 3 (5), 643–661. https://doi.org/10.1021/cg034083h.
(31) Steiner, T.; Desiraju, G. R. Distinction between the Weak Hydrogen Bond and the van Der Waals Interaction. Chemical Communications 1998, 0 (8), 891–892. https://doi.org/10.1039/A708099I.
(32) Steiner, T. The Hydrogen Bond in the Solid State. Angewandte Chemie International Edition 2002, 41 (1), 48–76. https://doi.org/10.1002/1521-3773(20020104)41:1<48::AID-ANIE48>3.0.CO;2-U.
(33) McCrone, W. C.; Fox, D.; Labes, M.; Weissberger, A. Physics and Chemistry of the Organic Solid State; Wiley-Interscience: New York, 1965; Vol. II.
(34) Hill, A.; Kras, W.; Theodosiou, F.; Wanat, M.; Lee, D.; Cruz-Cabeza, A. J. Polymorphic Solid Solutions in Molecular Crystals: Tips, Tricks, and Switches. J. Am. Chem. Soc. 2023, 145 (37), 20562–20577. https://doi.org/10.1021/jacs.3c07105.
(35) Braga, D.; Casali, L.; Grepioni, F. The Relevance of Crystal Forms in the Pharmaceutical Field: Sword of Damocles or Innovation Tools? Int J Mol Sci 2022, 23 (16), 9013. https://doi.org/10.3390/ijms23169013.
(36) Aoyama, T.; Shioiri, T. Trimethylsilyldiazomethane : A Convenient Reagent for the o-Methylation of Alcohols. Tetrahedron Letters 1990, 31 (38), 5507–5508. https://doi.org/10.1016/S0040-4039(00)97884-5.
(37) Stoochnoff, B. A.; Benoiton, N. L. The Methylation of Some Phenols and Alcohols with Sodium Hydride / Methyl Iodide in Tetrahydrofuran at Room Temperature. Tetrahedron Letters 1973, 14 (1), 21–24. https://doi.org/10.1016/S0040-4039(01)95566-2.
(38) Smith, M. B.; March, J. March's Advanced Organic Chemistry: Reactions, Mechanisms, and Structure, 1st ed.; Wiley, 2006. https://doi.org/10.1002/0470084960.
(39) de Almeida, G.; Sletten, E. M.; Nakamura, H.; Palaniappan, K. K.; Bertozzi, C. R. Thiacycloalkynes for Copper-Free Click Chemistry. Angewandte Chemie International Edition 2012, 51 (10), 2443–2447. https://doi.org/10.1002/anie.201106325.
(40) Jewett, J. C.; Sletten, E. M.; Bertozzi, C. R. Rapid Cu-Free Click Chemistry with Readily Synthesized Biarylazacyclooctynones. J. Am. Chem. Soc. 2010, 132 (11), 3688–3690. https://doi.org/10.1021/ja100014q.

(41) Lutz, J.-F.; Zarafshani, Z. Efficient Construction of Therapeutics, Bioconjugates, Biomaterials and Bioactive Surfaces Using Azide–Alkyne "Click" Chemistry. Advanced Drug Delivery Reviews 2008, 60 (9), 958–970. https://doi.org/10.1016/j.addr.2008.02.004.
(42) Staudinger, H.; Meyer, J. Über neue organische Phosphorverbindungen III. Phosphinmethylenderivate und Phosphinimine. Helvetica Chimica Acta 1919, 2 (1), 635–646. https://doi.org/10.1002/hlca.19190020164.
(43) Luo, J.; Liu, Q.; Morihiro, K.; Deiters, A. Small-Molecule Control of Protein Function through Staudinger Reduction. Nature Chem 2016, 8 (11), 1027–1034. https://doi.org/10.1038/nchem.2573.
(44) van Kalkeren, H. A.; Bruins, J. J.; Rutjes, F. P. J. T.; van Delft, F. L. Organophosphorus-Catalysed Staudinger Reduction. Advanced Synthesis & Catalysis 2012, 354 (8), 1417–1421. https://doi.org/10.1002/adsc.201100967.
(45) El Ashry, E. S. H.; Abdel-Rahman, A.; Rashed, N.; Awad, L. F.; Rasheed, H. A. Synthesis of AZT Analogues: 7-(3-Azido-2hydroxypropyl)-, 7-(3-Amino-2-Hydroxypropyl)-, 7-(3-Triazolyl-2-Hydroxypropyl)Theophyllines. Nucleosides, Nucleotides & Nucleic Acids 2006, 25 (3), 299–305. https://doi.org/10.1080/15257770500544495.

GENERAL DISCUSSION

The central aim of this Ph.D. manuscript is to demonstrate that the conventionally accepted boundaries of crystallization-based chiral resolution methods can actually be systematically bypassed by the clever use of both thermodynamics and kinetics. In doing so, we reveal the significant potential of studying families of chemically related derivatives.

We must acknowledge the number of conglomerate-forming systems identified among the 53 chiral molecules synthesized and studied in this work, yielding to a hits frequency of 7.5 % (4 out of 53). Although aligning with previously reported conglomerate frequencies,[1–3] one must remember that two of them are composed of a hardly-racemizable chiral core (praziquantel derivative **3u** and 1,3-dimethylxanthine-based derivative **2d**) and the two other are a case of a conglomerate cluster forming an isomorphous crystal structure (triazole ketone derivatives **1a** and **1c**). This analysis emphasizes that a substituting site in a directed evolution strategy is an important factor to consider. It can also be related to the large fluctuation of the conglomerate propensity from one series of molecule to another: from 75 % successful conglomerate hits for para-substituted triazole ketone derivatives to 33 % including the ortho-substituted ones.[4–6] Moreover, **3u** exhibited an uncommon case of eutectoid transition, further emphasizing the large propensity of nature to form heterochiral structure. It also definitely demonstrates the importance of a careful investigation of the solid-state behaviour of each newly engineer solid form, as enantiomeric systems can show complex solid-state behaviour (*e.g.* **3u**, **3t**, **3ae**, **3ag**, **2a**, PXL etc.) which should not be overlooked during, for instance, drug development and crystallization process design.

To address this large propensity of heterochiral structure, we here disclosed the proof-of-concept of a novel solid-state deracemization approach based on the formation of conglomerate host-guest mixed crystal structures by making use of a highly discriminative chiral recognition phenomenon, akin chirality transfer and Dutch resolution processes.[7–9] It allows the introduction of the substance to be deracemized within the lattice sites of a conglomerate host structure. The resulting mixed crystals can then undergo deracemization and only one mixed crystal enantiomorph will emerge. More precisely, it is possible to direct the complete symmetry breaking towards a single handedness for a racemic-compound-forming system by using a solid solution with a chemically related racemizable conglomerate through conventional deracemization routes (*e.g.* TCID). The main advantage of this method compared to conventional derivatization strategies (multicomponent crystal, reversible

synthesis etc.) is that the conglomerate behaviour is always ensure by the conglomerate host structure, while conventional derivatization strategies rely on trial-and-error iterations exhibiting the same 5-10% unfavourable outcomes.

Interestingly, conglomerate mixed crystals were systematically characterized for our two model systems, despite differing solid-state miscibility limit. This raises the question of how this chiral recognition phenomenon extends to other chemically related or unrelated systems. For instance, we could make use of the library of actually known conglomerate-forming system to find suitable chemical host to any racemic compound-forming system of interest. Furthermore, this statement echoes the natural library of chemically related derivative of amino acids, some of which crystallize as conglomerate (*e.g.* threonine, asparagine monohydrate etc.). One could speculate that such conglomerate mixed crystal may have played a role in the evolution of the homochirality of life observed nowadays.

Moreover, a clear example of a forced extension of the solid solution domain under neat high-energy milling is characterized, in which operative deracemization condition is successfully implemented. More importantly, we demonstrate that high energy inputs provide sufficient far-from-equilibrium conditions for accessing metastable structures with efficient chiral discrimination capabilities. We thereby open new pathways for chiral resolution of substances that do not form conglomerates and underline the tremendous potential of mechanochemistry in the field of chiral resolution and deracemization of metastable solid form. Among the two successful examples, we could deracemize up to 25 wt% of the racemic compound inside the conglomerate matrix. Although the solid-state miscibility limits could be extended through non-equilibrium forced extension, the effectiveness of this deracemization strategy remains limited by this phase boundary.

We also took advantage of fundamental kinetic asymmetries between enantiomers crystallizing as conglomerates under temperature variations, demonstrating a striking consistency in the out-of-equilibrium dissolution phenomenon and proportionality with respect to the temperature variation, even starting from a racemic solid mixture. These out-of-equilibrium phenomena induced sufficient *e.e.* imbalances to drive a complete chiral resolution of a conglomerate-forming system throughout a kind of chiral segregation induced by simple temperature cycling. This result may be considered in relation with the driving force

behind TCID processes. Additionally, this chiral resolution process could also be included in conventional conglomerate screening process for straightforward identification of conglomerate-forming system from racemic mixture. This could be done by simply monitoring the evolution of the *e.e.* while exchanging the solid-free liquid between two symmetrical racemic slurries under temperature variations. A deviation from the racemic composition would be indicative of a conglomerate-forming system.

Finally, the most important portion of results produced by this thesis, both in terms of scientific impact and time spent, is provided by chapter III and IV. In summary, by systematically investigating the energy differences between the racemic and enantiopure crystal forms of structurally related molecules, we introduce how combining directed evolution and combinatorial chemistry enables the expedient discovery of enantiopure crystal phases that can be, at least kinetically, stabilized for isolating enantiomers of the desired handedness. Until now, hindered by thermodynamic limitations, it was generally understood that merely 5-10% of chiral molecules were accessible as enantiopure crystals. In contrast, we here estimate that 45 to 60% of all chiral molecules are accessible as enantiopure crystals through non-equilibrium crystallization. Moreover, this estimation does not stand as an unbreachable boundaries as this approach may also work for systems with higher ΔG^{Φ}, provided that suitable non-equilibrium conditions are found.

Our insights can directly be implemented for the rational discovery of chiral compounds that can be separated by crystallization. Even though the change of even a single atom can drastically change the stability of crystal phases, we observe clustering of similar derivatives within a library which enables methodological library design. Specifically, we envision the autonomous construction of chemical libraries in self-driven labs,[10,11] following an iterative manner, in which a rapid assessment of ΔG^{Φ} serves as a diagnostic guide for the design of new library entries and the efficient discovery of targets for chiral resolution or deracemization. Analogous to directed evolution in catalysis,[12–14] we propose to synthesize a small library with very diverse entries that are ranked according to ΔG^{Φ} as a fitness parameter, after which the most favourable entry is selected for synthesis of the next generation of entries. This evolutionary strategy prevents that only unfavourable zones with high ΔG^{Φ} are screened, and instead iterate within only a few cycles towards favourable low ΔG^{Φ}. We foresee that making informed design choices may be further aided by integrating Crystal Structure Prediction (CSP)

methodologies. Ultimately, combining advanced machine learning, CSP methods, and our directed evolution strategy may enable the rapid discovery of (kinetic) conglomerates within self-driven laboratories.

Moreover, we shown that identifying key factors hindering the nucleation of the racemic compound, as in the case of DPL, helps inform our directed evolution strategy by targeting the right way to proceed derivatization. Specifically, our directed evolution strategy based on the conclusion of the work of Brandel *et al.*[15–17], allowed us to engineer a molecule exhibiting a higher H-bonding propensity for which the nucleation of the racemic compound is sufficiently unfavourable for its enantiopure counterpart to becomes thermodynamically stable. Conversely, reducing the H-bonding propensity enhanced the relative stability of the racemic compound, demonstrating an almost predictive discovery of chiral compounds that crystallize as stable conglomerates. However, this aspect needs to be the subject of a more in-depth case study on other model compounds to be confirmed.

Moreover, for entries with low ΔG^{Φ}, we here show that enantiopure crystals can successfully be isolated from racemic mixtures by applying suitable non-equilibrium conditions. The key next step is to systematically exploit non-equilibrium conditions under which crystallization rates, instead of thermodynamic stabilities alone, determine which crystalline phase is favoured such that for instance, the favoured kinetic conglomerate grows faster than the unfavoured racemic compound. Alternatively, specific non-equilibrium conditions can be exploited to supress the nucleation and growth rate of stable racemic compound crystals, such that the desired enantiopure crystals can be isolated. Furthermore, the crystallization process offers a large parameter space that can be exploited to achieve these favourable rates of nucleation and growth, ranging from choice of solvent, confinements such as microdroplets, and (chiral) additives to temperature gradients and mechanochemistry.[18–24] Importantly, mechanical grinding and temperature gradients have also been used to achieve deracemization of solid phases,[25–28] suggesting possibilities to simultaneously yield non-equilibrium conditions that destabilize racemic compounds and directly convert the solid into the desired enantiomer. Hence, both the library design through directed evolution and the exploitation of non-equilibrium conditions open many new opportunities for crystallization-based routes towards enantiopure molecules that are essential in our daily lives (Figure G.D. - 1).

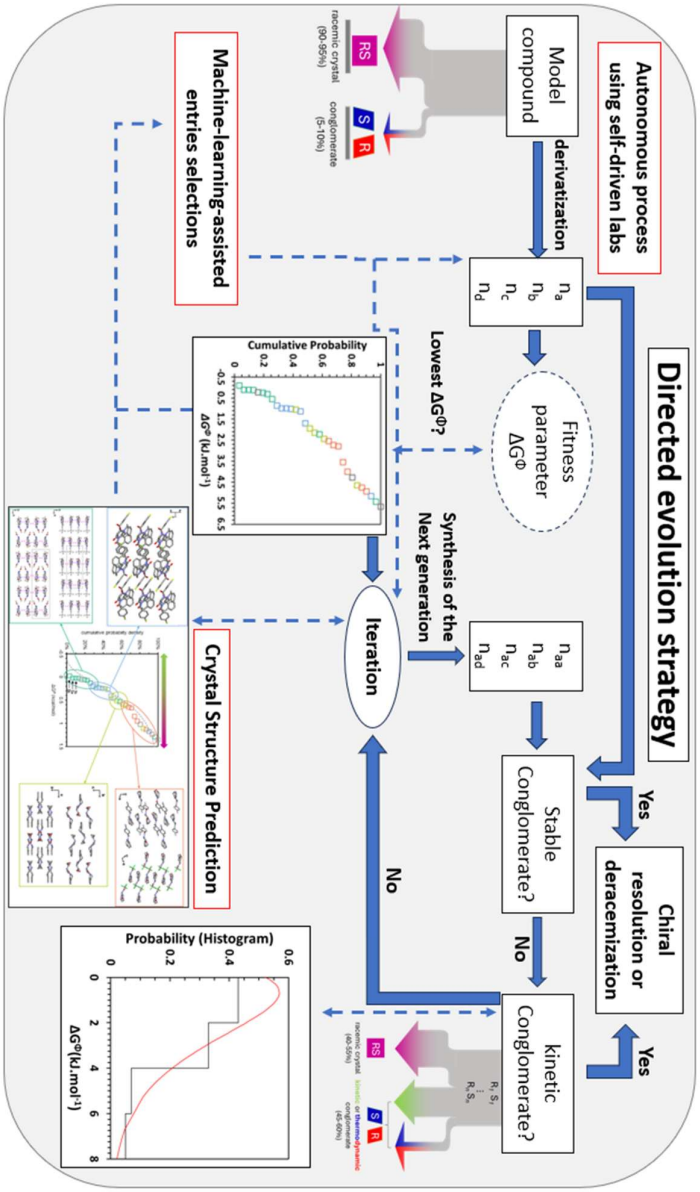

Figure G.D. - 1. Directed evolution strategy based on the derivatization of a model compound crystallizing as a racemic compound using ΔG^{Φ} as a fitness parameter, further assisted by CSP and machine learning methods, to iterate toward (kinetically) accessible conglomerate.

To further refine the limits of chiral resolution under non-equilibrium conditions, additional preferential crystallization experiments and nucleation behaviour assessment must be conducted on other systems within the praziquantel and proxyphylline libraries. More specifically, a thorough exploration of the solid-state landscape and nucleation behaviour of the amino-alcohol derivative of proxyphylline remains necessary. Moreover, the relevance and applicability of our directed evolution strategy must be expanded to other model compounds and more complex cases, for instance cocrystals or salts.

GENERAL CONCLUSION

This Ph.D. work contributes to our general understanding of crystallization-based route to enantiopurity, as well are reconsidering the admitted boundaries hindering any such chiral resolution for the overwhelming majority of chiral molecules.

This was firstly exemplified by introducing two unconventional strategies toward enantiopurity, both playing with crystallization kinetics, enabling the chiral resolution of racemic compound forming system and non-racemizable molecule. It demonstrates how a slight kinetic deviation to thermodynamic ideality enables a natural chiral segregation, likely driven an Ostwald's ripening process acting much like Pasteur's tweezers. This out-of-equilibrium nature of crystallization was leveraged in the deracemization of conglomerate mixed crystals, that initially occurs close to equilibrium. It demonstrated the numerous possibilities that must be included considered in our toolkit to improve any crystallization process, even if the method appears to rely on thermodynamic equilibrium. The results relative to the binary isoplethal section between triazole ketone derivatives and the TCID experiments on the engineered conglomerate mixed crystal were published in *Chemistry: A European Journal*.[29] The result relative to the out-of-equilibrium variation using high energy milling is currently being drafted for publication.

Bearing this in mind, we hence introduced the library of the praziquantel derivatives. Although the conventional conglomerate screening of this set of chemically related molecules would be definitely considered as a failure, interesting solid-state landscapes was investigated, characterized and discussed in detail. More importantly, careful analysis of this data set permitted the correlation of a thermodynamic data (ΔG^{Φ}) with their chemical and crystal structure. Notably, the statistical distribution of this thermodynamic data revealed that most systems exhibited a slightly stable the racemic compound form. This leaves significant room for kinetic factors to drive these systems toward enantiopurity, ultimately reversing the odd in our favour. Indeed, it was generally understood that merely 5-10% of chiral molecules were accessible as enantiopure crystals. In contrast, we here estimate that at least 45 to 60% of all chiral molecules are accessible as enantiopure crystals through non-equilibrium crystallization. This has been well exemplified for the two case studies **3t** and **3ag** for which successful preferential crystallization was implemented despite their racemic-compound nature, further demonstrating the impact of the solvent selection. Ultimately, the rational clustering of derivative within a set of chemically related molecules enabled us to depict a

directed evolution strategy, enabling rational experimental design and straightforward access to kinetically stabilizable conglomerate. The results relative to the determination of the enantiotropic solid-state landscape of derivative **3ag** (*i.e.* binary phase diagram, structural study, polymorph stability) were presented as an oral conference at a national congress (*Journées d'Étude des Équilibres entre phases 2023* in Rouen, France) and were published in *Organic Process Reasearch and Development* journal.[30] The results relative to the directed evolution strategy and crystallization under non-equilibrium condition were presented as an oral conference at two international congresses (*International Symposium on Industrial Crystallization 2023* in Glasgow, Scotland & *International Workshop on Industrial Crystallization 2024* in Delft, The Netherland) and are currently being drafted for publication.

Finally, the study of 1,3-dimethylxanthine-based chiral derivatives enabled the identification of specific molecular features favouring the enantiopure phase, already uncovered in the case of DPL by the work of Brandel *et al.*[15–17] The study of the solid-state landscape of PXL demonstrated the striking similarities of its solid-state behaviour with that of DPL and the impact of the molecular flexibility as well as the H-bonding propensity in its crystallization properties. Supporting this statement, modulating these two factors by slight chemical modifications enabled us to direct the solid-state classification of these derivative to either a relatively more stable racemic compounds or a relatively less stable racemic compound. Ultimately, enhancing these two factors yielded the formation of a conglomerate forming-system. The results relative to the polymorphic solid-state landscape of PXL (*i.e.* binary phase diagram, structural study, polymorph stability) were published in *Molecular Pharmaceutics* journal.

The study of chemically related chiral derivatives and the chiral resolution by crystallization under non-equilibrium conditions was at the centre of the present work. It demonstrated the relationship between the thermodynamic properties, molecular features, crystal structures and the macroscopic solid-state behaviour of the resulting crystals. More importantly, we bring a new practical directed evolution approach enabling the rational modulation to the access of chiral discrimination, either through stable or metastable equilibrium, that was previously unconsidered.

REFERENCES

(1) Rekis, T. Crystallization of Chiral Molecular Compounds: What Can Be Learned from the Cambridge Structural Database? *Acta Crystallogr B Struct Sci Cryst Eng Mater* **2020**, *76* (3), 307–315. https://doi.org/10.1107/S2052520620003601.

(2) Clevers, S.; Coquerel, G. Kryptoracemic Compounds Hunting and Frequency in the Cambridge Structural Database. *CrystEngComm* **2018**, *20* (15), 2093–2101. https://doi.org/10.1039/C8CE00075A.

(3) Jacques, J.; Collet, A.; Wilen, S. H. *Enantiomers, Racemates, and Resolutions*; Krieger Publishing Company: Malabar, 1994.

(4) Otero-de-la-Roza, A.; Hein, J. E.; Johnson, E. R. Reevaluating the Stability and Prevalence of Conglomerates: Implications for Preferential Crystallization. *Crystal Growth & Design* **2016**, *16* (10), 6055–6059. https://doi.org/10.1021/acs.cgd.6b01088.

(5) Mbodji, A.; Gbabode, G.; Sanselme, M.; Couvrat, N.; Leeman, M.; Dupray, V.; Kellogg, R. M.; Coquerel, G. Family of Conglomerate-Forming Systems Composed of Chlocyphos and Alkyl-Amine. Assessment of Their Resolution Performances by Using Various Modes of Preferential Crystallization. *Crystal Growth & Design* **2019**, *19* (9), 5173–5183. https://doi.org/10.1021/acs.cgd.9b00568.

(6) Kellogg, R. M. Practical Stereochemistry. *Acc. Chem. Res.* **2017**, *50* (4), 905–914. https://doi.org/10.1021/acs.accounts.6b00630.

(7) Hoquante, M. Homochiral vs. Heterochiral Crystal Packing Dilemma. Interplay between Intrinsic Chirality and Supramolecular Chirality, Rouen, 2021.

(8) Dutch Resolution of Racemates and the Roles of Solid Solution Formation and Nucleation Inhibition. In *Novel Optical Resolution Technologies*; Kellogg, R. M., Kaptein, B., Ton R., V., Eds.; Topics in Current Chemistry; Springer Berlin Heidelberg: Berlin, Heidelberg, 2007; Vol. 269, pp 159–197. https://doi.org/10.1007/978-3-540-46320-7.

(9) Kellogg, R. M.; Nieuwenhuijzen, J. W.; Pouwer, K.; Vries, T. R.; Broxterman, Q. B.; Grimbergen, R. F. P.; Kaptein, B.; Crois, R. M. L.; Wever, E. de; Zwaagstra, K.; Laan, A. C. van der. Dutch Resolution: Separation of Enantiomers with Families of Resolving Agents. A Status Report. *Synthesis* **2003**, *2003* (10), 1626–1638. https://doi.org/10.1055/s-2003-40508.

(10) Abolhasani, M.; Kumacheva, E. The Rise of Self-Driving Labs in Chemical and Materials Sciences. *Nat. Synth* **2023**, *2* (6), 483–492. https://doi.org/10.1038/s44160-022-00231-0.

(11) MacLeod, B. P.; Parlane, F. G. L.; Morrissey, T. D.; Häse, F.; Roch, L. M.; Dettelbach, K. E.; Moreira, R.; Yunker, L. P. E.; Rooney, M. B.; Deeth, J. R.; Lai, V.; Ng, G. J.; Situ, H.; Zhang, R. H.; Elliott, M. S.; Haley, T. H.; Dvorak, D. J.; Aspuru-Guzik, A.; Hein, J. E.; Berlinguette, C. P. Self-Driving Laboratory for Accelerated Discovery of Thin-Film Materials. *Science Advances* **2020**, *6* (20), eaaz8867. https://doi.org/10.1126/sciadv.aaz8867.

(12) Arnold, F. H. Directed Evolution: Bringing New Chemistry to Life. *Angewandte Chemie International Edition* **2018**, *57* (16), 4143–4148. https://doi.org/10.1002/anie.201708408.

(13) Yang, K. K.; Wu, Z.; Arnold, F. H. Machine-Learning-Guided Directed Evolution for Protein Engineering. *Nat Methods* **2019**, *16* (8), 687–694. https://doi.org/10.1038/s41592-019-0496-6.

(14) Romero, P. A.; Arnold, F. H. Exploring Protein Fitness Landscapes by Directed Evolution. *Nat Rev Mol Cell Biol* **2009**, *10* (12), 866–876. https://doi.org/10.1038/nrm2805.

(15) Brandel, C. Structural Purity and Solid-Solid Transitions in Molecular Crystals. PhD Manuscript, Université de Rouen, 2014.

(16) Brandel, C.; Amharar, Y.; Rollinger, J. M.; Griesser, U. J.; Cartigny, Y.; Petit, S.; Coquerel, G. Impact of Molecular Flexibility on Double Polymorphism, Solid Solutions and Chiral Discrimination during Crystallization of Diprophylline Enantiomers. *Mol. Pharmaceutics* **2013**, *10* (10), 3850–3861. https://doi.org/10.1021/mp400308u.

(17) Brandel, C.; Cartigny, Y.; Coquerel, G.; ter Horst, J. H.; Petit, S. Prenucleation Self-Assembly and Chiral Discrimination Mechanisms during Solution Crystallisation of Racemic Diprophylline. *Chemistry—A European Journal* **2016**, *22* (45), 16103–16112. https://doi.org/10.1002/chem.201602707.

(18) Candoni, N.; Grossier, R.; Lagaize, M.; Veesler, S. Advances in the Use of Microfluidics to Study Crystallization Fundamentals. *Annual Review of Chemical and Biomolecular Engineering* **2019**, *10* (Volume 10, 2019), 59–83. https://doi.org/10.1146/annurev-chembioeng-060718-030312.

(19) Gu, C. H.; Young, V.; Grant, D. J. Polymorph Screening: Influence of Solvents on the Rate of Solvent-Mediated Polymorphic Transformation. *J Pharm Sci* **2001**, *90* (11), 1878–1890. https://doi.org/10.1002/jps.1137.

(20) Belenguer, A. M.; Lampronti, G. I.; De Mitri, N.; Driver, M.; Hunter, C. A.; Sanders, J. K. M. Understanding the Influence of Surface Solvation and Structure on Polymorph Stability: A Combined Mechanochemical and Theoretical Approach. *J. Am. Chem. Soc.* **2018**, *140* (49), 17051–17059. https://doi.org/10.1021/jacs.8b08549.

(21) Linberg, K.; C. Sander, P.; Emmerling, F.; L. Michalchuk, A. A. In Situ Investigation of Controlled Polymorphism in Mechanochemistry at Elevated Temperature. *RSC Mechanochemistry* **2024**, *1* (1), 43–49. https://doi.org/10.1039/D3MR00019B.

(22) M. Belenguer, A.; I. Lampronti, G.; J. Cruz-Cabeza, A.; A. Hunter, C.; M. Sanders, J. K. Solvation and Surface Effects on Polymorph Stabilities at the Nanoscale. *Chemical Science* **2016**, *7* (11), 6617–6627. https://doi.org/10.1039/C6SC03457H.

(23) Yeom, J.; Yeom, B.; Chan, H.; Smith, K. W.; Dominguez-Medina, S.; Bahng, J. H.; Zhao, G.; Chang, W.-S.; Chang, S.-J.; Chuvilin, A.; Melnikau, D.; Rogach, A. L.; Zhang, P.; Link, S.; Král, P.; Kotov, N. A. Chiral Templating of Self-Assembling Nanostructures by Circularly Polarized Light. *Nature Mater* **2015**, *14* (1), 66–72. https://doi.org/10.1038/nmat4125.

(24) Weissbuch, I.; Lahav, M. Crystalline Architectures as Templates of Relevance to the Origins of Homochirality. *Chem. Rev.* **2011**, *111* (5), 3236–3267. https://doi.org/10.1021/cr1002479.

(25) Viedma, C. Chiral Symmetry Breaking During Crystallization: Complete Chiral Purity Induced by Nonlinear Autocatalysis and Recycling. *Phys. Rev. Lett.* **2005**, *94* (6), 065504. https://doi.org/10.1103/PhysRevLett.94.065504.

(26) Viedma, C. Chiral Symmetry Breaking and Complete Chiral Purity by Thermodynamic-Kinetic Feedback Near Equilibrium: Implications for the Origin of Biochirality. *Astrobiology* **2007**, *7* (2), 312–319. https://doi.org/10.1089/ast.2006.0099.

(27) Suwannasang, K.; Flood, A. E.; Rougeot, C.; Coquerel, G. Using Programmed Heating–Cooling Cycles with Racemization in Solution for Complete Symmetry Breaking of a Conglomerate Forming System. *Crystal Growth & Design* **2013**, *13* (8), 3498–3504. https://doi.org/10.1021/cg400436r.

(28) Lopes, C.; Cartigny, Y.; Brandel, C.; Dupray, V.; Body, C.; Shemchuk, O.; Leyssens, T. A Greener Pathway to Enantiopurity: Mechanochemical Deracemization through Abrasive Grinding. *Chemistry – A European Journal* **2023**, *29* (35), e202300585. https://doi.org/10.1002/chem.202300585.

(29) Pinètre, C.; Gendron, F.; Kuroda, R.; Oketani, R.; Aupetit, C.; Buffeteau, T.; Coquerel, G. Use of Conglomerate Mixed Crystals to Deracemize a Stable Racemic-Compound-Forming System. *Chemistry A European J* **2023**, e202300441. https://doi.org/10.1002/chem.202300441.

(30) Pinètre, C.; Ritou, L.; Gerard, C. J. J.; Cercel, H.; Leeman, M.; Kellogg, R. M.; Tinnemans, P.; Sanselme, M.; Brandel, C.; Dupray, V.; ter Horst, J. H. Rare Case of Polymorphism in the Binary System of Enantiomers of a Praziquantel Derivative. *Org. Process Res. Dev.* **2024**. https://doi.org/10.1021/acs.oprd.4c00035.

APPENDICES

A - I. Materials & Methods

A - I.1. Chemicals & Syntheses

A - I.1.1. Chemicals

Racemic Praziquantel was kindly provided by Symeres (Groningen, NL) or purchased from TCI EUROPE (purity >98%, Zwijndrecht, Belgium). Acyl chlorides were purchased from Sigma-Aldrich (purity >98%, USA). (-) or (+)-dibenzoyl-tartaric acid were purchased from Fisher Scientific (purity 98%, USA). Triazole ketone derivatives were previously synthesized by Céline Rougeot and used after assessing their chemical and purity by NMR, DSC, HPLC and XRPD. Racemic proxyphylline, racemic diprophylline and theophylline were respectively purchase from TCI EUROPE (purity >98%, Zwijndrecht, Belgium), Sigma-Aldrich (purity >98%, USA) and VWR chemical purity >98%,, France). All commercial chemicals were used without further purification. HPLC grade solvents and other reagents were purchased from Fisher Scientific and used as received.

A - I.1.2. Synthesis of the praziquantel library

50mg of derivatives **3a-ad** were provided by Symeres (Groningen, NL) in both enantiopure and racemic form. Additional materials were synthesized If needed (Figure A - I. 1).

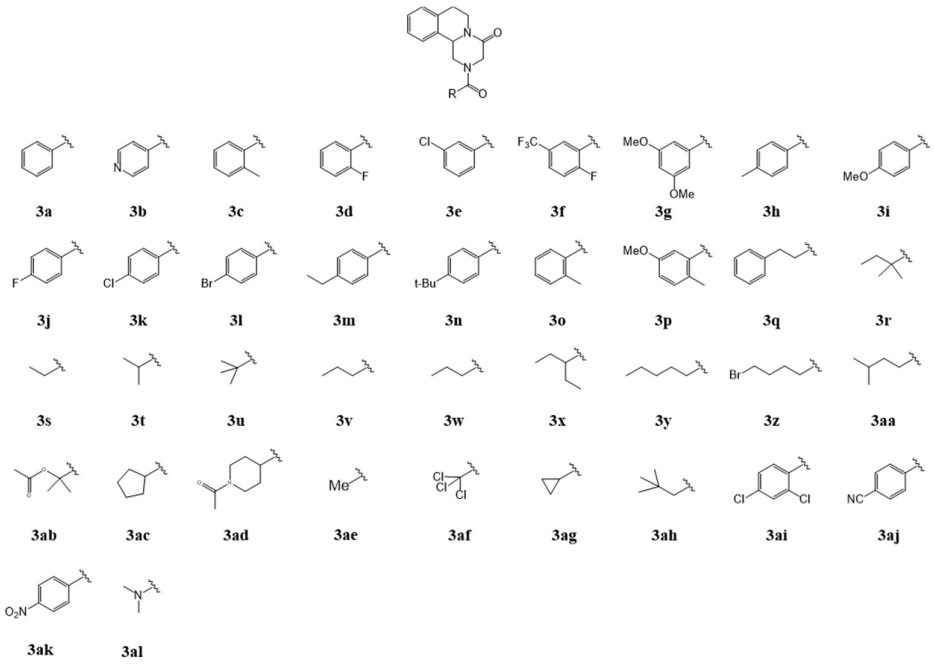

Figure A - I. 1. List of the synthesized praziquantel derivatives

Praziquantel derivatives **3ae-al** were synthesized in three steps (Figure A - I. 2):

(i) commercial racemic praziquantel was first hydrolysed into racemic praziquanamine by following a procedure previously published.[1] racemic praziquanamine was prepared with a satisfactory yield of 93 % (mp = 119.5°C), ^{1}H NMR (300MHz, $CDCl_3$) δ (ppm): 7.20-7.05 (m, 4H), 4.84-4.71 (m, 2H), 3.70-3.43 (m, 3H), 2.86-2.65 (m, 4H), 2.08 (s, 1H)).

(ii) After the hydrolysis step, racemic praziquanamine was either used in its racemic form or resolved to obtain (*R*) or (*S*)-praziquanamine by using the cyclic Pasteurian resolution procedure based on the reported one by Woelfle *et al*.[1] using a 1:1 ratio of IPA/H_2O ratio (*e.e.* = 99% (determined by polarimetry in dichloromethane:[1] $[\alpha]_D^{20}$= - 305 °), m_p = 122.1°C).

(iii) Finally, racemic and enantiopure derivative of were prepared following a reported procedure[2] with slight modifications: 1.1 eq of the corresponding acyl chloride was added dropwise under argon atmosphere to an ice-cooled solution of either racemic or (*R*)-praziquanamine (1eq) and triethylamine (1.5eq) in anhydrous dichloromethane (25mL). Water was added after 15h of stirring at room temperature and the biphasic liquid was stirred for an 1h. After removal of the water layer, the remaining organic layer was washed with a saturated solution of sodium carbonate, a 0.5 M hydrochloric acid solution and a saturated NaCl aqueous solution. Afterwards, the organic layer was dried over magnesium sulfate, filtered, and evaporated with a rotary evaporator to afford either racemic or enantiopure praziquantel derivative (> 70% yield). This method has been used at different scale (from few mg to ca. 10g of final product). All derivatives were then check for purity by NMR, DSC and XRPD. Derivatives

---

[1] Woelfle, M.; Seerden, J.-P.; de Gooijer, J.; Pouwer, K.; Olliaro, P.; Todd, M. H. Resolution of Praziquantel. *PLoS Negl Trop Dis* **2011**, *5* (9), e1260. https://doi.org/10.1371/journal.pntd.0001260.

[2] Valenti, G.; Tinnemans, P.; Baglai, I.; Noorduin, W. L.; Kaptein, B.; Leeman, M.; ter Horst, J. H.; Kellogg, R. M. Combining Incompatible Processes for Deracemization of a Praziquantel Derivative under Flow Conditions. *Angew. Chem.* **2021**, *133* (10), 5339–5342. https://doi.org/10.1002/ange.202013502.

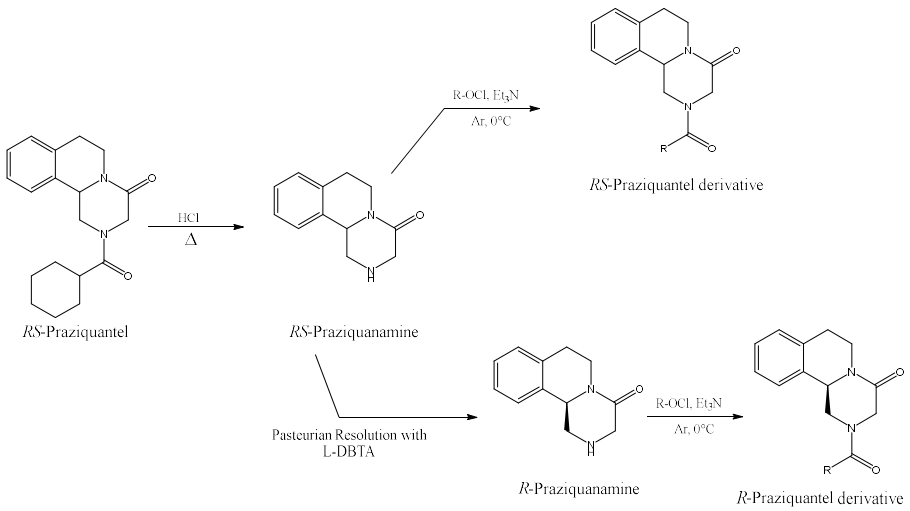

Figure A - I. 2. Scheme of the synthesis route of the praziquantel derivatives from racemic praziquantel.

A - I.1.3. Synthesis of the 1,3-dimethylxanthine-based chiral derivatives

Enantiopure diprophylline was synthesized following a published procedure.[3] Enantiopure proxyphylline was synthesized from theophylline and enantiopure propylene oxide following a published procedure with slight modifications (Figure A - I. 3).[4]

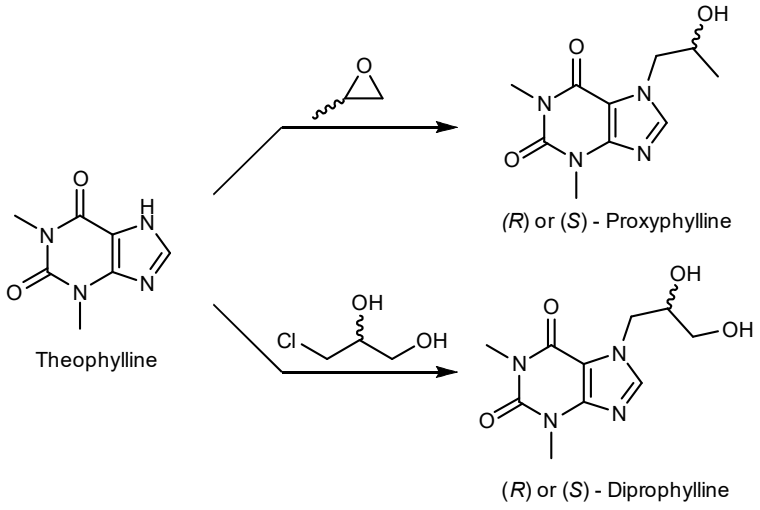

Figure A - I. 3. Synthesis route of enantiopure proxyphylline and diprophylline.

[3] Brandel, C.; Amharar, Y.; Rollinger, J. M.; Griesser, U. J.; Cartigny, Y.; Petit, S.; Coquerel, G. Impact of Molecular Flexibility on Double Polymorphism, Solid Solutions and Chiral Discrimination during Crystallization of Diprophylline Enantiomers. *Mol. Pharmaceutics* **2013**, *10* (10), 3850–3861. https://doi.org/10.1021/mp400308u.

[4] Borowiecki, P.; Paprocki, D.; Dudzik, A.; Plenkiewicz, J. Chemoenzymatic Synthesis of Proxyphylline Enantiomers. *J. Org. Chem.* **2016**, *81* (2), 380–395. https://doi.org/10.1021/acs.joc.5b01840.

A mixture of anhydrous theophylline (7.5 g, 41.6 mmol, 1 eq), (*R*) or (*S*)-propylene oxide (purity 99%, *e.e.* 97%) (3.5 mL, 49.9 mmol, 1.2 eq) and a catalytic amount of triethylamine (1.2 mL, 8.3 mmol, 0.2 eq) in methanol (50 mL) was stirred overnight at reflux. After cooling the mixture, the solvent was evaporated under reduced pressure. Then, the resulting solid was recrystallized from methanol, and the flask was stored in the freezer (-18 °C) overnight. The obtained solid was filtered off and washed with cold ethanol leading to the desired product (*R*) or (*S*)-7-(2-Hydroxypropyl) theophylline, (*R*) or (*S*)-PXL, as a white crystalline solid (8.4 g, 35.3 mmol, yield = 85 %, mp = 148.3 °C (DSC), $[\alpha]_D^{20}$= – 53° (c = 1.00 mg.mL^{-1}, $CHCl_3$, (*S*)-PXL), *e.e.* HPLC (*S*)-PXL = 99.9 %, ^{1}H NMR ($CDCl_3$, 300 MHz) δ (ppm): 1.25 – 1.27 (d, 3H, J = 6 Hz), 3.38 (s, 3H), 3.56 (s, 3H), 4.05- 4.19 (m, 2H), 4.46-4.52 (dd, 1H, J1 = 3 Hz, J2 = 15 Hz), 7.61 (s, 1H).

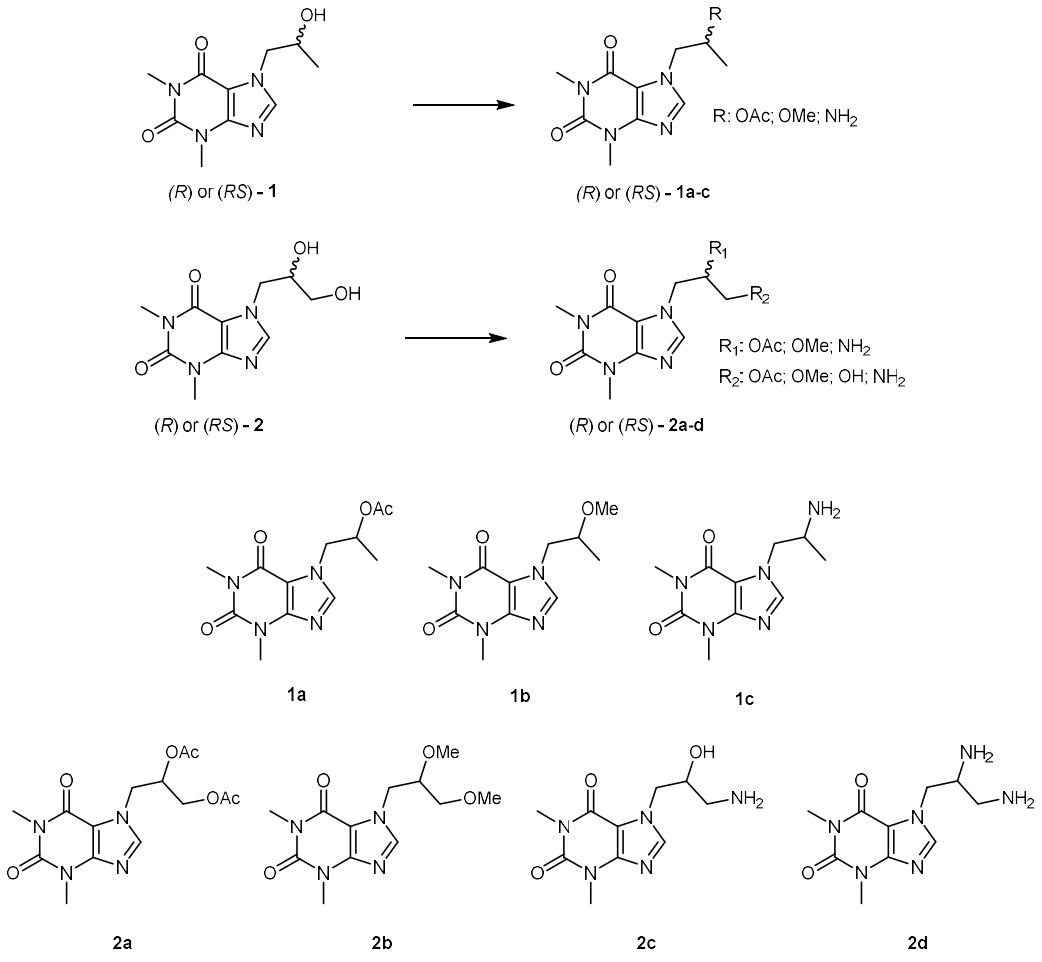

Figure A - I. 4. List of the 1,3-dimethylxanthine-base chiral derivatives.

The different 1,3-dimethylxanthine-base chiral derivatives (Figure A - I. 4) were synthesized as followed :

1-(1,3-dimethyl-2,6-dioxo-1,2,3,6-tetrahydro-7H-purin-7-yl)propan-2-yl acetate (1a) and 3-(1,3-dimethyl-2,6-dioxo-1,2,3,6-tetrahydro-7H-purin-7-yl)propane-1,2-diyl diacetate (2a): ca. 1g of either racemic or enantiopure proxyphylline or diprophylline were set at reflux in 60mL of in acetic anhydride for 8 hours. Thereby, the resulting reaction mixtures were cooled to room temperature and the solvent evaporated under vacuum and recrystallized in 10 mL of a 1:1 DCM/Hexane solvent mixture to produce white powders (> 80 % yield). ^{1}H NMR ($CDCl_3$, 300 MHz) δ (ppm, **1a**): 1.27 (d, 3H), 1.95 (s, 3H), 3.40 (s, 3H), 3.59 (s, 3H), 4.21 - 4.64 (dq, J^1 = 6 Hz, J^2 = 3 Hz 2H), 5.21 – 5.32 (m, 1H), 7.53 (s, 1H). ^{1}H NMR (DMSO-d6, 300 MHz) δ (ppm, **2a**) 1.93 (s, 3H), 2.03 (s, 3H), 3.23 (s, 3H), 3.43 (s, 3H), 4.05 - 4.29 (dq, J^1 = 6 Hz, J^2 = 3 Hz 2H), 4.44 - 4.60 (dq, J^1 = 6 Hz, J^2 = 3 Hz, 2H), 5.34 – 5.39 (m, 1H), 8.07 (s, 1H).

7-(2-methoxypropyl)-1,3-dimethyl-3,7-dihydro-1H-purine-2,6-dione (1b) and 7-(2,3-dimethoxypropyl)-1,3-dimethyl-3,7-dihydro-1H-purine-2,6-dione (2b): ca. 0.5g of either racemic or enantiopure proxyphylline or diprophylline were stirred with NaH (1eq per hydroxyl function) in anhydride DMF under argon at 0 °C for 30min. Thereby, MeI (1eq per hydroxyl function) was added dropwise and the resulting reaction mixtures were left stirring for an additional 24h at room temperature. The DMF was then evaporated under vacuum and the resulting oil was redissolve in DCM, washed with 0.1M aqueous LiCl solution and brine. The organic layer was dried over $MgSO_4$ and evaporated under vacuum to yield a pale white to brownish solid (> 50 % yield). For some reactions, a yellowish oil was obtained that necessitated a recrystallization step from pentane. ^{1}H NMR ($CDCl_3$, 300 MHz) δ (ppm, **1b**): 1.22 (d, 3H),3.25 (s, 3H), 3.42 (s, 3H), 3.62 (s, 3H), 3.64 – 3.68 (m, 1H), 4.07 - 4.51 (dq, J^1 = 9 Hz, J^2 = 6 Hz 2H), 7.62 (s, 1H). ^{1}H NMR (Acetone-d6, 300 MHz) δ (ppm, **2b**) 3.32 (s, 3H), 3.38 – 3.42 (s, s and m, 3H, 3H and 1H), 3.59 - 3.61 (s and m, 3H and 1H), 3.66 – 3.72 (m, 1H), 4.24 - 4.62 (dq, J^1 = 6 Hz, J^2 = 3 Hz, 2H), 7.60 (s, 1H).

7-(2-aminopropyl)-1,3-dimethyl-3,7-dihydro-1H-purine-2,6-dione (1c): ca. 10g of racemic proxyphylline were stirred with TsCl (1.2 eq) in 30 mL of dried DCM under argon. Then, Et_3N (1.2 eq) was added at 0 °C, and the resulting reaction mixture was stirred for 24h. Thereby, water was added to dissolve the remaining solid, the organic layer was washed with brine, dried over $MgSO_4$ and evaporated under vacuum. The residue was purified on a silicagel

column using 8:2 AcOEt/Heptane solvent mixture to afford racemic 1-(1,3-dimethyl-2,6-dioxo-1,2,3,6-tetrahydro-7H-purin-7-yl)propan-2-yl 4-methylbenzenesulfonate (89 % yield). ^{1}H NMR ($CDCl_3$, 300 MHz) δ (ppm, **tosylated 1c**): 1.55 (d, 3H), 2.34 (s, 3H), 3.32 (s, 3H), 3.54 (s, 3H), 3.98 - 4.36 (dq, J^1 = 9 Hz, J^2 = 6 Hz 2H), 4.88 - 4.97 (m, 1H), 7.09 – 7.49 (dd, 2H), 7.46 (s, 1H).

ca. 1g of racemic **tosylated 1c** and NaN_3 (3 eq) were dissolve in 15 mL of dry DMF and stirred at 80 °C for 3h under argon. Thereby, the resulting reaction mixture was cooled to room temperature and the solvent evaporated under vacuum. The residue was purified on a silicagel column using 8:2 AcOEt/Heptane solvent mixture to afford racemic 7-(2-azidopropyl)-1,3-dimethyl-3,7-dihydro-1H-purine-2,6-dione (83 % yield). ^{1}H NMR ($CDCl_3$, 300 MHz) δ (ppm, **azide 1c**): 1.27 (d, 3H), 3.36 (s, 3H), 3.55 (s, 3H), 3.95 - 4.04 (m, 2H), 4.36 - 4.45 (m, 1H), 7.58 (s, 1H).

ca. 0.5g of racemic **azide 1c** and PPh_3 (4 eq) was stirred in 7.5 mL of pyridine for 1h at room temperature. Thereby, 20 mL of aqueous NH_3 32% was added and stirred for an additional 3h. The water layer was then washed with PE and DCM, evaporated under vacuum, and the recovered residue was recrystallized from EtOH to yield racemic **1c** in its dehydrated solid form (62 % Yield). ^{1}H NMR (D_2O, 300 MHz) δ (ppm, **1c**): 1.39 (d, 3H), 3.38 (s, 3H), 3.58 (s, 3H), 3.95 - 4.00 (m, 1H), 4.60 - 4.62 (d, 2H), 8.09 (s, 1H).

7-(3-amino-2-hydroxypropyl)-1,3-dimethyl-3,7-dihydro-1H-purine-2,6-dione (2c) and 7-(2,3-diaminopropyl)-1,3-dimethyl-3,7-dihydro-1H-purine-2,6-dione (2d): ca. 3g of either racemic or enantiopure diprophylline were stirred with TsCl (1.2 eq) in 30mL of dried DCM under argon. Then, Et_3N (1.2 eq) was added at 0 °C, and the resulting reaction mixture was stirred for 24h. Thereby, water was added to dissolve the remaining solid, the organic layer was washed with brine, dried over $MgSO_4$ and evaporated under vacuum. The residue containing **mono-tosylated 2c** and **di-tosylated 2d** was purified on a silicagel column using 8:2 AcOEt/Heptane solvent mixture to afford either racemic or enantiopure 3-(1,3-dimethyl-2,6-dioxo-1,2,3,6-tetrahydro-7H-purin-7-yl)-2-hydroxypropyl-4-methylbenzenesulfonate (**mono-tosylated 2c**) and racemic or enantiopure 3-(1,3-dimethyl-2,6-dioxo-1,2,3,6-tetrahydro-7H-purin-7-yl)propane-1,2-diyl-bis(4-methylbenzenesulfonate) (**di-tosylated 2d**) (1 : 1.01 ; 54 % yield). ^{1}H NMR ($CDCl_3$, 300 MHz) δ (ppm, **mono-tosylated 2c**): 2.47 (s, 3H), 3.38 (s, 3H), 3.58 (s, 3H), 3.98 – 4.07 (m, 2H), 4.09 – 4.15 (m, 1H), 4.32 - 4.37 (m, 1H), 4.53 - 4.58 (m, 1H), 7.36 - 7.38 (dd, 2H), 7.64 (s, 1H), 7.79 – 7.81 (dd, 2H). ^{1}H NMR ($CDCl_3$, 300 MHz) δ (ppm, **di-tosylated**

2d): 2.33 (s, 3H), 2.48 (s, 3H), 3.29 (s, 3H), 3.53 (s, 3H), 4.32 – 4.51 (m, 4H), 4.96 – 5.02 (m, 1H), 7.04 - 7.06 (dd, 2H), 7.38 - 7.39 (dd, 2H), 7.41 - 7.42 (dd, 2H), 7.45 (s, 1H), 7.82 – 7.85 (dd, 2H)

ca. 1g of either racemic or enantiopure **mono-tosylated 2c** or **di-tosylated 2d** and NaN_3 (3 eq per tosylated function) were dissolve in 15 mL of dry DMF and stirred at 80 °C for 3h under argon. Thereby, the resulting reaction mixture was cooled to room temperature and the solvent evaporated under vacuum. The residue was purified on a silicagel column using 8:2 AcOEt/Heptane solvent mixture to afford racemic or enantiopure 7-(3-azido-2-hydroxypropyl)-1,3-dimethyl-3,7-dihydro-1H-purine-2,6-dione (**mono-azide 2c**) and racemic or enantiopure 7-(2,3-diazidopropyl)-1,3-dimethyl-3,7-dihydro-1H-purine-2,6-dione (**di-azide 2c**) (85 % yield). ^{1}H NMR ($CDCl_3$, 300 MHz) δ (ppm, **mono-azide 2c**): 3.41 (s, 3H), 3.42 - 3.44 (m, 1H), 3.59 (s, 3H), 3.71 – 3.72 (m, 1H), 4.16 – 4.18 (m, 1H), 4.31 - 4.36 (m, 1H), 4.50 - 4.54 (m, 1H), 7.63 (s, 1H). ^{1}H NMR ($CDCl_3$, 300 MHz) δ (ppm, **di-azide 2d**): 3.41 (s, 3H), 3.44 - 3.47 (m, 1H), 3.61 (s, 3H), 3.66 – 3.70 (m, 1H), 4.15 – 4.21 (m, 2H), 4.49 - 4.56 (m, 1H), 7.63 (s, 1H).

ca. 0.5g of racemic or enantiopure **mono-azide 2c** and PPh_3 (4 eq) was stirred in 7.5 mL of pyridine for 1h at room temperature. Thereby, 20 mL of aqueous NH_3 32% was added and stirred for an additional 3h. The water layer was then washed with PE and DCM, evaporated under vacuum, and the recovered residue was recrystallized from EtOH to yield racemic **2c** (85 % Yield). ^{1}H NMR (D_2O, 300 MHz) δ (ppm, **1c**): 2.63 - 2.85 (qd, 2H), 3.29 (s, 3H), 3.47 (s, 3H), 3.95 - 3.98 (m, 1H), 4.21 - 4.23 (m, 1H), 4.44 - 4.48 (m, 1H), 7.97 (s, 1H). ESI-MS$^+$ (calc. for $C_{10}H_{15}O_3N_5$ 253.12): m/z $[M+H]^+$ = 254.1248 (m_{th} = 254.12477) ; m/z $[M+Na]^+$ = 276.1066 (m_{th} = 276.10671). The same protocol using 8 eq of PPh_3 was applied to **di-azide 2d**, but **2d** did not crystallizes

A - I.2. Materials

A - I.2.1. Thermal analyses

DSC and TGA-DSC analyses were performed on a DSC 214 Polyma (Netzsch, Germany) and a STA 449C (Netzsch), respectively. Each analysis was performed using circa 2 to 6 mg of sample in aluminium pans with pierced lids. Most analyses involved a single heating step at a heating rate of 2 K.min^{-1}, but more complex temperature programs were also used, sometimes involving isothermal steps. The atmosphere of the analysis was regulated by a nitrogen flux (40mL.min^{-1}). The Proteus Software was used for data processing. Onset temperatures were

employed for invariants phenomena whenever feasible with an experimental error of ± 0.2 °C, while peak temperatures were employed for liquidus with an experimental error of ± 0.5 °C.

A - I.2.2. X-Ray Powder Diffraction (XRPD)

XRPD analyses were performed at 25 °C using a D8 Discover diffractometer (Bruker analytic X-ray Systems, Germany) with a Bragg-Brentano geometry. The instrument is equipped with a copper anticathode (40 kV, 40 mA, Kα radiation, λ =1.5418 Å), and a Lynx-Eye linear detector. The diffraction patterns were recorded with a scan rate of 0.04° (2θ) in the angular range of 3-30° 2θ, with a counting time of 0.5s per step. The Eva software was used for data processing.

A - I.2.3. Single Crystal X-Ray Powder Diffraction (SC-XRD)

Crystal structure resolutions were performed on three different apparatuses:

Reflections were measured on a Bruker D8 Quest diffractometer with sealed tube and Triumph monochromator (λ = 0.71073Å). Software package used for the intensity integration was Saint (v8.40a).[5] Absorption correction was performed with SADABS.[6] The structures were solved with direct methods using SHELXT-2014/5.[7] Least-squares refinement was performed with SHELXL-2018/3[8] against $\left|F_h^{\circ}\right|^2$ of all reflections. Non-hydrogen atoms were refined freely with anisotropic displacement parameters. Hydrogen atoms were placed on calculated positions or located in different Fourier maps. All calculated hydrogen atoms were refined with a riding model.

Reflections were measured on a Bruker SMART APEX diffractometer equipped with a CCD area detector (with Mo Kα1 = 0.71071 Å). The cell parameters and the orientation matrix of the

---

[5] SAINT+ V6.02 (1999), Saint Software Reference Manual, Bruker Advanced X Ray Solutions, Inc., Madison, Wisconsin, USA.

[6] Krause, L.; Herbst-Irmer, R.; Sheldrick, G. M.; Stalke, D. Comparison of Silver and Molybdenum Microfocus X-Ray Sources for Single-Crystal Structure Determination. *J Appl Crystallogr* **2015**, *48* (1), 3–10. https://doi.org/10.1107/S1600576714022985.

[7] Sheldrick, G. M. *SHELXT* – Integrated Space-Group and Crystal-Structure Determination. *Acta Crystallogr A Found Adv* **2015**, *71* (1), 3–8. https://doi.org/10.1107/S2053273314026370.

[8] Sheldrick, G. M. Crystal Structure Refinement with *SHELXL*. *Acta Crystallogr C Struct Chem* **2015**, *71* (1), 3–8. https://doi.org/10.1107/S2053229614024218.

crystal were preliminary determined by using SMART Software.[9] Intensities were integrated and corrected for Lorentz polarization and adsorption effects using SAINT Software.[5] The program package WinGX[10] was used for structure solution and refinement.

Reflections were measured on a SuperNova dual wavelength microfocus diffractometer, equipped with a 135 mm Atlas CCD detector, using Cu- K_α radiation (λ=1.54184 Å). The data collection, reduction, and analytical absorption corrections were performed with the CrysAlisPro program suite.[11]

The crystal structures have been solved by direct methods and successive Fourier difference syntheses and refined by weighted full-matrix least squares method against F^2 using SHELX suite.[8] All non-hydrogen atoms have been refined anisotropically. All H atoms were located in difference Fourier electron-density maps and were treated as riding on their parent atoms, with C-H = 0.950 Å, and Uiso(H) = 1.2x Uiso(C) for bond length distances and riding restraints, respectively. Views of the crystal structures have been prepared by using the Mercury[12] software and measurements were performed using the Diamond[13] software.

A - I.2.4. Temperature Resolved X-Ray Powder Diffraction (TR-XRPD)

Temperature Resolved- X-Ray Powder Diffraction analyses were performed on a Bruker- D8 Advance Series II diffractometers equipped with a hot-stage temperature cell TTK 450 Anton Paar. Measurements were performed from 20°C up to 130°C by 5°C steps. Between each measurement, heating rate was fixed at 2K/min. The analytical conditions of every analyzing step were as following: angular range: 4°-30° (2θ) ; step size : 0.04° ; measuring time per step: 0.5s ; kβ filter (Ni); cupper anode (40 kV, 40 mA) and fixed sample.

A - I.2.5. *In-situ* X-Ray Powder Diffraction (InSituX®)

---

[9] SMART for WNT/2000 V5.622 (2001), Smart Software Reference Manual, Bruker Advanced X Ray Solutions, Inc., Madison, Wisconsin, USA.
[10] WinGX: Version 1.70.01: An Integrated System of Windows Programs for the Solution, Refinement and Analysis of Single Crystal X-Ray Diffraction Data, By LouisJ. Farrugia, Dept. of Chemistry, University of Glasgow.
[11] CrysAlisPro (CCD & RED), 2021.
[12] Macrae, C. F.; Sovago, I.; Cottrell, S. J.; Galek, P. T. A.; McCabe, P.; Pidcock, E.; Platings, M.; Shields, G. P.; Stevens, J. S.; Towler, M.; Wood, P. A. Mercury 4.0: From Visualization to Analysis, Design and Prediction. *J Appl Cryst* **2020**, *53* (1), 226–235. https://doi.org/10.1107/S1600576719014092.
[13] Pennington, W. T. (reviewer). DIAMOND – Visual Crystal Structure Information System. *J Appl Cryst* **1999**, *32* (5), 1028–1029. https://doi.org/10.1107/S0021889899011486.

In situ X-ray diffraction data were collected using a prototype of diffractometer developed in our laboratory (Figure A - I. 5).[14] This apparatus has an original goniometer with a reverse-geometry (−θ/−θ). Its association with a dedicated reactor, with a bottom window transparent to X-ray, allows in situ analyses. The instrument is equipped with a copper anticathode (40 kV, 40 mA, Kα radiation, λ =1.5418 Å), and a Lynx-Eye linear detector. X-ray diffraction analyses were performed with a step of 0.04° (2θ), with 0.5 s/step from 5 to 30° (2θ).

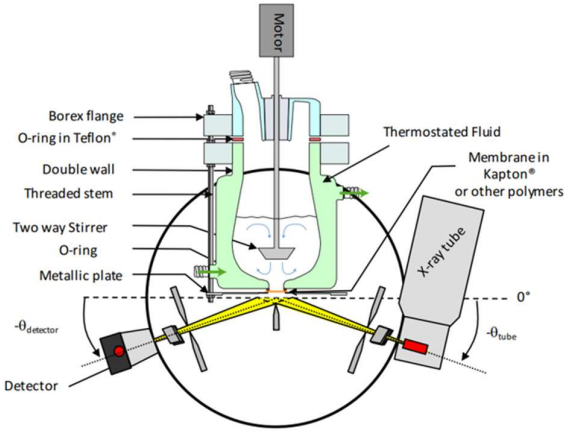

Figure A - I. 5. Schematic representation of the InSituX prototype.

A - I.2.6. Polarimetry

The optical rotations of praziquanamine samples were measured at 20 °C with an incident wavelength of λ = 589 nm on an Anton Paar 5100 polarimeter in DCM ($[\alpha]_D^{20}$= - 305 °)[1].

A - I.2.7. Hot Stage Microscopy (HSM)

Polarized light microscopy images and videos were taken with a Nikon Eclipse LV100 optical microscope, equipped with a Nikon Digital sight DS-Ri1 camera. The samples (a few milligrams of powder in a quartz cell) were placed in a computer-controlled heating–cooling stage (Linkam THMS-600). The temperature was regulated via Linksys software.

A - I.2.8. Second Harmonic Generation (SHG)

[14] Coquerel, G.; Sanselme, M.; Lafontaine, A. Method of Measuring Scattering of X-Rays, Its Applications and Implementation Device. WO2012/136921, October 11, 2012.

A Nd:YAG Q-switched laser (Quantel) operating at 1.06 µm was used to deliver up to 360 mJ pulses of 5 ns duration with a repetition rate of 10 Hz. An energy adjustment device made up of two polarizers (P) and a half-wave plate (λ/2) allowed the incident energy to vary from 0 to ca. 200 mJ per pulse. A RG1000 filter was used after the energy adjustment device to remove light from laser flash lamps. The signal generated by the sample (diffused light) was collected into an optical fibre (500 µm of core diameter) and directed onto the entrance slit of a spectrometer (Ocean Optics). A boxcar integrator allowed an average spectrum (spectral range 490-590 nm) with a resolution of 0.1 nm to be recorded over 3 s (30 pulses). SHG signal intensities were compared to the signal of a reference compound (α-quartz powder- 45 µm average size).

A - I.2.9. Second Harmonic Generation Microscopy (SHG-M)

Two photon fluorescence (TPF) and second harmonic generation (SHG) microscopy were performed by coupling an Insight X3 single laser with automated dispersion compensation (Spectra-physics, Santa Clara, USA) and a TCS SP8 confocal microscope (Leica Systems, Wetzlar, Germany). The laser emits pulsed light with a repetition rate of 80 MHz and a temporal width around 120 fs. It is also tuneable between 680 and 1300 nm, its average power at 900 nm is around 2.50 W. The effective power used during experiments can be controlled as a percentage of the maximum power. An electro-optical modulator is used to adjust the laser power at the entrance of the confocal system. A dedicated software (LASX Leica software, Leica Systems) is used to control the laser. The confocal microscope is equipped with a long working distance dry Leica objective (HC PL Fluotar 5x NA 0.15). Three detectors are used to record images. Two of them are Leica hybrid descanned detectors. They can collect light between 380 and 780 nm by dispersing photons with a prism and by selecting the spectral band with a motorized split mirror. The third detector is a photomultiplier detector operating in transmission and giving an image of the sample in shades of grey (bright field image). The whole coupled system permits to perform confocal microscopy of the samples, giving 3D information.

A - I.2.10. Chiral-High-Performance Liquid Chromatography (cHPLC)

Chiral HPLC analyses were performed using an Ultimate 3000 HPLC (ThermoFisher Scientific). For the determination of enantiomeric composition of samples from the praziquantel library,

HPLC analysis was performed on a Phenomenex Lux Cellulose 4 column (3.0 x 150 mm x 3 µm), Chiracel OJ-H, OD-H columns (4.6 x 250 mm, 5µm) or CHIRALPAK IC column (4.6 x 250 mm, 5µm) with a UV detection at a wavelength of 220 nm with a mobile phase consisting of n-heptane and 2-propanol at flow rate of 1 mL.min^{-1}.

For the determination of enantiomeric composition of samples from the triazole ketone library (*x*%-**1b**): cHPLC was performed using a Chiracel OD-H column (250 mm ×4.6mm×5 µm) with a UV detection at a wavelength of 220 nm, employing a mixture of isopropyl 2-propanol / n-heptane (3:97, v/v) as eluent at a flow rate of 1 mL.min^{-1}. (*x*%-**1d**): 2D-cHPLC method was performed using a Chiracel OD-H and Chiralpak AD-H columns (250 mm ×4.6mm×5 µm) with a UV detection at a wavelength of 220 nm using a mixture of 2-propanol / n-heptane / TFA (95:5:0.1, v/v/v) as eluent at a flow rate of 1 mL.min^{-1}.

A - I.2.11. Liquid Chromatography - Mass Spectrometry (UHPLC-MS)

Chromatography separation was achieved using a Vanquish UHPLC system (Thermo Scientific) equipped with a Acquity UPLC BEH column (C18 2.1 x 50 mm, 1.7 µm) set at 35 °C with a constant flow rate of 0.3 mL.min^{-1}. The injection volume and temperature were set at 0.5 µL and 10 °C. The mobile phase consisted of H_2O and ACN with the following gradient procedure: H_2O / ACN (98:2 v:v) to ACN 100 % in 4min, ACN 100 % for 1.3 min and H_2O / ACN (98:2 v:v) in 0.5 min. The chromatographic system was connected to an Orbitrap Exploris 120 mass spectrometer (Thermo Scientific GmbH; Dreieich, Germany) equipped with an electrospray ionization (ESI) source in positive mode at spray voltage 3.5 kV. Sheath gas, auxiliary gas and sweep gas were set at 50, 10 and 0 *a.u.*, respectively. The capillary temperature and the vaporizer temperature were set to 325 °C and 350 °C, respectively. Data acquisition was performed from 120 – 1800 m/z at a resolution of 60.000.

A - I.2.12. Nuclear Magnetic Resonance (NMR)

^{1}H spectra were recorded on a Fourier 300 MHz FT-NMR Spectrometer System (Bruker, Germany) using deuterated solvents (> 99.98 %). The data were processed using the MestReNova software.

A - I.2.13. High Energy Milling

Milling experiments were all conducted with a Mixer Mill MM400 equipped with two 10mL-jars. They are composed of ZrO2 as well as the 10mm diameter bead used to ensure the milling. The different compositions of the two binary racemic isopleth sections between the triazole ketone derivatives were prepared by grinding 150 mg of the targeted mixtures at 30 Hz for 30 minutes. In all mixed crystal deracemization experiments, ca. 100 mg of model compounds was ground with around NaOH (0.5eq) and 50 mg of NaCl. All jars were prepared in glove bags under nitrogen atmosphere. The mixtures were ground at 30 Hz for at least four consecutive hours. The maximum of the ground material was removed and washed with a sufficient amount of water to remove any trace of base before cHPLC analyses.

A - I.2.14. Scanning Electron Microscopy (SEM)

SEM pictures were obtained with a JEOL JCM-5000 NeoScope instrument (secondary scattering electron) at an accelerated voltage between 10 and 15 kV. Powder samples were stuck on an SEM stub with gloss carbon and coated with gold to reduce electric charges induced during analysis with a NeoCoater MP-19020NCTR.

A - I.3. Methods

A - I.3.1. Seeded Isothermal Preferential Crystallization procedure

SIPC method

$\sim$ 800 mg of racemic **3t** and **3ae** was dissolved in 10 mL and 30 mL IPA using a 20 mL and 50 mL vials respectively by heating the resulting stirred mixture (cross-shaped PTFE magnetic stirring bars (BOHLC369-25, VWR) and standard stirring plate at 700rpm) until a clear solution is obtained (double-jacketed flasks connected to a circulating cryostat (F34-HE, Julabo)). The clear solution was then filter through 0.22 µm syringe filter and cooled to reach a supersaturation $\beta = 2$ (15 °C and 20 °C respectively) with respect to the solubility of the racemic compound and seeded with 40 mg of pure enantiomer.

Sampling methods and sample preparation

For compound **3t** and **3ae**, the chiral resolution via preferential crystallization was monitored by sampling $\sim$ 0.5mL of the slurry from the crystallization flask using a single channel

mechanical pipettor (613-0155, VWR). The solid and liquid phases were isolated from the collected suspension following two procedures :

- By casting it on top of filter papier laid down on glass filter connected to a vacuum filtration setup
- By centrifuge filtration using standard micro centrifuge (Fisherbrand) and 0.22µm cellulose acetate centrifuge tube filter (525-0017, VWR)

$\sim$ 1.5 mg of the solid phase was dissolved in 1.5 mL of a n-Heptane/IPA mixture (80/20; v/v) with subsequent ultrasonication while the liquid phase was diluted 9 times with the same solvent mixture prior to HPLC analyses.

HPLC methods and SIPC monitoring

Enantioselective HPLC analyses for compound **3t** and **3ae** were performed on a Chiracel OD-H column (4.6 x 250 mm, 5µm) with a mobile phase consisting of n-heptane and 2-propanol (85/15 and 60/40 v:v respectively) at flow rate of 1 $mL.min^{-1}$ with a UV detection at 220 nm. Each run had a total time of 60 minutes.

The crystallized mass was obtained by (i) weighing the total amount of enantiopure solid recovered or (ii) determining the concentration of the solute based on a calibration curve.

A - I.3.2. Solubility measurements & Crystal16

Temperature-dependent solubilities were measure using the Crystal16 apparatus (Technobis, Alkmaar, the Netherlands) using four 1.5 mL vials at different concentrations. The temperature program consisted in three consecutive cycles involving a heating step at 0.3 $K.min^{-1}$, a holding step at the top temperature for 15 minutes, a cooling step at 0.5 $K.min^{-1}$ and a holding step at the bottom temperature for at least 6h to ensure the recrystallization of the samples. Clear points were characterized once 100% transmittivity was reach during the heating steps. The clear temperatures were fitted with the Van 't Hoff equation, allowing the estimation of any solubility of a pure component in the observed temperature. All vials were weighted after each experiment to ensure that no evaporation resulting from the successive cycles occurred.

Isothermal solubilities of the mixed crystal systems were measured in triplicate in various solvent and temperature by using the standard gravimetric method. The suspensions were prepared in targeted solvents and stirred at fixed temperatures using a thermostated double-jacket glass vessels. After equilibration for at least 2days, the suspension was filtered using a 13mm syringe filter (0.45 µm PTFE membrane), the solid phase in equilibrium with the solution was identified by XRPD and the saturated solution was weighed before and after evaporation.

A - II. Crystallographic data

	(*RS*)-**3t**	(*R*)-**3t**	(*RS*)-**3af**	(*S*)-**3af**	(*RS*)-**3ah**	(*RS*)-**3al**
Crystal System	orthorhombic	orthorhombic	monoclinic	orthorhombic	orthorhombic	orthorhombic
Space Group	*P*bca	$P2_12_12_1$	$P2_1$/n	$P2_12_12_1$	*I*ba2	*P*ccn
Z, Z'	16, 2	4, 1	4, 1	4, 1	8, 1	8, 1
***a* (Å)**	16.3560(6)	10.4553(5)	10.1228(3)	10.4629	44.0851(13)	34.2375(10)
***b* (Å)**	10.4483(3)	90	10.5106(3)	10.5045	7.5935(2)	7.5473(2)
***c* (Å)**	33.5637(12)	90	14.2364(4)	13.2819	10.2787(3)	10.6671(3)
***α* (°)**	90	90	90	90	90	90
***β* (°)**	90	90	103.5188(10)	90	90	90
***γ* (°)**	90	90	90	90	90	90
V (Å^3)	1472.74(7)	1431.65(12)	1472.74(7)	1459.78	3440.90(17)	2756.39(13)
Calculated Density (g.cm^{-3})	1.261	1.264	1.568	1.581(9)	1.156	1.317
Measured data	6595	3013	4495	3642	1920	4966
Observed data (F_0>4.0 σ(F_0))	3208	2922	4053	3617	1808	4518
No. Restraints/params	0/396	0/183	0/190	0/190	1/202	0/183
Goodness-on-fit on F2	1.014	1.040	1.068	1.071	1.07	1.084
R1/wR2 (F_0>4.0 σ(F_0))	0.0547/0.120	0.0393/0.110	0.0292/0.068	0.0191/0.052	0.0638/0.193	0.0443/0.107
R1 (all data)	0.1281	0.0405	0.0340	0.0192	0.0654	0.0404
Largest diff peak and hole (e$^-$.Å^{-3})	0.163/-0.175	0.132/-0.195	0.411/-0.387	0.243/-0.303	0.367/-0.212	0.424/-0.203

	(*RS*)-**3aj**	(*RS*)-**3aj**	(*RS*)-**3ak**	(*R*)-**3ak**
Crystal System	monoclinic	orthorhombic	Monoclinic	orthorhombic
Space Group	$P2_1/c$	$P2_12_12_1$	*C*2/*c*	$P2_12_12_1$
Z, Z'	8, 2	4, 1	8, 1	4, 1
a **(Å)**	19.3528(13)	6.10440(10)	22.7042(7)	6.6402(2)
b **(Å)**	10.3202(7)	13.2481(2)	10.3391(3)	13.1536(5)
c **(Å)**	16.1741(10)	20.6984(3)	14.8198(5)	18.6825(8)
α **(°)**	90	90	90	90
β **(°)**	95.757(2)	90	105.7620(10)	90
γ **(°)**	90	90	90	90
V (Å^3)	3214.1(4)	1673.91(4)	3348.00(18)	1631.78(11)
Calculated Density (g.cm^{-3})	1.370	1.315	1.394	1.430
Measured data	8012	3648	4508	4057
Observed data (F_o>4.0 σ(F_o))	6361	3648	3475	3948
No. Restraints/params	0/451	0/226	0/235	0/235
Goodness-on-fit on F2	1.031	1.042	1.121	1.016
R1/wR2 (F_o>4.0 σ(F_o))	0.0497/ 0.140	0.0348/0.095	0.0594/0.201	0.0289/0.082
R1 (all data)	0.0652	0.0369	0.0811	0.0299
Largest diff peak and hole (e$^-$.Å^{-3})	0.334/-0.287	0.178/-0.171	0.446/-0.351	0.274/-0.183

The four crystal structures of the praziquantel derivative **3ag** [(*RS-I*)-**3ag**, (*RS-II*)-**3ag**, (*RS-III*)-**3ag**, (*R*)-**3ag**] have been deposited to the CSD with refcodes 2328334 (POZFOD), 2328335 (POZFUJ), 2328336 (POZGAQ), 2328337 (POZGEU). The crystal structures of proxyphylline **RI** and **EI** have been deposited to the CSD with refcodes 2297554 and 2297602 (POZFIX).

A - III. Thermochemical data

Entry	Compound	T_m^{RS} (K)	ΔH_f^{RS} (kJ/mol)	T_m^{R} (K)	ΔH_f^{R} (kJ/mol)	ΔG^{ϕ} (kJ/mol)
3a	2-benzoyl-1,2,3,6,7,11b-hexahydro-4H-pyrazino[2,1-a]isoquinolin-4-one	165.0	34.6	134.5	20.4	4.76
3b	2-isonicotinoyl-1,2,3,6,7,11b-hexahydro-4H-pyrazino[2,1-a]isoquinolin-4-one	140.3	28.9	163.9	25.6	1.00
3c	2-(2-methylbenzoyl)-1,2,3,6,7,11b-hexahydro-4H-pyrazino[2,1-a]isoquinolin-4-one	116.6	22.0	105.7	16.8	2.80
3d	2-(2-fluorobenzoyl)-1,2,3,6,7,11b-hexahydro-4H-pyrazino[2,1-a]isoquinolin-4-one	127.6	27.8	162.8	25.7	0.23
3e	2-(3-chlorobenzoyl)-1,2,3,6,7,11b-hexahydro-4H-pyrazino[2,1-a]isoquinolin-4-one	183.4	37.1	161.6	31.5	4.28
3f	2-(2-fluoro-5-(trifluoromethyl)benzoyl)-1,2,3,6,7,11b-hexahydro-4H-pyrazino[2,1-a]isoquinolin-4-one	148.4	38.2	171.3	n/a	n/a
3g	2-(3,5-dimethoxybenzoyl)-1,2,3,6,7,11b-hexahydro-4H-pyrazino[2,1-a]isoquinolin-4-one	n/a	n/a	n/a	n/a	n/a
3h	2-(4-methylbenzoyl)-1,2,3,6,7,11b-hexahydro-4H-pyrazino[2,1-a]isoquinolin-4-one	187.1	36.4	185.9	37.5	2.74
3i	2-(4-methoxybenzoyl)-1,2,3,6,7,11b-hexahydro-4H-pyrazino[2,1-a]isoquinolin-4-one	218.3	40.9	209.0	52.2	3.55
3j	2-(4-fluorobenzoyl)-1,2,3,6,7,11b-hexahydro-4H-pyrazino[2,1-a]isoquinolin-4-one	187.1	30.7	206.2	40.9	1.02
3k	2-(4-chlorobenzoyl)-1,2,3,6,7,11b-hexahydro-4H-pyrazino[2,1-a]isoquinolin-4-one	217.9	49.2	237.2	52.0	0.87
3l	2-(4-bromobenzoyl)-1,2,3,6,7,11b-hexahydro-4H-pyrazino[2,1-a]isoquinolin-4-one	213.6	45.2	237.4	35.8	1.14
3m	2-(4-ethylbenzoyl)-1,2,3,6,7,11b-hexahydro-4H-pyrazino[2,1-a]isoquinolin-4-one	173.5	38.3	141.1	25.4	5.17
3n	2-(4-(tert-butyl)benzoyl)-1,2,3,6,7,11b-hexahydro-4H-pyrazino[2,1-a]isoquinolin-4-one	202.8	35.9	184.7	33.8	4.00
3o	2-(2-phenylacetyl)-1,2,3,6,7,11b-hexahydro-4H-pyrazino[2,1-a]isoquinolin-4-one	120.8	25.3	116	20.4	2.55

Entry	Compound	T_m^{RS} (K)	ΔH_f^{RS} (kJ/mol)	T_m^{R} (K)	ΔH_f^{R} (kJ/mol)	ΔG^{ϕ} (kJ/mol)
3p	2-(2-(4-methoxyphenyl)acetyl)-1,2,3,6,7,11b-hexahydro-4H-pyrazino[2,1-a]isoquinolin-4-one	n/a	n/a	n/a	n/a	n/a
3q		n/a	n/a	n/a	n/a	n/a
3r	2-(2,2-dimethylbutanoyl)-1,2,3,6,7,11b-hexahydro-4H-pyrazino[2,1-a]isoquinolin-4-one	164.9	35.6	126.5	27.7	5.43
3s	2-propionyl-1,2,3,6,7,11b-hexahydro-4H-pyrazino[2,1-a]isoquinolin-4-one	147.4	35.7	149.9	32.1	2.23
3t	2-isobutyryl-1,2,3,6,7,11b-hexahydro-4H-pyrazino[2,1-a]isoquinolin-4-one	114.8 117.5	24.1 26.2	146.2	31.1	-0.09 0.12
3u	2-pivaloyl-1,2,3,6,7,11b-hexahydro-4H-pyrazino[2,1-a]isoquinolin-4-one	152.0 154.4	33.2 30.6	180.9	36.8	0.11 0.31
3v	2-butyryl-1,2,3,6,7,11b-hexahydro-4H-pyrazino[2,1-a]isoquinolin-4-one	115.1	33.9	n/a	n/a	n/a
3w	2-(3-methylbutanoyl)-1,2,3,6,7,11b-hexahydro-4H-pyrazino[2,1-a]isoquinolin-4-one	111.9	20.3	n/a	n/a	n/a
3x	2-(2-ethylbutanoyl)-1,2,3,6,7,11b-hexahydro-4H-pyrazino[2,1-a]isoquinolin-4-one	124.5	27.0	n/a	n/a	n/a
3y	2-hexanoyl-1,2,3,6,7,11b-hexahydro-4H-pyrazino[2,1-a]isoquinolin-4-one	73.1	24.7	n/a	n/a	n/a
3z	2-(5-bromopentanoyl)-1,2,3,6,7,11b-hexahydro-4H-pyrazino[2,1-a]isoquinolin-4-one	95.2	23.5	n/a	n/a	n/a
3aa	2-(4-methylpentanoyl)-1,2,3,6,7,11b-hexahydro-4H-pyrazino[2,1-a]isoquinolin-4-one	65.5	14.6	n/a	n/a	n/a
3ab	2-methyl-1-oxo-1-(4-oxo-1,3,4,6,7,11b-hexahydro-2H-pyrazino[2,1-a]isoquinolin-2-yl)propan-2-yl acetate	151.6	36.2	n/a	n/a	n/a
3ac	2-(cyclopentanecarbonyl)-1,2,3,6,7,11b-hexahydro-4H-pyrazino[2,1-a]isoquinolin-4-one	133.9	33.0	140.17	25.8	1.95
3ad	2-(1-acetylpiperidine-4-carbonyl)-1,2,3,6,7,11b-hexahydro-4H-pyrazino[2,1-a]isoquinolin-4-one	139.8	14.0	n/a	n/a	n/a
3ae	2-acetyl-1,2,3,6,7,11b-hexahydro-4H-pyrazino[2,1-a]isoquinolin-4-one	142.6 143.6 148.2	25.7 27.6 22.4	180.7	26.3	0.11 0.25 0.55
3af	2-(2,2,2-trichloroacetyl)-1,2,3,6,7,11b-hexahydro-4H-pyrazino[2,1-a]isoquinolin-4-one	185.6	34.7	142.4	23.0	5.66
3ag	2-(cyclopropanecarbonyl)-1,2,3,6,7,11b-hexahydro-4H-pyrazino[2,1-a]isoquinolin-4-one	126.4 144.5 149.3	20.7 41.47 24.7	149.1	23.3	1.05 2.15 2.45

Entry	Compound	T_m^{RS} (K)	ΔH_f^{RS} (kJ/mol)	T_m^{R} (K)	ΔH_f^{R} (kJ/mol)	ΔG^{ϕ} (kJ/mol)
3ah	2-(3,3-dimethylbutanoyl)-1,2,3,6,7,11b-hexahydro-4H-pyrazino[2,1-a]isoquinolin-4-one	113.2	22.7	n/a	n/a	n/a
3ai	2-(2,4-dichlorobenzoyl)-1,2,3,6,7,11b-hexahydro-4H-pyrazino[2,1-a]isoquinolin-4-one	138.2	24.7	157.4	30.9	0.99
3aj	4-(4-oxo-1,3,4,6,7,11b-hexahydro-2H-pyrazino[2,1-a]isoquinoline-2-carbonyl)benzonitrile	217.0	34.5	184.4	27.3	4.93
3ak	2-(4-nitrobenzoyl)-1,2,3,6,7,11b-hexahydro-4H-pyrazino[2,1-a]isoquinolin-4-one	211.4	40.1	224.6	41.2	1.70
3al	N,N-dimethyl-4-oxo-1,3,4,6,7,11b-hexahydro-2H-pyrazino[2,1-a]isoquinoline-2-carboxamide	99.9	21.5	n/a	n/a	n/a
PZQ	2-(cyclohexanecarbonyl)-1,2,3,6,7,11b-hexahydro-4H-pyrazino[2,1-a]isoquinolin-4-one	140.7	34.1	111.14	23.6	4.65

Abstract

Crystallization is widely used for isolating biorelevant enantiopure molecules, which requires enantiomers to self-sort into separate enantiopure crystals. Unfortunately, this behaviour is unpredictable and rare (5-10%), as both enantiomers predominantly crystallize together into racemic crystals, hindering any such chiral sorting. Recognizing that non-equilibrium conditions may overcome these unfavourable statistics, we explored the solid-state landscapes and thermodynamic properties of different series of numerous analogous molecules derived from three distinct chiral cores: Praziquantel, Proxyphylline and Paclobutrazol. Our investigations led to three key approaches for enhancing crystallization-based chiral resolution methods: (i) A directed evolution strategy based on the energy differences between racemic and enantiopure crystal phases, (ii) the identification of specific molecular features favouring the crystallization of enantiopure crystals and (iii) engineering a crystal structure with efficient chiral discrimination capabilities that relies on a host-guest association strategy. These insights relying on the study of chemically related derivatives open new, previously unconsidered possibilities for isolating pure enantiomers that are essential in our daily lives.

Key words: Chirality, Enantiomeric purification, non-equilibrium conditions, Polymorphism, Phase diagram, directed evolution

Résumé

La cristallisation est beaucoup utilisée pour isoler des molécules d'intérêt pharmaceutique sous formes énantiopures, ce qui nécessite que les énantiomère s'auto-discriminent à l'état solide. Malheureusement, ce comportement est imprévisible et rare (5-10%), car les deux énantiomères cristallisent majoritairement sous forme de composé racémique, empêchant toute résolution chirale par cristallisation. Réalisant que des conditions hors équilibres peuvent surmonter ces statistiques défavorables, nous avons exploré les comportements à l'état solide et les propriétés thermodynamiques de différentes séries de molécules analogues dérivées de trois composés model chiraux : le praziquantel, la proxyphylline, le paclobutrazol. Nos investigations ont conduit à trois approches clés pour améliorer les méthodes de résolution chirale par cristallisation : (i) une stratégie d'évolution dirigée basée sur les différences d'énergie entre les phases cristallines racémique et énantiopure, (ii) l'identification de caractéristiques moléculaires spécifiques favorisant la cristallisation de cristaux énantiopures et (iii) la conception d'une structure cristalline avec des capacités de discrimination chirale efficaces reposant sur une stratégie d'association hôte-invité. Ces avancées, reposant sur l'étude de dérivés chimiquement apparentés, ouvrent de nouvelles possibilités, précédemment inconsidérées, pour l'obtention d'énantiomères purs qui sont essentiels dans notre vie quotidienne.

Mots-clés : Chiralité, Purification énantiomérique, conditions hors équilibre, Polymorphisme, Diagramme de phases, évolution dirigée